A STUDY OF CHARGED D^* MESONS PRODUCED IN e^+e^- ANNIHILATION AT $E_{\rm cm} = 29$ GEV

Thesis by

Hitoshi Yamamoto

In Partial Fulfillment of the Requirements

for the Degree of

Doctor of Philosophy

California Institute of Technology

Pasadena, California

1986

(Submitted November 26, 1985)

Acknowledgements

The analysis presented here was made possible by the effort and ingenuity of many people. I would like to acknowledge the contribution by the staff of the PEP storage ring who designed, constructed, and operated the highly sophisticated machine. Above all, I would like to thank the members of the DELCO collaboration: W. B. Atwood, P. H. Baillon, B. C. Barish, G. R. Bonneaud, A. Courau, G. J. Donaldson, R. Dubois, M. M. Duro, E. E. Elsen, S. G. Gao, Y. Z. Huang, G. M. Irwin, R. Johnson, H. Kichimi, J. Kirkby, D. E. Klem, D. E. Koop, J. Ludwig, G. B. Mills, A. Ogawa, D. Ouimette, T. Pal, D. Perret-Gallix, R. Pitthan, D. L. Pollard, D. Porat, C. Y. Prescott, L. Z. Rivkin, L. S. Rochester, W. Ruckstuhl, M. Sakuda, O. Saxton, S. Sherman, E. J. Siskind, R. Stroynowski, S. Sund, S. Q. Wang, S. G. Wojcicki, W. G. Yan, and C. C. Young.

I would like to express special thanks to my advisor Barry Barish who, in spite of his extremely busy schedule, managed to find time to give me advice and read this thesis, to Bill Atwood and Jasper Kirkby for their persistence and imagination without which this experiment could not have been a success, and to Leon Rochester and Ryszard Stroynowski who read the manuscripts and gave me valuable comments. Finally, I would like to thank all of my friends and my family for their support in the course of this study.

Abstract

Charged D^* mesons produced in e^+e^- annihilation at a center-of-mass energy of 29 GeV have been studied with the DELCO detector at the PEP storage ring. The selection criteria of D^* candidates exploit the π/K separation capability in the momentum range from 2.6 GeV/c to 9.2 GeV/c provided by the gas Čerenkov counter. The data correspond to an integrated luminosity of 147 pb^{-1}.

We have measured the total production cross section of $D^{*\pm}$ to be [0.16±0.02(statistical)±0.02(systematic)] nb [$x \equiv P_{D^*}/(E^2_{\rm beam} - M^2_{D^*})^{1/2} > 0.35$], and $(0.18 \pm 0.02 \pm 0.03)$ nb ($x > 0$) if the contribution from bottom quarks is subtracted. The branching fractions used are Br($D^{*+} \rightarrow D^0\pi^+$) = 64% and Br($D^0 \rightarrow K^-\pi^+$) = 3%. The systematic errors due to the branching ratios are not included in the errors. With Br($D^0 \rightarrow K^-\pi^+$) = 4.9%, which is a recent measurement by the MARK III group, the above two cross sections become 0.10±0.02±0.02 nb ($x > 0.35$) and 0.11±0.02±0.02 nb ($x > 0$ and after the subtraction of the contribution from b quarks).

The charm fragmentation function is harder than that for light quarks, and the shape is found to be consistent with the prediction of the string model with a uniform string-breaking probability. Assuming the string model, the string-breaking probability is determined to be $(0.019 \pm 0.05 \pm 0.09)$ GeV^2.

We have also determined the lifetime of D^0 meson which is detected in the D^* decay, with the result $\tau_{D^0} = (5.3 \pm 1.7^{+0.6}_{-0.5}) \times 10^{-13}$ sec. Together with the semileptonic branching fraction of D^0 measured elsewhere, the semileptonic decay rate of D^0 is estimated to be $(1.4 \pm 0.5) \times 10^{11}$ sec^{-1}, which corresponds to an effective charm quark mass of (1.54 ± 0.12) GeV/c^2.

Using part of the D^* candidates, we have set an upper limit on $D^0 - \overline{D}^0$ mixing: $r \equiv P(D^0 \rightarrow \overline{D}^0)/P(D^0 \rightarrow D^0 \text{ or } \overline{D}^0) < 8.3\%$ (90% c.l.), leading to a stringent limit on charm-changing neutral currents.

Table of Contents

List of Tables

List of Figures

Chapter 1.

Introduction

> When one looks back . . . everything progresses neatly from a few ideas of the past to the orderly situation that we find now. Well, as we know, it just was not like that.
>
> — J. D. Bjorken

In 1960's, the fog slowly started to fade away when the key ideas of the so-called standard model appeared among diverse alternatives. The success of the extension of the SU(2) isospin symmetry [a symmetry between u(up) and d(down) quarks] of the strong interaction to the SU(3) flavor symmetry[1] [a symmetry between u, d, and s(strange) quarks] and the lack of lepton-hadron symmetry in the weak interaction had motivated various authors to introduce a fourth quark — now called c(charm).[2] A few years later, Weinberg and Salam successfully unified the weak and electromagnetic interactions of leptons using the SU(2)×U(1) gauge symmetry.[3] Then, in 1970, Glashow, Iliopoulos and Maiani showed[4] that the introduction of a forth quark can lead not only to symmetry between leptons and hadrons but also to the suppression of strangeness changing neutral currents when the Weinberg-Salam model is extended to include hadrons. This explained the small mass splitting of the K^0 system and the suppression of decays such as $K_{\rm L} \to \mu^+\mu^-$, $K^+ \to \pi^+e^+e^-$, etc. Thus, the standard model of weak and electromagnetic interaction that includes two complete generations of fermions was constructed. Each generation contained two leptons and two quarks:

$$1)\quad \begin{pmatrix}\nu_e\\ e\end{pmatrix} \leftrightarrow \begin{pmatrix}u\\ d\end{pmatrix} \qquad \text{and} \quad 2)\quad \begin{pmatrix}\nu_\mu\\ \mu\end{pmatrix} \leftrightarrow \begin{pmatrix}c\\ s\end{pmatrix}.$$

The J/ψ particle, which was dramatically discovered in 1974,[5,6] was soon identified as a bound state of a c quark and its anti-particle $\bar{c}$, strongly supporting the hypotheses of the standard model.

Later, the discovery of the heavy lepton τ [7] and the Υ particle[8] [a bound state of a b(bottom) quark and its anti-particle $\bar{b}$] has led to the addition of one more generation to the model. This necessitated the introduction of two new particles — the τ neutrino (ν_τ) and the t(top) quark — in order to keep the symmetry between the generations intact. Other particles in the standard model are the gauge bosons that mediate electromagnetic, weak, and strong interactions — photon (γ), weak gauge bosons ($W^\pm, Z^0$), and gluons (g), respectively — and the Higgs particle (H^0) whose vacuum expectation value partially breaks the original gauge symmetries and gives masses to particles in the model. The weak gauge bosons have been observed at CERN in $p-\bar{p}$ interactions,[9] and the t quark may have been observed by the same group.[10] Even though τ neutrinos have not been seen directly, decays of τ leptons are consistent with the emission of a massless τ neutrino through the universal $V-A$ interaction. This leaves the Higgs as the only mystery particle in the standard model. Table 1.1 lists all the fundamental physical particles of the standard model, where 'physical' means mass-eigenstate. For detailed descriptions of the standard model and its impressive list of successes, the reader is referred to many excellent textbooks.[11]

Despite the successes of the model, there are still many questions to be answered, among which we will address the following questions in this thesis: 1) How are charm quarks generated in e^+e^- annihilations? Are there any signs of the unification of the weak and electromagnetic interactions? 2) No free quarks have been observed so far. Then, how do quarks materialize themselves into the real world? 3) How do quarks decay inside hadrons? Do they decay by themselves, or do they interact with the other quark(s) present in a hadron? 4) In the standard model, flavor changing neutral currents are suppressed. The suppression of strangeness changing neutral currents is an experimental fact that originally led

Table 1.1. Fundamental particles in the standard model of weak-electromagnetic and strong interactions. Charge Q and the third component of weak isospin I_3 are also shown. Masses in GeV/c^2 are given in parentheses, where the quark masses refer to current mass.[12] For the leptons and quarks, anti-particles are implicit. For each quark listed, there are three degenerate quarks associated with each type of color quantum number, and the gluon is a color octet.

		generation#			Q	I_3^*
		1	2	3		
fermions	leptons	$\nu_e(0)$	$\nu_\mu(0)$	$\nu_\tau(0)$	0	$+\frac{1}{2}$
		$e(0.0005)$	$\mu(0.106)$	$\tau(1.786)$	-1	$-\frac{1}{2}$
	quarks	$u(0.005)$	$c(1.3)$	$t(\sim 40)$	$+\frac{2}{3}$	$+\frac{1}{2}$
		$d(0.010)$	$s(0.2)$	$b(4.0)$	$-\frac{1}{3}$	$-\frac{1}{2}$
vector bosons			$W^+(81)$		$+1$	$+1$
		$\gamma(0)$	$Z^0(95)$	$g(0)$	0	0
			$W^-(81)$		-1	-1
scalars(Higgs)			$H(?)$ +more?		0	–

* For fermions, I_3 refers to their left-handed component. Their right-handed components are weak isospin singlets (except for neutrinos which do not have a right-handed component in the standard model).

to the introduction of the c quark by Glashow, Iliopoulos, and Maiani. Are flavor changing neutral currents absent for heavier quarks, also?

One can study heavy flavors by detecting heavy hadrons; but, there are additional reasons why heavy hadrons are suited to the study of problems which are not directly related to heavy quarks themselves. First, their masses are substantially larger than the energy scale of the strong interaction: thus, the effective coupling constant of the strong interaction is small enough to be manageable by perturbative quantum chromodynamics (QCD). Second, it is easy to trace the origin of a heavy hadron because heavy quarks are not abundantly produced in decays of other particles or from the sea. In this thesis, I will investigate these questions using

D^{*+} meson, which consists of a c quark and a $\bar{d}$ quark, (and its charge conjugation D^{*-}) produced in e^+e^- annihilations at a CM energy of 29 GeV.

The organization is as follows: In chapter 2, the relevant theoretical background for the subjects are reviewed. Then, in chapter 3, the instrumentation and the data reduction are described. This includes the PEP storage ring, the DELCO detector, the data collection system, the event triggers, and the selection criteria used to obtain the multi-hadron events. Chapters 4 through 6 detail the main part of the analysis, in which the D^* production cross sections, the lifetime of D^0, and the upper limit on the $D^0 - \overline{D}^0$ mixing are presented. The conclusion is given in chapter 6, and some detailed formulae and derivations are provided in the appendix.

Chapter 2.

Theoretical Background

> Whatever may be one's opinion as to the simplicity of either the laws or the material structure of nature, there can be no question that the possessors of some such conviction have a real advantage in the race for physical discovery.
>
> — P. W. Bridgeman

In this chapter, we will review the theoretical backgrounds for the following subjects in some detail. Unless stated, the standard model is used as the basis of discussion throughout the chapter.

1. How are charmed quarks produced in e^+e^- annihilation? Is there any signature of the unification of the weak and electromagnetic interactions?
2. How does a charmed quark turn into a charmed meson? What do we expect for the momentum distribution of charmed mesons?
3. How do the charmed mesons decay? What decay rates and decay modes are expected?
4. Can a meson generated as a D^0 turn into a $\overline{D}^0$ meson before it decays, namely, do we expect $D^0 - \overline{D}^0$ mixing? How does a limit on the mixing translate to that on charm-changing neutral currents?

Unless stated otherwise, the system of units used in this chapter is such that $c = \hbar = 1$.

2.1 Production of Charm Quarks

In e^+e^- annihilation, there is a class of events in which hadrons carry a substantial fraction of the CM energy of the incoming electron and positron. These events, called simply 'hadron events' or 'multi-hadron events', are thought to be final states of quark-antiquark pairs followed by their hadronizations. A quark-antiquark pair is generated primarily through a decay of a time-like photon as shown in Figure 2.1. Final-state hadrons will approximately follow the direction of the quark and antiquark, so the events will topologically consist of two 'jets.'[13]

In this section, we will discuss how charmed quarks (and any fermions in general) are produced in e^+e^- annihilations. As we will see, charmed quarks are expected to be produced copiously though the creation of $c\bar{c}$ pair at the vertex of e^+e^- annihilation. Various corrections to the lowest-order total cross section turn out to be small. However, some of the corrections change the features of events significantly such as the 3-jet events caused by hard gluon emissions. We will also see that the forward-backward asymmetry of charm production, caused by the interference of Z^0 and photon, is significant.

2.1.1 Lowest-Order QED Cross Sections

The process of Fig. 2.1 is calculated using the quantum electrodynamics (QED), and the differential cross section, $d\sigma^0$, is given by

$$\frac{d\sigma^0}{d\Omega} = Q_q^2 \frac{\alpha^2}{4s} \beta (2 - \beta^2 \sin^2 \theta) \tag{2.1}$$

where,

α is the electromagnetic coupling constant $e^2/4\pi\hbar c$ (=1/137.036),

s is the invariant mass (squared) of the e^+e^- system,

Q_q is the quark charge,

θ is the angle between the incoming electron and the outgoing quark (Fig. 2.1), and

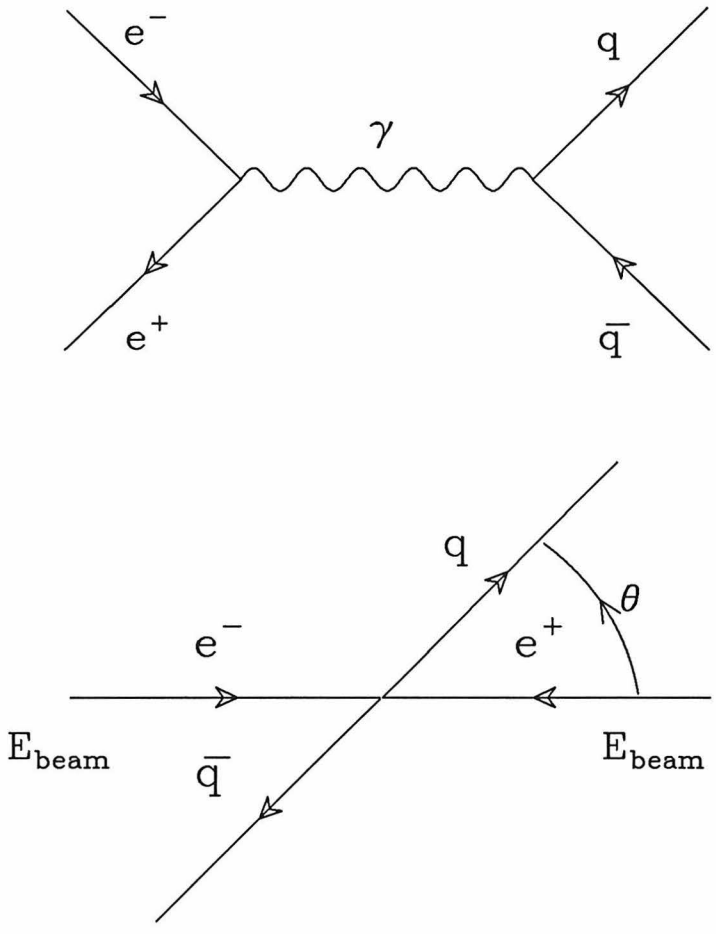

Figure 2.1. The process $e^+e^- \rightarrow q\bar{q}$ through single time-like photon. The top figure shows the Feynman diagram and the configuration in the lab system is shown at the bottom.

β is the velocity of the outgoing quark divided by the velocity of light.

For energies well above the quark pair threshold ($\beta \rightarrow 1$), the angular distribution reduces to $1 + \cos^2\theta$, which arises because the spin of the photon is parallel to the beam axis while the spins of the quark and antiquark are aligned along the axis of flight. The total cross section is obtained by integrating (2.1):

$$\sigma^0 = Q_q^2 \frac{4\pi\alpha^2}{3s}\beta\frac{3-\beta^2}{2} \quad \rightarrow \quad Q_q^2\frac{4\pi\alpha^2}{3s} = Q_q^2\sigma_\mu \quad (\beta \rightarrow 1), \tag{2.2}$$

where

$$\sigma_\mu \equiv \frac{4\pi\alpha^2}{3s} = \frac{21.7(\text{nb})}{E^2_{\text{beam}}(\text{GeV})} \tag{2.3}$$

is the lowest-order QED cross section for muon pair production at high energy. For $E_{\text{beam}} = 14.5$ GeV, the value of σ_μ is 0.103 nb. The formulae above are valid for the production of any point-like fermion-antifermion pair by e^+e^- annihilation through a timelike photon.

At our beam energy of 14.5 GeV, the quarks produced are u, d, s, c, and b. The suppression of the cross section due to the threshold effect in (2.2) is much less than 1% even for b-quark pairs. Each quark flavor consists of 3 quarks with identical mass but different color quantum numbers; the degeneracy is due to the exact color symmetry. The total cross section for the hadronic events is, then,

$$\sigma_{\text{had}} \approx \sigma_\mu \cdot 3 \sum_{f=udscb} Q_f^2 = \frac{11}{3}\sigma_\mu. \tag{2.4}$$

Thus, about 4/11's of the hadronic events originate from the production of $c\bar{c}$ pairs.

2.1.2 QED Corrections

There are various next-to-lowest-order corrections to the reaction $e^+e^- \rightarrow q\bar{q}$, which are listed in Figure 2.2. They can be divided into 3 groups; QED corrections to order α^3 [Fig. 2.2(a) through (i)], first-order quantum chromodynamics (QCD) corrections [Fig. 2.2(j) through (l)], and the electro-weak effect [Fig. 2.2(m)]. All

the diagrams with four vertices are not included by themselves; what is considered is the interference of the lowest-order QED diagram with them. All of these can be calculated reliably in the standard model.

The photon-emission diagrams [Fig. 2.2(a) and (b)] diverge for soft photons, but it is cancelled by the infinity that occurs in the interference of the vertex correction diagram of Fig. 2.2(c) and the lowest-order graph (Fig. 2.1). Similarly, the infrared (soft) divergences in Fig. 2.2(d) and (e) cancel with that of the interference between Fig. 2.2(f) and Fig. 2.1.

The photons accompanying a relativistic charged particle are approximately on-shell and the spectrum is given by

$$\begin{aligned} dn(k) &= \beta \frac{1+(1-k)^2}{4k} dk, \\ \beta &= Q^2 \frac{2\alpha}{\pi} (\ln \frac{s}{m} - 1) \begin{cases} \sim 0.1 & \text{for } e; \\ \sim 0.01 & \text{for } c \text{ quark}, \end{cases} \end{aligned} \tag{2.5}$$

with $k \equiv E_\gamma / E_{\text{beam}}$ (equivalent photon approximation). These photons can be reinterpreted as the initial or final state radiations. The direction of the radiated photons is peaked along the charged particle from which they are emitted. When the photon energy is small compared to the beam energy (i.e., $k \ll 1$), the differential cross section for photon emission from the initial (final) state, $d\sigma_{i(f)}$, is approximately given by[14]

$$d\sigma_{i(f)} = \beta_{i(f)} \sigma^0 \frac{dk}{k}, \tag{2.6}$$

where $\beta_{i(f)}$ is the corresponding value of β as defined in (2.5). In general, the radiation from quarks is smaller than that from electrons due to the smaller absolute charges and the larger masses. At our energy, the change in the total cross section due to the final state radiation is less than 1%.

When $k \to 0$, the differential cross section (2.6) diverges. Also, the initial state radiation changes the center of mass energy of the e^+e^- system at the time of annihilation, which changes the photon-emission cross section itself. A more careful

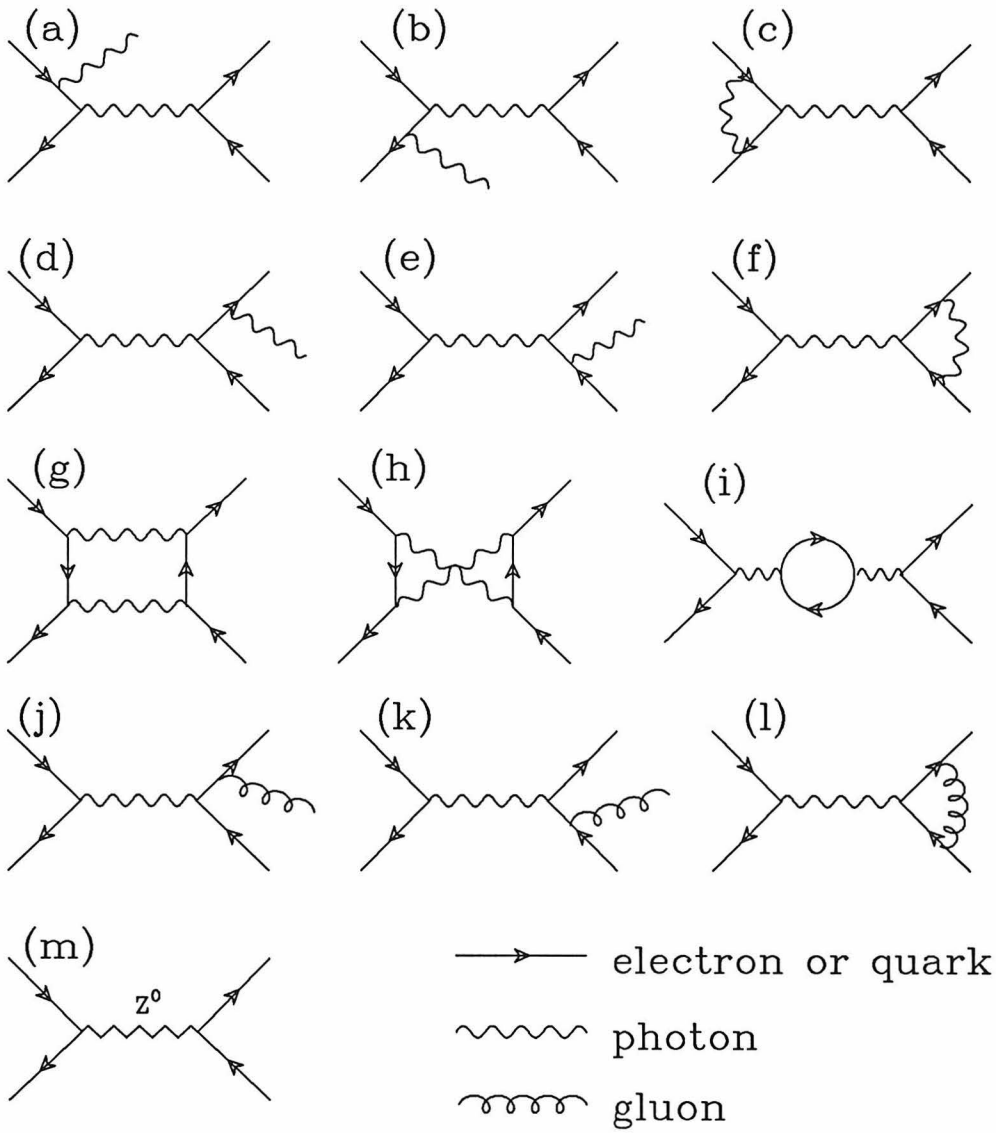

Figure 2.2. Feynman diagrams relevant to the next lowest-order corrections to the process $e^+e^- \rightarrow q\bar{q}$. The Z^0 exchange diagram (m) is treated as the same order as the box diagrams of (g) and (h). Also, the first-order QCD corrections are included [(j), (k), and (l)].

treatment is as follows. The cross section is well approximated by[15] the emission probability times the cross section of the process $e^+e^- \to q\bar{q}$ after the emission at a reduced CM energy s'. With a proper connection of soft and hard radiation (the exponentiation of leading logarithm), the total cross section for $k < k^0$ can be written as (for $m_f \ll E_{\rm beam}$), [16]

$$\sigma_i(k < k^0) = \sigma^0 \left[1 + \delta_v - \frac{\beta_i}{2}\{\ln(1-k^0) + k^0\}\right] k^{\beta_i} \tag{2.7}$$

where,

$$\delta_v = \frac{\alpha}{\pi}(\frac{3}{2}\ln\frac{s}{m_e^2} - 2 + \frac{\pi^2}{3}) \approx 0.08$$

is the finite offset left-over after the cancellation of infinities of the graphs Fig. 2.2(a), (b), and (c). The radiation spectrum peaks at small k and varies as $1/k$, which is consistent with (2.6). Since $\sigma(s')$ varies as $\sim 1/s' \sim 1/(1-k)$, it also peaks as $k \to 1$, i.e., when the photon carries away most of the beam energy. The total cross section depends on the effective cut-off on k. In fact, the peak for $k \to 1$ does not contribute to our hadronic event sample because we require a minimum amount of detected charged energy in the central detector corresponding to an effective k-cutoff at around 2/3.

The interference of the box diagrams [Fig. 2.2(g) and (h)] and the lowest-order QED diagram also has divergences, but they are cancelled by soft photon divergences that occur in the interference between the initial and final state radiation. The result is to generate a forward-backward asymmetry, where 'forward' is defined by $\vec{P}_{e^-} \cdot \vec{P}_q > 0$. This is because the final state is not an eigenstate of charge conjugation C; it is a mixture of a one-photon state ($C = -$) and a two-photon state ($C = +$). If the final state is an eigenstate of C, then applying C to the final state, i.e., interchanging the quark and antiquark, does not change the cross section, and there will be no forward-backward asymmetry. Although the amount of asymmetry depends on the cuts used to select events such as acceptance in $\cos\theta$ and total visible energy, a typical value is 1 to 2 %. This effect is often important

when one studies the asymmetry caused by the interference of the Z^0 diagram and the lowest-order QED diagram.

The same argument of the charge conjugation as above applies to the interference of the initial and final hard photon emission diagrams. When the photon is detected, it gives a large forward-backward asymmetry.[17] However, when the photon parameters are integrated, the asymmetry is generally small compared to the one caused by the box diagrams.[18]

In the vacuum polarization diagram of Fig. 2.2(i), the loop includes contributions from electron, muon, tau, and quarks. The effect of $W^{\pm}$ is small. The correction is multiplicative and is given by,[19]

$$\frac{d\sigma^0}{d\Omega} \rightarrow (1 + \sum_f \delta_f)\frac{d\sigma^0}{d\Omega}, \quad \text{with } \delta_f = Q_f^2 \frac{2\alpha}{\pi}(\frac{1}{3}\ln\frac{s}{m_f^2} - \frac{5}{9}), \tag{2.8}$$

where, $f = e$, μ, τ and quarks with different colors. The correction is larger for lighter fermions, and the total correction due to the vacuum polarization at our beam energy is +10%.

2.1.3 QCD Corrections

The first-order gluon emission diagrams Fig. 2.2(j) and (k) diverge as in the case of the photon emission diagrams Fig. 2.2(d) and (e). And, just as in the case of QED, the divergence is canceled by the corresponding vertex correction diagram Fig. 2.2(l) when the finite resolution of quark momenta is taken into account.[20] The total cross section including hard gluon emission is given by,

$$(1 + \frac{\alpha_s}{\pi})\sigma^0, \tag{2.9}$$

where

$$\alpha_s = \frac{4\pi}{b\ln(Q^2/\Lambda^2)}, \quad \text{with} \quad b = 11 - \frac{2}{3}n_f, \tag{2.10}$$

is the running coupling constant of strong interactions with n_f being the number of flavors. For $Q^2 = s$ and $\Lambda = 150$ MeV,[21] the value of α_s is about 0.16, leading

to an +5% correction for the total hadronic cross section. To first order in QCD, the differential cross section of gluon emission is given by,[22]

$$\frac{d\sigma_{q\bar{q}g}}{dx_q dx_{\bar{q}}} = \sigma^0 \frac{2\alpha_s}{3\pi} \frac{x_q^2 + x_{\bar{q}}^2}{(1-x_q)(1-x_{\bar{q}})} \tag{2.11}$$

where, $x_q = E_q/E_{\text{beam}}$ and $x_{\bar{q}} = E_{\bar{q}}/E_{\text{beam}}$. This determines the configuration of q, $\bar{q}$, and g relative to each other, apart from the angular orientation with respect to the beam axis. The cross section is divergent when the gluon is soft or parallel to the quark or antiquark, in which case the gluon cannot be observed as a separate jet anyway. This is the region where the vertex correction diagram of Fig. 2.2(l) cancels the divergence. When the gluon energy is substantial and its direction is away from the quark or antiquark, the event will topologically appears as a 3-jet event.

2.1.4 Electro-Weak Effects

At our energy, the Z^0 diagram (m) is suppressed by $|\chi|^2 \sim (s/M_Z^2)^2 \sim 0.01$ compared to the lowest-order QED cross section, where χ is the reduced Z^0 propagator

$$\chi(s) = \frac{s}{s - M_z^2 + iM_z\Gamma_z}. \tag{2.12}$$

On the other hand, the interference of (m) and the lowest-order QED diagram is of order $\text{Re}(\chi) \sim s/M_Z^2 \sim 0.1$ times the lowest order QED cross section. The contribution of this interference to the total hadronic cross section is [23]

$$2\frac{v_e v_q}{Q_q}\text{Re}(\chi)\,\sigma^0 \sim -0.2\frac{v_e v_q}{Q_q}\sigma^0 \begin{cases} \sim 0.01\sigma^0 & \text{for } u, c \text{ quarks} \\ \sim 0.02\sigma^0 & \text{for } d, s, b \text{ quarks,} \end{cases} \tag{2.13}$$

where $E_{\text{beam}} = 14.5$ GeV is used. The parameters

$$v_f = \frac{I_3^f - 2Q_f \sin^2\theta_W}{\sin 2\theta_W} \quad \text{and} \quad a_f = \frac{I_3^f}{\sin 2\theta_W} \qquad (f = \text{fermion}) \tag{2.14}$$

are the vector and axial couplings of fermions to the Z^0 defined by the Lagrangian term

$$e\,\bar{f}\gamma_\mu(v_f - a_f\gamma_5)f\,Z^\mu,$$

where e is the electron charge (positive), I_3^f is the third component of the weak isospin (see Table 1.1), and θ_W is the weak mixing angle ($\sin^2\theta_W \sim 0.22$ or $\theta_W \sim 28°$).[24] The formula (2.13) gives values smaller than the crude estimate of $0.1\sigma^0$; this is because the electron-Z^0 coupling happens to be almost purely axial, i.e., $v_e \sim 0$. However, this interference introduces a substantial forward-backward asymmetry. For $s \ll M_Z^2$, the asymmetry is given by,

$$A \equiv \frac{F-B}{F+B} = \frac{3}{2}\frac{s}{M_Z^2}\frac{a_e a_f}{Q_f}g(c) \tag{2.15}$$

where,

$$F = \int_0^c \frac{d\sigma}{d\cos\theta}d\cos\theta, \quad B = \int_{-c}^0 \frac{d\sigma}{d\cos\theta}d\cos\theta, \quad \text{and}$$

$$g(c) = \frac{4c}{1+3c^2} \quad (\to 1 \text{ as } c \to 1).$$

The parameter c defines the acceptance in polar angle. For c=0.6, the asymmetry is -5.5% for charge $2/3$ quarks and -11% for charge $-1/3$ quarks. When one takes e, M_Z, and $\sin^2\theta_W$ to be the basic parameters, and not G_F, as is done in our case, the asymmetry is sensitive to the weak mixing angle through (2.14).

To summarize, in the standard model, the charmed quarks are produced in e^+e^- annihilation at CM energy of 29 GeV primarily by $e^+e^- \to \gamma \to c\bar{c}$. About 4/11 of all hadronic events are such $c\bar{c}$ events. The radiative correction is larger for the initial state radiation than for the final state radiation, and the exact amount of the correction depends on how much energy is allowed for the emitted photon. A typical radiative correction to the total cross section is a few percent, and it also reduces the momentum of heavy hadrons by a few percent. The box diagrams cause the forward-backward asymmetry which has to be considered in the analysis of the

weak-electromagnetic interference effects. The vacuum polarization of the timelike photon increases the total cross section by 10%. The first-order QCD correction increases the total cross section by about 5%, and hard gluon emissions are expected to result in 3-jet events. At our energy, the effect of e^+e^- annihilation through Z^0 is small in the total cross section due to the small value of v_e, but it generates a substantial forward-backward asymmetry, which may be measurable. Charm quarks are also produced by decays of bottom quarks, which will be discussed in a later chapter.

2.2 Hadronization of Charm Quarks — String or QCD Cascade?

2.2.1 Quark Hadronization

The force responsible for the hadronization of quark is the strong interaction, and it is believed to be described (in principle) by the quantum chromodynamics (QCD). QCD is a non-abelian gauge theory based on the unbroken SU(3) color symmetry with quarks and gluons as its basic constituents, and carries the strong interaction part of the standard model.

At a short distance, namely for a large value of Q^2, the equation (2.10) shows that the effective coupling constant α_s becomes small (asymptotically free),[25] and the perturbation theory can be used to calculate various quantities. However, at a large distance, or for a small value of Q^2, the effective coupling becomes too large for the perturbation theory to be reliable. It is commonly believed that when two quarks are placed more than a few fm (10^{-15} m) apart, the self-coupling of gluons, which arises from the non-abelian nature of QCD, pushes together the gluon flux lines to form a flux tube. This leads to a potential that increases linearly with the distance, preventing the quarks to escape ('confinement'). Rigorous proof of the above picture is yet to come, but suggestive clues abound: the interquark potentials of ψ's and Υ's seem to increase linearly when the distance between the quarks becomes large; in the dual resonance model, the string picture explains

many aspects of the strong interaction including resonances; the lattice QCD calculations[26] support the linearly rising potential; and some analytical studies of QCD also indicate the existence of strings.[27]

As we understand at present, the time development of hadronization in e^+e^- annihilation is as follows:

1. Creation of $q\bar{q}$ (+ hard gluons) at the e^+e^- vertex.
2. In a few fm/c($\sim 10^{-23}$) sec of proper time, the strong interaction finishes its job, turning the original quarks and the gluon field into stable hadrons.
3. Much later, some hadrons decay electromagnetically or weakly.

The first stage is calculable and has already been discussed. The time scale of the last stage is well separated from the second by many orders of magnitude, and we will not discuss it further here. The second stage includes decays of strong resonances such as ρ and K^*. This classification is more natural than combining strong decays with weak and electromagnetic decays: the time-scale of hadronization is about the same as the lifetimes of these particles (the $c\tau$ of ρ is $\sim$1 fm).

The lattice QCD and powerful computers may soon make it possible to calculate various aspects of hadronization. Currently, however, QCD cannot give a precise description of hadronization, and it has led to various phenomenological models. These models are roughly divided into two groups: flux tube models (string models) and QCD cascade models.

2.2.2 Flux Tube Based Models — Early Models

Flux tube models[28] are the natural outcome of the confinement picture discussed above. As a quark separates from an antiquark, a flux tube will stretch between the two, which soon breaks up creating a $q\bar{q}$ pair somewhere along the tube [Figure 2.3(a)]. The stretching and breaking process will continue until all the energy turns into hadrons. This leads to the following observations: 1) the creation of $q\bar{q}$ pair is independent of the flavor of the original $q\bar{q}$ pair; and 2) the

central part of rapidity distribution becomes flat due to the Lorentz invariance of flux tube, that is, apart from edges, a flux tube looks exactly the same when it is boosted longitudinally.[29]

A pioneering work was done by Field and Feynman.[30] In their model, a jet of hadrons is generated from an original quark q with momentum P (in the $+z$ direction) as follows [Fig. 2.3(b)]: 1) a new pair $q'\bar{q}'$ is generated according to a fixed ratio for various flavors, and $\bar{q}'$ is combined with q to form a meson. The momentum and energy of the meson E_1 and P_{1z} are given by the fragmentation function $f(z)dz$, where

$$z \equiv (E_1 + P_{z1})/(E_0 + P_0). \tag{2.16}$$

2) The q' is assumed to carry the left-over energy-momentum $(1-z)(E_0+P_0)$. Then, another pair $q''\bar{q}''$ is generated, and the process is repeated treating q' as if it is the original quark.

The value of z becomes smaller and smaller as one repeats the process, corresponding to a more and more negative P_z. In fact, this procedure describes a fragmentation of a $q\bar{q}$ pair where q has $P_z = P$ and $\bar{q}$ has an infinitely negative P_z. The parameter z defined by (2.16) is invariant under longitudinal boosts, and it assures that, deep into the cascade, the hadron distribution is flat in rapidity.

In order to generate a jet of finite energy, this recursive process has to be artificially terminated, typically when the energy of the original quark is used up. (The process is no longer Lorentz invariant.) Two such jets, one from a quark and the other from an antiquark, can be combined back-to-back to form an e^+e^- event. In this scheme, however, it is difficult to conserve charge, energy, and momentum in a natural way. The Monte Carlo programs by Ali *et al.*[31] and Hoyer[32] belong to this category.

In these e^+e^- models, a hard gluon is treated similarly to a quark, making a jet of its own. This results in another problem when $q\bar{q}g$ 3-jet events are generated according to the first-order QCD cross section (2.11), which diverges when the gluon

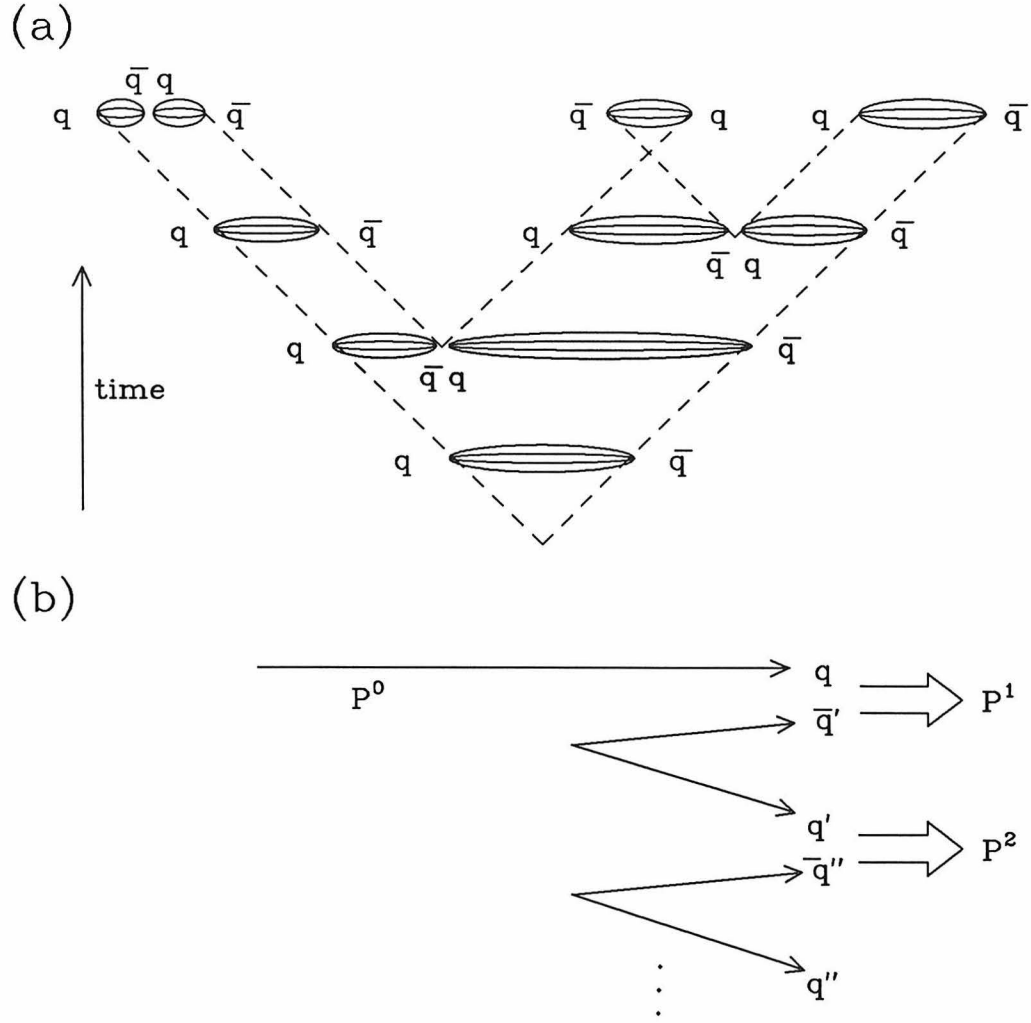

Figure 2.3. (a) Flux tube model of hadronization. As a flux tube stretches between the original quark and antiquark, a new $q\bar{q}$ pair is formed breaking the flux tube. Eventually all the energy is transformed into hadrons. (b) The fragmentation scheme of Field and Feynman is inspired by the flux tube model, and describes the hadronization of a semi-infinite flux tube.

is parallel to the quark or antiquark. The final distributions should be insensitive to the exact value of the cutoff needed to avoid the divergence. Thus, a $q\bar{q}g$ event should result in an event similar to a $q\bar{q}$ event when the angle between the gluon and quark (or antiquark) is small. However, in these models, an event differs substantially (for example in multiplicity) depending on whether it is generated as a $q\bar{q}$ event or as a $q\bar{q}g$ event. This problem can be avoided, at least in principle, if a gluon is treated as a kink of a string, as we will discuss later.

2.2.3 Flux Tube Based Models — String Models

The models by the LUND group[33], by Artru and Mennessier[34], and by Gottschalk.[35] take the string-like features of hadronization more seriously. We will start by briefly reviewing the basics of string models.

A string is, at best, an approximation of reality. A flux tube can be thought of as a stretched meson bag,[36] thus the actual width would be of order fm; the uncertainty principle tells us that the transverse fermi motion of a particle confined within a tube is a few hundred MeV/c; there might be constant disturbances by soft gluon emissions or transverse vibrations ('roughening');[37] in addition, there are spin-spin interactions and other quantum mechanical effects which become stronger when the quark and antiquark get closer. Bearing these limitations in mind, we approximate a flux tube by a classical massless string with no width.

It is possible to formulate string motion in a relativistically consistent way.[38] We will not cover the details of the formalism here; but some of the key features are listed below:

1. A quark or antiquark is attached at each end of a string, which carries energy and momentum.
2. *In any Lorentz frame*, the string tension is a global constant κ:

$$\frac{dP}{dt} = \pm\kappa \quad \text{and} \quad \frac{dE}{dx} = \kappa, \tag{2.17}$$

where t, x, P and E are those of the quark (or antiquark), and the sign in the

first equation depends on whether or not the string is on the positive side of the quark. The quark is always pulled by the force κ, and when a length dx of string is 'eaten' by the quark, the quark gains energy by κdx.

3. Because of its longitudinal Lorentz invariance, a string does not carry a momentum in the longitudinal direction. When a string has a transverse velocity β_t, the energy density becomes $\gamma_t \kappa$ [$\gamma_t \equiv (1-\beta_t^2)^{-1/2}$], and a string now has a transverse momentum $\beta_t \gamma_t \kappa$ per unit length.

The string tension κ can be estimated as follows: One type of string excitation is the rotating rod [Figure 2.4(c)]. This mode maximizes the angular momentum for a fixed energy, and is identified with the leading Regge slope α'. The mass M and angular momentum J the rod are given by (assuming that the edges are moving at the speed of light, i.e., for massless quarks)

$$M = \frac{\pi}{2}\kappa l, \qquad J = \frac{\pi}{8}\kappa l^2, \tag{2.18}$$

where l is the length of the rod. The leading Regge slope is then

$$\alpha' \equiv \frac{J}{M^2} = \frac{1}{2\pi\kappa} \quad \Rightarrow \quad \kappa \approx 0.2\text{GeV}^2 \approx 1\text{GeV/fm}. \tag{2.19}$$

The linear slope is verified up to spin 7 for the ρ family,[39] which corresponds to a length of about 3 fm. This strongly supports the string picture without 'roughening' or blowing up of the tube radius at the center.

Integrating (2.17), one gets $P = \kappa(t - t^0)$ and $E = \kappa(x - x^0)$, where t^0 and x^0 are the integration constants. This and $E^2 - P^2 = m^2$ gives

$$(x - x^0)^2 - (t - t^0)^2 = \frac{m^2}{\kappa^2}, \tag{2.20}$$

where m is the mass of the quark. Thus, the trajectory in x-t space is a hyperbola. A massless quark moves always at the speed of light, and the trajectory becomes a straight line that switches back at (t^0, x^0) where it loses all of its energy to the string.

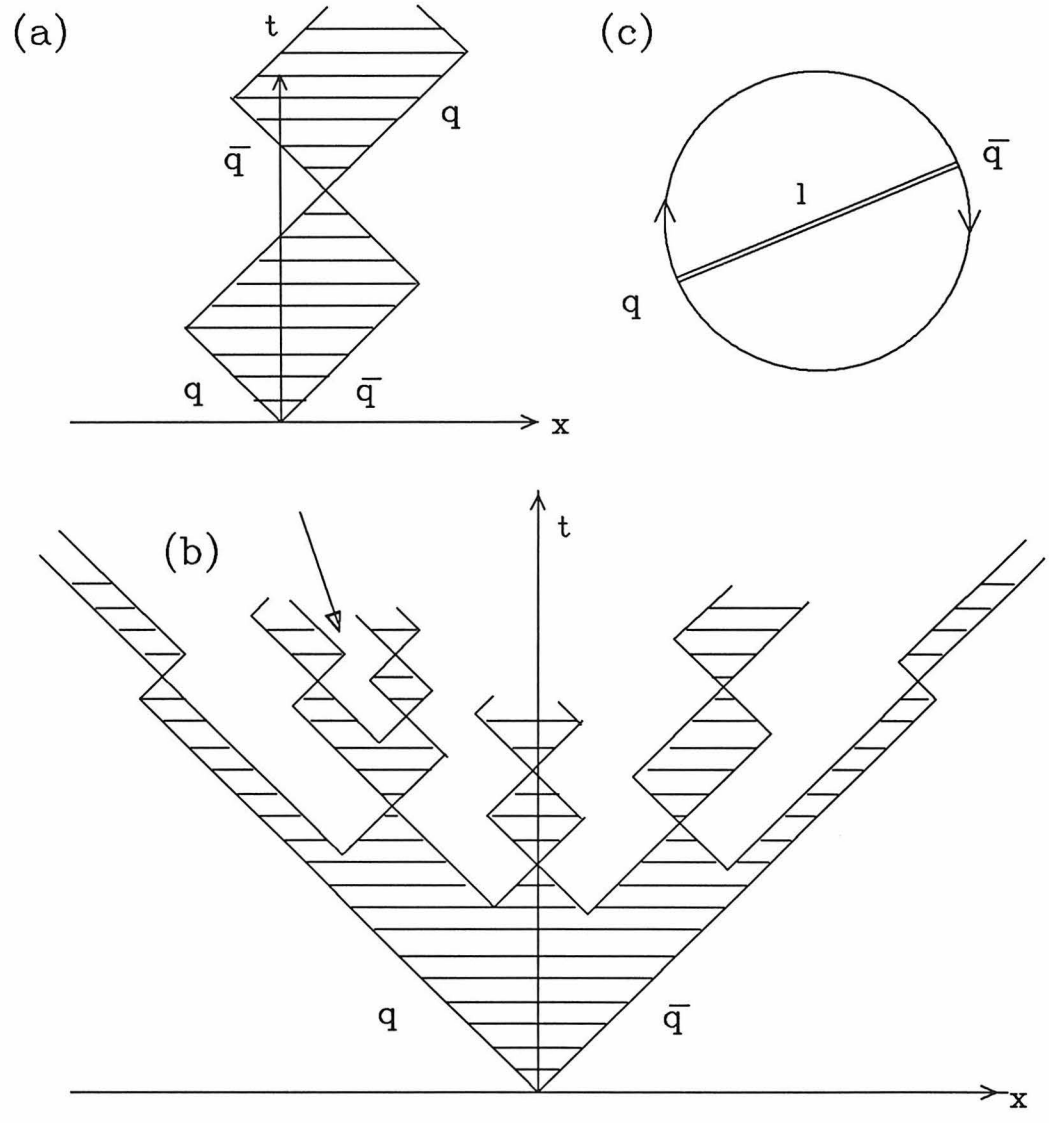

Figure 2.4. (a) Yoyo mode of string motion in space-time. The hatched area is the space-time region of string. (b) String-model picture of hadronization. A pair of $q\bar{q}$ is generated at the origin at $t = 0$. Compare with Fig. 2.3(a). The arrow indicates a string breakup occurring after the first crossing of $q\bar{q}$. (c) Rotating rod mode of string motion, corresponding to the leading Regge trajectories. This can be used to determine the string tension κ.

A quark-antiquark pair stretched by a string, which we call a 'stringlet', has a yoyo-like motion shown in Fig. 2.4(a). The invariant mass of a stringlet is proportional to the area spanned by the string per period of oscillation. A stringlet can be a simple model of meson when its mass is a typical meson mass of order 1 GeV/c^2; when the mass is the CM energy of an e^+e^- annihilation, it can represent a hadronic event as shown in Fig. 2.4(b).

There are options on prescribing the way a string breaks:

1. Allow a string to breakup after a quark and antiquark has crossed once? [as indicated by the arrow in Fig. 2.4(b)].
2. Take the breakup probability to be uniform in space-time? Namely,

$$\frac{dP}{dtdx} = b \text{ (const)}. \tag{2.21}$$

In the LUND model, breakup is not allowed after the first crossing of $q\bar{q}$, and is not uniform in space-time. Instead, the breakup point is determined by the mass of resulting meson and the fragmentation function. Thus, in a sense, the string 'knows' what discrete values of masses are allowed when it breaks, and all the first crossings of $q\bar{q}$ turn into hadrons. Since the time-scale of hadronization is the same as that of the formation and decay of resonances, this is not as strange as it may seem: the quantum dynamics that result in the actual mass spectrum is already in action when a string breaks to create a low-mass stringlet. However, when the mass of the stringlet is substantially more than ~ 1 GeV/c^2, it seems reasonable to allow breakups to occur also after the first crossing of $q\bar{q}$.

When one assumes the uniform breaking of string, then the mass M of a stringlet produced by the first crossing has a continuous distribution

$$f(M)dM = 2bE_1(bM^2)MdM, \tag{2.22}$$

where E_1 is the exponential integral. This distribution extends down to 0 even though there is no singularity. Thus, in order to generate real hadrons, some

cutoff has to be made. One way is to restrict the breaking point to the region where the resulting stringlets have masses greater than a certain cut value, and let these stringlets (clusters) decay to ordinary hadrons. This approach was taken by Gottschalk[35]. It has an advantage of naturally conserving energy-momentum.

In string models, a hard gluon can be represented by a kink of the string which carries a local energy-momentum as shown in Figure 2.5(a).[40] When the angle between the quark and gluon is small, the system looks similar to a simple straight $q\bar{q}$ string. Thus, in this scheme, the problem of infrared divergences of gluon emission is not as serious as the models in which gluons hadronize independently. This can be seen more clearly by tracing the motion of string. We choose a coordinate system where q and $\bar{q}$ are back-to-back and g is perpendicular to them, and compare a $q\bar{q}g$ system of $(P_q, P_{\bar{q}}, P_g) = (2, 6, 2)$ GeV/c with a $q\bar{q}$ system of $(P_q, P_{\bar{q}}) = (3, 7)$ GeV/c. The total energy is the same for both systems. As can be seen in Fig. 2.5(b), the difference becomes small when the invariant mass of qg or $\bar{q}g$, tends to zero, and one can expect that, when uniform string breaking is turned on, they will result in similar events. It is interesting to note that the oscillation period is the same for systems of the same energy.

2.2.4 QCD Cascade Models

We now turn to another class of hadronization models which are based on the perturbative QCD calculations for the branching process of quarks and gluons. By generalizing the equivalent photon approximation by Weizsäcker and Williams[41] to QCD, Altarelli and Parisi showed[42] that, in the leading-log approximation and in the axial gauge, it is possible to define a classical branching probability (namely without interferences) of partons. It was then extended to more general rules of the 'jet calculus' by Konishi, Ukawa, and Veneziano.[43]

Just like an electromagnetic shower, a high energy parton is expected to result in a shower of partons as shown in Figure 2.6(a). The probability distribution $P_{i\to jk}(x)$, where the parton j carries a fraction x of the initial longitudinal

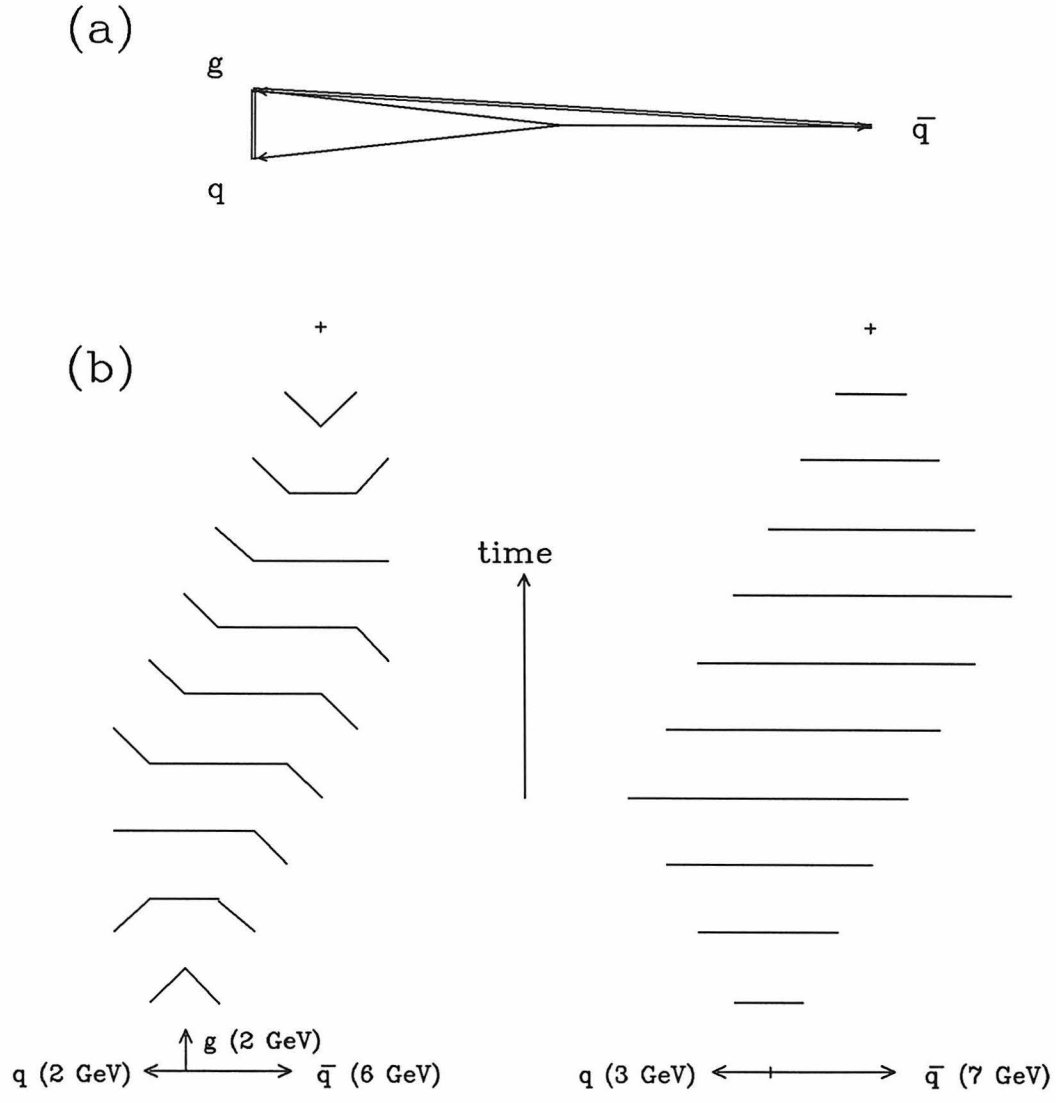

Figure 2.5. (a) Configuration of string in the lab system for a $q\bar{q}g$ event. All three particles are traveling with the speed of light. When the angle between q and g is small, it practically becomes a single straight string. (b) Motion of string is traced for a $q\bar{q}g$ system and a $q\bar{q}$ system. The two dimensional shape of the string is shown for every time interval of $1/\kappa$. String breaking is turned off. It can be seen that, as the gluon energy becomes small, the string motion of a $q\bar{q}g$ system approaches that of a $q\bar{q}$ system with the same energy.

momentum of the parton i, is given by,[42]

$$\begin{aligned} P_{q\to qg} =& \frac{4}{3}\frac{1+x^2}{1-x} \\ P_{g\to q\bar{q}} =& \frac{1}{2}\left[x^2+(1-x)^2\right] \\ P_{g\to gg} =& 3\left[\frac{1-x}{x}+\frac{x}{1-x}+x(1-x)\right]. \end{aligned} \tag{2.23}$$

An off-shell parton starts with a large invariant mass and undergoes a series of branchings reducing the invariant masses at each stage. This is different from the string picture where partons are treated as on-shell. In practice, one faces several choices and problems:

1. The leading-log approximation is expected to be good only if

$$\frac{\alpha_s}{\pi} \ll 1 \quad \text{or} \quad \frac{Q^2}{\Lambda^2} \gg 1. \tag{2.24}$$

   Thus, the branching process has to be stopped before the parton invariant masses become of order 1 GeV. The right cutoff value, however, is not well-defined.

2. Except for $P_{g\to q\bar{q}}$, the distributions (2.23) have infrared divergences. Again, one can avoid the problem by applying a minimum invariant-mass cutoff for the daughter partons. However, the cutoff value is more like an free parameter.

3. The final partons have to be turned into ordinary hadrons. This has to be done in such a way that the final distributions are insensitive to the above cutoff value. We will discuss it in some more detail.

One easy way is to use the Field-Feynman scheme for each of the final partons as done by Odorico[44] or by Paige and Protopopescu (ISAJET).[45] However, this method is not Lorentz invariant and the result depends on the frame in which the Field-Feynman scheme is applied. Also, it suffers the same problem of the infrared cutoff dependence as for the simulation of $e^+e^- \to q\bar{q}g$ events.

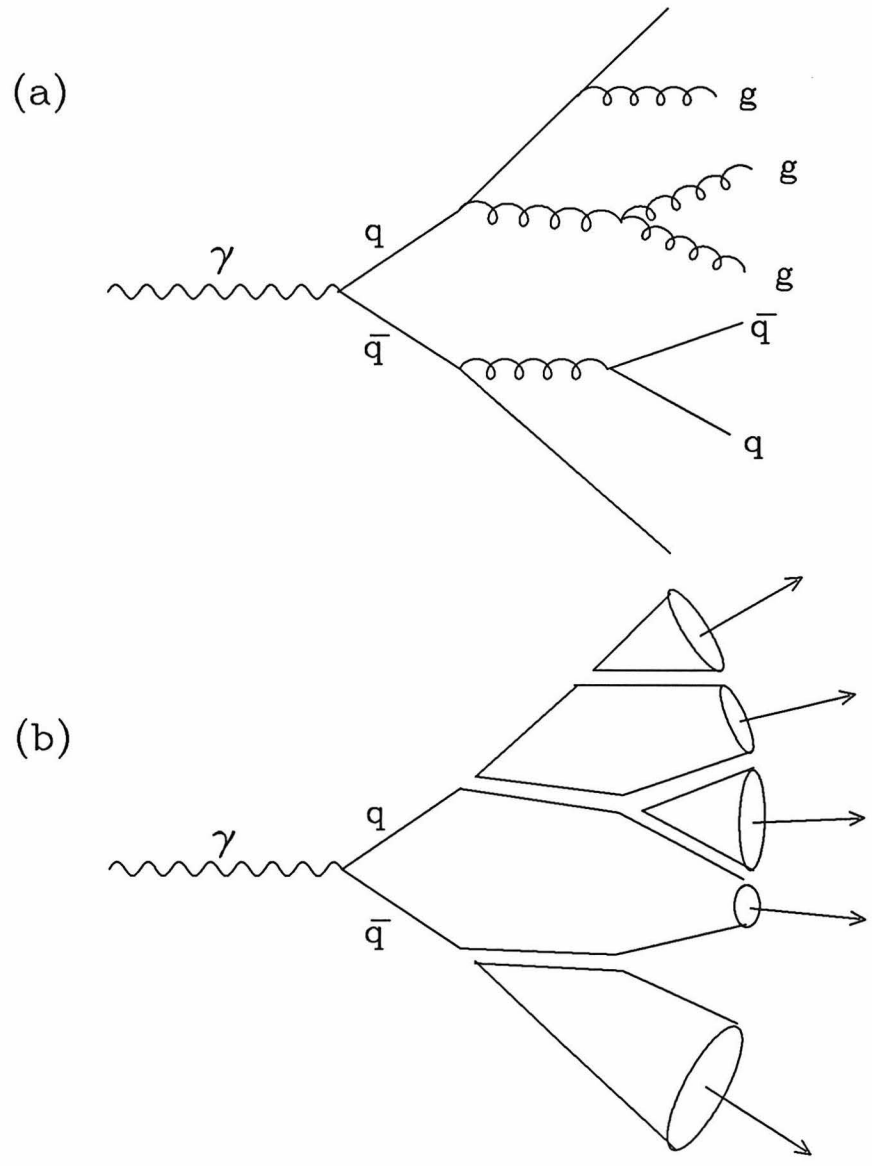

Figure 2.6. (a) In the QCD cascade model, a parton branches to form a parton shower. Note that a gluon can split to two gluons. The invariant masses are constantly decreasing throughout the branching process and it is stopped when a minimum mass is reached. (b) The concept of 'pre-confinement' arises when one traces the color flow in (a). Final partons are naturally organized to form colorless clusters, which then decay to ordinary hadrons.

An alternative is to form a set of color singlets. It was pointed out by Amati and Veneziano[46] that the branching process of partons naturally results in clusters of color singlets ('pre-confinement') as shown in Fig. 2.6(b). These clusters can then decay to ordinary hadrons. Monte Carlo models based on this idea include one by Field and Wolfram,[47] its variation by Gottschalk (his earlier model),[48] and one by Webber,[49] the last with soft gluon interference effects that strongly order emission angles in the cascade process.[50] There still remains choices on how to decay the colorless clusters:

1. Treat a cluster as a resonance that decays to two daughters uniformly in phase space (Ref. 47, 48).
2. Treat a high-mass cluster as a string (Ref. 49).

When clusters decay spherically by 2-body decays, the transverse momentum distribution of a jet depends on the cluster mass at which the parton shower is terminated. This is not a problem when the clusters are treated as a string, where transverse momentum is limited regardless of the length of string. Also, the same argument can be made as in the case of $q\bar{q}g$ events that the string scheme is insensitive to the cutoff value of the infrared divergence. Thus, the string scheme is favored over the resonance scheme at least for large mass clusters.

One last comment on the QCD cascade models is that the branching scheme is necessarily an approximation. For example, the azimuthal angle of a branch is taken uniformly in 2π, which is not correct in reality: it does not give the correct first-order QCD cross section for a gluon emission (2.11), where the azimuthal angle of g with respect to q depends on the direction of $\bar{q}$. Usually the 'correct' differential cross section is used for the first gluon emission in the QCD cascade models mentioned above.

This section on hadronization models can be summarized as follows. The inability of QCD to reliably calculate the hadronization process has led to two types

of hadronization models: string (flux tube) models and QCD cascade models. In string models, a fluxtube stretches and breaks resulting in hadrons. Two questions are: 1) does a string break uniformly in space-time? 2) does a string break after a stringlet is formed? It seems reasonable to assume that both are expected to be true for a large-mass stringlet, where the string breaking does not overlap with resonance formations. The QCD cascade models push the perturbative QCD to its limit (and beyond?). The basic picture is a parton shower which result from a classical branching process, which in turn has to be turned into hadrons by other hadronization mechanisms. One important criterion here is that the hadronization scheme should be employed in such a way that within a reasonable range of cutoff values the final distributions of hadrons should not depend on the cutoffs. On this account, the string scheme with 'pre-confinement' is favored. At our energy of 29 GeV, the 'exact' 3 or 4 parton cross sections plus the string scheme seems to be a reasonable model. As the energy of accelerators becomes higher, the number of clearly resolvable parton emissions will become larger, making the exact calculation of cross sections more difficult. Thus, the QCD cascade model terminated at a relatively high invariant mass (5 to 10 GeV) combined with the string hadronization scheme seems to be the most promissing path to take.

2.3 Heavy Quark Fragmentation Function

How much of the quark momentum is carried by the hadron containing the original quark can provide valuable information on the hadronization mechanism. Heavy mesons are particularly suited for this study since it is easy to identify the meson that contains the original quark and the effect of resonance decays on the momentum distribution is small (e.g., the decay $D^* \rightarrow D$ hardly changes the momentum).

2.3.1 *Plausibility Arguments*

There are several plausibility arguments that point to a harder fragmentation function for a heavier quark. When a $q\bar{q}$ pair is generated by a e^+e^- annihilation, q or $\bar{q}$ is assumed to be in a excited state surrounded by a gluon cloud. This excited state would carry most of the beam energy and decay to a meson of mass $\sim m_Q$ plus light hadrons, where m_Q is the heavy quark mass. When the energy of the gluon cloud is m_0, then the average fraction of momentum carried by the heavy meson, $< x >$, will be

$$< x > \sim \frac{m_Q}{m_Q + m_0} \sim 1 - \frac{m_0}{m_Q} \quad (m_Q \gg m_0).$$

If we assume the distribution of m_0 to be the Boltzman factor $\exp(-\beta E)$[51] times the Lorentz invariant phase space $d^3P/(2E)$ and assume that the heavy meson have the same velocity as the excited state, then a simple calculation gives

$$f(x) = A\frac{1-x}{x^3}e^{-a/x}, \tag{2.25}$$

where $x = P_{\text{meson}}/P_{\text{beam}}$ and

$$a = \beta m_Q = \frac{2m_Q}{< m_0 >}, \quad A = a^2 e^a.$$

Figure 2.7(a) shows the functional shape for $m_Q = 2$ and 5 GeV/c^2 with $< m_0 >= 1$ GeV/c^2. A similar argument was given by Suzuki for his 'fire ball' model.[52] In QCD cascade models with cluster decays, a similar mechanism gives harder fragmentation functions for heavier quarks,[53] but the shape of the function strongly depends on the mass cutoff (the smaller the cutoff, the softer the shape). Bjorken was led to the same conclusion by noting that the heavier the leading quark, the shorter becomes the length of the normal rapidity plateau (excluding the heavy hadron), thus more momentum has to be carried by the heavy hadron itself.[54]

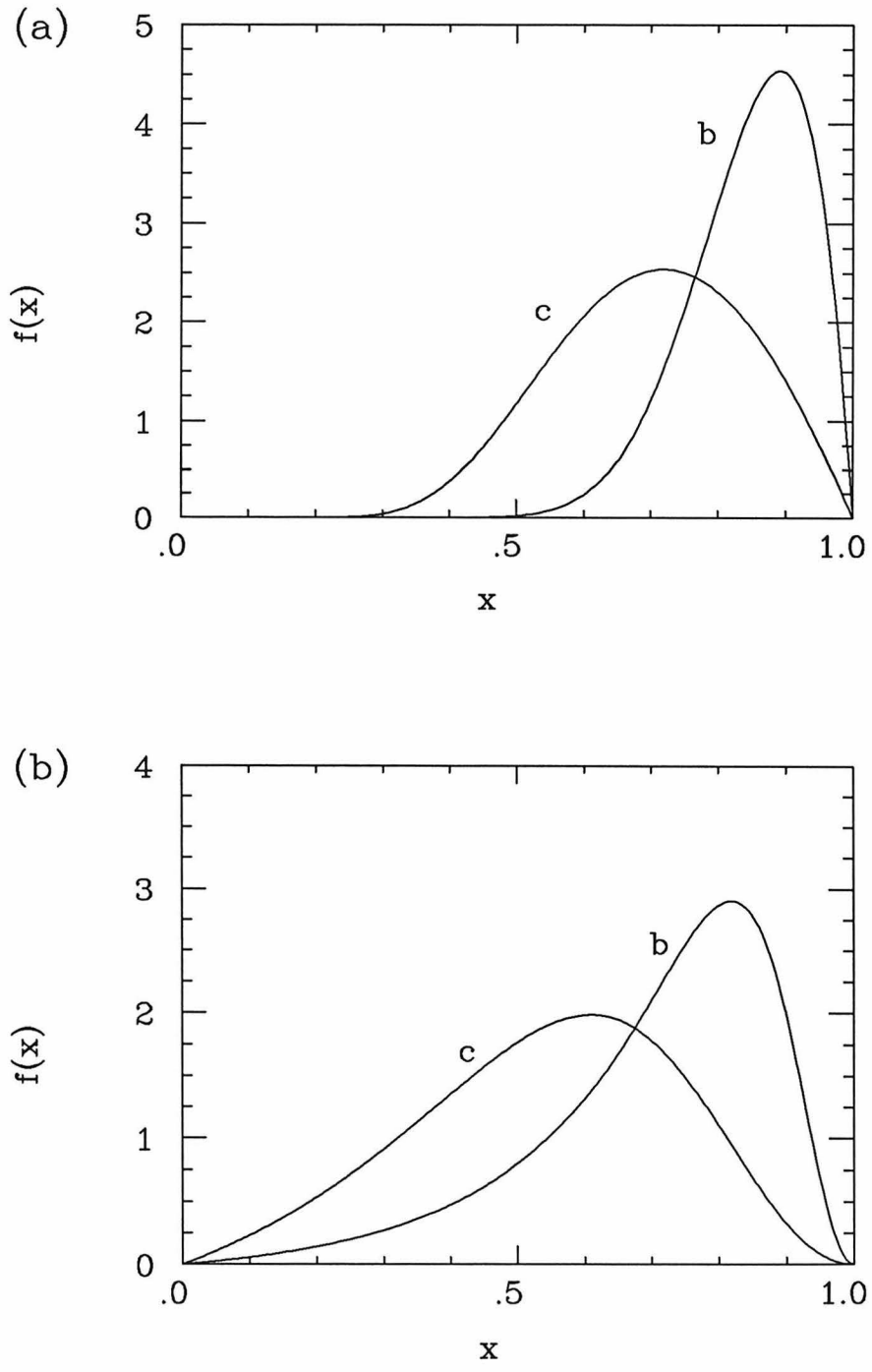

Figure 2.7. (a) Heavy quark fragmentation curves predicted by the model described in the text [Formula (2.25)]. (b) The shape suggested by Peterson *et al.* from a general quantum mechanical argument. In both figures, the curve labeled c (b) is for $m_Q = 2(5)$ GeV/c^2. For both $< m_0 >$ and m_q, we used 1 GeV/c^2.

A simple quantum mechanical argument also leads to a functional shape which becomes peaked at high x for heavy quarks,[55]

$$f(x) = \frac{A}{x(1 - \frac{1}{x} - \frac{\varepsilon}{1-x})^2}, \tag{2.26}$$

where A is a normalization constant. This parametrization is obtained by considering the transition

$$Q \rightarrow (Q\bar{q}) + q,$$

where the meson $(Q\bar{q})$ carries a fraction x of the momentum of the heavy quark Q and the light quark q carries the rest. The ansatz, (transition rate)$\propto$(phase space)$\times(E_{\text{final}} - E_{\text{initial}})^{-2}$, leads to the above formula with $\varepsilon = m_q^2/m_Q^2$. A reasonable value for the light quark mass would be the typical hadronic scale of $\sim$ 1 GeV. The shape is shown in Fig. 2.7(b) for m_Q = 2 and 5 GeV/c^2. This function has a maximum at x_{max}, which is given by

$$\varepsilon = x_{\text{max}} + \frac{1}{x_{\text{max}}} - 2.$$

Thus, $x_{\text{max}} \sim 1 - m_q/m_Q$ for $m_q \gg m_Q$.

It is worth noting that not all kinematical arguments lead to a harder fragmentation function for a heavier quark. For example, when a quark with momentum P inelastically picks up a light quark at rest to form a meson, then the momentum of the meson is always P and independent of the quark mass.

2.3.2 Heavy-Quark Fragmentation Functions in The String Model

In the string model with a uniform string breaking probability, a harder fragmentation for a heavy quark arises because of the way the mass of the heavy quark restricts the point of string breaking.[56] Figure 2.8(a) shows the trajectories of a heavy $Q\bar{Q}$ pair, which are hyperbolas [see (2.20)]. The string is assumed to break uniformly according to (2.21). The heavy quark combines with the light antiquark

produced at the vertex which has the smallest value of $t - x$, where (t, x) are the coordinates of the vertex. Because of the curvature of the heavy quark trajectory, this vertex tends to occur at an early time. And the earlier the breakup, the faster becomes the outgoing heavy meson h: in fact

$$z \equiv \frac{E_h + P_h}{E_q + P_q} = \frac{b}{a},$$

where a and b are shown in the figure. The resulting z distribution can be expressed by the incomplete gamma function

$$f(z) = e^{\alpha}\alpha^{-\alpha}\Gamma(\alpha + 1, \frac{\alpha}{z}), \tag{2.27}$$

with $\alpha = \frac{1}{2}m_Q^2 b/\kappa^2$. Thus, the hardness of the fragmentation function is determined by the string tension κ, the heavy quark mass m_Q, and the string breakup probability b. Since m_Q and κ are reasonably well known, the measurement of heavy quark fragmentation function gives b. Also, note that the function is scale invariant:[57] no E_q appears in (2.27).

The solid lines in Fig. 2.8(b) shows (2.27) for $m_Q = 2$ (labeled c) and 5 GeV/c^2 (labeled b) for $\kappa = 1$ GeV/fm and $b = 1/\text{fm}^2$. The function (2.27) does not go to 0 at $z = 1$. However, if we allow string breakups after the first crossing of Q and $\bar{q}$, the function comes down to 0 at $z = 1$. A Monte Carlo calculation was performed to find the limiting shape where the string keeps breaking until the meson mass is close to the heavy quark mass. In this case also, the shape is scale invariant and determined by the parameter $\alpha \equiv \frac{1}{2}m_Q^2 b/\kappa^2$. The shape is similar even if one stops breaking the string when the meson mass is about a pion mass above the heavy quark mass. The result is shown as histograms for the same set of parameters. The average z value is found to be $\sim 1 - m_0/m_Q$ with $m_0 \sim 1$ GeV/c^2, thus consistent with the plausibility arguments.

The LUND group does not use the uniform breakup probability. Instead, they derive the allowed form of fragmentation function as below.[58] The two-point distribution of two neighboring vertices that result in a meson of mass m

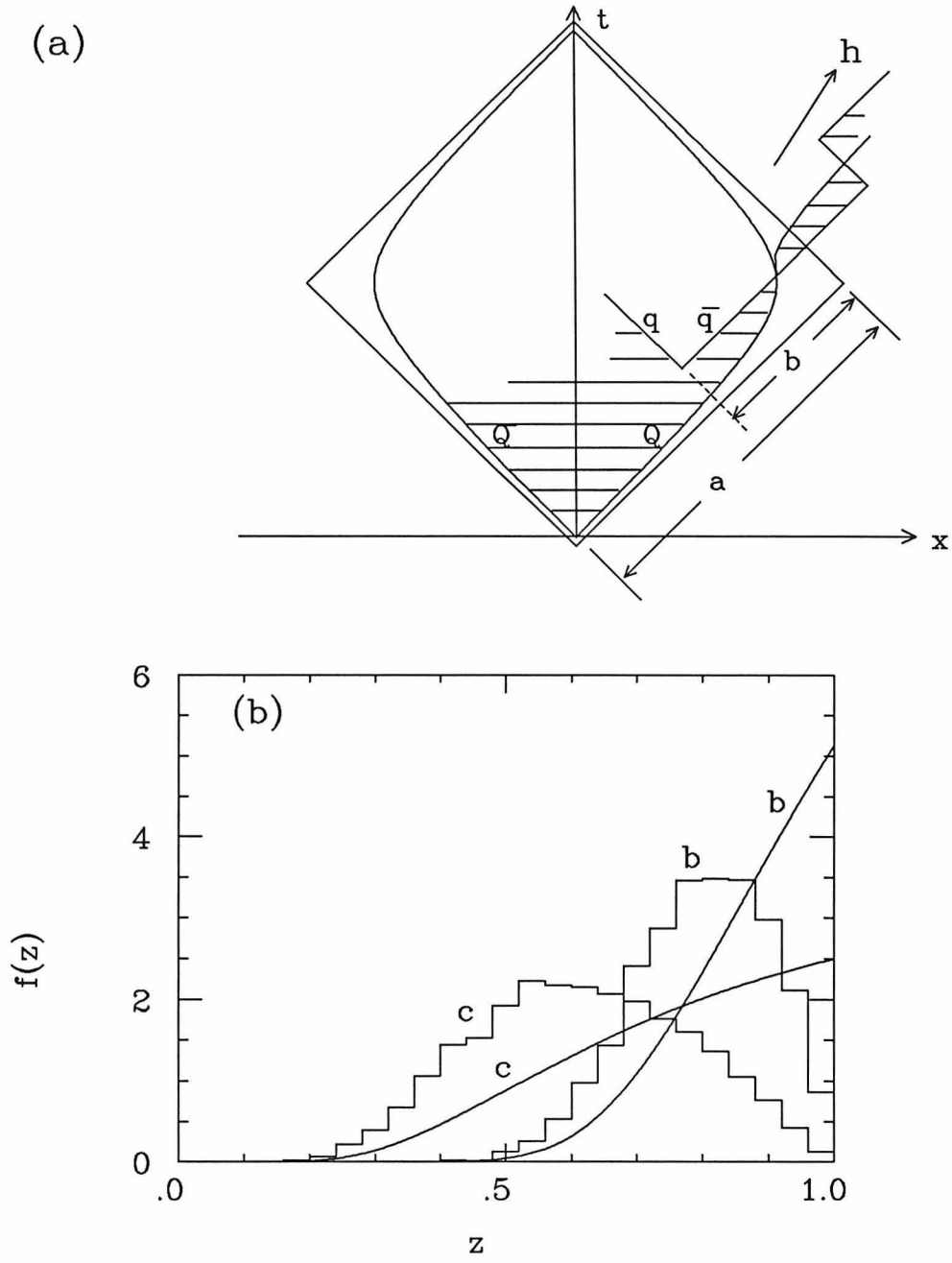

Figure 2.8. (a) Hyperbolic trajectories of a heavy quark pair $Q\bar{Q}$ are shown together with a string breakup that forms a leading heavy meson. The asymptotes of the hyperbola are also shown. The missing string section at the corner due to the curvature of heavy quark trajectory leads to a harder fragmentation function. (b) The solid curves are the fragmentation functions for $m_Q = 2$ GeV/c^2 (labeled c) and $m_Q = 5$ GeV/c^2 (labeled b) with $\kappa = 1$ GeV/fm and $b = 1/\text{fm}^2$. These curves transform to the shapes shown by histogram when string breakings inside the leading stringlet are allowed.

is determined by the distribution of one of the vertices plus the fragmentation function; and it should be independent of whether one start from the vertex on the right or that on the left. This leads to the following fragmentation function when a quark of type α picks up an antiquark of type β to form a meson:

$$f_{\alpha\beta}(z) = N_{\alpha\beta}\frac{dz}{z}z^{a_\alpha}\left(\frac{1-z}{z}\right)^{a_\beta}\exp(-\frac{bm^2}{z}), \tag{2.28}$$

where a_α and a_β are constants that depend only on the quark flavor, and b is a constant independent of the quark flavor. This is a very strong restriction on the form of fragmentation function. However, since the function depends on the quark mass through a_α which is not determined by the argument of the left-right symmetry, the mass dependence prediction of (2.28) is not well defined.

To summarize, the quark fragmentation function is expected to be harder for a heavier quark. This can be derived from various arguments ranging from the relativistic kinematics to the quantum mechanics of general transition. They consistently predict $< x > \sim 1 - m_0/m_Q$, where m_0 is the typical strong interaction scale ($\sim$ 1 GeV). Especially interesting is the string model, which predicts the same behavior of the fragmentation function from its well-defined dynamics, where the hardness of the function depends on the string breaking probability b. This can be used to derive b from the measured D^* momentum distribution.

2.4 Decays of Charmed Mesons

In this section, we will examine the status of the standard model in explaining the decays of charmed mesons. First, we will review the general structure of the weak charged current, then the semileptonic decays of heavy mesons which is relatively well understood, followed by the more uncertain nonleptonic decays.

2.4.1 Weak Charged Current - Kobayashi-Maskawa Matrix

In the standard model, weak decays of fermions in general proceed through their coupling to the charged weak vector bosons $W^{\pm}$. The relevant part of the Lagrangian is (the hermitian conjugate is implied),

$$\frac{g}{\sqrt{2}}(\bar{\nu}_L\gamma_\mu l_L + \bar{p}_L\gamma_\mu U n_L)W^\mu, \tag{2.29}$$

where

$$\nu = \begin{pmatrix} \nu_e \\ \nu_\mu \\ \nu_\tau \end{pmatrix}, \quad l = \begin{pmatrix} e \\ \mu \\ \tau \end{pmatrix}, \quad p = \begin{pmatrix} u \\ c \\ t \end{pmatrix}, \quad n = \begin{pmatrix} d \\ s \\ b \end{pmatrix},$$

$g/\sqrt{2}$ is the coupling constant, and the subscript L indicates left-handed component: $\nu_{eL} \equiv \frac{1}{2}(1-\gamma_5)\nu_e$, etc. The 3 by 3 unitary matrix U mixes generations. This is because the eigenstates of weak isospin are in general not the same as those of mass (i.e., flavor). There is no corresponding mixing for leptons [the first term in (2.29)] since all neutrinos are assumed massless in the standard model: for example, we can always redefine the neutrino state that forms a weak isospin doublet with e_L to be ν_e. A 3 by 3 unitary matrix has 9 degrees of freedom, of which 5 can be removed by adjusting the relative phases among 6 flavors, leaving 4 free parameters. Since a real 3 by 3 orthogonal matrix has three rotation angles, there is one non-trivial complex phase left. Thus, U may be parametrized as

$$\begin{pmatrix} U_{ud} & U_{us} & U_{ub} \\ U_{cd} & U_{cs} & U_{cb} \\ U_{td} & U_{ts} & U_{tb} \end{pmatrix} = \begin{pmatrix} 1 & 0 & 0 \\ 0 & c_2 & s_2 \\ 0 & -s_2 & c_2 \end{pmatrix} \begin{pmatrix} c_1 & s_1 & 0 \\ -s_1 & c_1 & 0 \\ 0 & 0 & 1 \end{pmatrix} \begin{pmatrix} 1 & 0 & 0 \\ 0 & 1 & 0 \\ 0 & 0 & e^{i\delta} \end{pmatrix} \begin{pmatrix} 1 & 0 & 0 \\ 0 & c_3 & s_3 \\ 0 & -s_3 & c_3 \end{pmatrix}$$

$$= \begin{pmatrix} c_1 & s_1c_3 & s_1s_3 \\ -s_1c_2 & c_1c_2c_3 - s_2s_3e^{i\delta} & c_1c_2s_3 + s_2c_3e^{i\delta} \\ s_1s_2 & -c_1s_2c_3 - c_2s_3e^{i\delta} & -c_1s_2s_3 + c_2c_3e^{i\delta} \end{pmatrix}, \tag{2.30}$$

where c_i and s_i stand for $\cos\theta_i$ and $\sin\theta_i$, respectively, for $i = 1, 2, 3$. The complex phase δ can lead to CP violation. In fact, this 6-quark model was proposed by

Kobayashi and Maskawa as a candidate model of CP violation.[59] The matrix U is called the 'generalized Cabibbo matrix' or 'KM mixing matrix.'

Present knowledge of the absolute values of the mixing matrix elements comes from the following measurements:

1. Nuclear β decays[60] ($|U_{ud}|$).
2. Hyperon and K_{e3} decays[61] ($|U_{us}|$).
3. Charm productions in neutrino-nucleon interactions[62] ($|U_{cd}|$).
4. Lepton spectrum in the semileptonic decays of D mesons[63] ($|U_{cd}|/|U_{cs}|$).
5. Lepton spectrum in the semileptonic decays of B mesons[64] ($|U_{bu}|/|U_{bc}|$).
6. Average b-hadron lifetime[65,66] ($|U_{bc}|$).

Here, we quote the result of the combined fit by Kleinknecht (with the unitarity constraint):[67]

$$\begin{pmatrix} |U_{ud}| & |U_{us}| & |U_{ub}| \\ |U_{cd}| & |U_{cs}| & |U_{cb}| \\ |U_{td}| & |U_{ts}| & |U_{tb}| \end{pmatrix} =$$

$$\begin{pmatrix} 0.9730 \pm 0.0007 & 0.231 \pm 0.003 & < 0.004(1\sigma) \\ 0.231 \pm 0.003 & 0.9719 \pm 0.0008 & 0.045 \pm 0.06 \\ 0.010 \pm 0.005 & 0.044 \pm 0.006 & 0.9990 \pm 0.0003 \end{pmatrix}. \qquad (2.31)$$

It is interesting to note that this can be closely approximated by

$$\begin{pmatrix} 1 & \lambda & \lambda^3 \\ \lambda & 1 & \lambda^2 \\ \lambda^3 & \lambda^2 & 1 \end{pmatrix} \quad \text{with} \quad \lambda \sim 0.23.$$

Namely, the transition amplitude between the first and second generation is suppressed by s, that between the second and third by λ^2, and that between the first and third by $\lambda \cdot \lambda^2 = \lambda^3$. This strongly suggests an existence of some structure beyond the standard model. There have been many attempts to derive the mixing angles within the framework of grand unified theory or by introducing a symmetry among generations (horizontal symmetry).[68] Even though substantial progress has been made, we are still far from a satisfactory theory.

Based on the above observation, Wolfenstein has proposed a parametrization of the KM matrix as an expansion in powers of λ.[69] To order λ^3, it reads

$$U = \begin{pmatrix} 1-\lambda^2/2 & \lambda & \lambda^3 A(\rho - i\eta) \\ -\lambda & 1-\lambda^2/2 & \lambda^2 A \\ \lambda^3 A(1-\rho-i\eta) & -\lambda^2 A & 1 \end{pmatrix} + O(\lambda^4), \tag{2.32}$$

where λ, A, ρ, and η are all real. Note that the phase convention has been changed from the one in (2.30) so that the CP violating phase is now associated with the two smallest elements. In terms of these parameters, the values in (2.31) translate to $\lambda = 0.231 \pm 0.003$, $A = 0.82 \pm 0.13$, and $\rho^2 + \eta^2 < 0.2(1\sigma)$.

The allowed range for the complex phase is derived from the measured CP-violation parameter ϵ_K of the K^0-$\bar{K}^0$ system:[70,71]

$$|\epsilon_K| = (2.29 \pm 0.03) \times 10^{-3}. \tag{2.33}$$

The standard model prediction for ϵ is given by[72]

$$\epsilon_K = 3.1 \times 10^{-3} A^2 \eta B_K \left[1 + 0.5A^2(1-\rho)(\frac{m_t}{45\text{GeV}})^2\right], \tag{2.34}$$

where B_K is the parameter that characterizes the making of K^0 out of d and $\bar{s}$ quarks (a non-perturbative effect) and is in the range $1/3 \lesssim |B_K| \lesssim 1$.[73] Using the upper limits for A, B_K, and $\rho^2 + \eta^2$, the formula (2.34) gives $|\epsilon_K| < 1.8 \times 10^{-3}$. The maximum corresponds to $\rho \sim 0$, namely an almost purely imaginary U_{ub}. Thus, the measured value of $|\epsilon_K|$ is around the upper limit of the theoretical prediction, and U_{ub} is likely to have a large imaginary component.[74]

2.4.2 Semileptonic Decays of Charmed Mesons

An old technique to estimate the semileptonic decay rate of a charmed meson is to calculate each exclusive channel independently,[75] in analogy to the case of the kaon semileptonic decays. In fact, it is known that the semileptonic decay rate of D

meson is saturated by $D \to Ke\nu_e$ and $D \to K^* e\nu_e$.[76] However, the main difficulty of this technique is that the calculation requires knowledge of the form factors. Even though one can guess the values using flavor SU(4) symmetry, current algebra etc., the uncertainty is large. Since, for charmed mesons the typical wave length of the emitted strange quark is smaller than the confinement scale of $\sim$ 1 fm, it seems more natural to discuss the decay at the quark level.[77] Even then, as we will see below, non-perturbative effects give rise to some uncertainties.

In the quark model, semileptonic decays of the charmed meson are caused by the decay of the charmed quark inside the meson to a lighter quark plus a neutrino-lepton pair. This is a special case of 3-body weak decay of fermion. The fermion decay, $f_0 \to f_1 f_2 \bar{f}_3$, proceeds through an 'emission' and subsequent 'decay' of a W boson as shown in Figure 2.9(a). The corresponding amplitude is given by

$$M = U_{f_3 f_2} U_{f_1 f_0} (\bar{f}_{3L} \gamma^\mu f_{2L}) [\frac{g^2}{2} \frac{g_{\mu\nu} - q_\mu q_\nu / M_W^2}{M_W^2 - q^2}] (\bar{f}_{1L} \gamma^\nu f_{0L}), \tag{2.35}$$

where M_W is the W boson mass (81 GeV/c^2), and $q = p_{f_0} - p_{f_1}$. The charged currents $(\bar{f}_{3L}\gamma_\mu f_{2L})$ and $(\bar{f}_{1L}\gamma_\nu f_{0L})$ are parts of (2.29), and $U_{f_3 f_2}$ and $U_{f_1 f_0}$ are corresponding elements of the Kobayashi-Maskawa matrix or their complex conjugate ($U_{ff'} = U^*_{f'f}$). For leptons, $U_{ll'} = \delta_{ij}$, where i and j are the generation number of l and l' respectively.

When the 4-momentum transfer q is much less than M_W, the value inside the square bracket in (2.35) is well approximated by a constant $2\sqrt{2}G_F$ [Fig. 2.9(b)]:

$$M = U_{f_3 f_2} U_{f_1 f_0} [2\sqrt{2} G_F] (\bar{f}_{3L} \gamma^\mu f_{2L}) (\bar{f}_{1L} \gamma_\mu f_{0L}) \quad (|q_\mu| \ll M_W), \tag{2.36}$$

where

$$G_F = \frac{g^2}{4\sqrt{2} M_W^2} = 1.16637 \pm 0.00002 \times 10^{-5} \mathrm{GeV}^{-2}$$

is the Fermi coupling constant. In other words, the distance of the weak interaction ($\sim 1/M_W$) is much smaller than the wavelength of fermions involved so that the interaction can be approximated by a point interaction.

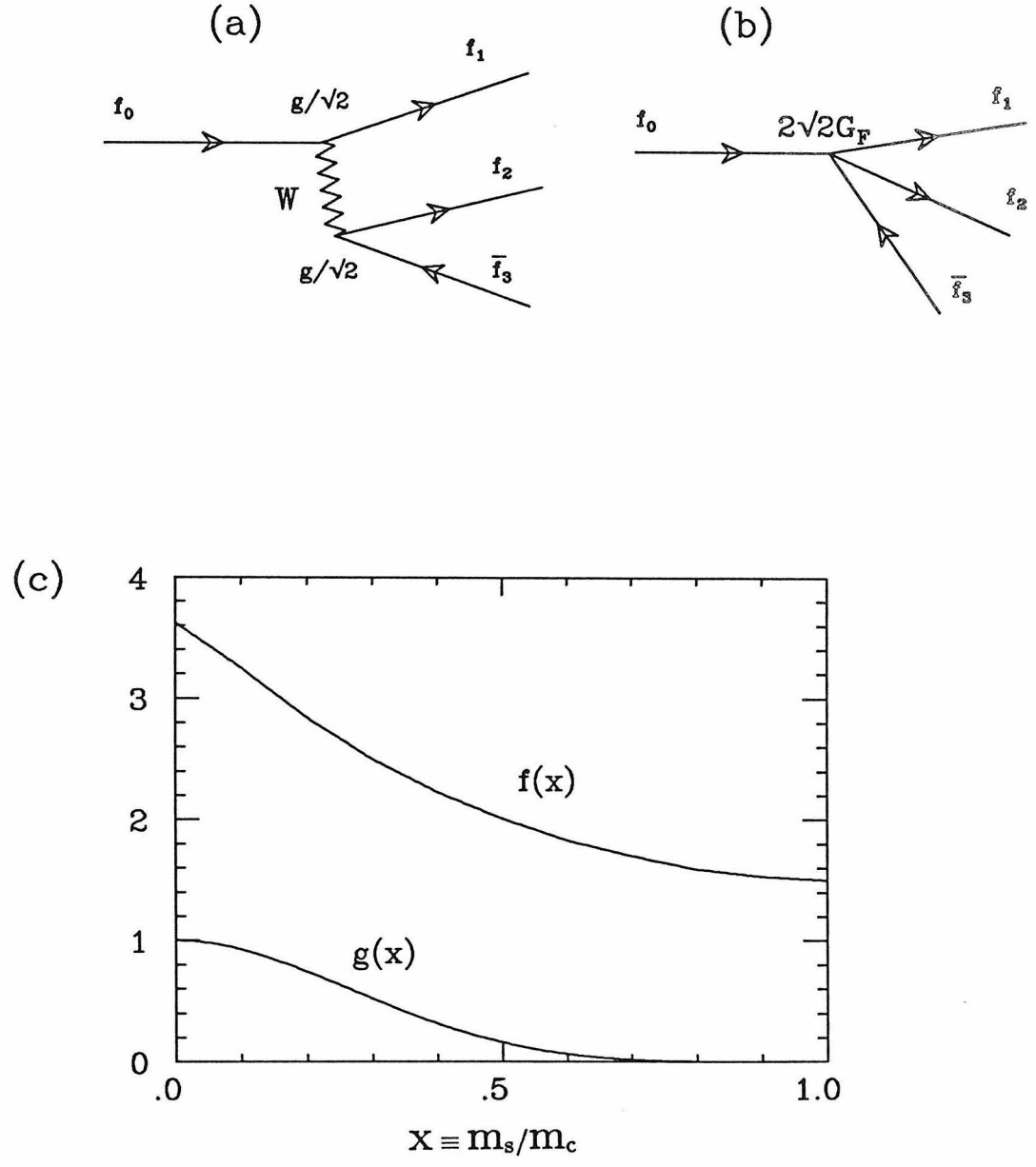

Figure 2.9. (a) The decay $f_0 \to f_1 f_2 \bar{f}_3$ through the W boson propagator with coupling constant $g/\sqrt{2}$. If $q^2 \ll M_W$, it can be approximated by the Fermi 4-point coupling (b) with the coupling constant $2\sqrt{2}G_F$. All fermions are taken to be left-handed. (c) The phase space correction function $g(x)$ and the QCD correction function $f(x)$ are shown, where $x = m_s/m_c$, or in general, $x = m_{f_1}/m_{f_0}$

For muon, the only allowed channel is $\mu^- \to \nu_\mu e^- \bar{\nu}_e$. The decay rate Γ_μ is proportional to $G_F^2 \sim \text{GeV}^{-4}$, while the dimension of Γ_μ is energy (GeV). Since the only mass scale available (ignoring the electron mass) is m_μ, Γ_μ should have the form (constant)$\times G_F^2 m_\mu^5$. The actual calculation yields

$$\Gamma_\mu = \frac{G_F^2 m_\mu^5}{192\pi^3} = 3.0 \times 10^{-19}\text{GeV} = (2.2\mu\text{sec})^{-1}.$$

For $f^0 = c$ (charmed quark decay), f_1 is s or d, and the pair $(\bar{f}_3, f_2)$ can be (e^+, ν_e), (μ^+, ν_μ), $(\bar{d}, u)$, or $(\bar{s}, u)$. We define the semileptonic decay rate Γ_{SL} to be the rate of decay that contains the pair (e^+, ν_e) where the electron mass can be ignored. Thus, the charmed quark decays relevant to Γ_{SL} are $c \to d\nu_e e^+$ and $c \to s\nu_e e^+$. The ratio of the two is of order $|U_{cd}/U_{cs}|^2 \sim 5\%$, and we will assume that $c \to s$ 100% of the time. This will not change the estimated decay rate significantly. Without neglecting the strange quark mass, and with the first order QCD radiative correction, the semileptonic decay rate Γ_{SL}^{QCD} is given by [78]

$$\Gamma_{SL}^{QCD} = \Gamma_0\, g(x)[1 - \frac{2\alpha_s(m_c^2)}{3\pi} f(x)], \tag{2.37}$$

where

$$\Gamma_0 \equiv \Gamma_\mu \frac{m_c^5}{m_\mu^5} \sim 2 \times 10^{-13}\text{GeV} \sim (4\text{psec})^{-1},$$

and

$$g(x) = 1 - 8x^2 - 24x^4 \ln x + 8x^6 - x^8,$$

with $x = m_s/m_c$. The function $g(x)$ is the phase space correction factor, and the quantity inside the square bracket in (2.37) is the first order QCD radiative correction. Fig. 2.9(c) shows the functions $g(x)$ and $f(x)$. Note that the suppression due to the phase space factor can be quite large ($\sim$1/2 at $m_s/m_c = 1/3$), and the QCD correction also reduces the semileptonic decay rate.

There is an uncertainty in the formula (2.37) because the charmed quark in the initial state and the strange quark in the final state are not free but confined.

We know that the final state strange quark appears almost always as a K or K^* meson. Can we still assume that the quarks are free? The answer is a conditional 'yes.' The justification for (2.37) is that the wavelength of the strange quark is in general sufficiently small compared to the size of mesons that the charmed quark decay decouples from the formation of final state resonances. In other words, the quark model is expected to reproduce the effect of strong resonances in the sense of duality.[79] However, it is difficult to quantify the accuracy of the above claim.

In addition, we still do not know exactly what values to use for the quark masses. Fermi motion can also shift the effective quark masses.[80] Instead of guessing the value of the charmed quark mass, we will derive it from the measurement of the semileptonic decay rate of D^0 meson. The resulting value can be interpreted as the average invariant mass of the charmed quark inside a D^0 meson.

2.4.3 Nonleptonic Decays of Charmed Mesons

For nonleptonic decays, the four relevant fermions in the Hamiltonian (2.36) [see also Fig. 2.9(b)] are all quarks, and they interact strongly by exchanging gluons. Also, the role of the light valence quark in the parent meson (the spectator quark) is more active than for semileptonic decays. These effects increase the uncertainties in the calculation of nonleptonic decays. In general, only the Cabibbo favored decays are considered below.

2.4.3.1 Nonleptonic Effective Hamiltonian

First, we assume the charmed quark decays independently of the spectator quark, ignore the masses of final-state fermions, and disregard QCD corrections. The Hamiltonian responsible for nonleptonic decays is then

$$H^0_{NL} = 2\sqrt{2}G_F(\bar{s}c)_L(\bar{u}d)_L. \tag{2.38}$$

In the above, we have introduced an abbreviation for the left-handed current

summed over three colors:

$$(\bar{f}f')_L = \sum_{i=1}^{3}(\bar{f}_L\gamma_\mu f'_L)$$

where i is the color index, and the summation forms a color-singlet current. The possible decay channels of a charmed quark with color i are $c_i \to s_i\nu_e e^+$, $s_i\nu_\mu\mu^+$, and $s_i u_j \bar{d}_j (j = 1,2,3)$. The decay rates of these channels are the same, and the nonleptonic decay rate and the semileptonic branching ratio are simply

$$\Gamma_{NL}^{(0)} = 3\Gamma_0, \qquad B_{NL}^{(0)} = 20\%. \tag{2.39}$$

Under the assumptions made above, this holds for all charmed hadrons. The experimental data on the semileptonic branching ratios by the MARK III collaboration[81] are

$$\begin{aligned} B_{SL}(D^0) &= 7.5 \pm 1.1 \pm 0.4\% \\ B_{SL}(D^+) &= 17.0 \pm 1.9 \pm 0.7\%. \end{aligned} \tag{2.40}$$

The first error in each branching fraction is statistical and the second systematic. One notices two discrepancies between the prediction and the measurements: (1) the average of the two measured semileptonic branching fractions is smaller than the expected value of 20%, and (2) the semileptonic branching fraction of D^+ is larger than that of D^0 by a factor ~ 2. The first is partially explained by QCD corrections to the lowest order diagram [Fig. 2.9(b)]. The second discrepancy suggests that the spectator quark also participates in the decay process because the only difference between D^0 and D^+ seems to be the type of spectator quark.

2.4.3.2 QCD Correction to the Nonleptonic Hamiltonian

The QCD correction changes the color flows of the 4-quark interaction (2.38) through the exchange of gluons. Two quarks flow into the interaction point and two flow out. Thus, there are two ways to combine these quarks to make color-singlet currents: (a) $(\bar{s}c)_L(\bar{u}d)_L$, and (b) $(\bar{u}c)_L(\bar{s}d)_L$. These are shown in Figure 2.10(a)

and (b). The original Hamiltonian [Eq. (2.38)] is of type (a), while QCD corrections generate an effective neutral-current interaction of type (b). The QCD corrected nonleptonic Hamiltonian can be written as

$$H_{NL}^{(1)} = 2\sqrt{2}G_F(c_+\mathcal{O}_+ + c_-\mathcal{O}_-), \tag{2.41}$$

where

$$\mathcal{O}_\pm = \frac{1}{2}[(\bar{s}c)_L(\bar{u}d)_L \pm (\bar{u}c)_L(\bar{s}d)_L].$$

The operator $\mathcal{O}_+$ is symmetric under interchange of s and u; thus, its V-spin is 1. On the other hand, $\mathcal{O}_-$ is antisymmetric under the interchange; thus, its V-spin is 0. More generally, $\mathcal{O}_+$ ($\mathcal{O}_-$) transforms as a 15-plet (sextet) under the flavor SU(3) and as a 84-plet (20-plet) under SU(4). The leading-logarithm approximation (LLA) gives[82]

$$c_\pm = \left[\frac{\alpha_s(Q^2)}{\alpha_s(M_W^2)}\right]^{d_\pm/(2b)}, \tag{2.42}$$

where α_s and b are defined by (2.10), and $d_- = -2d_+ = 8$. Thus, c_+ and c_- are related by $c_+^2 c_- = 1$. If QCD corrections are ignored, $c_+ = c_- = 1$, which recovers (2.38). The formula (2.41) leads to the following nonleptonic decay rate and the semileptonic branching ratio:[83]

$$\begin{aligned} \Gamma_{NL}^{(1)} &= (2c_+^2 + c_-^2)\Gamma_0 \\ B_{SL}^{(1)} &= (2 + 2c_+^2 + c_-^2)^{-1}. \end{aligned} \tag{2.43}$$

For $Q = 1.5$, $\Lambda = 150$ MeV, and $n_f = 4$, c_+ is 0.78 and c_- is 1.7; the QCD correction enhances the SU(3) sextet (or $V = 0$) part of the interaction. The corresponding nonleptonic decay rate $\Gamma_{NL}^{(1)}$ is enhanced by a factor of 1.3 over the non-corrected decay rate $\Gamma_{NL}^{(0)}$ leading to $B_{SL}^{(1)} = 17\%$.

2.4.3.3 QCD Radiative Correction and NLLA

In order to compare the nonleptonic rate with the semileptonic decay rate of (2.37), the phase space correction and the QCD radiative correction have to be taken

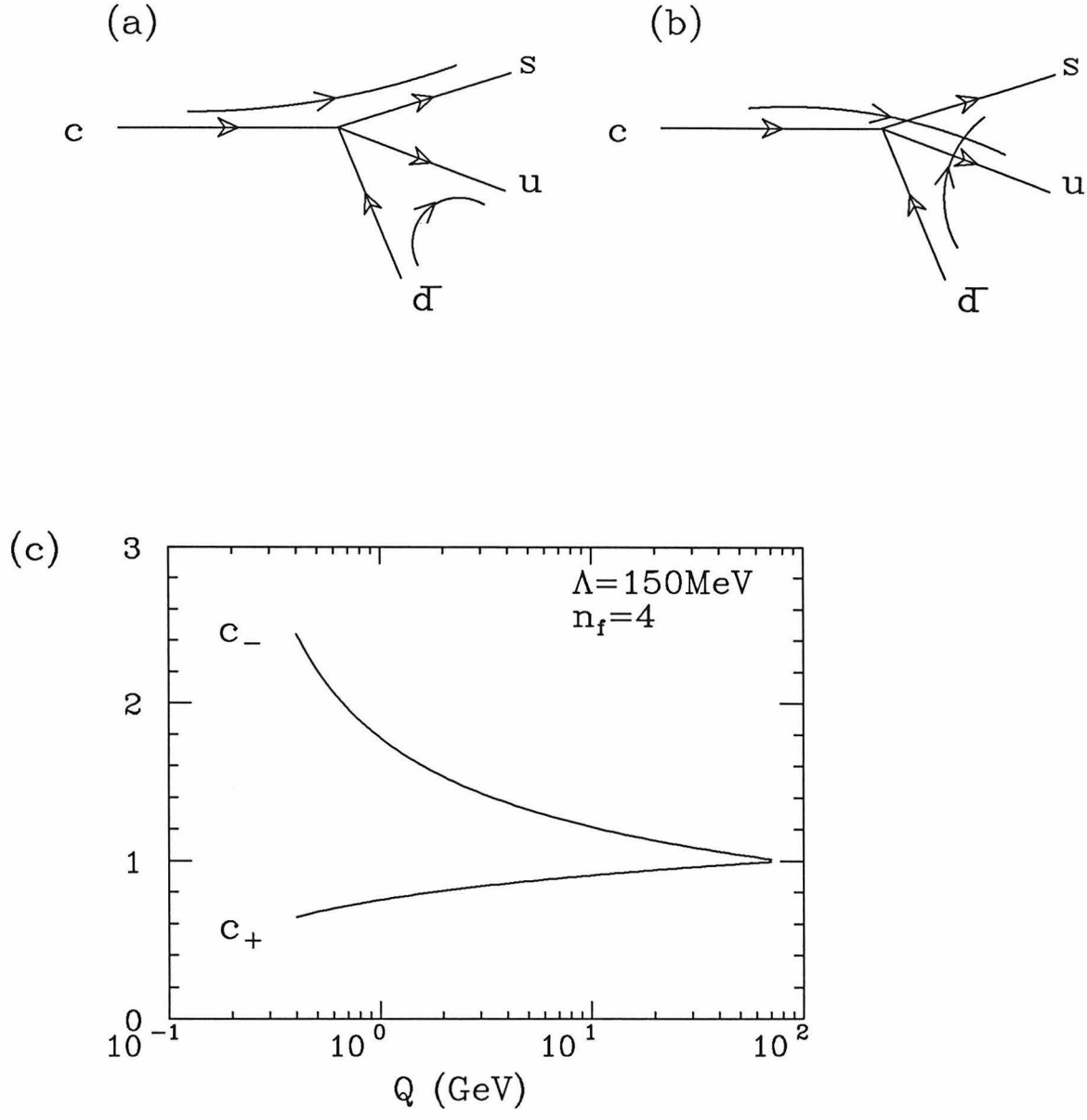

Figure 2.10. (a) and (b) show the two ways to form color-singlet currents for the 4-quark interaction $c \to su\bar{d}$. The original Hamiltonian before the QCD correction has the color flows as shown in (a). The effective neutral currents shown in (b) are generated by gluon exchanges. The coefficients $c_\pm$ are plotted in (c) as functions of Q. The values are calculated by the leading-logarithm approximation (LLA). The Λ parameter is defined by (2.10).

into account. The QCD correction (2.10) includes gluon exchanges but not gluon radiation. The consistent treatment of both effects requires the next-to-leading-logarithm approximations (NLLA) including two-loop diagrams,[84] and the result is given by[85]

$$\Gamma_{NL}^{QCD} = \Gamma_0 \, I(x_1, x_2, x_3)(2c_+^2 + c_-^2) \left[1 + \frac{2}{3} \frac{\alpha_s(Q^2)}{\pi} h \right], \tag{2.44}$$

where $I(x_1, x_2, x_3)$ is the phase-space correction factor given in Appendix. The parameter h is a function of $\alpha_s(Q^2)$[86] and its typical value is 2.2. The strong coupling constant in (2.44) is given by a formula that includes two-loop effects:[87]

$$\alpha_s = \frac{4\pi}{b \ln \frac{Q^2}{\Lambda^2}} \left[1 - (102 - \frac{38}{3} n_f) \frac{\ln \ln \frac{Q^2}{\Lambda^2}}{b^2 \ln \frac{Q^2}{\Lambda^2}} \right]. \tag{2.45}$$

The parameters $c_\pm$ are still defined by (2.42), but with the improved formula above for α_s. Apart from the phase-space factor $I(x_1, x_2, x_3)$, the masses of final-state fermions are ignored. The semileptonic branching fraction from (2.37) and (2.44) is then

$$B_{SL}^{QCD} = \left[2 + \frac{I(x_1, x_2, x_3)}{g(x_1)} (2c_+^2 + c_-^2) \frac{1 + \frac{2\alpha_s(Q^2)}{3\pi} h}{1 - \frac{2\alpha_s(Q^2)}{3\pi} f(0)} \right]^{-1}. \tag{2.46}$$

When the current masses are used for u and d quarks (several MeV), the phase space is practically the same for the semileptonic decay and for the nonleptonic decay, and does not change the semileptonic branching fraction. When the constituent masses are used, however, the nonleptonic decay is considerably suppressed with respect to the semileptonic decay.[88] The relative suppression factor due to the mass effect varies from 0.9 for $m_{u,d} = 100$ MeV to 0.6 for $m_{u,d} = 250$ MeV (see Appendix).

Figure 2.11(a) shows the nonleptonic enhancement factors relative to the semileptonic rate. They are shown for no-correction, for the LLA correction, and for the NLLA plus QCD radiative correction. The last is shown for two values of

m_{ud}: 0 and 250 MeV. The corresponding branching ratios for $Q = 1.5$ GeV are plotted as functions of Λ in Fig. 2.11(b). The value Λ is defined by the improved formula for the effective strong coupling constant (2.45); at $Q = 1.5$ GeV, $\Lambda = 280$ MeV for (2.45) gives the same α_s as $\Lambda = 150$ MeV for (2.10).[89] For $\Lambda = 200$ to 400 MeV and $m_{ud} = 0$ to 250 MeV, the expected semileptonic branching ratio from the spectator model is thus 10 to 19%. The mass effect cannot be ignored: if constituent masses are used, it almost cancels the effect of QCD corrections. For $m_{ud} = 0$, the suppression of the semileptonic rate accounts for about 40%, the enhancement of the nonleptonic rate for about 60% of the relative nonleptonic enhancement.

As can be seen in Fig. 2.11, the LLA correction alone is not adequate. This, however, does not mean that the perturbation calculation is not valid. In fact, the NLLA calculation of the coefficients corresponding to $c_\pm$ in (2.41) changes the LLA values by only ~10% (toward the direction that reinforces the LLA correction). The large difference is mainly due to the QCD radiative correction including real-gluon emission, and the NLLA calculation is needed to treat it in a consistent way.

2.4.3.4 Enhancement of The D^0 Nonleptonic Decays

We now turn to the difference between $B_{SL}(D^0)$ and $B_{SL}(D^+)$. As mentioned earlier, the difference implies the effect of the spectator quark. The comparison of the expected semileptonic branching ratio, 10 to 19%, with the experimental values (2.40) suggests that the spectator quark enhances the nonleptonic decay in D^0 and/or suppresses it in D^+. We will start from a candidate model for the enhancement of D^0 nonleptonic decay.

Figure 2.12 shows possible processes for charmed-meson decays. In the diagram (a), the emitted W decays by itself (W-emission), in (b) and (c), the W boson annihilates the valence quarks in the meson (annihilation), and in (d), the emitted W boson is absorbed by the same quark line from which it is emitted (penguin). The annihilation diagram for D^+, (c), is Cabibbo-suppressed, while that for D^0, (b), is not. Thus the enhanced D^0 nonleptonic rate may be explained if the annihilation

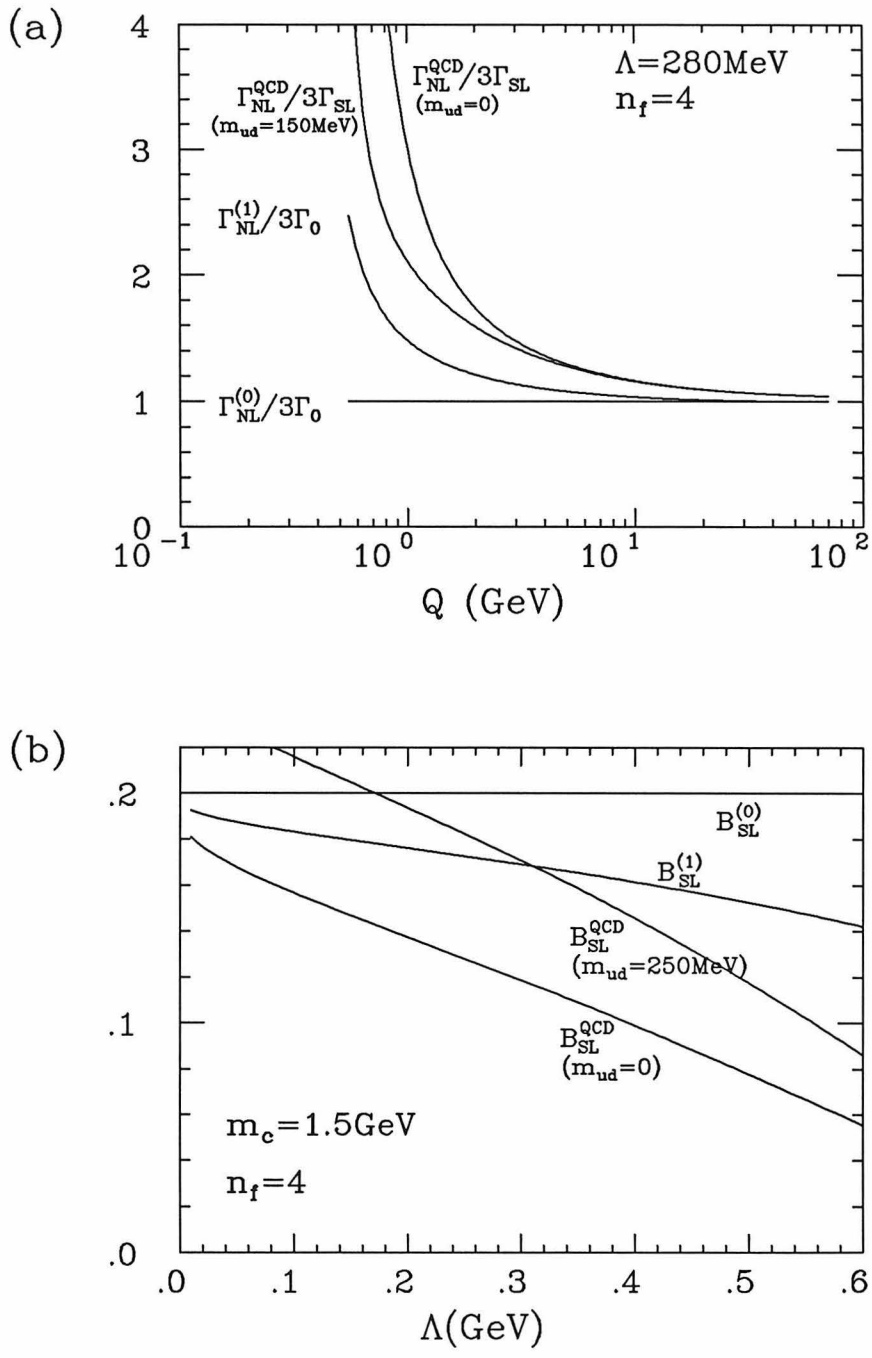

Figure 2.11. (a) The relative nonleptonic enhancement factors are shown for no-correction ($\Gamma_{NL}^{(0)}/3\Gamma_0$), for the LLA correction ($\Gamma_{NL}^{(1)}/3\Gamma_0$), and for the NLLA correction plus QCD radiative correction ($\Gamma_{NL}^{QCD}/\Gamma_{SL}^{QCD}$). The last is shown for the two values of m_{ud}. (b) The corresponding expected semileptonic branching ratios are shown as functions of Λ for $Q = m_c = 1.5$ GeV. The Λ parameter is defined by the improved formula for the strong coupling constant (2.45).

process is important. Table 2.1 shows the Cabibbo factors for each mode and each meson of interest.

Even though it was noted that the annihilation process may contribute to some exclusive modes,[90] until recently, the effect was generally thought to be negligible because of the helicity suppression;[91] just as the decay $\pi^+ \to e^+\nu_e$ is suppressed by the $V-A$ nature of the interaction and the conservation of angular momentum, any $J=0$ state cannot decay to a massless fermion-antifermion pair through the $V-A$ interaction.

In direct analogy to the π^+ decay, the decay rate of $D^{0,+} \to$ quark+antiquark is given by

$$\Gamma_{\rm ann} = a_{0,+} 24\pi^2 \frac{(m_q^2 + m_{\bar{q}}^2) f_D^2 m_D}{m_c^5} \Gamma_0 \quad \begin{cases} a_0 = 1/3 & \text{for } D^0 \\ a_+ = 3\lambda^2 & \text{for } D^+ \end{cases}, \tag{2.47}$$

where $m_{q,\bar{q}} \ll m_c$ is assumed, the constants $a_{0,+}$ consist of the color factor and the KM mixing factor (λ) and f_D characterizes the overlap of the two valence quarks in the meson. The color factor 1/3 for D^0 arises because the contribution comes only from the part of the Hamiltonian (2.38) that combines $c\bar{u}$ in a color singlet state, while the color factor 3 for D^+ is simply the number of possible colors in the final state.

With $m_c = 1.5$ GeV, f_D =0.15 MeV,[92] and using the constituent masses (m_{ud} =0.25 GeV and m_s =0.5 GeV) for the final quarks, (2.47) gives $\Gamma_{\rm ann} = 0.14\Gamma_0$ for D^0 and $0.03\Gamma_0$ for D^+. If the current masses are used for the final quarks, $\Gamma_{\rm ann}$ will be even smaller, especially for D^+. With the QCD corrected Hamiltonian (2.41), a_0 is replaced by $(2c_+ - c_-)^2/3$ and a_+ by $\lambda^2(2c_+ + c_-)^2/3$. For $c_+ = 0.78$ and $c_- = 1.7$, a_0 becomes nearly zero: the annihilation mode for D^0 is highly suppressed. The QCD correction makes the $c\bar{u}$ pair in the Hamiltonian almost purely color-octet, leaving the Hamiltonian unable to annihilate the $c\bar{u}$ pair in the meson. Since the total decay rate is $\sim 5\Gamma_0$, the naive estimation gives the annihilation contribution of at most a few percent.

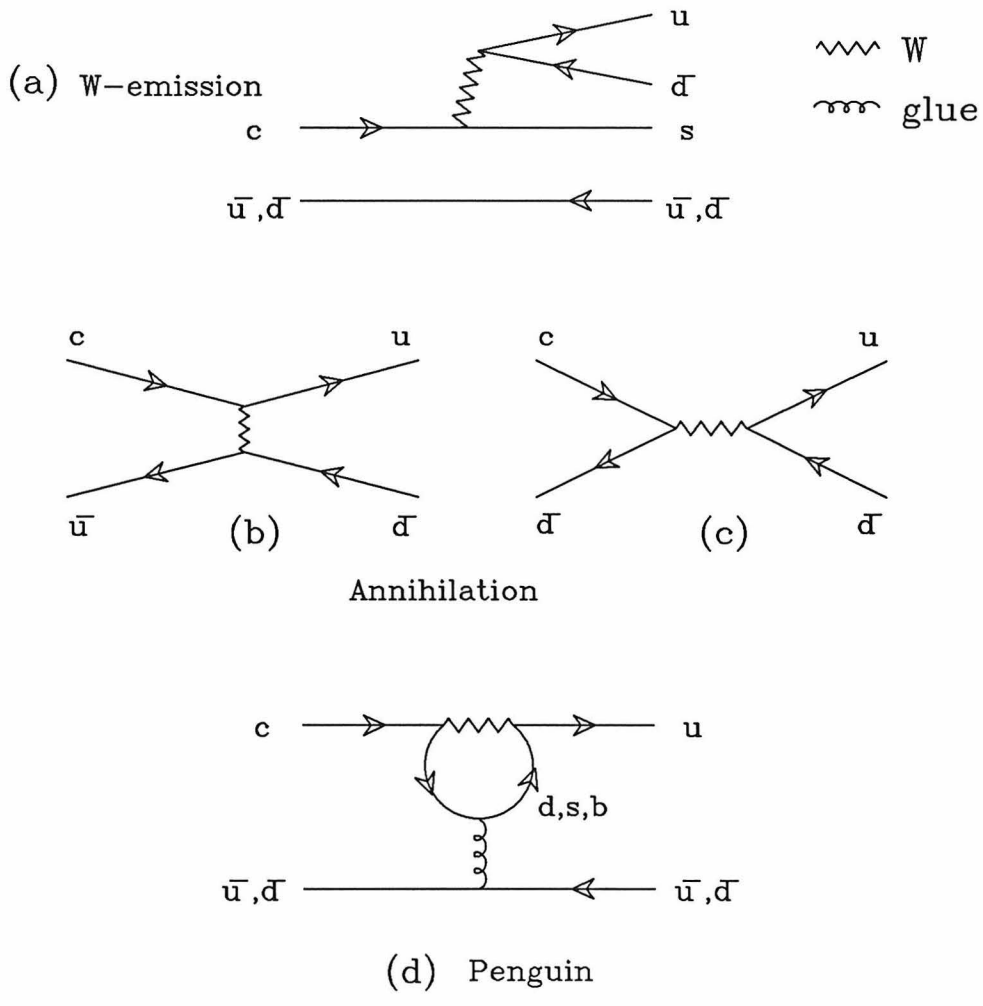

Figure 2.12. Charm decay diagrams without the QCD correction. With QCD correction, there is another set of diagrams in which each W vertex is replaced by the effective neutral current.

Table 2.1. Cabibbo factors of various meson decays are shown for the W-emission mode, the annihilation mode, and the penguin mode. The value of λ is ~ 0.23. See the equation (2.32).

mode	K^+	K^0	D^0	D^+	F^+	B^+	B_d^0	B_s^0
W-ex.	λ	λ	1	1	1	λ^2	λ^2	λ^2
Ann.	λ	λ	1	λ	1	λ^3	λ^2	λ^2
Pen.	λ	λ	λ^{5*}	λ^{5*}	λ^{5*}	λ^2	λ^2	λ^2

*The GIM cancellation between the d loop and the s loop is assumed to be complete.

The estimate (2.47) assumes that the valence quarks $c\bar{q}$ are in the color singlet state with the total angular momentum $J = 0$. However, the gluons may act as spectators allowing the pair $c\bar{q}$ to be in $J = 1$ state, thus lifting the helicity suppression,[93] or may be emitted from the initial-state quarks to the same effect.[94,95] In either case, single gluon leaves the $c\bar{q}$ pair in a color-octet state, which can be annihilated by the $c\bar{q}$-color-octet part of the Hamiltonian. Without the QCD correction, the annihilation rate of D^0 is given by[93]

$$\Gamma_{\rm ann}(D^0) = \rho 32\pi^2 \frac{\tilde{f}_D^2}{m_c^2}\Gamma_0, \tag{2.48}$$

where ρ is the probability that the $c\bar{u}$ pair is in a vector or axial-vector state. The value of $\tilde{f}_D$, which describes the overlap of c and $\bar{u}$ when they are in a vector or axial-vector state, is not known from other measurements. If we take $\tilde{f}_D \sim f_D \sim 0.15$ GeV, then,

$$\Gamma_{\rm ann}(D^0) = 3.2\rho\Gamma_0,$$

corresponding to about 40% of the total decay rate for $\rho = 1$, which is about the right amount to explain the difference between $B_{SL}(D^0)$ and $B_{SL}(D^+)$. More recently, other estimates of $\Gamma_{\rm ann}(D^0)$ have been made using the Regge model,[96] QCD multipole expansion,[97] the relativistic quark model,[98] and lattice QCD theory.[99] Their results, however, ranges from small effects[98,99] to the annihilation

dominance.[96,97] The difficulty is due to the non-perturbative nature of the problem. Thus, at present, the size of $\Gamma_{\rm ann}$ needs to be determined from experiments.

Clean signals for the annihilation process are $D^0 \to K^0\overline{K}^0$[100] and $\overline{K}^0\phi$,[101,102] which do not contain $\bar{u}$ quarks in the final state.[103] The $K^0\overline{K}^0$ mode is Cabibbo-suppressed; in addition, there are two contributing amplitudes with opposite sign:

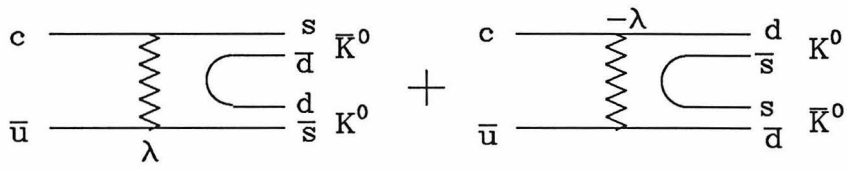

If the $s\bar{s}$ pair is created from the vacuum with the same probability and phase as $d\bar{d}$ pair [the SU(3) limit], the cancellation is exact. This mode, so far, has not been observed. On the other hand, the $\overline{K}^0\phi$ mode is not Cabibbo-suppressed, even though it may be suppressed to the extent that the $s\bar{s}$ creation from the vacuum is less likely than the $u\bar{u}$ or $d\bar{d}$ creation. If the annihilation channel dominates D^0 decays, the $\overline{K}^0\phi$ branching fraction is expected to be 0.2 to 1%.[104] Recently, the ARGUS collaboration has observed a preliminary signal from the $\overline{K}^0\phi$ mode with a branching fraction of $\sim 1\%$.[105] It is important that the measurement be confirmed.

Since the isospin of the final state is 1/2 for the Cabibbo-favored annihilation mode of D^0 (one $\bar{u}$), another signal of annihilation dominance would be

$$r \equiv \frac{\Gamma(\overline{K}^0\pi^0)}{\Gamma(K^-\pi^+)} = \frac{1}{2}, \tag{2.49}$$

where an experimental value is $r = 0.45 \pm 0.08 \pm 0.05$.[106] From the W-emission diagram [Fig. 2.12(a)], the expected value is[91,107] $r = \frac{1}{2}(2c_+ - c_-)^2/(2c_+ + c_-)^2 \sim 0$ with $c_+ = 0.78$ and $c_- = 1.7$. This is similar to the suppression of the annihilation mode of D^0 in the absence of gluon effects: in the effective Hamiltonian (2.41), the pair $s\bar{d}$ is in a state almost purely color-octet; thus, it cannot form a $\overline{K}^0$. However, this argument, which simply assumes that the color-singlet part of a free quark pair turns into a meson ('factorization'), has been questioned by several authors.[96,95,108–111] The exchange of soft gluons in the final state may lift the

color suppression,[110] and final state interactions can change $\overline{K}^0\pi^0$ to $K^-\pi^+$, especially if there is a resonance near the D^0 mass that can couple to both of these modes.[109] Also, factorization seems to fail in evaluating $\Gamma(D^+ \to \overline{K}^0\pi^+)/\Gamma(D^+ \to \overline{K}^0 e^+\nu)$.[111] If the color factor is ignored, then r for the W-emission becomes $1/2$, which comes simply from the $u\bar{u}$ content of π^0. Thus, the experimental value of r does not necessarily imply a large contribution from the annihilation mode.

2.4.3.5 Suppression of The $D^{\pm}$ Nonleptonic Decays

We now discuss candidate models that suppress the nonleptonic rate of D^+, in which interference effects together with the enhancement of the sextet part of the Hamiltonian play important roles. The W-emission mode of D^+ decay amplitude by the sextet part of (2.41), $\mathcal{O}_-$, can be graphically rewritten as

(2.50)

where ')' implies a color singlet. Since the two amplitudes with opposite signs have the same color singlets in the final state, it was argued[112,113] that if these color singlets act as point-like particles (strong 'color clustering'), then the cancellation would suppress the nonleptonic rate of D^+. For D^0, the two corresponding diagrams do not result in the same final state; thus, no interference is expected for D^0.

The cancellation in (2.50) is exact for $D^+ \to \overline{K}^0\pi^+$ in the SU(3) limit. Including the contribution from $\mathcal{O}_+$ and assuming factorization to be valid, we estimate the decay amplitude to be

$$A(D^+ \to \overline{K}^0\pi^+) = \frac{2c_+ + c_-}{3}a_s + \frac{2c_+ - c_-}{3}a_u, \tag{2.51}$$

where a_s (a_u) is the reduced amplitude when the s (u) quark combines with the spectator $\bar{d}$ quark, and corresponds to the first (second) diagram in (2.50). If

$m_s = m_u$, s and u have the same wave function (just like e^- and ν_μ in the μ^- decay), thus $a_s = a_u = a$, which leads to $A(D^+ \to \overline{K}^0\pi^+) = \frac{4}{3}c_+a$. It vanishes if $c_+ = 0$ (sextet dominance). This is true even without assuming factorization.[114] Since D^+ is V-spin singlet (no s or u), and so is $\mathcal{O}_-$, the final state is also V-spin singlet if $c_+ = 0$. Thus, the V-spins of $\overline{K}^0$ and π^+, which are both V-spin doublets, have to be combined antisymmetrically, but this is forbidden by the Bose statistics because the final state is an S-wave state. The essential assumptions for the suppression of $D^+ \to \overline{K}^0\pi^+$ are, therefore, sextet dominance and V-spin symmetry, i.e., $m_s = m_u$.

A sizable cancellation in (2.50) for general cases, however, is not plausible: the color singlets (strings?) would have a large number of energy, rotational, and vibrational states. Also, the same V-spin argument given above leads to an enhancement, not a suppression, when one of the final-state pseudo-scalars is replaced by the corresponding vector.[114]

On the other hand, the two $\bar{d}$'s in the final state can interfere at the quark level,[112,115] namely before the final-state meosns are formed. With the non-relativistic approximation for the quark motion inside the meson, the D^+ decay rate is given by[115,116]

$$\Gamma(D^+ \to u\bar{d}s\bar{d}) = (2c_+^2 + c_-^2)\Gamma_0 + (2c_+^2 - c_-^2)16\pi^2\frac{f_D^2}{m_c^2}\Gamma_0, \qquad (2.52)$$

where the second term is the interference term, while the first term is identical to (2.43). Since $c_-^2 > 2c_+^2$ by the QCD correction, the interference term is negative and results in a suppression of the nonleptonic rate of D^+. For $c_+ = c_- = 1$, namely without the QCD correction, the interference enhances the D^+ nonleptonic rate.

The two $\bar{d}$'s interfere only insofar as their colors, spins and momenta match. Since the state of $\bar{d}$ in the meson is essentially a non-perturbative problem, it is difficult to predict reliably the size of the interference effect. With $c_+ = 0.78$, $c_- = 1.7$, $m_c = 1.5$ GeV/c^2, and $f_D = 0.15$ GeV in (2.52), the nonleptonic rate

reduces to about 1/3 of the original value. Predictions by more careful analyses range from a small effect[98,117] to 40% reduction[118] of the D^+ nonleptonic rate.

Before leaving the subject of the interference effect, a few comments are in order. 1) The typical momentum of the $\bar{d}$ from the weak decay is much higher than that of the Fermi motion ($\sim$ 150 MeV), and the interference depends on the overlap in momentum space. Thus, the more rapid the Fermi motion is, the larger the interference effect becomes. Consequently, the interference effect is expected to be much smaller for B_d meson, where the momentum of $\bar{d}$ from the weak decay is much higher and does not overlap significantly with that of the Fermi motion. 2) In D^+ decays, the interference discussed above is relevant only to the Cabibbo-favored modes. Therefore, the suppression of nonleptonic rate by the interference effect implies a relative enhancement of Cabibbo suppressed decays of D^+. The inclusive measurements[70]

$$\frac{Br(D^+ \to K^+ + X)}{Br(D^+ \to K^- + X)} = 0.38 \pm 0.22, \qquad \frac{Br(D^0 \to K^+ + X)}{Br(D^0 \to K^- + X)} = 0.18 \pm 0.08$$

indicate the interference effect, but the errors are not small enough to be conclusive. The new exclusive measurement[119]

$$\frac{\Gamma(D^+ \to \overline{K}^0 K^+)}{\Gamma(D^+ \to K^- \pi^+)} = 0.317 \pm 0.086 \pm 0.048,$$

on the other hand, indicates a significant suppression of the $D^+ \to \overline{K}^0 \pi^+$ decay mode: the ratio is much larger than the naive expectation $\lambda^2 \sim 0.05$. However, no similar suppression in the 3-body decays has been observed.[119]

2.4.3.6 The Penguin Diagrams

The penguin diagram [Fig. 2.12(d)], which is always Cabibbo-suppressed, contributes to both D^0 and D^+ in the same way; thus, it does not cause the difference in the semileptonic branching fractions. However, it was pointed out[120,121] that the observed ratio[119] $\Gamma(D^0 \to \pi^-\pi^+)/\Gamma(D^0 \to K^-K^+) = 0.27 \pm$

0.09, which is expected to be unity, can be explained by the penguin interaction: since the Cabibbo-suppressed W-emission (or annihilation) mode gives opposite signs for the $\pi^-\pi^-$ and K^-K^+ amplitudes (with Cabibbo factors λ and $-\lambda$ respectively), any diagram that contributes with a same sign, such as the penguin diagram, interferes differently to the above amplitudes resulting in different rates for the two decay modes.[122]

There is no helicity suppression for the penguin diagram because the coupling of the light valence quark to the gluon is V and not $V-A$. On the other hand, the d-loop and s-loop in Fig. 2.12(d) cancel in the SU(3) limit (GIM suppression), and the b-loop is highly suppressed by the Cabibbo factor λ^5. In the literature, there are conflicting conclusions on the importance of the penguin diagram in charm decays.[122–124] The rate difference between the $\pi^-\pi^+$ and K^-K^+ can be due to SU(3) breaking[125] or to final state interactions.[126] Thus, there are no compelling data that require the penguin diagram, even though moderate effects in Cabibbo-suppressed decays are not ruled out.

To summarize: in the spectator model, the next-to-leading-logarithm QCD correction together with the gluon radiative correction gives 10$\sim$19 % for the semileptonic branching fraction of all charmed hadrons. The observed difference between $B_{SL}(D^0)$ and $B_{SL}(D^+)$ suggests a participation of the spectator quark. Two candidate models are: the enhancement of D^0 nonleptonic rate by the annihilation mechanism, and the suppression of D^+ nonleptonic rate by the interference effect. Both models have a possibility of explaining the difference between $B_{SL}(D^0)$ and $B_{SL}(D^+)$. Due to the non-perturbative nature of the problems, the theoretical predictions are not precise enough to estimate the relative importance of the two models. More experimental input is needed. Particularly, it is important to measure the total decay rates of D^0 and D^+. This would make it possible to check the absolute partial decay rates, not just the branching fractions.

Two decay modes from D^+ and D^0 can then be compared, and the semileptonic decay rate, which is theoretically more certain than the nonleptonic decay rate, can be used to derive the effective charmed quark mass.

2.5 $D^0 - \overline{D}^0$ MIXING

So far, we have ignored the transition $D^0 \leftrightarrow \overline{D}^0$. In the $K^0 - \overline{K}^0$ system, however, such a transition occurs at a rate comparable to the average decay rate of neutral K. In this section, we examine $D^0 - \overline{D}^0$ mixing in the framework of the standard model. First, the phenomenological formulae are reviewed. Then, it is shown that when only the short distance effects are considered, the expected $D^0 - \overline{D}^0$ mixing is very small ($\lesssim 10^{-7}$), and that $D^0 - \overline{D}^0$ mixing probes charm-changing neutral currents with good sensitivity. Lastly, we discuss the long-distance effects in $D^0 - \overline{D}^0$ mixing, which turn out to be significant.

2.5.1 Phenomenological Framework

The scheme is similar to that of the $K^0 - \overline{K}^0$ system.[127] Let $|D^0\rangle$ and $|\overline{D}^0\rangle$ be eigenstates of the Hamiltonian responsible for the strong and electromagnetic interactions with charm quantum number $+1$ and -1 respectively. The phase convention is such that

$$|\overline{D}^0\rangle = CP|D^0\rangle. \tag{2.53}$$

We take a space G spanned by $|D^0\rangle$ and $|\overline{D}^0\rangle$. The transitions between the two states and those out of G — i.e., decays — are described by the Schrödinger equation

$$i\frac{d}{dt}\psi = H\psi, \tag{2.54}$$

where H is the effective Hamiltonian defined in G, and

$$\psi \equiv a(t)|D^0\rangle + \bar{a}(t)|\overline{D}^0\rangle \quad \text{or} \quad \psi = \begin{pmatrix} a(t) \\ \bar{a}(t) \end{pmatrix}.$$

The probability is not conserved inside G due to decays. Thus, the 2 by 2 matrix H is not hermitian, but can be divided into a hermitian part and an anti-hermitian part as can any other 2 by 2 matrix:

$$H = M - i\frac{\Gamma}{2},$$

where M and Γ are 2 by 2 hermitian matrices. CPT invariance leads to [128]

$$M_{11} = M_{22}, \quad M_{21} = M_{12}^*, \qquad \Gamma_{11} = \Gamma_{22}, \quad \Gamma_{21} = \Gamma_{12}^*, \tag{2.55}$$

and the two eigenstates of H are obtained by diagonalizing H:

$$\begin{aligned} |D_1\rangle &= A\left[(1+\epsilon)|D^0\rangle + (1-\epsilon)|\overline{D}^0\rangle\right] \\ |D_2\rangle &= A\left[(1+\epsilon)|D^0\rangle - (1-\epsilon)|\overline{D}^0\rangle\right] \end{aligned}, \quad A = [2(1+|\epsilon|^2)]^{-1/2}, \tag{2.56}$$

where ϵ is given by

$$\left(\frac{1-\epsilon}{1+\epsilon}\right)^2 = \frac{M_{12}^* - i\Gamma_{12}^*/2}{M_{12} - i\Gamma_{12}/2}.$$

The eigenvalue equations are

$$H|D_i\rangle = (m_i - i\frac{\gamma_i}{2})|D_i\rangle \quad (i = 1,2), \tag{2.57}$$

where the eigenvalues are given by

$$m_i - \frac{i}{2}\gamma_i = M_{11} - \frac{i}{2}\Gamma_{11} \pm \left[(M_{12}^* - \frac{i}{2}\Gamma_{12}^*)(M_{12} - \frac{i}{2}\Gamma_{12})\right]^{1/2}. \tag{2.58}$$

The numbers m_i, γ_i $(i = 1,2)$ are real; each of the two eigenstates has a definite mass and a decay rate. When CP is conserved, $|D_i\rangle$ $(i = 1,2)$ are simultaneous eigenstates of CP, M and Γ, with eigen values $(-)^{i+1}$, m_i, and γ_i, respectively; and they are orthogonal to each other. In addition, our phase convention (2.53) and

CP invariance lead to $M_{21} = M_{12}$ and $\Gamma_{12} = \Gamma_{21}$; together with (2.55), it follows that M_{12} and Γ_{12} are both real. Thus, (2.58) becomes

$$m_i = M_{11} \pm M_{12}, \qquad \gamma_i = \Gamma_{11} \pm \Gamma_{12} \qquad (CP). \tag{2.59}$$

When CP is not conserved, however, $|D_1\rangle$ and $|D_2\rangle$ are in general not eigenstates of M and Γ separately and not orthogonal to each other:

$$\xi \equiv \langle D_1|D_2\rangle = \frac{2\mathrm{Re}\,\epsilon}{1+|\epsilon|^2} \quad \text{(real)}. \tag{2.60}$$

All the parameters needed for describing the mixing rates are now ready. We define f ($\bar{f}$) to be a final state, or a collection of final states, that only D^0 ($\overline{D}^0$) can decay to at a given time. Then the mixing rate p is defined to be the ratio of the probability for a particle generated as D^0 decaying to $\bar{f}$ to that for a particle generated as D^0 decaying to f. The parameter $\bar{p}$ is defined by the charge conjugation of the above. Namely,

$$p \equiv \frac{Br(D^0 \to \bar{f})}{Br(D^0 \to f)}, \quad \bar{p} \equiv \frac{Br(\overline{D}^0 \to f)}{Br(\overline{D}^0 \to \bar{f})}, \tag{2.61}$$

where $Br(D^0 \to f)$ represents the time-integrated probability that a state that is D^0 at $t = 0$ decays to f, etc. As shown in the appendix, the mixing parameters p and $\bar{p}$ are given by[129]

$$\begin{aligned} p &= \frac{1-\xi}{1+\xi}\cdot\frac{1-\alpha}{1+\alpha} \\ \bar{p} &= \frac{1+\xi}{1-\xi}\cdot\frac{1-\alpha}{1+\alpha} \end{aligned} \quad \text{with} \quad \alpha = \frac{1-y^2}{1+x^2}, \tag{2.62}$$

where

$$x \equiv \frac{\delta m}{\Gamma_+}, \quad y \equiv \frac{\Gamma_-}{\Gamma_+}, \quad \Gamma_\pm \equiv \frac{\gamma_1 \pm \gamma_2}{2}, \quad \delta m \equiv m_2 - m_1.$$

In deriving (2.62), it is assumed that, at a given time, the decay rate of the pure D^0 state to f is the same as that of the pure $\overline{D}^0$ state to $\bar{f}$ even in when CP is

violated. It can be seen that the mixing rate of D^0 and that of $\overline{D}^0$ are different to the extent that the two eigenstates of mass and decay rate are not orthogonal. When CP is conserved, then $\epsilon = \xi = 0$ and $p = \bar{p}$. The product $p\bar{p}$, however, is independent of the CP violation parameter ξ.

Alternatively, one can define the mixing rate r to be

$$r \equiv \frac{Br(D^0 \to \bar{f})}{Br(D^0 \to \bar{f} \text{ or } f)} = \frac{1}{2}\frac{y^2 + x^2}{1 + x^2} \qquad (CP), \tag{2.63}$$

where CP invariance is assumed. The maximum mixing [130] corresponds to $r = 1/2$ or to $p = 1$. When the mixing is small, r and p are similar and given by

$$r \sim p \sim \frac{1}{2}(x^2 + y^2) \quad (\text{if } x, y \ll 1 \text{ and } CP).$$

From (2.62) or (2.63), one can see that there are two situations which result in large mixing. 1) $\delta m \gtrsim \Gamma_+$: the mass difference is comparable to or larger than the average decay rate. 2) $|\Gamma_-| \sim \Gamma_+$: one of the decay rates is much larger than the other. In the first case, the mixing is genuinely caused by the $D^0 - \overline{D}^0$ transition, while in the second, the fast decaying component quickly disappears leaving the slow decaying component which is a mixture of D^0 and $\overline{D}^0$.

For the $K^0 - \overline{K}^0$ system, the two mass eigenstates are K_S and K_L, and the relevant parameters are[70]

$$\begin{aligned}
\Gamma_S &= (7.377 \pm 0.018) \times 10^{-15}\,\text{GeV} \quad (\sim 580\Gamma_L) \\
\Gamma_L &= (1.270 \pm 0.010) \times 10^{-17}\,\text{GeV} \\
\delta m &= (3.521 \pm 0.014) \times 10^{-15}\,\text{GeV} \quad (\sim \Gamma_+ \sim \Gamma_-) \\
\xi &= (3.24 \pm 0.18) \times 10^{-3}.
\end{aligned}$$

Thus, in the $K^0 - \overline{K}^0$ system, p and $\bar{p}$ differ by $\sim 4\xi \sim 1.3\%$. The mixing is almost complete; it comes about by the decay rate difference, even though the mass difference also contributes.

When D^0 can also decay to $\bar{f}$ (and $\overline{D}^0$ to f), as in $D^0 \to K^+\pi^-$, (2.62) has to be modified because there is an interference between the mixing and the direct decay. Here, we take f to be an exclusive channel consisting of two spin-0 particles.[131] We also assume CP invariance, and define the phases of f and $\bar{f}$ such that $CP|f\rangle = |\bar{f}\rangle$. Then the apparent mixing rate defined by (2.61) is (see Appendix):

$$\begin{aligned} p = \bar{p} &= \frac{1-\alpha'}{1+\alpha'}, \\ \alpha' &= \frac{1-|\kappa|^2-2|\kappa|x\sin\phi}{1+|\kappa|^2+2|\kappa|y\cos\phi}\cdot\frac{1-y^2}{1+x^2}, \end{aligned} \qquad (CP) \tag{2.64}$$

where $x = \delta m/\Gamma_+$ and $y = \Gamma_-/\Gamma_+$ as before, and κ is the ratio of the two decay amplitudes:

$$\kappa \equiv |\kappa|e^{i\phi} \equiv \frac{A(\overline{D}^0 \to f)}{A(D^0 \to f)} = \frac{A(D^0 \to \bar{f})}{A(\overline{D}^0 \to \bar{f})} \qquad (CP). \tag{2.65}$$

When $\kappa = 0$, (2.64) reduces to (2.62) with $\xi = 0$; when there is no mixing, namely $x = y = 0$, then $p = \bar{p} = |\kappa|^2$ as expected. When there are both effects, the result depends on the phase of κ and the signs of x and y.

2.5.2 *Standard Model Predictions of $D^0 - \overline{D}^0$ Mixing*

As shown in Figure 2.13(a), $D^0 - \overline{D}^0$ mixing can occur when there is a flavor-changing neutral current of a type $c \leftrightarrow u$. It is a non-spectator process; as such, it involves the uncertainties inherent in such processes, e.g., those of the overlap of c and $\bar{u}$ in the meson, their color state (singlet or octet?), etc. Thus, we are interested only in a rough estimate. The color factor and the QCD corrections are ignored. The current is assumed to be left-handed.[132] We also limit ourselves to two generations; because of the small mixing angles between the third generation and the rest, the effect of including the b quark can be ignored. CP invariance is also assumed.

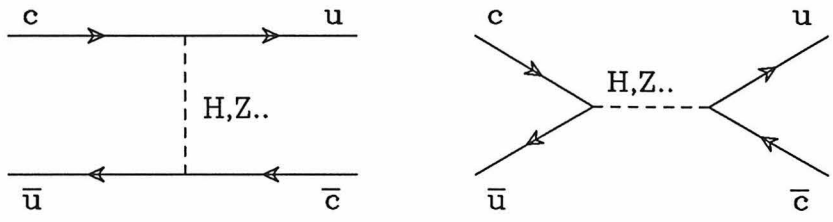

(a) Trees

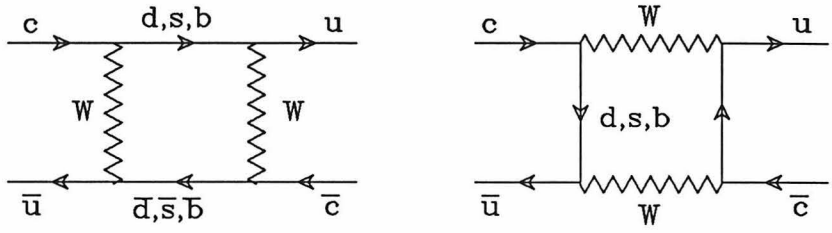

(b) Boxes

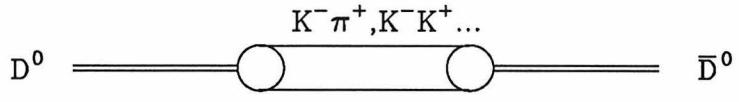

(c) Long Distance

Figure 2.13. Various mechanisms that can introduce $D^0 - \overline{D}^0$ mixing. (a) Direct charm-changing neutral currents at the tree level. A neutral vector boson or a Higgs is exchanged. This type of interactions are absent in the standard model. (b) Effective charm-changing neutral currents through box diagrams. When the bottom contribution is ignored, $\delta m^{(\mathrm{box})}$ is proportional to $m_s^2 - m_d^2$. (c) Long-distance or dispersive effect through hadronic intermediate states.

Fig. 2.13(a) corresponds to an effective four-fermion interaction

$$H_{\rm eff} = G_{\rm eff}(\bar{u}_L\gamma_\mu c_L)(\bar{u}_L\gamma^\mu c_L), \tag{2.66}$$

where $G_{\rm eff}$ is a coupling constant (taken to be real). Here, the exchanged particle is assumed to be a vector. From (2.59), the mass difference is given by

$$\delta m = 2M_{12} = 2\langle\overline{D}^0|H_{\rm eff}|D^0\rangle.$$

Thus,

$$\begin{aligned}\delta m &= 2G_{\rm eff}\langle\overline{D}^0|(\bar{u}_L\gamma_\mu c_L)(\bar{u}_L\gamma^\mu c_L)|D^0\rangle \\ &= G_{\rm eff}Bf_D^2 m_D,\end{aligned} \tag{2.67}$$

where the parameter B contains all the uncertainties in how the D^0 is made out of c, $\bar{u}$, and gluons:

$$\langle\overline{D}^0|(\bar{u}_L\gamma_\mu c_L)(\bar{u}_L\gamma^\mu c_L)|D^0\rangle \equiv \frac{B}{2}f_D^2 m_D. \tag{2.68}$$

The definition above is such that if the vacuum insertion approximation is used, then $B = 1$. When color is taken into account, $B/2$ should be replaced by $B/3$. Hereafter, we take $B = 1$ assuming the vacuum insertion approximation. If the neutral particle exchanged is a Higgs, then all needed is a substitution

$$\langle\overline{D}^0|(\bar{u}_L\gamma_\mu c_L)(\bar{u}_L\gamma^\mu c_L)|D^0\rangle \;\rightarrow\; \langle\overline{D}^0|(\bar{u}_L c_L)(\bar{u}_L c_L)|D^0\rangle.$$

For a heavy meson, these two values are expected to be similar. The coupling constant $G_{\rm eff}$ for Higgs, however, is expected[133] to be of order $(m_q/m_H)^2 G_F$, where m_H is the Higgs mass and m_q is the typical quark mass (~ 1 GeV).

With $G_{\rm eff} = 2\sqrt{2}G_F$, namely with a full strength coupling for the flavor-changing neutral current and a vector boson, δm is $\sim 1\times 10^{-6}$ GeV, which is $\sim 10^6$ times the expected $\Gamma_+ \sim 5\Gamma_0 \sim 10^{-12}$GeV; the mixing would certainly be complete

[see (2.63)]. For a Higgs exchange, the coupling is smaller. However, the mixing is still likely to be complete unless the Higgs is super-heavy ($\gtrsim$TeV). On the other hand, an upper limit of, say, 5% on r corresponds to a strong limit on G_{eff} of less than $\sim 10^{-6} G_{\text{eff}}$.

In the standard model, however, direct flavor-changing neutral currents are missing, and two W's need to be exchanged to generate an effective flavor-changing neutral current [Fig. 2.13(b)]. The corresponding effective coupling constant in (2.66) has been evaluated first by Gaillard and Lee[134] and given by

$$G_{\text{eff}}^{(\text{box})} = \frac{G_F^2}{4\pi^2}(m_s^2 - m_d^2)\cos^2\theta_c \sin^2\theta_c. \tag{2.69}$$

With $f_D = 0.15$ GeV, $m_c = 1.5$ GeV, $m_s = 0.15$ GeV, and $m_d \ll m_s$, this leads to

$$\delta m^{(\text{box})} = \left[\frac{G_F^2}{4\pi^2}(m_s^2 - m_d^2)\cos^2\theta_c \sin^2\theta_c\right] B f_D^2 m_D \sim 1.6 \times 10^{-16}\text{GeV}.$$

With $\Gamma_+ \sim 10^{-12}$ GeV and $\Gamma_- \sim 0$, this means a mixing rate r of less than 10^{-7}. In deriving (2.69), the momenta and masses of external legs are ignored. When the mass effect of external fermions is included,[135] $\delta m^{(\text{box})}$ is further suppressed by m_s^4/m_c^4. Thus, the expected $D^0 - \overline{D}^0$ mixing from the box diagrams is negligible.

It is instructive to recall the case of the $K^0 - \overline{K}^0$ system. The δm given by (2.67) with $G_{\text{eff}} = 2\sqrt{2}G_F$ is 7 to 8 orders of magnitude larger than the experimental value. Thus, direct strangeness changing neutral currents seem to be missing in the nature. The box diagrams give

$$\delta m^{(\text{box})} = \frac{G_F^2}{4\pi^2}(m_c^2 - m_u^2)\cos^2\theta_c \sin^2\theta_c B_K f_K^2 m_K, \tag{2.70}$$

which is consistent with the experimental value within the error. In fact, Gaillard and Lee correctly predicted the mass of charmed quark to be $\sim$ 1.5 GeV using (2.70). However, if one calculates without a c quark, the mass difference estimate

(2.70) becomes $\sim (m_W/m_c)^2$ times larger; namely, it becomes of order $G_F\alpha$ (note that $G_F \sim \alpha/m_W^2$), which is incompatible with experimental data. This is the observation that originally led Glashow, Iliopoulos and Maiani to introduce the charmed quark.

In general, the missing flavor-changing neutral currents at the tree level and the suppression of the effective flavor-changing neutral current of order $G_F\alpha$ impose strong conditions on theoretical models. If we restrict ourselves to SU(2)×U(1) gauge theory and require that the conservation of flavor obeyed by neutral currents is a natural result of the structure of theory rather than of adjustment of parameters, the model has to satisfy the following conditions (obtained by Glashow and Weinberg[133]): all quarks with the same charge and helicity

1. have the same I_3 of the weak SU(2),
2. have the same I^2 of the weak SU(2), and
3. receive the quark mass from a single source (Higgs).

The first condition is from the absence of tree-level neutral currents generated by gauge bosons, the second from the suppression at the level of $G_F\alpha$, and the third from the Higgs-induced neutral current. If we take $2/3$ and $-1/3$ to be only quark charges, then it follows from the conditions (1) and (2) that the only acceptable way to arrange the quarks is to put all left-handed quarks in weak doublets and all right handed quarks in singlets, or all quarks of each helicity in doublets. The condition (3) disfavors the latter possibility. The Higgs sector is not well established; thus, the condition (3) is accordingly less conclusive.

The conditions above apply separately to quarks of fixed charge, and the $K^0 - \overline{K}^0$ system probes strangeness-changing neutral currents, namely the transitions between quarks with charge $-1/3$. It is possible that the flavor-changing neutral currents are suppressed among charge $-1/3$ quarks and not among charge $2/3$ quarks. Thus, it is important to see if charm-changing neutral currents are also suppressed.

2.5.3 *Long-Distance Effects on $D^0 - \overline{D}^0$ Mixing*

In the $K^0 - \overline{K}^0$ system, the success of the box diagrams has led people to downplay the importance of long-distance or dispersive effects, which was actually the original method of estimating the $K^0 \leftrightarrow \overline{K}^0$ transition.[136] It was then pointed out by Wolfenstein[74] that the long-distance effects are indeed not negligible nor can they be absorbed into the correction factor B of (2.68). Since the box interaction is local and takes place within a scale smaller than the size of a meson, hadronic intermediate states such as $\pi^0, \eta, 2\pi$, etc... are not included and have to be added to the box diagram contribution. More recently, new attempts have been made to estimate the long-distance effects.[137] The results, however, are not conclusive. At present, the range of uncertainty for the long-distance effects in the $K_S - K_L$ mass difference is of the same order as the experimental mass difference, but even the sign is not definitive due largely to the cancellation between η and π^0 intermediate states.

In the case of the $D^0 - \overline{D}^0$ system, the situation is even worse because there are many possible intermediate states, and a reliable estimate of the mass difference due to long-distance effects is extremely difficult. It was recently pointed out,[138] however, that the long-distance effects are likely to be dominant component of $D^0 - \overline{D}^0$ mixing. In the limit of SU(3) symmetry,[139] the two body intermediate states, $K^-\pi^+$, K^-K^+, $\pi^-\pi^+$, and $K^+\pi^-$, cancel between themselves in a manner similar to the GIM mechanism, that is, due to the way the Cabibbo suppression factor $\pm \sin\theta_c$ enters the amplitudes. As we have seen in the previous section, however, the actual decay rates to K^-K^+ and $\pi^-\pi^+$ channels are far from the naive expectation based on the Cabibbo factors [$\mathrm{Br}(K^-K^-)/\mathrm{Br}(\pi^-\pi^+) \sim 4$ instead of 1]. A crude estimate for the mass difference using two-body intermediate states is

$$\begin{aligned}\delta m^{(\mathrm{long})} &\sim Br(D^0 \to KK, \pi\pi)\Gamma_+ \times (\text{GIM suppression factor}) \\ &= (10^{-3} \sim 10^{-2})\Gamma_+ = (10^{-15} \sim 10^{-14})\mathrm{GeV}.\end{aligned}$$

More-than-two-body decays also are likely to contribute significantly and can in principle cancel the two-body effect, but this is considered unlikely. Wolfenstein[138] sets an over-all upper limit of $\delta m^{(\mathrm{long})} \lesssim 0.05\,\Gamma_+$. The resulting upper limit on the mixing rate r is $\sim 10^{-3}$; much larger than estimated from the box diagrams, but still below the current experimental sensitivity.

It is worth noting that the same long-distance effects [or SU(3) breaking] can lead to the difference in decay rate, which also contributes to the mixing. The D_2 state has $CP = -$ (CP invariance is assumed), and thus cannot decay to K^-K^+ or $\pi^-\pi^+$ final state. Assuming factorization and SU(3) symmetry, the amplitude of $D_1 \to K^-K^+, \pi^-\pi^+$ is given by

$$A(D_1 \to K^-K^+) = -A(D_1 \to \pi^-\pi^+) = \sqrt{2}\cos\theta_c \sin\theta_c A_0,$$

where the reduced amplitude A_0 is defined by

$$A(D^0 \to K^-\pi^+) \equiv \cos^2\theta_c A_0.$$

On the other hand, there is a difference in the amplitudes of $D_1 \to K^-\pi^+, K^+\pi^-$ and $D_2 \to K^-\pi^+, K^+\pi^-$:

$$A(D_1 \to K^-\pi^+) = -A(D_1 \to K^+\pi^-) = \frac{1}{\sqrt{2}}(\cos^2\theta_c - \sin^2\theta_c)A_0$$
$$A(D_2 \to K^-\pi^+) = -A(D_2 \to K^+\pi^-) = \frac{1}{\sqrt{2}}A_0.$$

Namely, the rate $D_1 \to K^\pm\pi^\mp$ is $\cos^2 2\theta_c \sim 0.8$ times the rate $D_2 \to K^\pm\pi^\mp$, which cancels out the missing $K^-K^+, \pi^-\pi^+$ modes of D_2, giving the same total two-body decay rate for D_1 and D_2. In reality, SU(3) is broken; thus, the cancellation is not exact. This leads to a non-vanishing Γ_- of the same order as $\delta m^{(\mathrm{long})}$. Again, there are effects from more-than-two-body decays; nevertheless, it seems unlikely that they precisely cancel the SU(3) breaking effects in the two-body decays.

To summarize, the phenomenological analysis of $D^0 - \overline{D}^0$ mixing can be done similarly to that of the $K^0 - \overline{K}^0$ system. The mixing can be caused either by the mass difference or decay rate difference of the two mass eigenstates of the $D^0 - \overline{D}^0$ system. The mass difference is generated by direct or effective flavor-changing neutral currents, and an upper limit on the mixing can put a strong limit on the size of such couplings. This, in turn, restricts allowed theoretical models. In the standard model, the mass difference is often calculated by the box diagrams which gives a value consistent with the measurement for the $K^0 - \overline{K}^0$ system. For the $D^0 - \overline{D}^0$ system, the mass difference calculated using the box diagrams is much smaller than for the $K^0 - \overline{K}^0$ system, and the resulting mixing is of order 10^{-7} or less. The main reason why the mixing is much smaller for the $D^0 - \overline{D}^0$ system is that the mass difference for $D^0 - \overline{D}^0$ system is proportional to $\sim m_s^2$ while for $K^0 - \overline{K}^0$ system it is proportional to $\sim m_c^2$ and also that the average decay rate is much larger for the $D^0 - \overline{D}^0$ system. The long-distance effects, however, are likely to be dominant in the mixing of D^0 and $\overline{D}^0$. They cause both the mass difference and the decay rate difference to be non-zero by the same order of magnitude, but a quantitative estimate is not possible at present. A conservative upper limit on the mixing is $\sim 2 \times 10^{-3}$.

Chapter 3.

Instrumentation and Data Reduction

> Whether it is becoming politicians or becoming laboratory directors or becoming plumbers, God knows that one does what must be done to get at good physics.
>
> — Robert R. Wilson

3.1 The PEP Storage Ring

In this section, the PEP storage ring is described. The emphasis is on the expected beam size, which is relevant to the measurement of the D^0 lifetime.

PEP is a e^+e^- colliding-beam storage ring at the Stanford Linear Accelerator Center. Figure 3.1(a) shows the geometry of the ring, and Table 3.1 lists[140] some of the parameters. Three bunches each of electrons and positrons are accumulated in the ring through the injection from the 2-mile-long linear accelerator (Linac). The electron bunches counter-rotate against the positron bunches, and collisions occur at six locations (interaction points). Under optimum conditions, the injection takes about 10 minutes and the collisions take place for a few hours until the beam currents reduce to about one half of the initial value. The bunch-crossing frequency at a given interaction point, 408.81 kHz or one crossing every 2.446 μsec, is three times the orbital frequency.

The injection energy is 14.5 GeV and the beam energy is not increased by the storage ring itself. The circulating particles, however, lose their energy through the synchrotron radiation. The average energy loss per turn per particle is (for

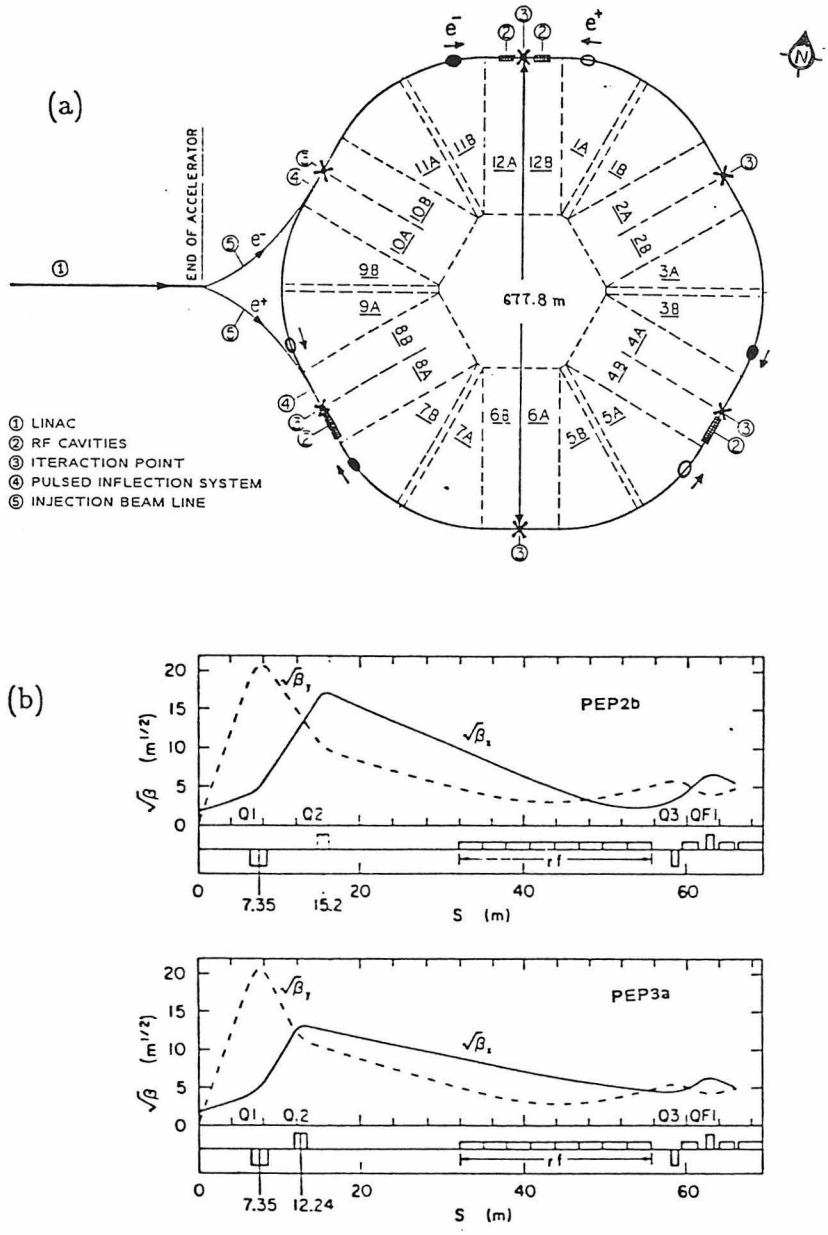

Figure 3.1. (a) The PEP storage ring. There are bending sections and straight sections. RF cavities, final-focusing quadrupoles, and detectors occupy the straight sections. (b) Betatron functions for the two configurations.[140] The first configuration (PEP2b) corresponds to the 1982 data, and the second (PEP3a) to the 1983 and 1984 data. Note that the second quadrupole Q2 was moved toward the interaction point after 1982.

Table 3.1. The PEP storage ring parameters (as operated for experiments).

Beam energy	14.50 GeV
Circumference	2200.00 m
Number of interaction regions	6
Number of bunches	$3(e^-), 3(e^+)$
Frequency of bunch crossings (f)	408.81 kHz
Magnet bending radius (ρ)	165.52 m
Length of straight section/IR	117.09 m

$E_{\text{beam}} \gg m_e$)[142]

$$\Delta E(\text{MeV}) = 8.846 \times 10^{-2} \frac{E^4_{\text{beam}}(\text{GeV}^4)}{\rho(\text{m})} \quad = 23.6\,\text{MeV},$$

where ρ is the magnetic bending radius (165.52 m). An additional few MeV is lost due to the excitation of parasitic modes at various places around the ring. These energy losses are replenished by the RF cavities clustered at three locations.

The above energy losses are average energy losses; in reality, there are quantum fluctuations which broaden the energy distribution. Radiation damping, on the other hand, reduces the width of the energy distribution. The energy spread σ_ϵ is given by the equilibrium between these two effects:[143]

$$\left(\frac{\sigma_\epsilon}{E_{\text{beam}}}\right)^2 = \frac{C_q \gamma^2}{J_\epsilon \rho} \quad = (0.10\%)^2, \tag{3.1}$$

where $C_q = 3.84 \times 10^{-13}$ m, $J_\epsilon = 2.0$ (for the PEP ring), and $\gamma \equiv E_{\text{beam}}/m_e$. Since the orbital radius depends on the energy of particle, this energy spread generates a spatial spread of the particles in a bunch. The horizontal (x) displacement of the orbit relative to the design orbit is given by the relative energy displacement times the value of the η (the off-energy function) at the point. Thus, the horizontal beam width due to this effect, $\sigma_{x\epsilon}$, is

$$\sigma_{x\epsilon} = \eta^* \frac{\sigma_\epsilon}{E_{\text{beam}}}, \tag{3.2}$$

where η^* is the value of η at the interaction point.

Another source of the horizontal beam width is betatron oscillation. For a given particle, the horizontal displacement with respect to the design orbit at a given location, $x(s)$, is (for a particle with the nominal energy)

$$x(s) = a\sqrt{\beta_x(s)}\cos\left[\int_0^s \frac{ds}{\beta_x(s)} - \theta\right], \tag{3.3}$$

where s is the distance along the design orbit from an arbitrary origin on the ring, $\beta_x(s)$ is the horizontal betatron function which is determined by the configuration of the magnets around the ring, and a and θ are the constants determined by the initial conditions of the particle. One of the characteristics of the function $\beta(s)$ is that it is proportional to the square of the beam size at point s; thus, it describes how the beam bunch shrinks and broadens as it moves along the orbit. As shown below, the formula (3.3) gives the relation between the emittance of the beam and the beam width.

At an interaction point, the root-mean-squares of x and $\dot{x} \equiv dx/ds$ are, from (3.3),

$$< x^2 >= \frac{1}{2} < a^2 > \beta_x^*, \quad < \dot{x}^2 >= \frac{1}{2}\frac{< a^2 >}{\beta_x^*},$$

where the bracket indicates the average over all the particles in a bunch, β_x^* is the value of $\beta_x(s)$ at the interaction point, and we used the fact that $\dot{\beta}_x = 0$ at an interaction point. The horizontal emittance ϵ_x is then

$$\epsilon_x \equiv (< x^2 >< \dot{x}^2 >)^{1/2} = \frac{1}{2} < a^2 > .$$

and thus the horizontal beam width due to betatron oscillation, $\sigma_{x\beta}$, is related to the emittance by

$$\sigma_{x\beta}^2 =< x^2 >= \epsilon_x \beta_x^*. \tag{3.4}$$

Thus, if the emittance is known, the beam width due to the betatron oscillation can be obtained for a given value of β_x^*. The emittance can be calculated from the ring

configuration based on the balance between the radiation damping and quantum fluctuation:[143]

$$\epsilon_x = C_q \frac{\gamma^2 < \mathcal{H}/\rho^3 >_s}{J_x < 1/\rho^2 >_s}, \tag{3.5}$$

where $<>_s$ indicates the average around the ring, $J_x = 1.0$ (for the PEP ring), and $\mathcal{H}$ is the characteristic function of the ring configuration.

The total horizontal beam width is then

$$\sigma_x = (\sigma_{x\epsilon}^2 + \sigma_{x\beta}^2)^{1/2} = \left[\eta^{*2}\left(\frac{\sigma_\epsilon}{E_{\text{beam}}}\right)^2 + \epsilon_x \beta_x^*\right]^{1/2}, \tag{3.6}$$

where $\sigma_\epsilon/E_{\text{beam}}$ is given by (3.1) and ϵ_x by (3.5). It should be noted that this result assumes that there is no non-linear effects such as beam-beam effects and the coupling of the vertical and horizontal motions.

The vertical beam size σ_y is more difficult to evaluate. First of all, generally the largest source is the coupling between the horizontal and vertical motions; and the amount of the coupling changes depending on the beam conditions. Also, often the vertical shape is not a gaussian due to non-linear effects such as the beam-beam interaction and the head-tail instability due to the wake field in the RF cavities. If one assumes that the coupling is maximum, namely that the original horizontal emittance is equally shared by the horizontal and vertical motions, then the vertical beam width is given by

$$\sigma_y = \left(\frac{1}{2}\epsilon_x \beta_y^*\right)^{1/2} \qquad \text{(maximum coupling)},$$

where β_y^* is the value of the vertical betatron function at the interaction point.

The geometrical length of the bunch can be calculated from the RF voltage (as a function of time) and the energy spread, and is estimated to be $\sigma_z = 2.3$ cm for the PEP ring. On the other hand, it can also be measured using the Bhabha scattering events. The distribution of the event origins is related to the density distribution of electrons inside the bunch, and is found to have a width of 1.5 cm.

The width of the beam itself is $\sqrt{2}$ times this value, namely $\sigma_z = 2.1$ cm, which is consistent with the expected size.

Two lattice configurations were used during the data taking: PEP2b and PEP3a. The corresponding beta functions near the interaction point are shown in Fig. 3.1(b). The configuration PEP2b was used during the data taking in 1982, and the configuration PEP3a during the 1983 and 1984 data takings. The main difference is the location of Q2 (the second quadrupole from the interaction region). Table 3.2 shows[141] the typical parameters for the two configurations. The actual value of η^* is $\sim$ 10 cm for both configurations,[144] even though the calculated value is zero. However, this leads to $\sigma_{x\epsilon}$ of $\sim$ 0.10 mm, which increases σ_x by only 2%, and thus the effect of the non-zero η^* is small. In sum, a typical beam bunch is 4 cm long, 1 mm wide, and 0.1 mm high, where the dimensions refer to twice the corresponding standard deviations. The integrated luminosity accumulated for this analysis is 22 pb^{-1} with PEP2b and 125 pb^{-1} with PEP3a, giving a total of 147 pb^{-1}.

The luminosities given in the table are the measured ones. One can also estimate the luminosity from the calculated beam sizes, the beam currents, and the bunch crossing frequency. If the electron density in the bunch has a gaussian distribution, then the luminosity is given by

$$\begin{aligned} L &= \frac{1}{4e^2 f}\frac{I_+ I_-}{A_{\rm eff}} \\ &= \frac{3.10\times 10^{36}}{f(\mathrm{Hz})}\frac{I_+(\mathrm{A})I_-(\mathrm{A})}{\sigma_x(\mathrm{cm})\sigma_y(\mathrm{cm})} \quad (\mathrm{cm}^{-2}\mathrm{sec}^{-1}), \end{aligned}$$

where e is the electron charge, $A_{\rm eff} = \pi\sigma_x\sigma_y$ is the effective interaction area, f is the bunch crossing frequency, and $I_\pm$ are the currents of the electron beam and the positron beam which we assume to be the same. If one uses the no-coupling value for σ_x and the maximum-coupling value for σ_y, this formula gives $L_{\rm max} = 1.0\times 10^{31}$ cm^{-2}sec^{-1} for the PEP3a configuration, which is about factor of 3 smaller than the observed value. As we will see later, the value of σ_x is consistent with our

Table 3.2. Typical ring parameters for the two configurations.

	PEP2b (1982)	PEP3a (1983,1984)
ν_x	25.275	21.25
ν_y	20.175	18.19
β_x^* (m)	2.95	3.0
β_y^* (m)	0.11	0.11
η^* (m)	0.0†	0.0†
$\epsilon_x^\ddagger$ (mm − mrad)	0.099	0.117
$I_{\max}$ (mA/beam)	16.7	24.8
$L_{\max}$ (10^{31}cm^{-2}sec^{-1})	1.0	3.23
$\Delta\nu_{x\ \max}$	0.30	0.50
$\Delta\nu_{y\ \max}$	0.22	0.46
σ_x (mm)(no coupling)	0.540	0.592
σ_y (mm)(max. coupling)	0.074	0.080

† Theoretical value. The actual value is ~ 0.10 m.
‡ Calculated from the ring configuration using the formula (3.5).

measurement; thus, the discrepancy is probably due to the overestimation of σ_y.

3.2 THE DELCO DETECTOR

The D^* analysis presented in this thesis uses data taken with the DELCO detector, which is an upgraded version of the first DELCO detector which operated at the SPEAR storage ring. Figure 3.2 shows its end and side views. One of its unique features is the good particle identification provided by the gas threshold Čerenkov counter. An open-coil magnet design minimizes the amount of material in front of the Čerenkov counter. The parts of the detector that are relevant to this analysis are the charged-particle tracking system and the Čerenkov counter. These are also the parts significantly upgraded over the old version.

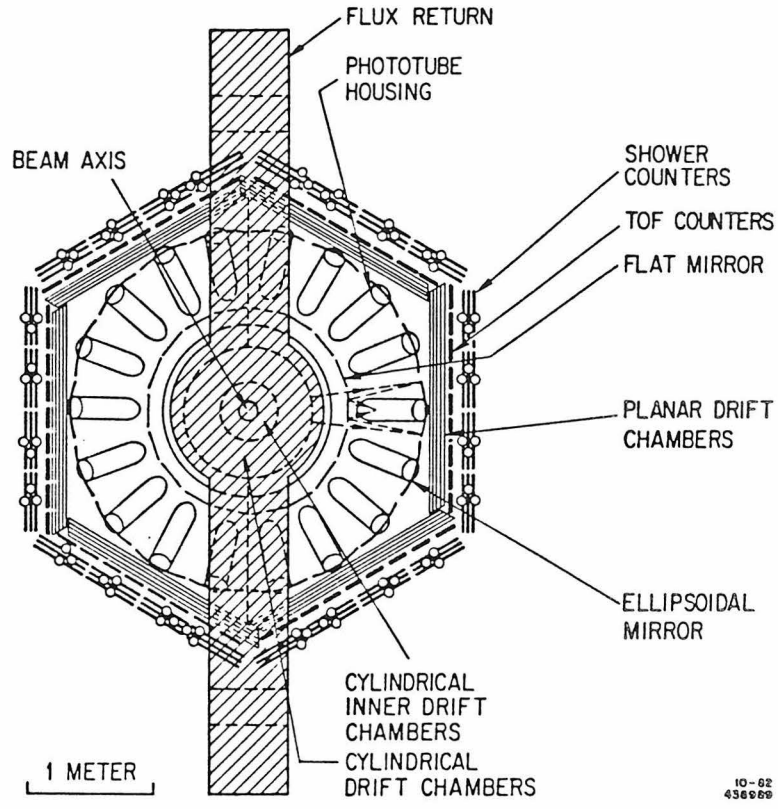

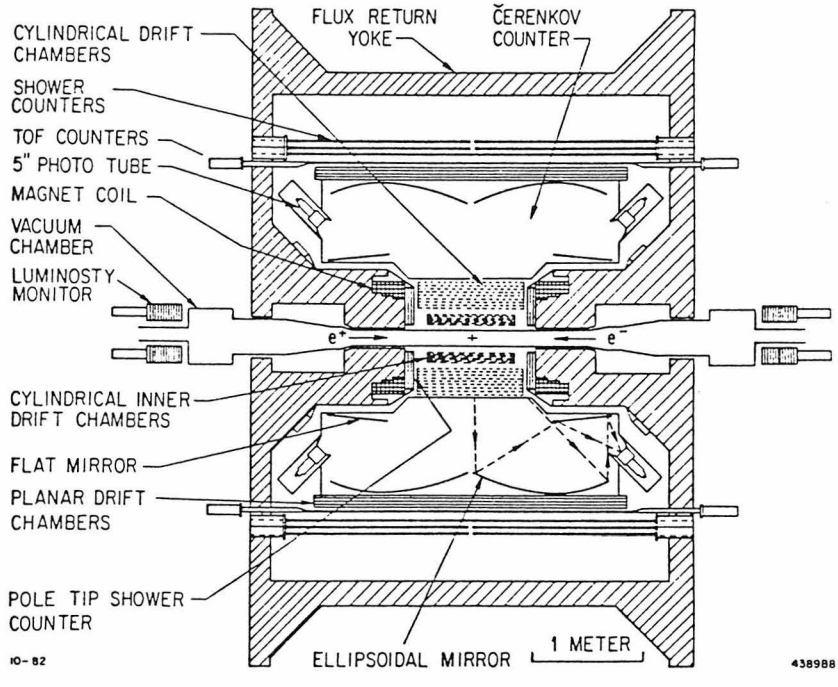

Figure 3.2. The side and end views of the DELCO detector. In order to reduce the gamma-converting materials in front of the Čerenkov counter, the magnet is of an open-geometry type.

3.2.1 Tracking System

3.2.1.1 Geometry and Constructions

Charged particles are tracked by three drift-chamber systems: the inner drift chamber (IDC), the central drift chamber (CDC), and the planar drift chamber (PDC). The PDC consists of six sets of planner drift chambers forming a hexagon, and mounted outside the Čerenkov counter. The CDC and the PDC sandwich the Čerenkov counter; thus the trajectories of particles through the Čerenkov counter are well determined by interpolation.

Figure 3.3 shows the cell structures for the IDC and PDC. The cell structure of the CDC is similar to that of the IDC. There are six sense-wire layers in the IDC, ten in the CDC, and six in the PDC; a charged particle within the geometrical acceptance, 65% of 4π, is measured at 22 points along its path. One half of the IDC and CDC layers and one third of the PDC layers are stereo layers, whose wires are tilted with respect to the beam axis in order to obtain the z-coordinate information. The stereo angle is 2° to 3° for the IDC and CDC, and 30° for the PDC. Except for the uv layers of the PDC, all the drift-chamber layers are paired. In each pair, the two layers are staggered by a half cell in order to help resolve the left-right ambiguity.

Each wire in the IDC and CDC is attached to the endplate by a feedthrough equipped with a spring which kept the wire tension constant during the wire-stringing process. After all the wires were strung, the ends of the wires were glued to the feedthroughs. Because of this procedure, we had little problem of breaking wires. The tension of a field or guard wire (gold-plated tungsten wire) is about 160 g and that for a sense wire (gold-plated Beryllium-Copper wire) is about 80 g. This amounts to a total tension of 0.3 ton for the IDC and 0.7 ton for the CDC. This tension is supported by the inner honeycomb wall for the IDC, and both the inner and outer honeycomb walls for the CDC.

The IDC is mounted on the beam pipe and cannot be removed without breaking

(a)

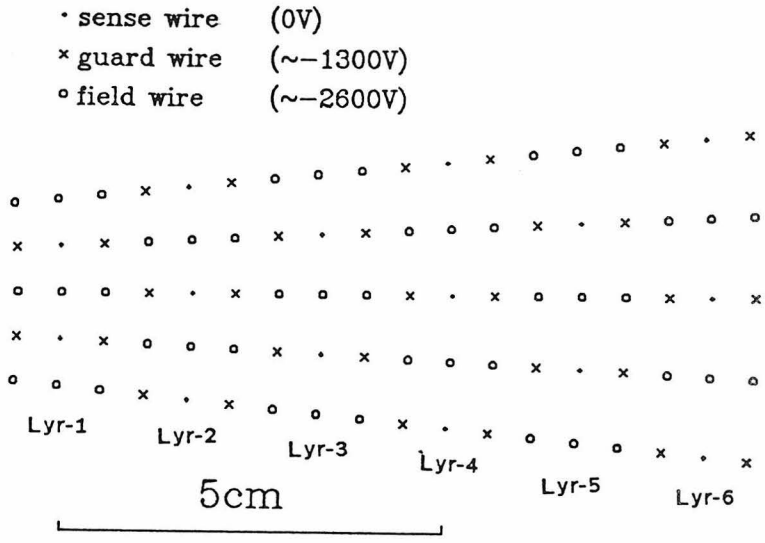

(b)

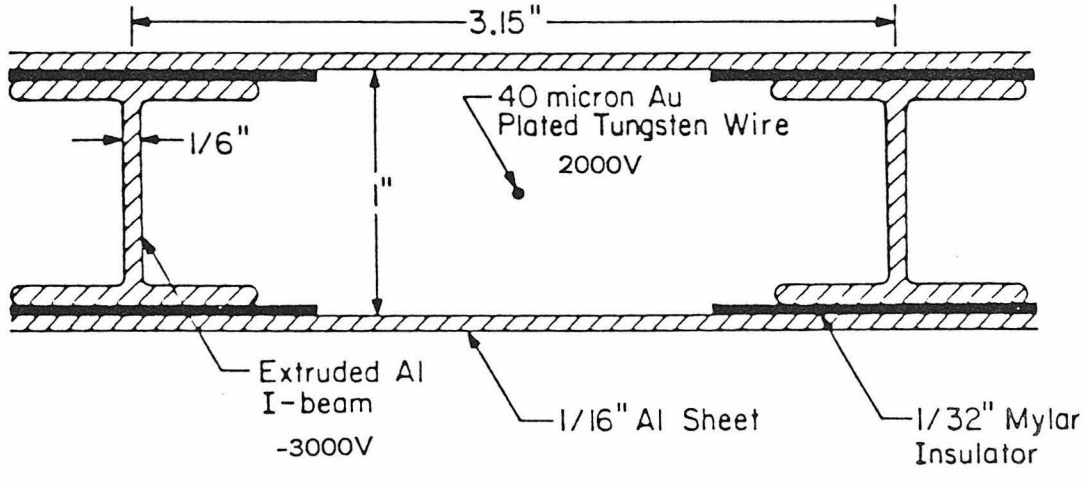

Figure 3.3. (a) The IDC wire pattern at an endplate is shown for a 1/32 sector. The field and guard wires shape the electric field and the sense wires collect the electrons from the ionizations caused by passing charged particles. (b) The cell structure of the PDC. The sense wire is held at high voltage in order to allow the outer aluminium plates to be grounded.

the vacuum of the storage ring. However, the CDC is made in two halves, and can be easily removed for the access to the IDC. The rest of the detector surrounding the CDC is split at the center, and can be separated by a electric motor in a matter of a few minutes.

3.2.1.2 Principle of Operation and Resolutions

Figure 3.4 shows the equipotential contours of the IDC cells and the trajectories of electrons ionized by a charged particle. The electrons drift toward the sense wire, and the first electron to reach the wire initiates an avalanche giving a signal pulse. Thus, the distance of closest approach of the track to the sense-wire can be calculated from the electron drift velocity and the time between the passage of the track and the generated signal. The drift velocity is a function of the electric field and depends on the type of gas used.

The same gas was used for all three drift-chamber systems. Originally a mixture of Ar-C_2H_6 (55%-45%) was used (for the 1982 data). Near the end of the 1982 data taking, however, several high-voltage wires started to discharge uncontrollably. When the chamber was opened later, carbon whiskers were found on those wires, which were effectively cleaned by a toy water gun. The rest of the data were taken with a mixture that contain less organic gas: Ar-CO_2-CH_4 (89%-10%-1%), which turned out to be satisfactory.

The drift velocity as a function of electric field is determined by the cross sections for collision of an electron and the molecules in the gas mixture. These cross sections generally are complicated functions of the electron energy, and the functional shape depends on the molecule type. As a result, the drift velocity strongly depends on the composition of the gas mixture. The two mixtures we used have similar electron drift-velocity curves, which rise smoothly from 0 cm/μsec at 0 kV/cm to around 5 cm/μsec at 0.7 kV/cm and then flatten out. This plateau shape makes the operation of the chamber insensitive to slight fluctuations of the high voltages; for, in actual operation, the electric field in most of the drift region

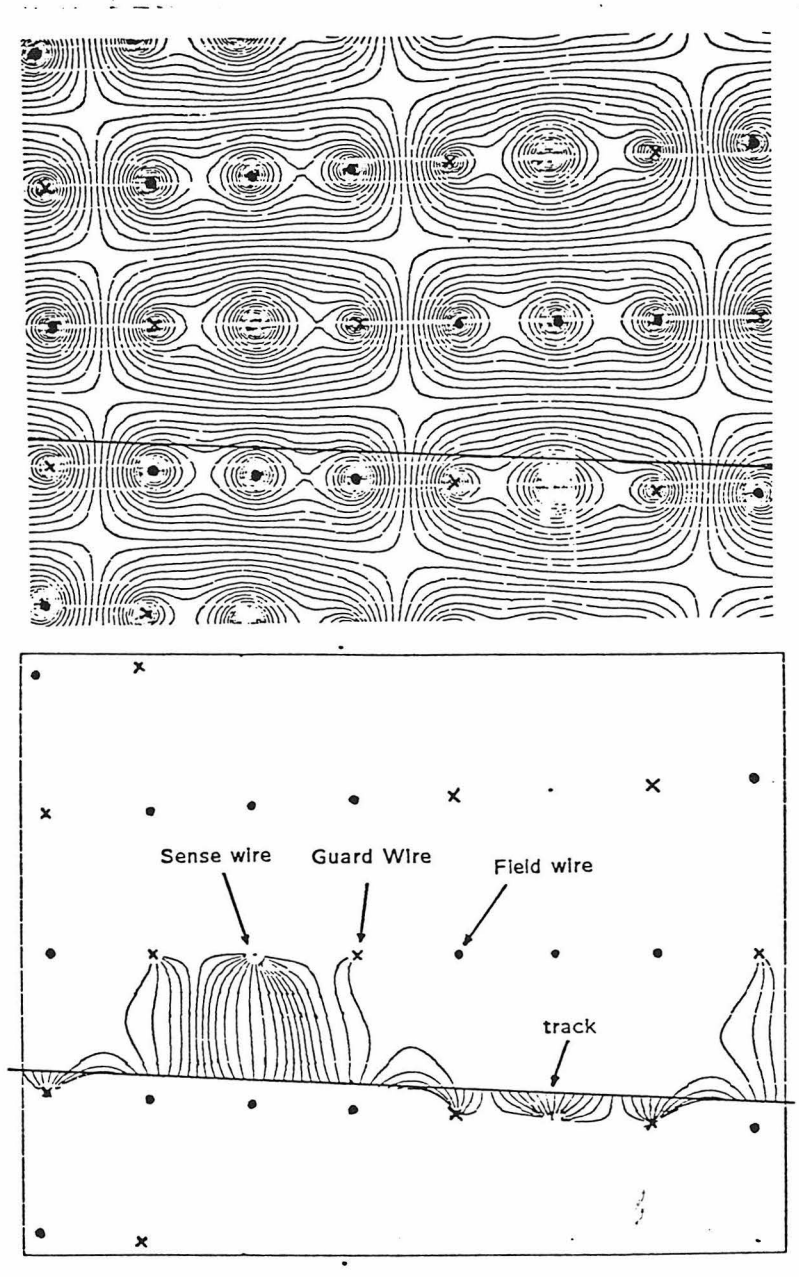

Figure 3.4. The equipotential contours of the IDC cells and the electron trajectories for a typical track. It can be seen that about one half of the track length is in active regions, which means that the ionized electrons drift toward one of the sense wires instead of the guard wires.

is above 0.7 kV/cm.

When the magnetic field is present, the electron drift velocity acquires a component proportional to $\mathbf{E} \times \mathbf{B}$. For a magnetic field perpendicular to the electric field, the angle between the electric field and the drift direction, α_H, is well approximated by[145]

$$\tan \alpha_H = \frac{Bw}{kE} = \frac{0.01}{k} \frac{B(\text{kG})\, w(\text{cm}/\mu\text{m})}{E(\text{kV})}, \tag{3.7}$$

where $k = 0.75$, w is the electron drift velocity in the absence of magnetic field, and the first expression is in MKSA units. The approximation is good when $B \lesssim 5$ kG and $E \lesssim 1$ kV/cm. For larger E and/or B, k should be slightly smaller ($k \sim 2/3$ at $E = 1.5$ kV/cm and $B = 10$ kG). If $\mathbf{B}$ is not perpendicular to $\mathbf{E}$, then B in (3.7) should be replaced by $|\mathbf{E} \times \mathbf{B}|/E$. In our case, a typical angle is $\sim 10°$ in the IDC and CDC, and very small in the PDC. The angle α_H, however, hardly changes the shape of isochronal contours, which are all that are needed to convert a drift time to a distance of closest approach. For the IDC and CDC, they are approximately concentric around the sense wire and almost equally spaced. The magnetic field, however, shortens the spacing between the isochronal contours. In practice, the time-to-distance relations are derived for each layer of the drift chambers using the actual tracks in Bhabha events.

The resolution of the distance of closest approach depends on the electronics used to process the signal as well as on the type of gas mixture. The signals are processed by the discriminator-preamplifiers attached to the drift chambers and then sent over twisted-pair cables to the multihit drift time digitizers (DTD's)[146] located in the control room. The least significant bit of the digitizer is 4 nsec, which corresponds to a spatial resolution of 60 μm. This resolution can be improved by using a gas mixture with a slower drift velocity. This, however, is not a limiting factor in our case.

Table 3.3 summarizes the parameters of the drift chambers, where the single hit resolutions are obtained from the residuals of fits of measured Bhabha tracks.

The resolutions for the 1983 data are worse than those for the 1982 and 1984 data. This is mainly due to the slow risetime of the preamplifiers installed after the 1982 runs and fixed for the 1984 runs.

Table 3.3. The parameters for the IDC, CDC, and PDC.

	IDC	CDC	PDC
# of layers	6	10	6
configuration*	vvzzuu	zzuuzzvvzz	zzuvzz
stereo angle(°)	2.18-3.71	1.56-1.88	30.0
# of sense wires	384	830	960
sense wire diameter (μm)	30,38	38	40
" material (Au-plated)	Be-Cu	Be-Cu	tungsten
1/2 cell width (mm)	5.9-9.8	11.6-15.3	40.0
r(innermost layer) (cm)	12.01	27.30	144.7†
r(outermost layer) (cm)	20.52	48.90	158.9†
length in z (cm)	62.2	94.0	284.5
acceptance‡ (% of 4π)	83.5	69.3	64.9
resolution (μm) (1982)	142	168	482
" (1983)	207	228	555
" (1984)	160	197	485

* z: with sense wires parallel to z-axis. uv: with stereo wires.
† The distance of closest approach from the interaction point to the PDC plane.
‡ The acceptance for a straight track going through all the layers.

3.2.1.3 The Magnetic Field and The Momentum Resolution

The curvature of a charged particle in a magnetic field gives a measure of its momentum. Figure 3.5 shows the magnetic field lines calculated by the computer program POISSON,[147] which reproduces the measured field. The magnet coils are wound on the pole tips of the return yoke. A solenoid would generate an intolerable amount of gamma conversion in front of the Čerenkov counter. The highest field strength in the $z = 0$ plane is 3.16 kG at $r = 0$. The total $\int Bdl$ for a almost straight track perpendicular to the beam axis is 1.79 kG·m. The significance of $\int Bdl$ is that

it gives the total angular deflection $\Delta\phi$ for a track with momentum P:

$$\Delta\phi = \frac{0.03}{P(\mathrm{GeV}/c)} \int Bdl\,(\mathrm{kG}\cdot\mathrm{m}).$$

For a Bhabha track (P = 14.5 GeV/c) the angular deflection is 3.7 mrad. The corresponding displacement at the center of the PDC is 4.0 mm.

The non-uniformity of the magnetic field necessitates a sophisticated pattern recognition program, and the final fitting of the measured track was done with respect to the expected shape given by the simulation using the actual magnetic field shape. The inverse-momentum distribution for the Bhabha events is shown in Fig. 3.5(b). The non-gaussian tails are due to the initial and final state radiations which makes the momentum of the electron or positron smaller. The momentum resolution for a stand-alone track averaged over all runs is given by

$$\frac{\sigma_P}{P} = \sqrt{[2P(\mathrm{GeV}/c)]^2 + 6^2} \quad (\%).$$

The part proportional to P is due to measurement error and the constant part is due to multiple Coulomb scattering. For a track with P less than 3 GeV/c, the momentum measurement error is dominated by the latter. For the maximum momentum of 14.5 GeV/c, the resolution is 30%. This is larger than the value expected from the displacement at the PDC of 4 mm and the position resolution of 0.5 mm for each PDC hit. The reason is that the exact point of the track origin is not known.

When a track is in the middle of a congested jet, the resolutions are worse due to the overlapping of tracks. This problem, however, can be substantially alleviated by applying quality cuts on the tracks.

3.2.2 The Čerenkov Counter

Just as an object moving faster than the speed of sound generates a shock wave in air, a charged particle moving faster than the phase velocity of light in a medium

(a)

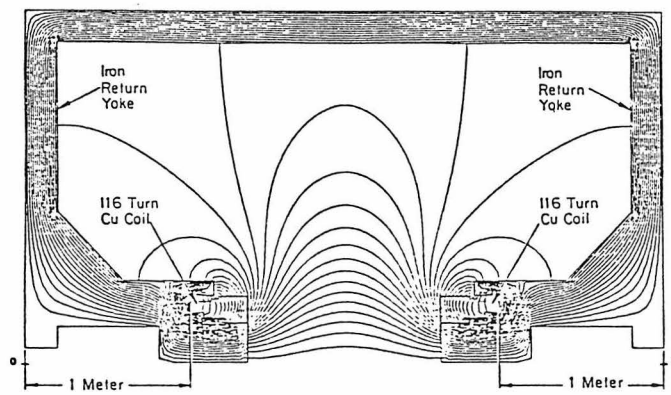

(b)

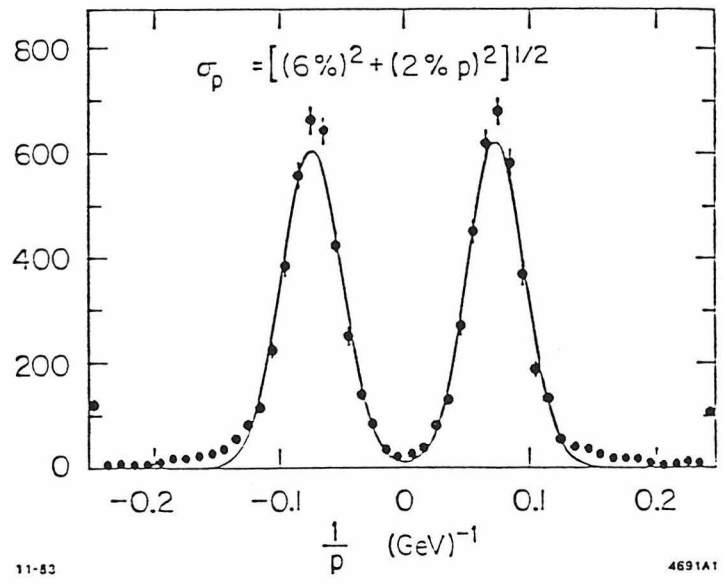

Figure 3.5. (a) Magnetic Field calculated by the computer program POISSON, which was found to be within the measurement error of the result of a field mapping using a Hall probe. (b) The inverse-momentum distribution for the Bhabha tracks. The solid curve is the result of a two-gaussian fit. The non-gaussian tails are due to the radiative corrections to the Bhabha scattering process.

radiates Čerenkov light. Whether or not a particle of a known momentum radiates Čerenkov light depends on the mass of the particle; thus, it gives information on the type of the particle. Our purpose is to separate pions from kaons in the momentum range above a few GeV/c. We start from a review of the basic formulae of Čerenkov radiation.

3.2.2.1 Čerenkov Radiation

As a charged particle passes through a medium (radiator) it generates time-varying polarizations, and they in turn radiate electromagnetic waves. When the particle is moving faster than the phase velocity of the electromagnetic wave, a shock wave front is formed. This phenomenon was analyzed by Tamm and Frank in 1937,[148] three years after the effect was first observed by Čerenkov. The energy spectrum and the angular distribution of the radiated photon are given by[149]

$$\begin{aligned} dN &= \frac{2\alpha}{\pi n}\frac{\sin^2(\frac{\pi l}{\lambda}x)}{x^2}\sin^2\theta\,\frac{d\epsilon}{\epsilon}\,d\cos\theta, \\ x &\equiv \frac{1}{\beta n} - \cos\theta, \end{aligned} \tag{3.8}$$

where α is the fine structure constant, θ is the angle between the direction of the photon emission and that of the particle, λ is the wave length of the photon in the radiator, ϵ is the energy of the photon, l is the length of the radiator, β is the velocity of the particle divided by the speed of light, and $n = n(\epsilon)$ is the index of refraction of the radiator.

The angular distribution has the $\sin^2 x/x^2$ shape which often appears in studies of diffraction phenomena, and peaks at θ_0 where $\cos\theta_0 = 1/(\beta n)$. The width of the central peak is of order $\lambda/(l\theta_0)$, and the angular spectrum tends to a delta function as l/λ becomes large. Using

$$\frac{1}{\pi}\frac{\sin^2(ax)}{ax^2} \to \delta(x) \quad (a \to \infty),$$

the formula (3.8) reduces to the familiar Tamm-Frank formula for $l \gg \lambda$ when the

angle is integrated over:

$$\begin{aligned} \frac{dN}{dl\,d\epsilon} &= \frac{\alpha}{\hbar c}\sin^2\theta \\ &= 370\sin^2\theta \quad (\mathrm{cm}^{-1}\mathrm{eV}^{-1}), \end{aligned} \tag{3.9}$$

where the Čerenkov angle θ is given by

$$\cos\theta = \frac{1}{\beta n}.$$

In this limit, there is no radiation when β is smaller than $1/n$. Thus, the momentum threshold for a particle of mass m is

$$\begin{aligned} P_0 &= m\eta_0, \\ \eta_0 &= \frac{1}{\sqrt{n^2-1}} \approx \frac{1}{\sqrt{2\delta}}, \end{aligned} \tag{3.10}$$

where $\delta \equiv n-1$, and the approximation is good when $n \approx 1$. In (3.10), n is assumed to be a constant. Under the same assumption, the photon energy spectrum becomes flat. For $\beta = 1$, namely at well above the threshold, the Čerenkov angle θ_0 is

$$\theta_0 \approx \frac{1}{\eta_0} \quad (n \approx 1). \tag{3.11}$$

The width of the angular distribution in (3.8) is generally very small. For isobutane gas at atmospheric pressure and for a particle with β close to 1, the angular spread is of order 0.01 mrad. However, when n is very close to 1, e.g., for light gas radiators, and/or l is small (as in the counters used for the measurement of particle fractions in some beam lines[150]) the difference between the exact formula and the Tamm-Frank formula becomes significant especially around threshold. The formula (3.8) also shows that there is a finite amount of radiation even below threshold. This can be interpreted as transition radiation at the entrance and the exit of the Čerenkov radiator. For our counter, transition radiation is negligible.

3.2.2.2 Choice of Čerenkov Radiator

From (3.10), the pion Čerenkov threshold is at $\eta_0 m_\pi$ and the kaon threshold is at $\eta_0 m_K$; thus, if a particle has a momenta between these two values and if there is no Čerenkov radiation, then the particle is not a pion, namely it should be a kaon or heavier. The type of radiator gas has to be chosen such that this momentum range of π/K separation covers the optimum region for the analysis, namely above a few GeV/c. Thus, η_0 should be 15~20, which corresponds to n of 1.00125~1.002. Without pressurization, it requires one of the densest gases available.

The other requirement is that the transmission cutoff of UV light be at as short wavelength as possible; for generally the limiting factor of a Čerenkov counter is the intensity of the usable Čerenkov light, namely the number of the photoelectrons generated at the photon detector (the photomultiplier in our case). Also, the amount of scintillation should be modest so that the background level will be low. We chose isobutane at atmospheric-pressure which has $n = 1.00144$ and a UV cutoff at 182 nm.[151] The scintillation of isobutane caused by a charged track has been measured[152] to be 6.4×10^{-4} photons per cm within the typical spectrum range of photomultipliers, which has a negligible effect on our background.

In reality, the index of refraction depends on the photon energy (dispersion). The functional shape is well approximated by the formula indicated by the single-oscillator model:

$$n^2(\epsilon) - 1 = \frac{E_d E_0}{E_0^2 - \epsilon^2}, \tag{3.12}$$

where we used $E_d = 0.0336$ eV and $E_0 = 13.5$ eV as obtained by Wemple.[153] The number of photoelectron n_e detected at the photomultiplier per cm of radiator is then given by [from (3.9)]

$$\begin{aligned} \frac{dn_e}{dl} &= \frac{\alpha}{\hbar c}\int \varepsilon(\epsilon)\sin^2\theta\, d\epsilon \\ &= 370\int \varepsilon(\epsilon)\left(1 - \frac{1}{\beta^2 n^2(\epsilon)}\right) d\epsilon \quad (\epsilon \text{ in eV}), \end{aligned} \tag{3.13}$$

where $\varepsilon(\epsilon)$ contains all the efficiencies that a emitted Čerenkov photon generates a

photoelectron at the photomultiplier. The effective index of refraction $n = 1.00144$ was obtained by requiring that it gives the correct mean number of photoelectrons as a function of the particle momentum. The corresponding η_0 is 18.6, and the maximum Čerenkov angle θ_0 is 3.1° from (3.11). Table 3.4 shows the threshold momenta for various particles. The momentum region of π/K separation is thus from 2.6 GeV/c to 9.2 GeV/c. Since there are very few hadrons above 9.2 GeV/c, the region of π/K separation is practically the whole region above 2.6 GeV/c.

Table 3.4. The Čerenkov thresholds of various particles for isobutane gas at atmospheric pressure. ($n = 1.00144$ and $\eta_0 = 18.6$).

	e	μ	π	K	P
P_0(GeV/c)	0.0095	1.97	2.60	9.20	17.5

We also used nitrogen as the radiator in order to obtain electron identification up to 5.5 GeV/c. Those data are not used in this analysis.

3.2.2.3 Čerenkov Light Collection

There are 36 Čerenkov cells as shown in Fig. 3.2. The acceptance of a single cell is 20° in ϕ and $0 < \cos\theta < 0.62$ or $-0.62 < \cos\theta < 0$, where θ is the polar angle with respect to the beam axis. The total acceptance is 62% of 4π. The whole counter is split along the vertical plane containing the beam axis, and the surfaces are sealed by 0.075 mm membranes of aluminized mylar reinforced by nylon. The 18 cells within each half are not optically separated by buffers. The entrance window is 5 mil mylar, and mechanically supported by a layer of honeycomb wall.

Figure 3.6 shows the geometry of a single Čerenkov cell. The simulated Čerenkov light trajectories are also shown for a straight track. The usable Čerenkov light is emitted along the track from the window to the ellipsoidal mirror, which focuses the light on to the photomultiplier (PMT). One of the foci is at the interaction point (F1) and the other (F2') is just in front of the photomultiplier

when reflected by the flat mirror.

The ellipsoidal and flat mirrors are made of 1/4-in-thick glass. The ellipsoidal mirrors were shaped by heat-slumping on to graphite molds. The mirror surfaces are fabricated by vacuum-deposition of a 75 nm layer of aluminium immediately followed by a 25 nm layer of MgF_2. The MgF_2 coating protects the surface from oxidization. Glass was chosen as the substrate rather than plastic because with glass, it is possible to achieve better vacuum during the vacuum deposition process, which results in better reflectivities especially at shorter wave lengths. The reflectivity of the mirror was measured to be 85% down to $\lambda = 175$ nm: shorter than the cutoff wave length of isobutane (182 nm).

Each photomultiplier is equipped with a light-collecting cone made of epoxy. The inner surface of the cone is aluminized. The shape is a rotated parabola where the axis of the parabola is tilted 30° with respect to the axis of rotation. It effectively collects photons entering the cone if the incident angles are less than 30°, while almost all photons are bounced back out of the entrance if the angles are larger than 30°. This type of light-collecting cone is called a Winston cone.[154] Figure 3.7(a) shows the photomultiplier assembly including the light-collecting cone.

We chose RCA8854 (Quantacon) as the photomultiplier for the Čerenkov counter because of its large aperture (5 in diameter) and its ability to see the single photoelectron peak. The latter is due to the high-gain first dynode ($\times 25$), and is used to calibrate the photomultipliers so that the single photoelectron peak appears at the same channel number.

The photomultiplier is housed inside two layers of μ-metal to reduce the magnetic field in the first dynode region. In addition, a bucking coil is placed around the same region to cancel the axial component of the left-over magnetic field. The current on each coil is independently adjusted by a computer controlled program to maximize the gain.

RCA8854 is equipped with a 1.9 mm UV glass window (Corning 9741) and an efficient bialkali (K_2CsSb) photocathode. The window absorbs photons for $\lambda \lesssim 300$

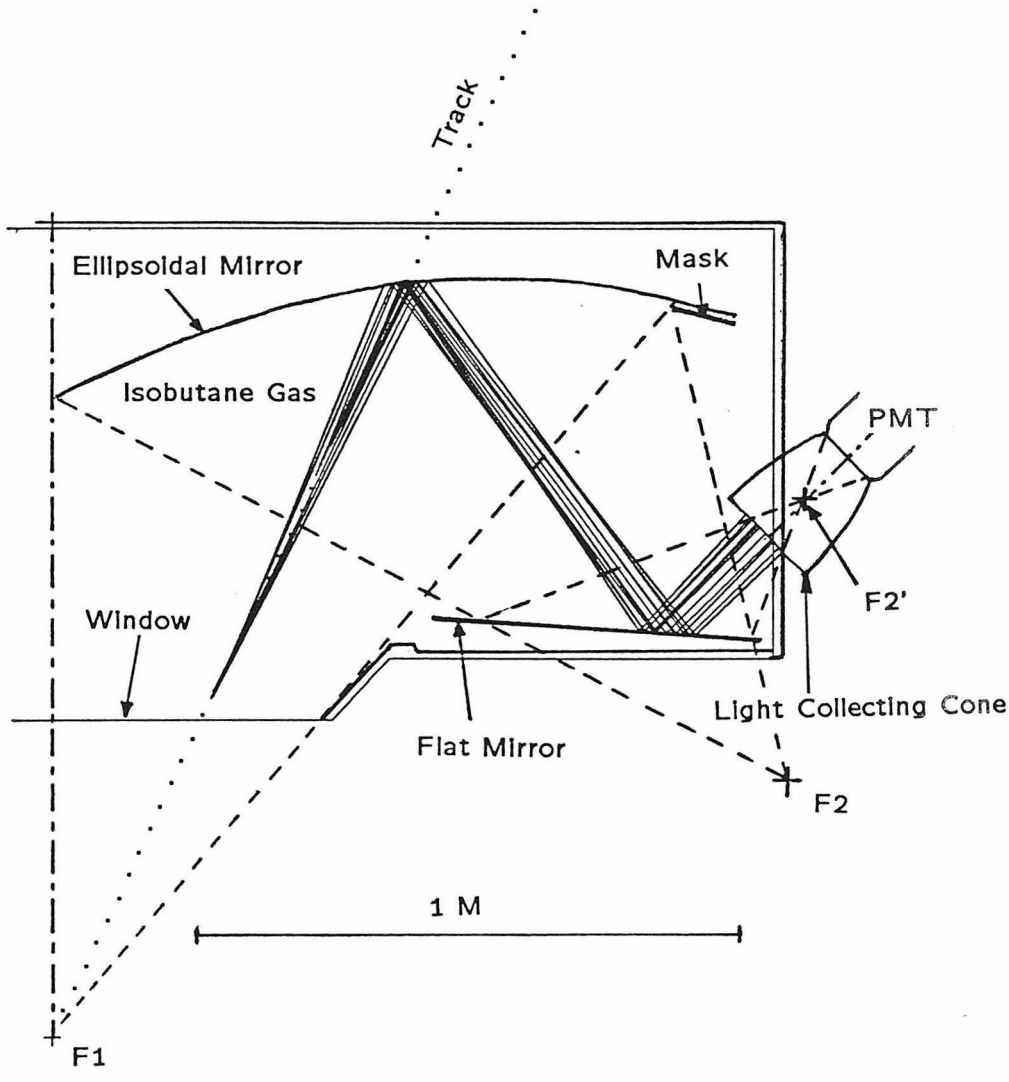

Figure 3.6. The geometry of a single Čerenkov cell. The ellipsoidal mirror focuses the Čerenkov light onto the photomultiplier. One of the foci is at the interaction point and the other is just in front of the photomultiplier (PMT) when reflected by the flat mirror. Simulated photon trajectories are shown for a high-momentum charged track.

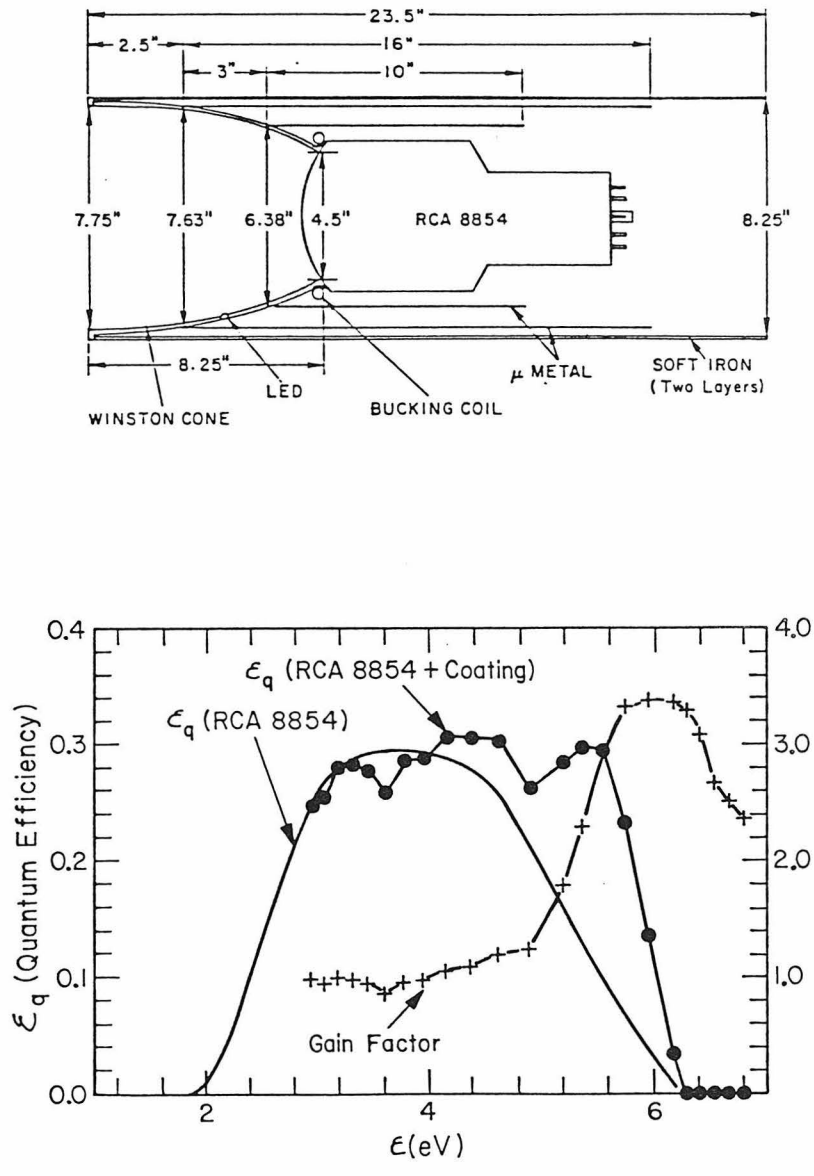

Figure 3.7. (a) The Čerenkov counter photomultiplier assembly. (b) The gain factor obtained by the *p*-terphenyl coating, and the quantum efficiency of the photomultiplier with and without the coating.

nm. In order to improve the quantum efficiency in the UV region, the surface of the window is coated with *p*-terphenyl (1,4 diphenylbenzol: $C_{18}H_{14}$). It absorbs UV photons of $\lambda = 200 \sim 300$ nm and re-emits (decay time $\sim$ 1ns) photons of λ around 350 nm, which can then cross the window and for which the bialkali photocathode has a good efficiency. The wave shifter (*p*-terphenyl) was applied by the dip coating method developed by Eigen and Lorenz.[155] The dipping solution was 0.5 g *p*-terphenyl in 300 cc methylene chloride with 2 g B66 Acryloid as the binder.

We have used a monochrometer to measure the gain factor obtained by the wave-shifter coating. Fig. 3.7(b) shows the gain factor as a function of the incident photon energy. The conversion between the wave length and the energy is conveniently given by

$$\lambda\epsilon = 1240 \quad (\text{nm} \cdot \text{eV}).$$

It is difficult to know how many photons from the monochrometer are incident on the photomultiplier window for a given photon energy. Thus, we have taken the efficiency curve supplied by the manufacturer and multiplied it by the measured gain factor to estimate the final quantum efficiency. The result is overplotted in Fig. 3.7(b). The final shape of the quantum efficiency is consistent with the result of Ref. 155. Roughly speaking, the band width is from 3 eV to 6 eV, and the quantum efficiency is 30% in the region. The index of refraction $n(\epsilon)$ changes from 1.00131 to 1.00155 in the range, but for our purposes, it is adequate to assume that n is constant.

3.2.2.4 The Čerenkov Response for Electrons

Figure 3.8 shows the distribution of n_e for Bhabha tracks. Bhabha events are selected without applying any cuts on the Čerenkov-counter response. Each track is required to hit well inside the cell by at least the maximum Čerenkov angle of 3.1° from the edges. The average number of photoelectrons is 18.8, and out of 2340 tracks there is no track that generates less than 2 photoelectrons. The inefficiency

of the counter is negligible.

The photoelectron yield (3.13) is often written as (for a constant index of refraction)

$$\frac{dn_e}{dl} = N_0 \sin^2\theta,$$

with

$$N_0(\mathrm{cm}^{-1}) = 370 \int \varepsilon(\epsilon) d\epsilon \quad (\epsilon \text{ in eV}).$$

The efficiency $\varepsilon(\epsilon)$ includes the reflectivities of the mirrors, the transmissivity of the radiator gas, the light-collection efficiency of the Winston cone, and the quantum efficiency of the photomultiplier. Thus, the parameter N_0 is a measure of the overall light collection efficiency. Using $< n_e >= 18.8$, $< l >$=83 cm (for the Bhabha tracks), and $\sin^2\theta = 0.00287$, N_0 is found to be 79 cm^{-1}. The value of N_0 differs slightly from cell to cell; the width of the distribution is ~ 10 cm^{-1}.

A rough estimation of N_0 can be made from our knowledge of the individual efficiencies. The $\varepsilon(\epsilon)$ is approximately a step function which is nonzero from 3 eV to 6 eV, and the efficiency in that region is

$$0.85^2(\text{mirror}) \times 0.80(\text{transmission}) \times 0.70(\text{cone}) \times 0.30(\text{PMT}) = 0.12.$$

Thus, the expected N_0 is $370 \times (6-3) \times 0.12 = 135$ cm^{-1}. Admittedly, the above estimate is crude. However, the expected N_0 is not far from the measured value especially if one takes into account that the quantum efficiencies supplied by manufacturers are often overestimated[156] by up to a factor of 2.

At lower momenta, the curvature of the track reduces the light-collection efficiency even at well above the electron threshold of 9.5 MeV/c. To study this, we used the two-photon interaction $e^+e^- \to e^+e^-e^+e^-$ where the electromagnetic field accompanied by the initial e^- and that from the initial e^+ collide and generate a low-energy e^+e^- pair. Most of the time, the initial e^+e^- pair goes down the beam pipe and is not detected, while the low-energy e^+e^- pair is detected in the central detector. We take two-prong events and require that one of the pair to be an

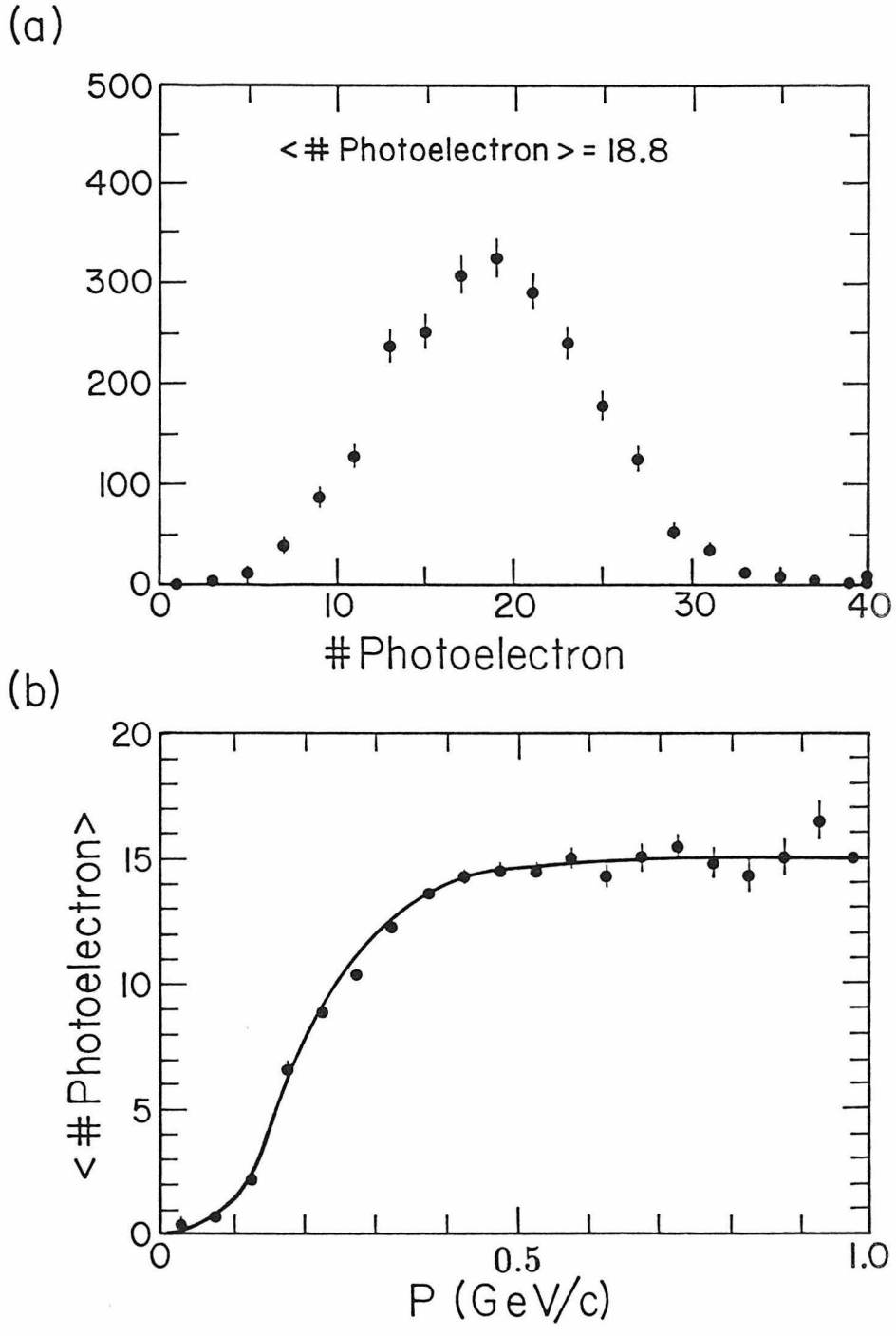

Figure 3.8. (a) The number of photoelectrons for the Bhabha tracks. The tracks are required to hit well inside the cell. (b) The average photoelectron yield for electrons as a function of the electron momentum. At low momentum, the light collection is inefficient due to curvature of the track. The solid curve is the prediction of the ray-tracing Monte Carlo program.

electron by the Čerenkov response.[157] Then, the other track in each event is highly likely to be an electron. The contamination from other processes is negligible. Fig. 3.8(b) shows the average number of photoelectrons vs P for the tracks that are not required to be electrons by the Čerenkov response. Each track is associated with the cell whose ellipsoidal mirror is crossed by the track, and no requirement is made that the crossing point be far from the edges. The solid curve is the estimation by the ray-tracing Monte Carlo program, which includes the effects of the curvature, the small gaps between the mirrors, and the geometry of the light collecting cone. The curve is normalized to the data in the region above 0.7 GeV/c. The agreement is good.

3.2.2.5 The Čerenkov Response in Hadronic Events

Figure 3.9 shows the Čerenkov pulse height vs the momentum of track. The pulse height is normalized to an N_0 of 100 cm^{-1} and a path length of 100 cm so that the average yield becomes the same for a given particle of a given momentum independent of the cell and the path length. The expected average pulse heights are overplotted for e, μ, π and K. A clear band of π rising at 2.6 GeV/c is seen. The kaon band is not clearly seen because of the low statistics in the high momentum region as well as the momentum smearing and the statistical fluctuations of n_e. Most of the tracks that have substantial response below the pion threshold are electrons. The tracks with no Čerenkov response above the kaon threshold, i.e., in the region labeled 'P', are contaminated by the kaons whose true momenta are below the kaon threshold.

The horizontal band at around 1.5 photoelectrons in the low momentum region $P \lesssim 3$ GeV/c is a noise signal that corresponds to a single photoelectron before the normalization is done. The probability that a cell has this noise is measured to be about 1% when averaged over all cells. It is slightly greater in the center of a jet and smaller in regions away from jets. This noise is almost non-existent in Bhabha events. Therefore, it cannot be due to the synchrotron radiation, stray beam

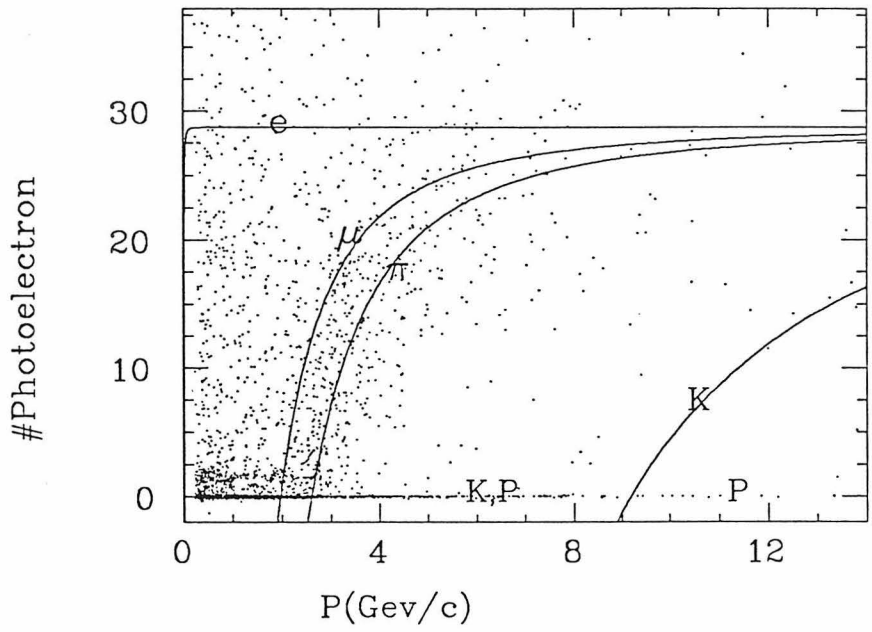

Figure 3.9. Čerenkov pulse height vs momentum of track for the hadronic datasets. The curves overplotted are the average expected number of photoelectrons for e, μ, π and K.

particles, nor any other beam related sources. Dark currents in photomultipliers are also excluded for the same reason. A study using the Čerenkov ray-tracing simulation program has shown that it is mostly due to low energy electrons (below $\approx$100 MeV/c) whose curvature is large enough so that the Čerenkov photons are scattered in various directions. An example of Čerenkov photon trajectories for a 50 MeV electron is shown in Figure 3.10. A small contribution from Čerenkov radiation at the entrance window is not excluded. Because of its low rate and randomness, the single electron level noise is harmless in our analysis.

Figure 3.11 shows n_e vs the time in nsec of all the cells in the multi-hadron events that have enough pulse height for the time measurement. The offset of the time is defined such that the responses to Bhabha electrons have a mean of 0 ns. One can see a vertical band at around -3ns. This is due to particles that point directly toward the photomultipliers. Some are direct hits on the face of the photo cathode by charged particles. Such hits generate about 30 photoelectrons per hit, which is consistent with the number of Čerenkov photons ($\sim$ 120) generated at the 1.9 mm thick photomultiplier window. Others are due to particles above their Čerenkov threshold whose light is directly collected by the light collecting cone and the photomultiplier, producing about 10 photoelectrons per track. These early direct hits could be effectively eliminated by a timing cut. The time of these hits expected from the geometry is -3.1 ns, which is consistent with the observation. Approximately 10% of the hits with $n_e > 2$ are the early hits. On the other hand, the probability that a given cell has an early hit is less than 1%.

3.3 Data Acquisition

The purpose of the data-acquisition system is to log efficiently the events of interest to the tapes and to monitor the state of the experiment. Figure 3.12 shows the block diagram of the data-acquisition system. One important feature is that there are four separate systems that transfer data in parallel. The four systems

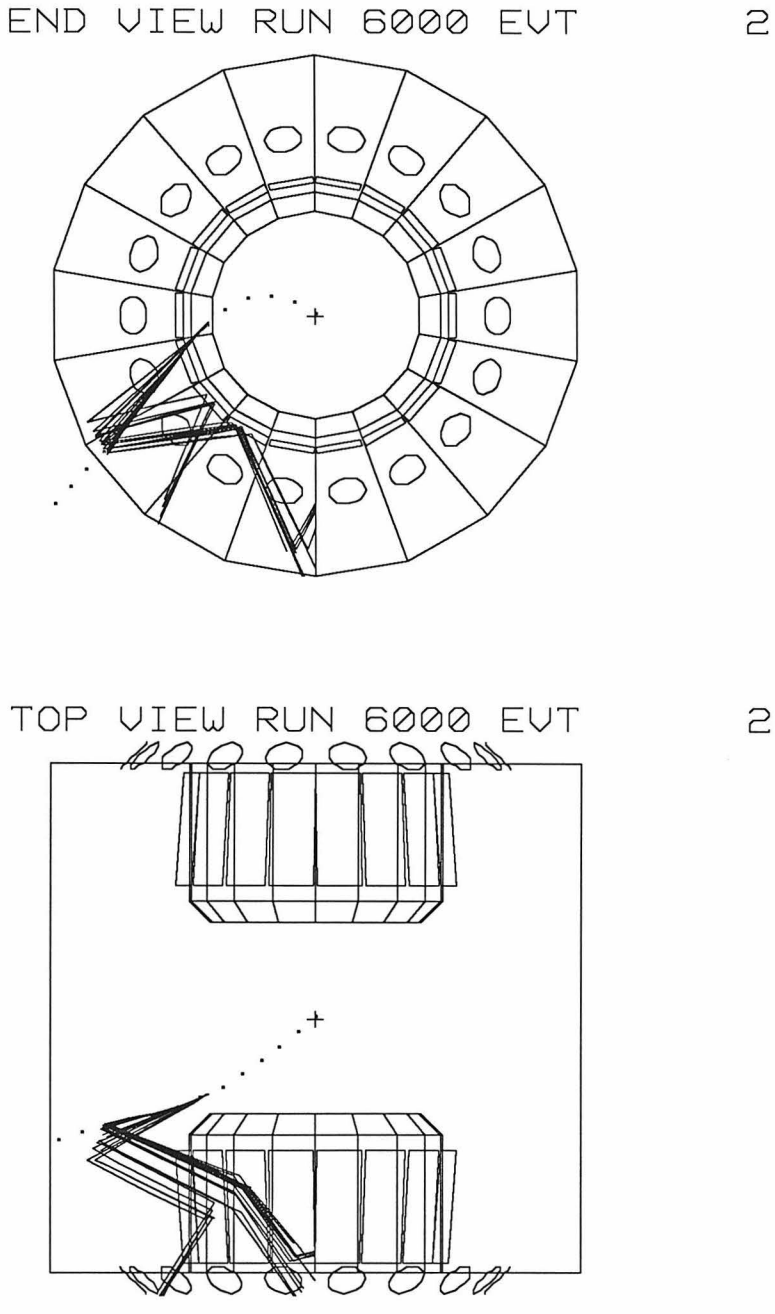

Figure 3.10. Čerenkov photon trajectories for a 50 MeV electron. The end view and the top view are shown. The dotted line is the trajectory of the electron. The ellipsoidal mirrors are not shown explicitly. The randomly scattered photons are considered to be the primary source of the single photoelectron level noise.

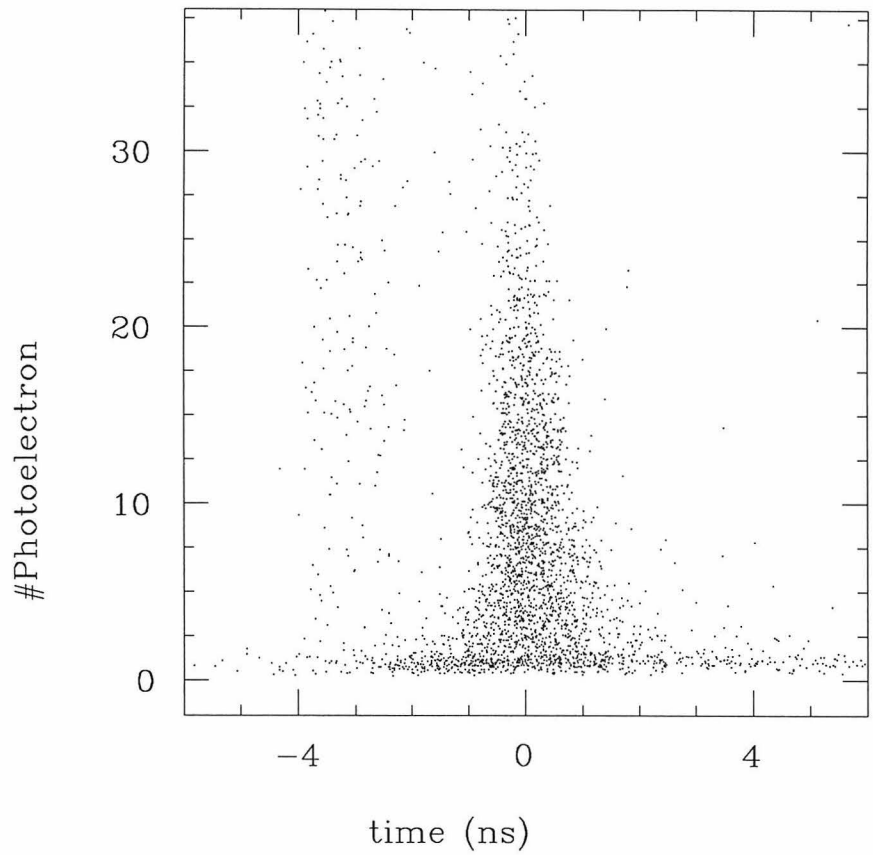

Figure 3.11. The number of photoelectrons vs time (nsec) for all the cells in hadronic events. The vertical band at around -3 ns is due to the tracks directly pointing toward the photomultipliers. The time distribution of the single-photoelectron noise is broad.

are the IDC, the CDC, the PDC, and the rest — namely the ADC's, TDC's, and latches. In addition, each of the four systems is monitored by a dedicated LSI-11 minicomputer, which was also used to debug the corresponding part of the detector before the main data-acquisition system became ready. The main data-acquisition computer is the PDP-11/40 which runs a multi-task program (MULTI) based on the RT11 operating system. The events are actually written to tape by the VAX-11/780. The data transmission from the front-end electronics up to the PDP-11/40 is controlled by the Buffer Controller. The data logging of a single event is described step-by-step below.

When the trigger logic decides that the event is to be accepted, it sends a trigger signal TRIG to the Buffer Controller. Upon receipt of the trigger signal, the Buffer Controller sets the experiment deadtime level (Exp.DT) which prohibits the trigger logic from sending another trigger. After a wait of 120 μsec, the Buffer Controller sends the first interrupt (I0) to the PDP-11/40, provided that all four Buffer Memories are empty (BE), to which PDP-11/40 responds by raising the computer deadtime level (Comp.DT; takes about 350 μsec). The Comp.DT level prohibits the Buffer Controller from sending the first interrupt I0. At the same time as the Buffer Controller sends out the I0 to the PDP-11/40, it signals the four scanners to start transferring the data from the front-end electronics to the Buffer Memories (SCAN signals). While the Buffer Memories are being loaded, the PDP-11 prepares for the data transfer from the Buffer Memories to its own memory: it allocates one of the eight event buffers (if no event buffer is empty, it waits until one becomes available), calculates the absolute addresses in the event buffer for each of the four Buffer Memories, sets up the control blocks for the CAMAC branch driver (Jorway 411), and prepares the event header containing, among others, the run and event numbers, the date, and the status of the PEP ring.

When a Buffer Memory is loaded by the scanner, it sends a buffer-full signal (BF) to the Buffer Controller. When all the four Buffer Memories become full, the Buffer Controller sends the second interrupt (I1) to the PDP-11/40 and resets

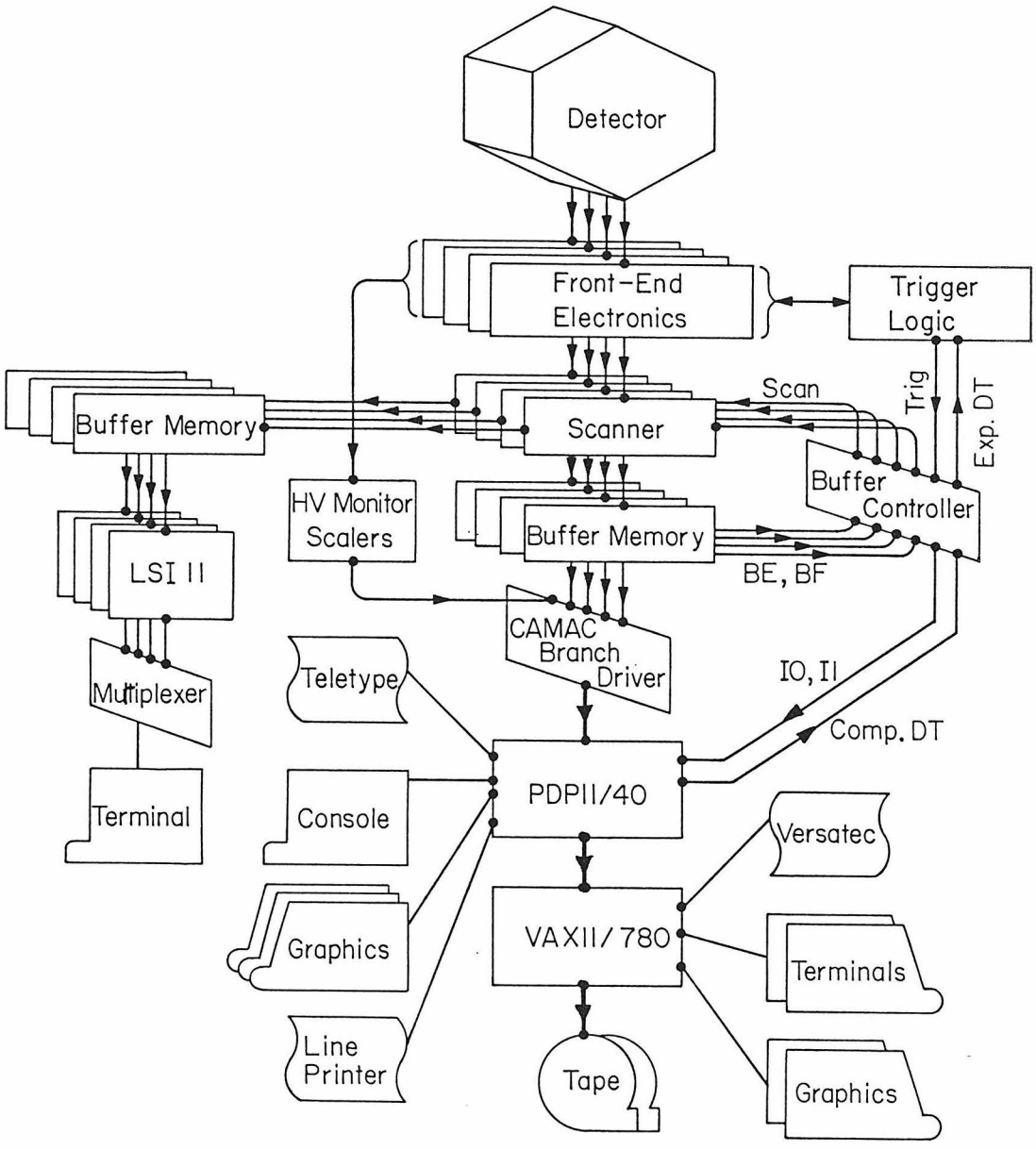

Figure 3.12. The block diagram of the data-acquisition system. There are four parallel data flows (systems) up to the Buffer Memories, and the Buffer Controller controls the timing of the data transfers from the front-end electronics up to the PDP-11/40. Each of the four systems can be independently monitored by a dedicated LSI-11 minicomputer.

the experiment dead time level (Exp.DT). Normally, i.e., if the PDP-11/40 can allocate an event buffer without waiting, it takes about 2 to 3 msec from the event trigger up to this point, and this is when the experiment comes back alive again even before any of the event data are sent to the PDP-11/40. The PDP-11/40 then starts loading the contents of the Buffer Memories to the event buffer, and upon its completion, it turns off the computer deadtime level (Comp.DT), which completes the cycle.

The aim of the first interrupt (I0) is to notify the PDP-11/40 to prepare for a new event while the Buffer Memories are being loaded. The second interrupt signals the actual data transfer from the Buffer Memories to the event buffer in the PDP-11 memory. The use of two interrupts allows parallel processing.

Now the event is in one of the eight event buffers of the PDP-11/40. It is then queued for spooling to the tape drive that in fact is the VAX-11/780, which actually writes the event to a tape. Namely, the VAX-11/780 looks like a tape drive to the PDP-11/40. When an event is written to a tape, the event buffer is released for a new event. The time required for writing a single event to the tape depends on the length of the event record which is determined by the number of drift chamber hits; usually it is about 0.1 sec. However, as long as the event buffer is allocated without waiting, namely if the rate of the TRIG signal is much less than 10 Hz, then the tape-writing time does not contribute to the deadtime. The purpose of the multiple event buffers is to average out the random arrivals of events and minimize the dead time.

The program MULTI consists of a data-acquisition part and an analysis part. The analysis part accepts commands from the console terminal, displays the events currently taken, processes histograms, and monitors the experiment. The histograms are dynamically defined and accumulated. It also has a built-in expression evaluator that allows conditioned accumulations of histograms. The analysis part does not directly communicate with the data-acquisition part except when a run is begun, ended, paused, or resumed. The analysis program accesses

the events through the shared disk file to which the data-acquisition program writes the events at the same time as it writes them to tape.

Calibration events are taken every 30 seconds (cycle). They are LED events, in which the photomultipliers are tested by the LED's (light-emitting diodes) for gain and timing calibrations, and pedestal events which are essentially LED events in which the LED's are not fired. The pedestals are updated constantly and used in the analysis programs. Also included in the calibration events is a HV-scaler event which is taken once every cycle. This event record monitors the high voltages of the photomultipliers, the drift chambers, etc., and counts the rates of various signals such as trigger rates, noise level of the beam, and the luminosity.

The internal consistency of the data is checked whenever is possible. For example, if the timing information is present for a counter and the corresponding latch is not on, then the latch information is lost somewhere along the line; if the latches shows that a certain trigger criteria is satisfied and yet the corresponding trigger bit is not on, then it is likely that one of the modules that generate the trigger signal is malfunctioning. These data are summarized in a one page run summary and printed out at the end of each run. In addition, the operator is notified during the run when the malfunction can be detected quickly enough. The hardware errors detected by the data-acquisition programs are logged to the teletypewriter.

The VAX-11/780 also has access to the events as they pass through its CPU on the way to the tape. It runs the large part of the offline program which is able to find and fit tracks, as well as a copy of the MULTI program that runs in the PDP-11/40. The single-track events, which are dominantly from the two-photon interaction $e^+e^- \rightarrow e^+e^-e^+e^-$ where only one prong is detected in the central detector, are used to check the efficiencies of drift-chamber wires and counters. This requires high statistics, and the result is printed out approximately three times a day. Thus, the monitoring of the experiment is done in three stages: for the problems that can be found immediately, the operator is notified during the run; the ones that require more statistics but do not require tracking are printed out at

each end of run; and the ones that require tracking are checked every eight hours or so.

3.4 TRIGGER SYSTEM

The beam-crossing signal is picked up by a button located 20 m from the interaction point, and arrives in the control room on a fast cable. The beam crossing occurs every 2.446 μsec; thus, if one takes more than 2.446 μsec to decide whether or not there is an interesting event in the crossing, at least 50% of the luminosity is lost. The input to the trigger systems are the pulses from the counters (photomultipliers) and the track information given by the hardware tracker. While the time required for the processing of the counter information is well below 1 μsec, that for the tracker is about 6 μ sec. There is not enough time for the tracker information to be used for each beam crossing. The problem is solved by a two-stage trigger system.

The first-stage decision must be made before the next beam crossing. If an event is not accepted then the track-finding process is aborted. If accepted, then further beam crossings are rejected until the second-stage decision is completed. This deadtime is set to 20 μsec to allow an ample time for the track information to be processed. If the second-stage trigger condition is met, the whole front-end memories that contain the event information are frozen and the final trigger (TRIG) is sent to the data-acquisition system, namely to the Buffer Controller. Meanwhile, the beam-crossing signals are vetoed until the data are transferred to the Buffer Memories, i.e., the 20 μsec deadtime is extended to 2 to 3 msec, or longer if the PDP-11/40 cannot find an empty event buffer. Figure 3.13 shows the block diagram for the trigger system. We will discuss the components of the trigger system below.

The latches record one bit per counter. Since they can be processed quickly, they are strobed for each beam crossing (X signal) and the bit is reset before the next X unless the event is accepted by the first trigger.

The ADC's (analog to digital converters) record the pulse heights of counters,

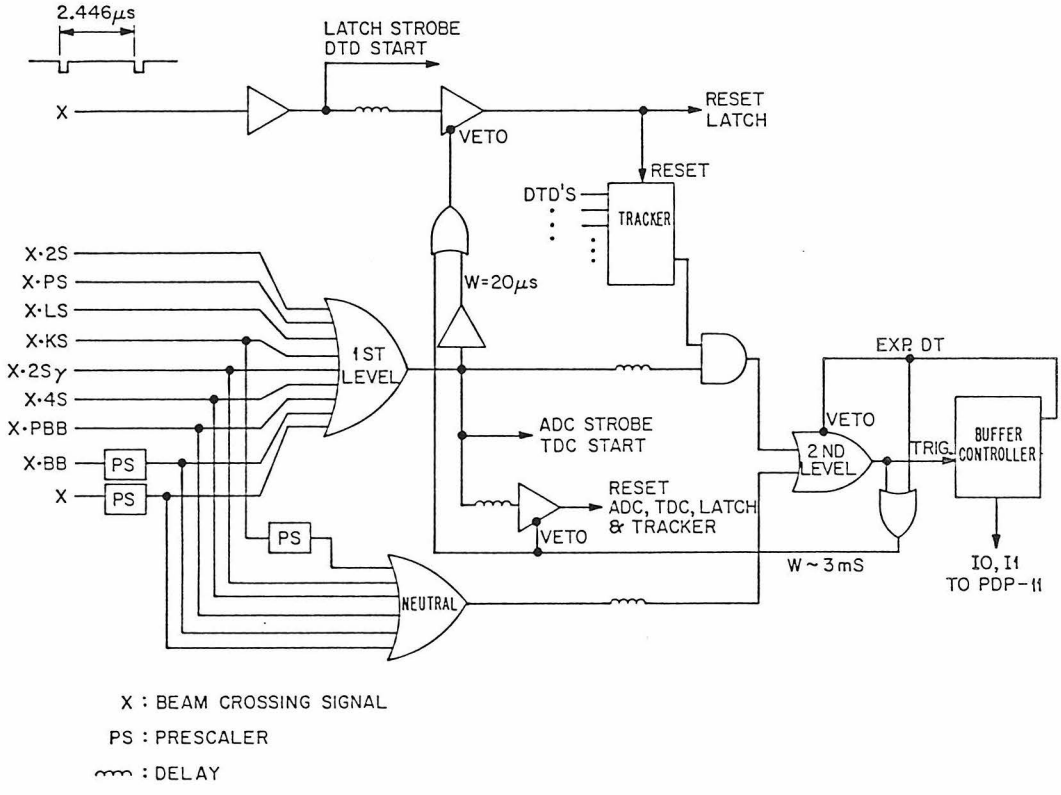

Figure 3.13. Block diagram of the trigger logic. The trigger is processed in two stages. The first-stage trigger uses the counter information and takes about 0.5 μsec, while the second-stage trigger requires the charged track information and takes about 6 μsec.

and the TDC's (time to digital converters) record their times. They are strobed or started by the first-trigger signal and reset if the second-trigger condition is not met.

The digitization of the drift times is done in about 1 μsec, and the process can be repeated for each beam crossing without causing any deadtime. The X signal starts the drift-time digitizers (DTD's), and they are cleared before the next X unless the first-trigger condition is met.

The tracker[158] finds tracks in the IDC and CDC and matches them with the hits in the barrel shower counters. The information on whether a given drift-chamber wire is hit or not is stored in a register in the DTD. The registers that belong to one layer are daisy-chained and, as soon as the drifts are complete, the wire-hit information is shifted into the tracker by a 20 MHz clock. The information on all 16 layers is separately shifted into the tracker. As mentioned earlier, the layers in the IDC and CDC are half-cell-staggered pairs: 3 pairs in the IDC and 5 pairs in the CDC. First, the tracker finds the paired hits in the paired layers, then it searches for coincidences between the paired hits that are consistent with a track of momentum greater than 200 MeV/c. At the same time, the hits in the barrel shower counters are searched for a matching with the tracks. The conditions actually used are: 2 IDC pairs, 3 CDC pairs, and at least one barrel shower counter hit associated with it. When there is at least one track that satisfies the conditions, a signal is sent to the second-stage trigger logic.

There are nine types of first triggers employed, and when the tracker signal is also on, the final trigger is asserted. Six of the first triggers can directly result in the final trigger regardless of the tracker output, and are called neutral triggers. These are listed below.

X·2S At least two sextants of the barrel shower counter are hit.

X·PS At least one sextant of the barrel shower counter is hit, and there is enough energy deposited in at least one of the 36 pole-tip shower counters.

X·LS At least one sextant of the barrel shower counter is hit, and there is an enough

energy deposited in at least one of the 12 luminosity-monitor modules.

X·KS (Neutral) At least one sextant of the barrel shower counter is hit, and there is at least one hit in the Čerenkov counter in the same sextant. When used as a neutral trigger, it is prescaled by 1/128.

X·2Sγ (Neutral) At least two sextants of the barrel shower counter are hit, and there is enough energy deposited in the whole barrel shower counter.

X·4S (Neutral) At least four sextants of the barrel shower counter are hit.

X·PBB (neutral) The Bhabha events that hit the pole-tip shower counters.

X·LBB (Neutral) The Bhabha events that hit the luminosity monitor (prescaled by 1/128).

X (Neutral) Limited to 0.1 Hz. This is to check the background.

A typical hadronic event passes X·2S, X·KS, X·2Sγ, and X·4S. As we will discuss later, the final hadronic dataset is defined by the offline cuts and not restricted by the triggers.

The deadtime of the experiment is given by

$$(f_1 - f_2)d_1 + f_2 d_2,$$

where f_i Hz (d_i sec) is the frequency (deadtime) of the i-th trigger. Thus, $d_1 = 20$ μsec and $d_2 = 2$ to 3 msec. The typical trigger frequencies are f_1 =100 Hz and f_2 =2 Hz; thus the deadtime is 0.6 to 0.8 %. The actual deadtime is a little higher, and is about 1 %. This is because the PDP-11/40 cannot allocate an event buffer from time to time, such as when there is an burst of beam noise. Here, the advantage of the double interrupts (I0 and I1) and the multiple event buffers is clear. Even if the events are being written at a close-to-the-maximum rate (~10 Hz), the deadtime will be at an acceptable level (~10 %).

3.5 Selection of Hadronic Events

The events are written to the tapes by the VAX-11/780 in a condensed format,

which are read by the offline computer (the IBM 3081/3033), unpacked, rearranged in a more convenient form, and sent through a pattern-recognition or track-finding process. At this stage, a crude classification is made to select candidates for the final hadronic events, and those events that pass the selection criteria are then fitted, namely the momenta and directions of the found tracks are determined using the correct values for the non-uniform magnetic field. Then the final hadron classification is applied as below.

1. The number of 'good' tracks $\geq$ 5. The good track is defined to be a successfully fitted track with $b < 2$ cm, where b is the distance of closest approach to the beam axis.
2. Each event hemisphere contains at least 2 good tracks that have at least 12 drift-chamber hits. The hemispheres are defined by the plane perpendicular to the jet axis.
3. The sum of the absolute momenta of the successfully fitted tracks $\geq$ 6 GeV/c.

The above cuts are the main cuts that defines the hadronic dataset. There are other cuts[159] that eliminate background events.

4. The total electromagnetic energy into the pole-tip counters $\leq$ 20 GeV. The events rejected by this cut are the hadronic events whose jet axes are pointing to the pole-tips. These events often have many soft tracks generated by the showering process, and they are useless for physics.
5. The number of drift-chamber hits in the CDC that are not associated with tracks $\leq$ 150 in each half cylinder. This rejects the events with large number of drift chamber hits due to the beam bursts or electronic noise.

The number of events that are rejected by the last two cuts is less than 0.1 % of the final hadronic dataset. Figure 3.14 shows a typical hadronic event.

The crude selection criteria applied after track finding and before track fitting is found not to reject a significant number of events that pass the final criteria. This was checked by processing a block of events through the final filter without applying the crude filter. In addition, the hardware triggers are redundant enough

$$D^{*+} \rightarrow D^0\pi^+ \rightarrow (K^-\pi^+)\pi^+$$
$$(\Pi)\ (\pi)$$

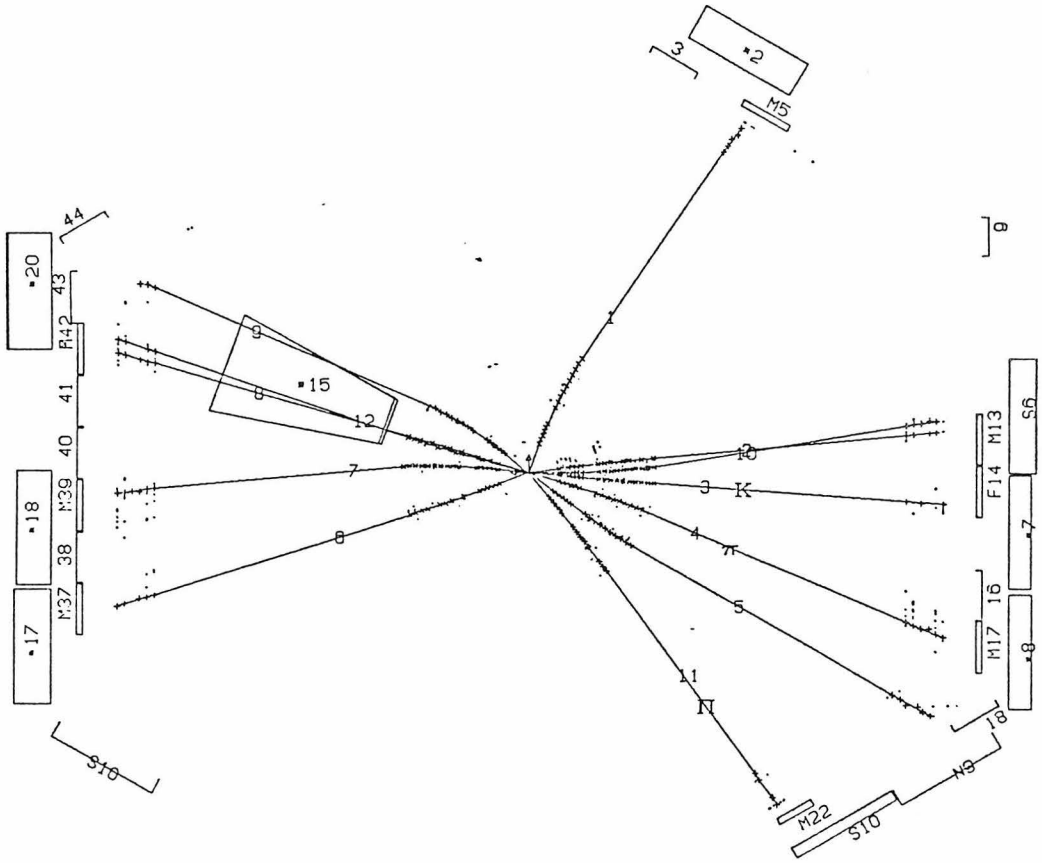

Figure 3.14. The end view of a typical hadronic event. It is typical except that a D^* candidate was found in this event. The decay products of the D^* are labeled on the corresponding tracks.

so that the effect on the final hadronic dataset is negligible. Thus, the final hadron filter described above defines the hadronic dataset.

Figure 3.15(a) shows the distribution of the total visible charged energy. The corresponding distribution for the Monte Carlo dataset is overplotted. The dominant background comes from hadronic two-photon events, where the photon accompanying the incoming electron collides with another photon accompanying the incoming positron [Fig. 3.15(b)]. The spectrum of the photons is given by (2.5), and the cross section for $\gamma\gamma \to q\bar{q}$ varies as $1/W^2$ as in the case of $e^+e^- \to q\bar{q}$, where W is the CM energy of the $\gamma\gamma$ system. These lead to a cross section for the hadronic two-photon events that varies approximately as $1/W^3$. The excess of the data over the Monte Carlo below the cut at 6 GeV/c is due to this source, and the background in the hadronic dataset is estimated to be $(5 \pm 3)\%$.

The effective efficiency of the hadronic filter is defined as the number of hadronic events that pass the filter divided by the number of events that would have been generated if there were no radiative effect. Figure 3.16 shows the spectrum of the initial state radiation (Monte Carlo) before and after the hadronic filter. In the Monte Carlo generation, there is an artificial cutoff on k at the high end. However, the efficiency defined as above is independent of the cutoff as long as the curve b in Fig. 3.16 vanishes below the cutoff, which is indeed the case. The Monte Carlo generates 1.308 times the number of events that would have been generated without the radiative correction, and 60.0% of them pass the hadronic filter. Thus, the effective efficiency of the hadronic filter estimated by the Monte Carlo simulation is thus $60 \times 1.308 = 78.5\%$.

3.6 Monte Carlo Simulation

For a detector as complicated as DELCO, a detailed Monte Carlo simulation of the detector responses is necessary to estimate various efficiencies. We have already encountered an example in the previous section when the efficiency of the hadron

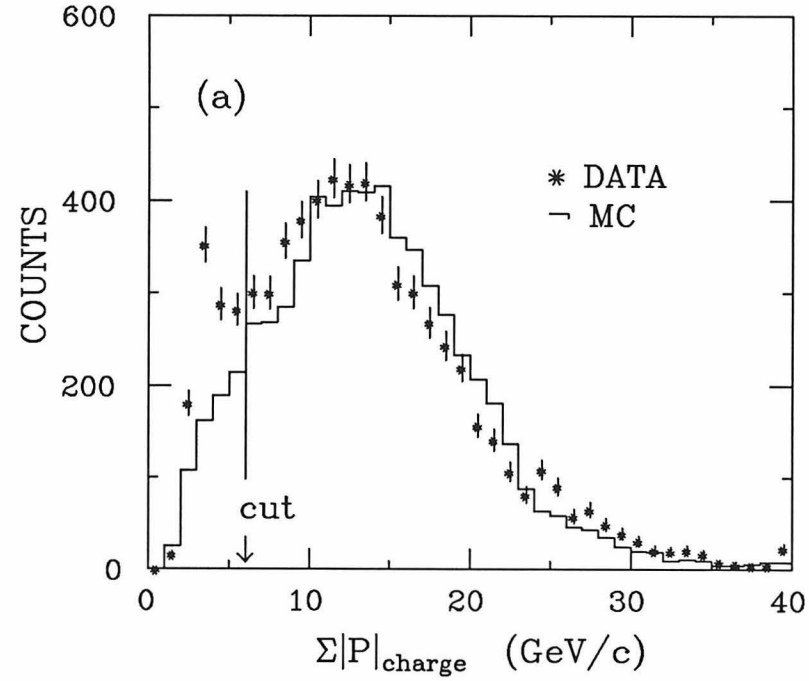

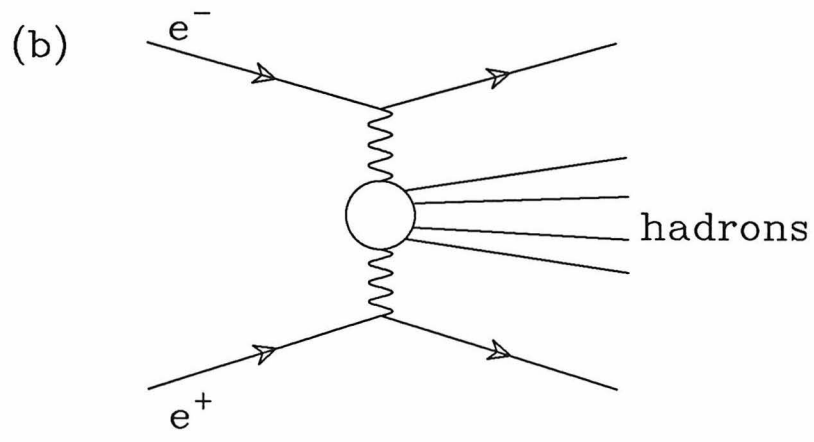

Figure 3.15. (a) The distribution of the visible charged energy per event right before the charged energy cut is shown for the data and the Monte Carlo dataset. The position of the cut is indicated by the arrow. (b) The diagram for the two-photon hadron production which is the primary source of the background.

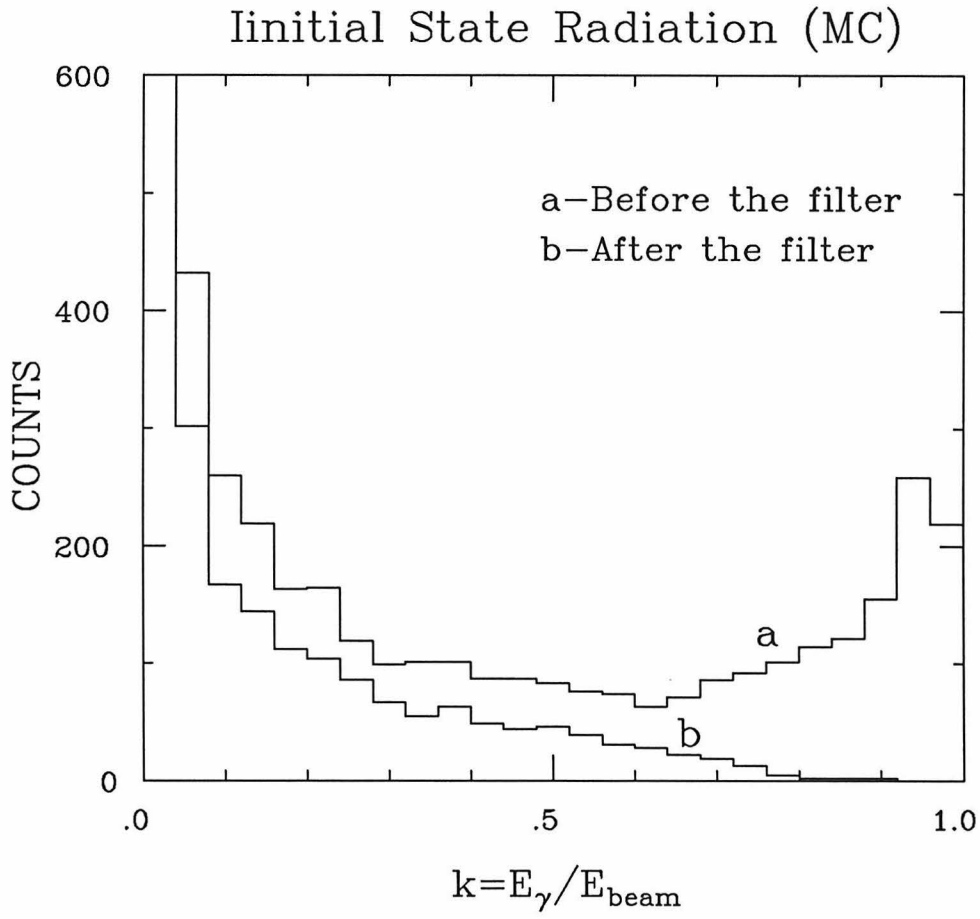

Figure 3.16. The energy distribution of the initial-state photon before and after the hadronic filter. When the energy of the radiation is large, the event is unlikely to pass the filter mostly due to the visible charged energy cut.

filter was estimated. In this section, the Monte Carlo simulation of hadronic events is described.

The hadronic event generator is the LUND Monte Carlo program, and its main features have already been described earlier. However, a few modifications have been made. First, initial-state radiation has been added according to the formula (2.7). Second, the heavy quark fragmentation functions have been adjusted to give momentum distributions consistent with existing data. In addition, the branching fractions of charmed and bottom hadrons have been updated.

The event origin is distributed according to the known beam shape, and each of the final particles of the event is swum through the detector. The photons are traced until they convert to e^+e^- pairs or hit one of the shower counters or exit the detector. The charged particles are traced through the detector using the Runge-Kutta integration of the equation of motion in the non-uniform field. Multiple Coulomb scattering and energy loss due to the ionization are also simulated. The tracing is stopped when the charged particle exits the detector or loses all of its energy in the detector. The decays in flight for the strange, charmed, and bottom hadrons are included except for $K^{\pm}$'s and K_L's. The charged pions are assumed stable.

The drift-chamber hits are generated by calculating the distances of closest approach to the sense wires. The time-to-distance relations are nearly linear, but there are small deviations. The drift cells in the PDC are flat, and the drift distance is not simply the distance of closest approach from the sense wire to the track. These effects are also simulated. The wire-hit resolutions and inefficiencies as well as noise hits are also included in accordance with observation.

The simulation of the Čerenkov counter involves the curvature effect (Fig. 3.8), the crosstalk between cells, and the effect of the small gaps between the mirrors. It does not employ ray-tracing simulation for each event, but the result of the ray-tracing simulation is parametrized and incorporated.

The result of these simulations is stored in the same common blocks used for

the regular events, and the same subsequent analysis is performed on the simulated data.

Figure 3.17 and Figure 3.18 show the comparison between the hadronic dataset and the Monte Carlo simulated dataset after the hadron filter. The thrust parameter, T, is defined by

$$T \equiv \max_{\mathbf{n}} \frac{\sum_i |\mathbf{P}_i \cdot \mathbf{n}|}{\sum_i |\mathbf{P}_i|},$$

where the maximum is taken by varying the direction of the unit vector $\mathbf{n}$. When an event is spherical, the value of T is close to its minimum 0.5, and when it is pencil-like, the value of T is close to its maximum 1. When the number of tracks becomes large, the conventional calculation of T becomes prohibitive. We have used an efficient algorithm[160] that is about 10^6 times faster for $N_{\rm trk} \sim 30$. The greater the number of charged tracks and the higher the thrust, the more will tracks tend to overlap in the detector elements. The distributions of the track momenta and the transverse momenta with respect to the jet axis are shown in Fig. 3.18. The agreement between the data and the Monte Carlo simulation is reasonable.

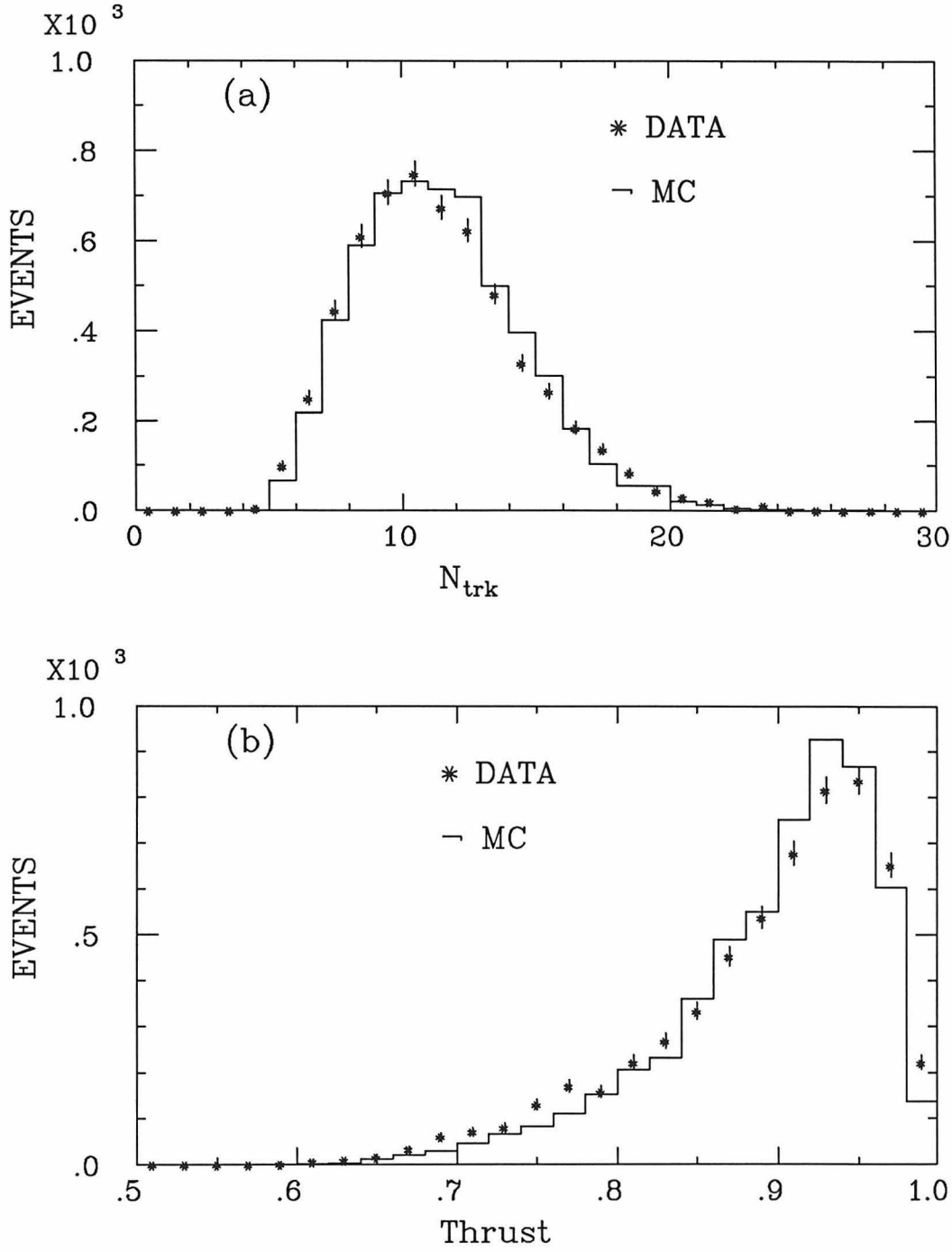

Figure 3.17. Comparison of the data and the Monte Carlo simulation after the hadron filter. (a) The number of observed charged tracks. (b) The thrust parameter.

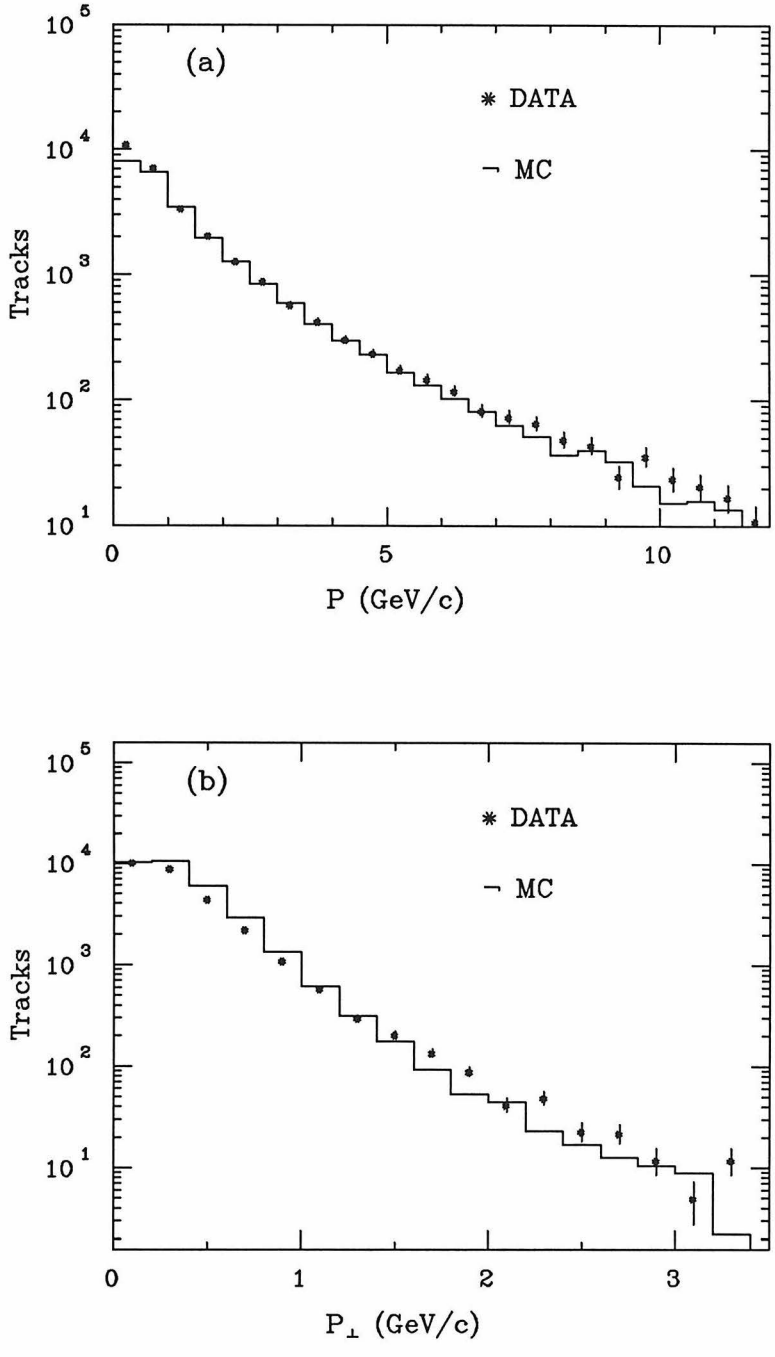

Figure 3.18. Comparison of the data and the Monte Carlo simulation after the hadron filter. (a) The momenta of charged tracks. (b) The transverse momenta of charged tracks with respect to the jet axis.

Chapter 4.

D^* Production Cross Sections

4.1 INTRODUCTION

In this chapter, I will describe the selection of D^* candidates and the determination of the production cross section as a function of the D^* momentum. The physics we wish to obtain is the total D^* production cross section, the charm fragmentation function, and the forward-backward asymmetry of the $c\bar{c}$ production. We will start from an overview of the strategy.

4.2 STRATEGY

The low Q value, 5.8 MeV/c^2, of the charged D^* decay mode,

$$D^{*+} \rightarrow D^0 \pi^+_{D^*}$$

has been exploited extensively as a signature to identify it in various experiments.[161–167] (The subscript 'D^*' attached to the pion is to distinguish it from the pion(s) in the D^0 decay. Also, charge conjugate states are implied in the following unless stated otherwise.) When the mass difference $M_{D^*} - M_{D^0}$ is plotted for the D^* candidates, the small Q value suppresses the combinatorial background in the signal region. Equivalently, the velocity vectors of the D^0 and $\pi^+_{D^*}$ are similar both in magnitude and direction; thus, for a given D^0 candidate, there is a limited phase space to search for the true $\pi^+_{D^*}$ track.

We will study D^0's in the decay mode

$$D^0 \rightarrow K^- \pi^+ X,$$

where X is nothing or typically a π^0 which we do not detect. The Čerenkov counter is used to select the candidates for either the kaon or the pion from the D^0 decay. These tracks are called 'leading' tracks since their momenta are required to be greater than the pion Čerenkov threshold and are usually the fastest track coming from each D^* candidate. A leading track is combined with another track of opposite sign ('nonleading' track) to form a D^0 candidate which is then combined with a π_{D^*} candidate to form a D^* candidate.

When the charge sign of the π_{D^*} candidate is opposite to the charge sign of the kaon candidate, the combination is called 'right-sign', and 'wrong-sign' if not. The D^* signal will appear as an enhancement of the right-sign sample over the wrong-sign sample. By comparing the two, the amount of background can be estimated in a self calibrating way. Thus, the K/π separation by the Čerenkov detector not only reduces the random combinatorial background, but also is crucial in estimating the amount of the background.

4.3 Selection of D^* Candidates

A D^* candidate consists of three charged tracks: a leading track, a nonleading track, and a π_{D^*} candidate track. First, we will select the leading track sample using the Čerenkov information, then each of them is combined with two more tracks to form a D^* candidate.

4.3.1 Selection of Leading Track Candidates

The leading tracks are the tracks that are selected by the Čerenkov identification criteria, and they are either kaon candidates or pion candidates. The idea for selecting kaon candidates is as follows. If the momentum of a track is well

above the pion threshold (2.6 GeV/c), the number of photoelectrons expected for a pion is 13 to 23 depending on the path length. Therefore, the probability of a pion giving no photoelectrons is very small, and the lack of the response can be used to identify heavy particles. This is even true for multiple hit cells, since any particle that emits Čerenkov light contributes to the detection inefficiency but not to the contamination in the kaon sample. On the other hand, pion candidates are selected by requiring Čerenkov response for the tracks with momenta between the pion threshold and the kaon threshold.

First, each candidate for a leading track is required to meet the following criteria in order to ensure good momentum resolution and to reject trivial background tracks:

1. The number of hits in the central tracking chambers (IDC and CDC) must be at least 9 out of 16 total, and the number of hits in the outer tracking chambers (PDC) must be greater than or equal to 2 out of 6 total.
2. The χ^2 per degree of freedom (n_d) of the track fit is required to be less than 3.0.
3. The distance of closest approach to the beam axis measured by the beam position monitor (b) must be less than 3 mm, and the z coordinate of the corresponding point on the track (z^0) must be within ± 4 cm of the center of the expected interaction point distribution.

The first two cuts are loose and designed to reject tracks that are mistracked. The third cut is not stringent, either. Figure 4.1 shows the distribution of the track origin, b and z^0, right before the cuts are made. The impact parameter has a long tail that contains mostly the decay products of strange particles and other unwanted tracks such as the result of nuclear interactions at the beam pipe region. Also, the tracks that are mistracked tend not to point back to the beam axis. The lifetime of D^0 is, as we will see later, small enough so that the inefficiency caused by this cut is negligible.

We define a kaon candidate to be a track that satisfies the following criteria in

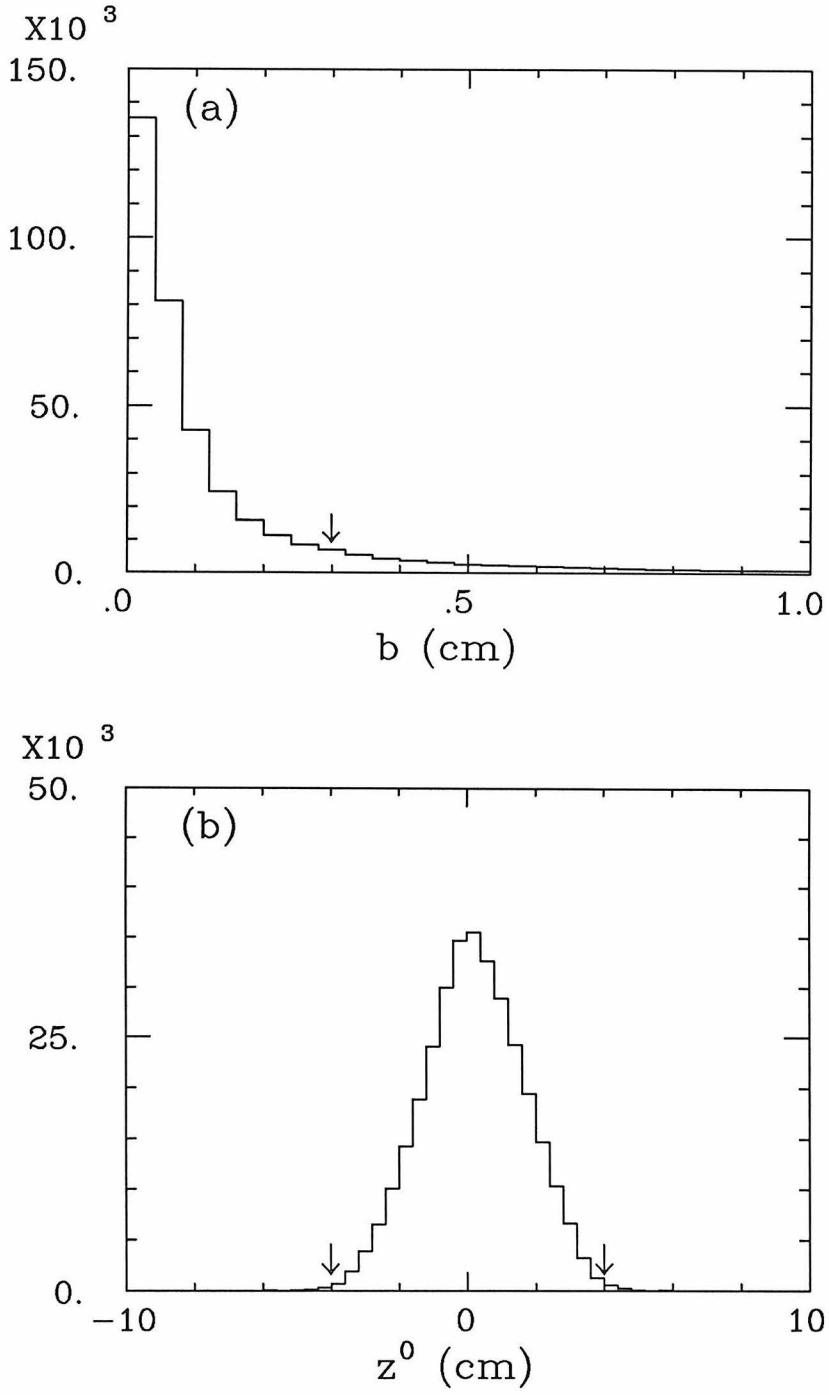

Figure 4.1. Distribution of the track origin, b and z^0, for general tracks in hadronic events. The impact parameter to the beam axis, b, is shown in (a), and z coordinate of the track origin, z^0, in (b). The arrows indicate the location of the cuts. These are a part of the track quality cuts used for all the tracks that form a D^* candidate.

addition to the track quality cuts above;

1. The momentum of the track must be greater than 3.2 GeV/c ($\approx 3\sigma$ above the pion threshold in order to minimize misidentifications due to momentum smearing).
2. The number of photoelectron (normalized to the quality factor of 100 and the path length of 100 cm) recorded in the Čerenkov cell traversed by the track must be less than 0.5. This causes a cell with the single photoelectron noise to be rejected. As we have seen, however, this noise occurs only 1% of the time, and it is random; thus, it does not impair the kaon detection efficiency.

The Monte Carlo is used to estimate the fractions of particles in the kaon sample, and the results are given in Table 4.1. I note that about 30% of the kaon sample are actually protons;[168] however, this misidentification only increases the amount of random combinatorial background, and does not affect the right-sign wrong-sign analysis. The pion contamination is due to momentum errors which occasionally result in pions below Čerenkov threshold being wrongly included in the sample.

Table 4.1. Monte Carlo estimation of the particle fractions in the kaon sample.

	e	μ	π	K	P
fraction(%)	0.0	0.1	6.1	63.3	30.5

A leading pion candidate is defined to be a track that satisfies following requirements in addition to the track quality cuts;

1. The momentum of the track greater than 2.6 GeV/c and less than 9.2 GeV/c.
2. The number of photoelectrons (normalized to the quality factor of 100 and the path length of 100 cm) greater than 3.0.
3. The timing of hits is required to be within ± 1.5 ns.

4. There is no other track with a momentum greater than 2.6 GeV/c entering the same cell.
5. There is no track that is one of the pair of a gamma conversion candidate entering the same cell.

The minimum momentum cut of 2.6 GeV/c is lower than the 3.2 GeV/c cut used for the selection of kaon candidates. This is because the requirement of positive Čerenkov response ensures that kaons do not significantly contaminate the pion sample. The maximum momentum cut corresponds to the kaon threshold above which kaons emit Čerenkov light and thus not separable from pions. The cut value for the number of photoelectron is chosen to be above the single photoelectron noise in order to avoid the cells with the noise imitating pion signals. Finally, the last two cuts require that there are no other particles within a cell that are likely to emit Čerenkov light.

Table 4.2 shows the fraction of particles in the pion sample estimated by the Monte Carlo. The kaon contamination is only 2% and is mostly due to the high momentum kaons that are above the kaon threshold but are mismeasured to be below 9.2 GeV/c. There are leptons in the sample at 7% level; however, as in the case of protons in the kaon sample, their effect is only to increase the random background.

Table 4.2. Monte Carlo estimation of the particle fractions in the pion sample.

	e	μ	π	K	P
fraction(%)	3.5	3.2	90.7	2.1	0.5

4.3.2 Construction of $D^{*\pm}$ Combinations

No Čerenkov information is used to select the nonleading and π_{D^*} candidate tracks. Table 4.3 summarizes the cuts applied to individual tracks and the average number of tracks per event that pass each set of cuts. The cuts are tighter for

the leading tracks and the π_{D^*} candidates, which define whether a D^* candidate is right-sign or wrong-sign, than for the nonleading tracks.

Table 4.3. Cuts made to individual tracks of D^* candidates. Average number of tracks per event that pass the cuts are listed at the bottom.

track type	leading K	leading π^*	nonleading	π_{D^*}
quality cuts				
# IDC,CDC hits	$\geq$9	$\geq$9	$\geq$9	$\geq$12
# PDC hits	$\geq$2	$\geq$2	—	—
χ^2/n_d	<3.0	<3.0	<3.0	<3.0
b(cm)	<0.3	<0.3	<0.3	<0.3
$\|z^0\|$(cm)	<4.0	<4.0	<4.0	<4.0
Čerenkov				
momentum(GeV/c)	$P > 3.2$	$2.6 < P < 9.2$	—	—
# photoelectron	< 0.5	> 3.0	—	—
time (ns)	—	$-1.5 < t < 1.5$	—	—
< #/event>	0.19	0.33	7.9	6.6

* In addition, it is required that the cell contains no other tracks with $P > 2.6$ GeV/c and no track that is identified as one of a pair of a gamma conversion.

Each of the leading track candidates is combined with a nonleading track candidate of *opposite charge sign* that satisfies the following cuts to form a D^0 candidate;

1. The cosine of the angle between the leading and nonleading tracks, $\cos\theta_{K\pi}$, is greater than 0.4.
2. The invariant mass of the pair, $M_{K\pi}$, is greater than 1.45 GeV/c^2 and less than 2.2 GeV/c^2.

The first cut effectively limits the combinations to be within a jet, and the cut value was chosen using the Monte Carlo so that the inefficiency caused by this cut is negligible. When the leading track is a kaon candidate (we call it K-mode), the invariant mass is calculated by assigning the kaon mass to the leading track and

the pion mass to the nonleading track. When the leading track is a pion candidate (π-mode), the mass assignments are inverted accordingly. Figure 4.2 shows the invariant mass distributions for the K-mode and π-mode combinations right before the invariant mass cuts (indicated by the arrows). The nominal D^0 mass[70] is 1.865 GeV/c^2. At this stage, the distributions are dominated by random backgrounds.

Each of the D^0 candidates is then combined with any of π_{D^*} candidates in the same event, and a combination is defined to be right-sign when the charge sign of the kaon candidate is opposite to that of the π_{D^*} candidate, and wrong-sign if not. Figure 4.3 shows the mass difference $\Delta M \equiv M_{K\pi\pi_{D^*}} - M_{K\pi}$ vs the sine of the opening angle between the D^0 candidate and the π_{D^*} candidate ($\sin\theta_{D\pi}$). An alternative is to constrain the $K\pi$ mass to the nominal D^0 mass, but the improvement is found to be negligible. The plots are shown separately for the K-mode and π-mode candidates, as well as for the right-sign and wrong-sign combinations. Because of the low Q value of $D^{*\pm}$ decay, the signal region is the region of small $\sin\theta_{D\pi}$ and small ΔM. The nominal value of the mass difference is 0.1454 GeV/c^2,[70] and $\sin\theta_{D\pi}$ is found to be less than 0.13 by the Monte Carlo. One can see an enhancement in the signal region for the right-signs over the wrong-signs in each mode.

The ΔM distributions after the cut $\sin\theta_{D\pi} < 0.13$ are shown in Figure 4.4. The ΔM resolution is consistent with what is expected from the Monte Carlo. We define the $D^{*\pm}$ candidates to be the ones with ΔM less than 0.1625 GeV/c^2. To summarize, the cuts applied to the combinations of D^0 and π_{D^*} candidates are;

1. The sine of the angle between the D^0 and π_{D^*} candidates, $\sin\theta_{D\pi}$, be less than 0.13.
2. The mass difference, ΔM, be less than 0.1625 GeV/c^2.

Before the numbers of final candidates are quoted, multiple solutions have to be resolved when more than one $D^{*\pm}$ candidate is found in a jet. We group together the $D^{*\pm}$ candidates in a event whose π_{D^*} candidate track belong to a same jet, where the jets are defined by dividing the tracks of an event into two groups by a

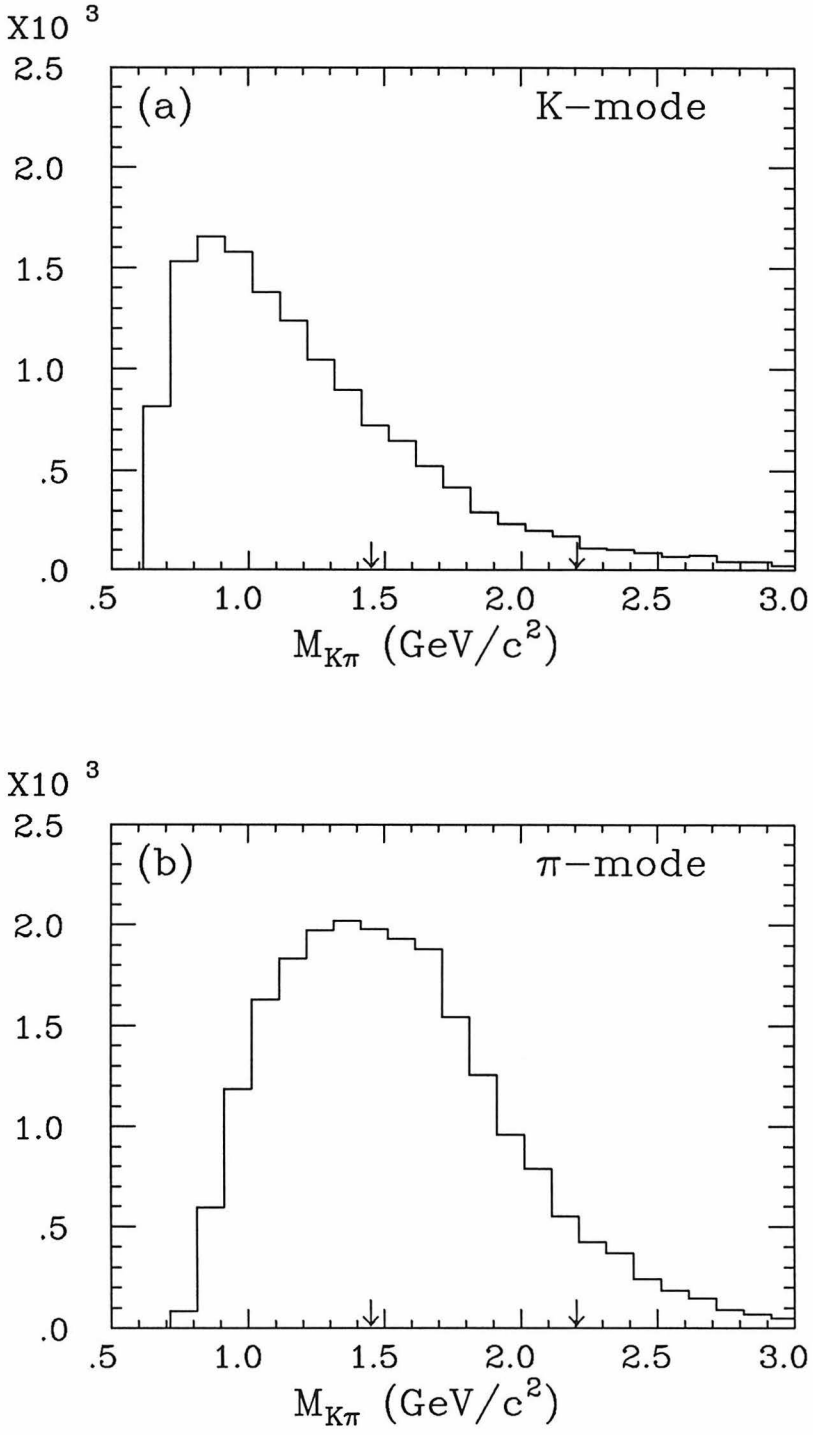

Figure 4.2. Invariant mass distribution of K-π pairs for K-mode (a), and π-mode combinations (b). The arrows indicate the accepted range for the D^0 candidates.

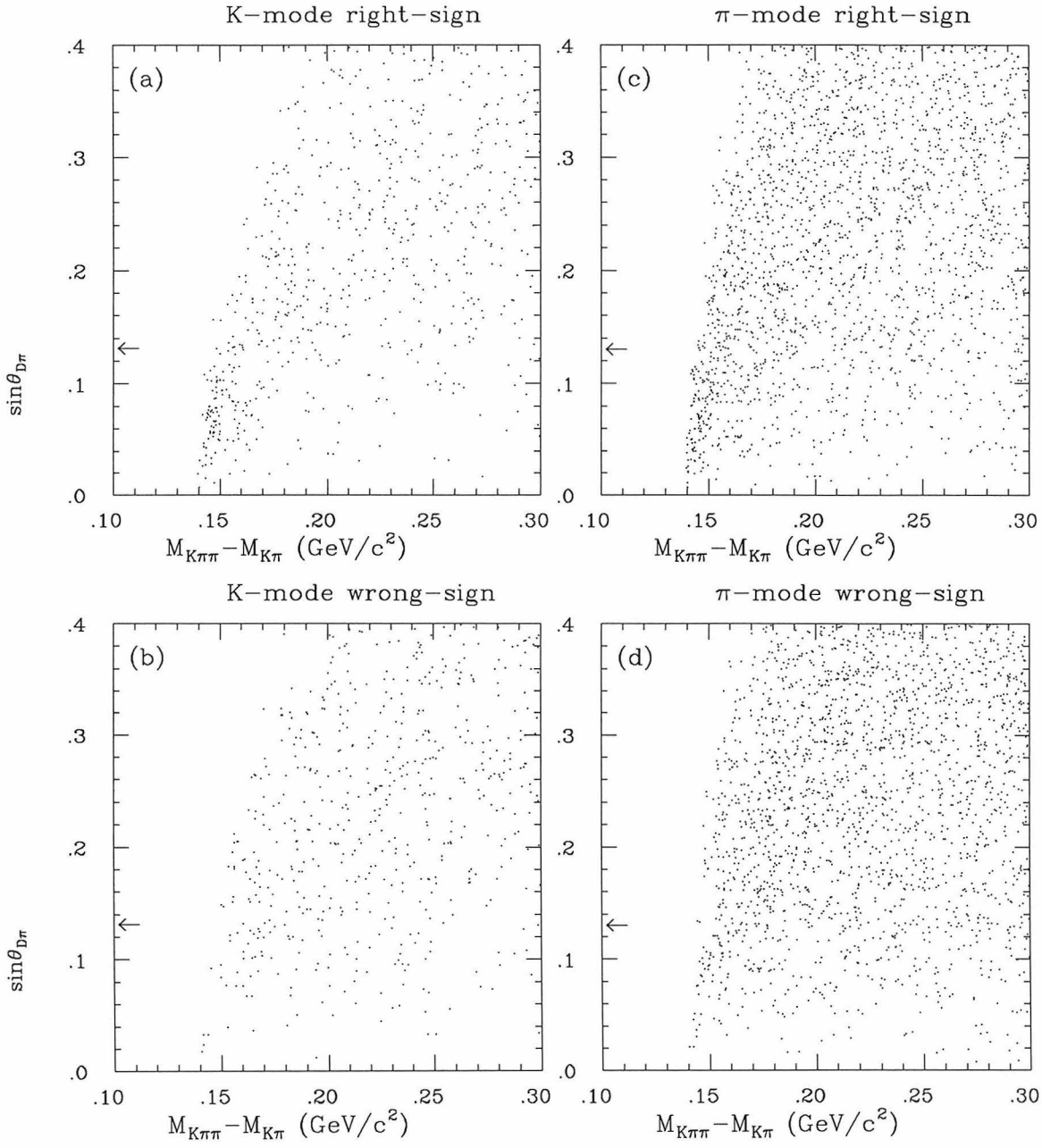

Figure 4.3. ΔM vs $\sin\theta_{D\pi}$ for the K-mode right-signs (a), K-mode wrong-signs (b), the π-mode right-signs (c), and π-mode wrong-signs. For each mode, there is a clear enhancement for the right-sign sample in the region of small $\sin\theta_{D\pi}$ and small ΔM. The arrows show the position of $\sin\theta_{D\pi}$ cut.

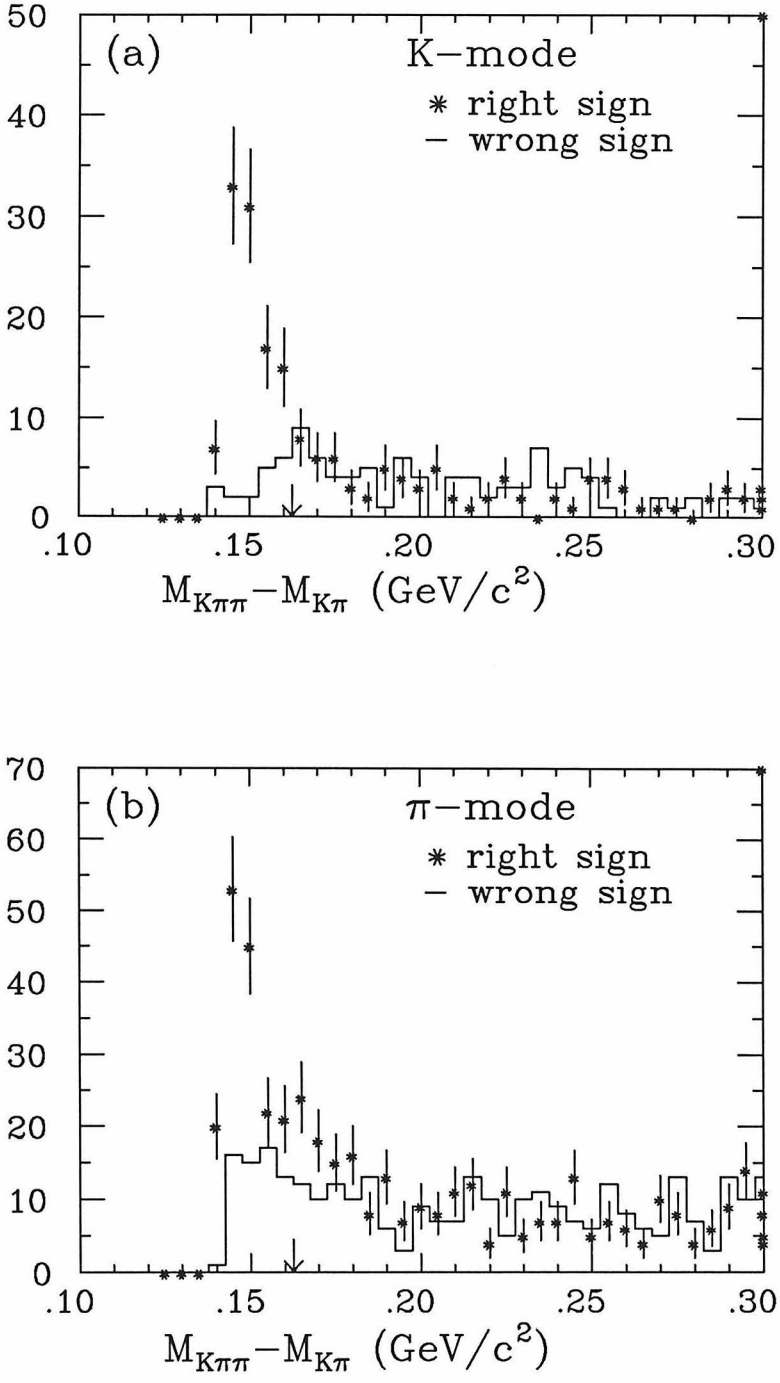

Figure 4.4. ΔM distributions after the cut $\sin\theta_{D\pi} < 0.13$ for K-mode (a) and π-mode candidates. The distributions for the wrong-sign combinations (histogram) are plotted over those for the right-signs (points with error bars). The arrows show the position of ΔM cut which defines the D^* signal region.

plane that is perpendicular to the thrust axis. When a group has more than one candidate, it is found that they typically share the π_{D^*} track or the leading track, in which case they do not correspond to genuinely multiple D^*'s. Thus, when the number of $D^{*\pm}$ candidates in a group is more than one, the one with ΔM closest to the nominal value is selected. After the multiple solutions are resolved, there are 14 events that belong to both the K-mode and π-mode. All of these are in the right-sign samples and they are counted in both modes. Table 4.4 summarizes the numbers of $D^{*\pm}$ candidates before and after the multiple solutions are resolved.

Table 4.4. Numbers of $D^{*\pm}$ candidates in the K-mode and π-mode samples (data) before and after the multiple solutions are resolved.

	with multiples		multiples resolved	
	K-mode	π-mode	K-mode	π-mode
right-sign	103	161	97	139
wrong-sign	18	62	15	51

In order to check if there is any other effects that may create the enhancement of the right-sign sample over the wrong-sign sample, the standard hadronic Monte Carlo events which contained no $D^{*\pm}$ are analyzed with the same set of cuts as the real data. Table 4.5 shows the resulting numbers of $D^{*\pm}$ candidates. There is no indication of enhancement of the right-sign sample over the wrong-sign sample either in the K-mode nor in the π-mode. Thus, we do not expect any source other than $D^{*\pm}$ which can produce the observed right-sign enhancement.[169]

Table 4.5. Numbers of $D^{*\pm}$ candidates for the Monte Carlo dataset that contains no $D^{*\pm}$. Multiple solutions are resolved. No significant enhancement of the right-sign samples are seen.

	K-mode	π-mode
right-sign	89	237
wrong-sign	97	222

4.4 Estimation of $D^{*\pm}$ Production Cross Sections

Since the background is expected to contribute similarly to the right-sign sample and the wrong-sign sample, we are interested only in the difference between the two samples. Accordingly, the detection efficiency is defined by how much of the true D^*'s contribute to the difference. It should be noted that the amount of the wrong-sign sample does not directly indicate the amount of the non-D^* background; for the D^0 decay modes such as $K^-K^+(X)$ and $\pi^-\pi^+(X)$ will contribute to both the right-sign and wrong-sign samples by the same amount. Here, we are not concerned about how much of the candidates are really D^*'s. We will address this question in the next chapter when we measure the D^0 lifetime.

The detection efficiency is estimated by the Monte Carlo simulation. However, the D^* signal obtained in the previous section contains D^0 decay modes other than the $K^-\pi^+$ mode. Thus, the D^0 branching fractions in the Monte Carlo should be consistent with reality in order to obtain the correct detection efficiency. Also, the performance of the Monte Carlo needs to be checked against the data, and an adjustment must be made if there is a significant difference,

4.4.1 D^0 Branching Fractions in the Monte Carlo

The D^0 branching fractions are adjusted to match the present knowledge as close as possible. Table 4.6 shows the branching fractions used compared with the measurements by the SLAC-LBL Magnetic Detector collaboration (referred to as MARK-I),[170] by the MARK-II collaboration,[171] the MARK-III collaboration,[172] and the values quoted by the Particle Data Group.[70] The Monte Carlo values listed in the table are obtained by actually generating D^0 decays and counting the occurrences of each decay mode. This was necessary because the LUND generator generates charm decays by a jet-like generation scheme rather than by a long list of explicit decay modes. The branching fractions used in the Monte Carlo are

consistent with the measurement values, but uncertainties in the measurements are quite large.

Table 4.6. Comparison of the D^0 decay branching fractions used in the Monte Carlo and the measurements. The value of σ_{D^0} used is also listed for each experiment.

decay mode	MC(%)	MK-I(%)	MK-II (%)	MK-III (%)	PDG (%)
$K^-\pi^+$	3.0	2.2 ± 0.6	3.0 ± 0.6	$3.7 \pm 0.6 \pm 0.7$	2.4 ± 0.4
$K^-\pi^+\pi^0$	9.7	12 ± 6	8.5 ± 3.2	$7.1 \pm 1.2 \pm 1.7$	9.3 ± 2.8
K^-+anything	42.7	35 ± 10	55 ± 11	—	44 ± 10
K^-K^+	0.27	—	0.34 ± 0.11*	$0.46 \pm 0.10 \pm 0.09$*	0.27 ± 0.08
σ_{D^0} (nb)	—	11.5 ± 2.5	$8.0 \pm 1.0 \pm 1.2$	$7.5 \pm 1.1 \pm 1.2$	—

* Calculated from $\mathrm{Br}(K^-K^+)/\mathrm{Br}(K^-\pi^+)$ quoted in the paper and their own value of $\mathrm{Br}(K^-\pi^+)$.

Only the decay modes that contain a charged K are included in the table. As we will see later, other decay modes do not contribute to the difference between the right-sign sample and the wrong-sign sample. The K^-K^+ mode does not contribute to the difference, either, and is included here for a later reference.

It is worth noting that the measured values for the branching fractions in the table were obtained from data collected in the reaction $e^+e^- \rightarrow \psi'' \rightarrow D^0\overline{D}^0$ [except for $\mathrm{Br}(K^-K^+)/\mathrm{Br}(K^-\pi^+)$ by MARK-II]. Since the actual measurement is done on the quantity $\sigma_{D^0}\cdot\mathrm{Br}(D^0 \rightarrow X)$, the branching ratios are inversely proportional to the D^0 production cross section σ_{D^0} used in the calculation. The values used are 11.5 nb, 8.0 nb, and 7.5 nb for MARK-I, MARK-II, and MARK-III, respectively. It can be seen from the table that the discrepancies of the branching ratios are largely due to the differences in the D^0 production cross sections. The MARK-III collaboration also has tried a different method that does not depend on the D^0 production cross section,[172] which is to compare the number of doubly tagged events [e.g., $\psi'' \rightarrow (K^-\pi^+)_{D^0}(K^+\pi-)_{\overline{D}^0}$] to that of singly tagged events [e.g., $\psi'' \rightarrow (K^-\pi^+)_{D^0}$ + anything, and its charge conjugate]. They report a

substantially larger branching fraction, $4.9 \pm 0.9 \pm 0.5\%$, for the $K^-\pi^+$ decay mode. This corresponds to the D^0 production cross section of $5.7 \pm 1.1 \pm 0.9$ nb, which is not consistent with the value used by MARK-I, and substantially smaller than the values used by MARK-II and MARK-III. Therefore, if the value 5.7 nb turns out be the correct value, all the experimental values in the table have to be increased accordingly. However, the ratios between the different decay modes are more reliable.

4.4.2 Contributions from Various D^0 Decay Modes

The contributions from four types of decay modes, $K^-\pi^+$, $K^-\pi^+\pi^0$, K^-X (excluding the first two, and X does not contain any K^+) and modes with no charged kaons, are estimated using the Monte Carlo simulation, and the results are shown in Figure 4.5 and Figure 4.6 as functions of the pair mass $M_{K\pi}$. As can be seen in the figures, when there is no charged kaons among D^0 decay products the difference between the right-sign and wrong-sign samples is consistent with zero for both the K-mode and the π-mode. Also, the pair mass peaks at the nominal D^0 mass of 1.865 GeV/c^2 for the $K^-\pi^+$ mode, while they populate lower mass regions for other modes.

The $D^0 - \overline{D}^0$ mixing can dilute the right-sign enhancement. However, the mixing rate is expected to be very small in the standard model of Weak and Electromagnetic interactions ($\lesssim 10^{-3}$), and the mixing effect is assumed to be negligible in this chapter. An upper limit on $D^0 - \overline{D}^0$ mixing will be set in a subsequent chapter using our data.

The only decays modes that are not included in the table are those that contain a K^+,i.e., a wrong-sign kaon. The contribution from these decay modes is found to be dominated by the K^-K^+ decay mode, which gives an equal number of right-sign and wrong-sign candidates. Therefore, one can conclude that the difference of the right and wrong-sign samples is due to the D^0 decays that contain a K^- and no other charged kaons.

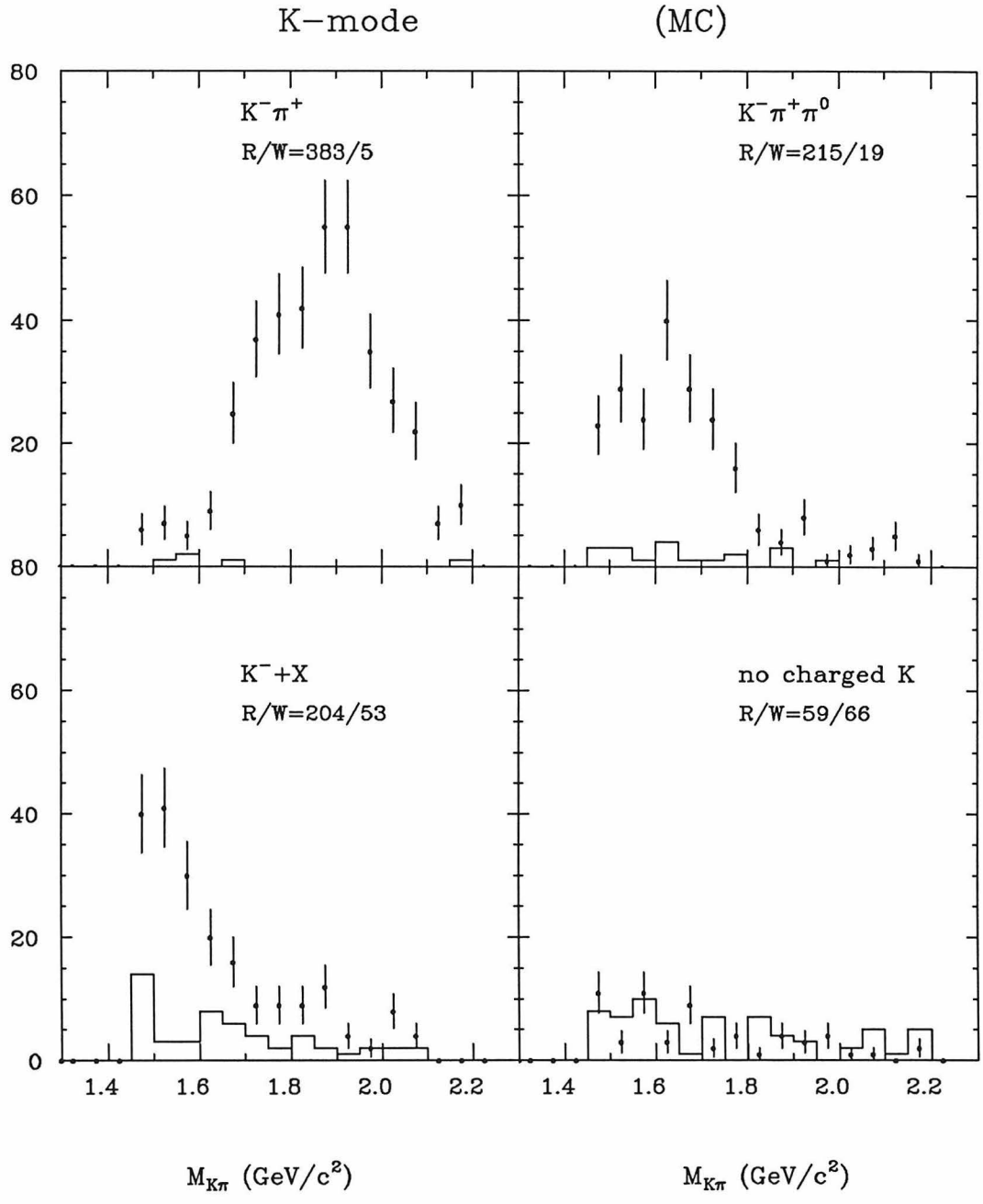

Figure 4.5. Contributions to the K-mode sample from various D^0 decay modes (Monte Carlo) plotted against $M_{K\pi}$. The distributions are taken after all the D^* cuts. In each plot, the wrong-sign distribution (histogram) is plotted over the right-sign distribution (points with error bars). The distribution for the $K^-\pi^+$ mode peaks at the nominal D^0 mass (1.865 GeV/c^2), while for $K^-\pi^+\pi^0$ and K^-X it peaks at lower values.

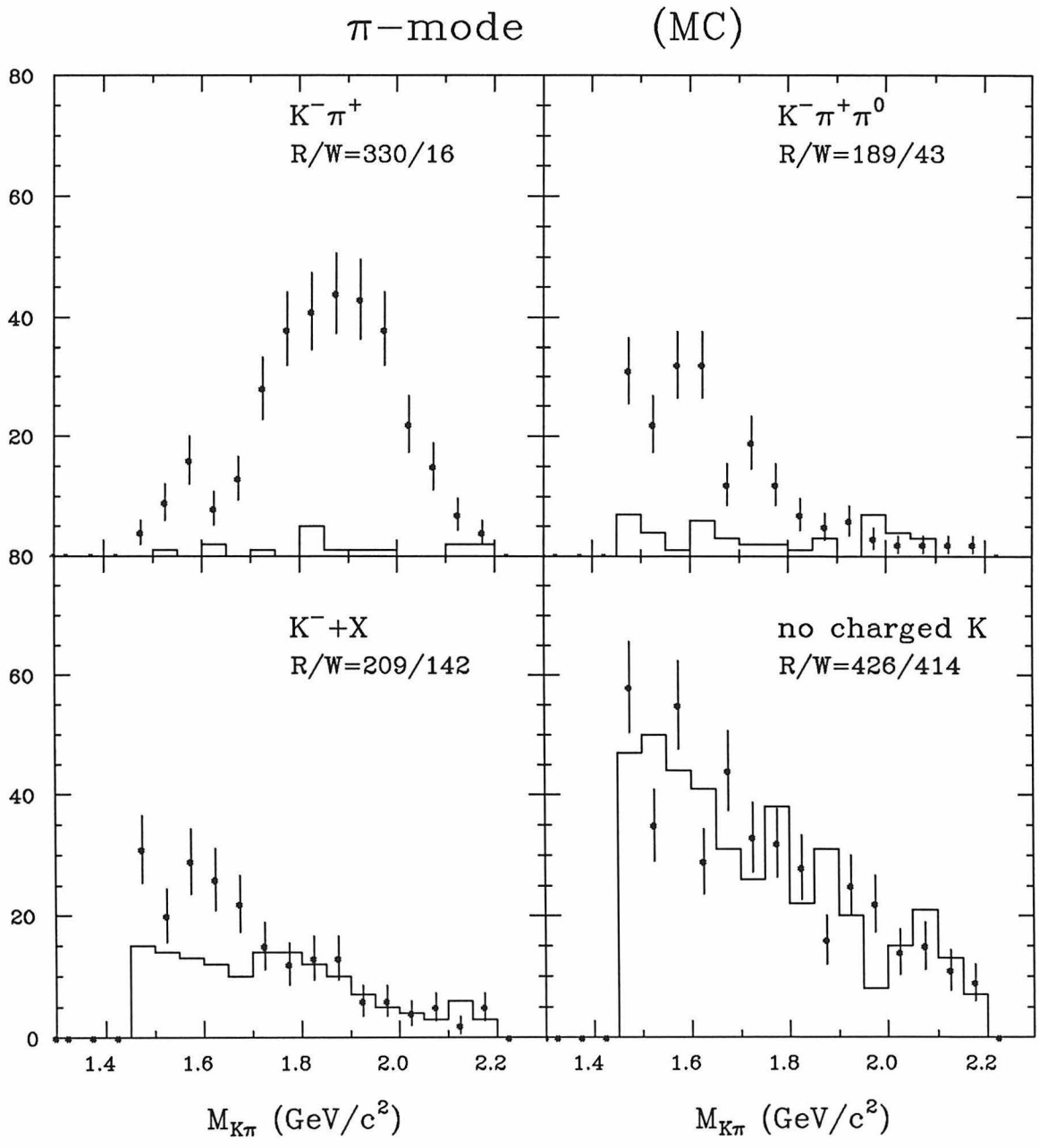

Figure 4.6. Contributions to the π-mode sample from various D^0 decay modes (Monte Carlo). In each plot, the distribution for the wrong-sign combinations (histogram) is plotted over that for the right-sign combinations (points with error bars). Decay modes with no charged K do not contribute to the difference between the right-sign sample and the wrong-sign sample.

There is an effect by which a $K^-\pi^+\pi^0$ can fake a $K^-\pi^+$ mode when only charged tracks are detected. The decay mode $K^-\pi^+\pi^0$ is known to be dominated by decays with a pseudoscalar meson plus a vector meson as an intermediate state,[171] of which $K^-\rho^+$ is the major component. In such cases the vector meson is in a pure helicity 0 state in the D^0 rest frame due to angular momentum conservation. As a result, the angle between the π^+ and the D^0 in the rest frame of the ρ^+ (helicity angle) is strongly peaked forward and backward. When the π^+ is emitted in the forward direction it carries a large fraction of the ρ^+ momentum thus imitating a $K^-\pi^+$ decay. This angular distribution has been implemented in the Monte Carlo, and Figure 4.7 shows the $K^-\pi^+$ invariant mass distribution for the decay chain

$$D^{*+} \to D^0\pi^+_{D^*}, \quad D^0 \to K^-\rho^+, \quad \rho^+ \to \pi^+\pi^0,$$

where momenta are not smeared. Without the cuts on $\sin\theta_{D\pi}$ and $\Delta M \equiv M_{K\pi\pi_{D^*}} - M_{K\pi}$ (Fig. 4.7 histogram *a*), there are two peaks, one at 1.6 GeV/c^2 and the other at around 0.75 GeV/c^2. The dip between the peaks is a reflection of the dip at 90° in the helicity angle distribution, and absent when the ρ is not polarized. With the cuts on $\sin\theta_{D\pi}$ and ΔM (Fig. 4.7 histogram *b*), the lower peak, which corresponds to the cases where π^+ is emitted backward, almost disappears, and with the $M_{K\pi}$ cut at 1.45 GeV/c^2, only the cases where the π^+ is emitted strongly forward survives. For these events, the loss of the π^0 does not hurt the $\mathbf{P}_{D^*}$ resolution significantly. The $D^{*\pm}$ detection efficiency for this mode is found to increase by 65% when the ρ is polarized compared to the case when the ρ is not polarized.

In the Monte Carlo, the $D^{*\pm}$'s are generated in jets according to a fragmentation function adjusted to match the measured $D^{*\pm}$ momentum distributions. Nonetheless, the results shown above are found to be insensitive to the shape of the fragmentation function.

Figure 4.8. shows the $M_{K\pi}$ distribution of our $D^{*\pm}$ samples. The distribution for the wrong-sign sample has been subtracted from that for the right-sign sample

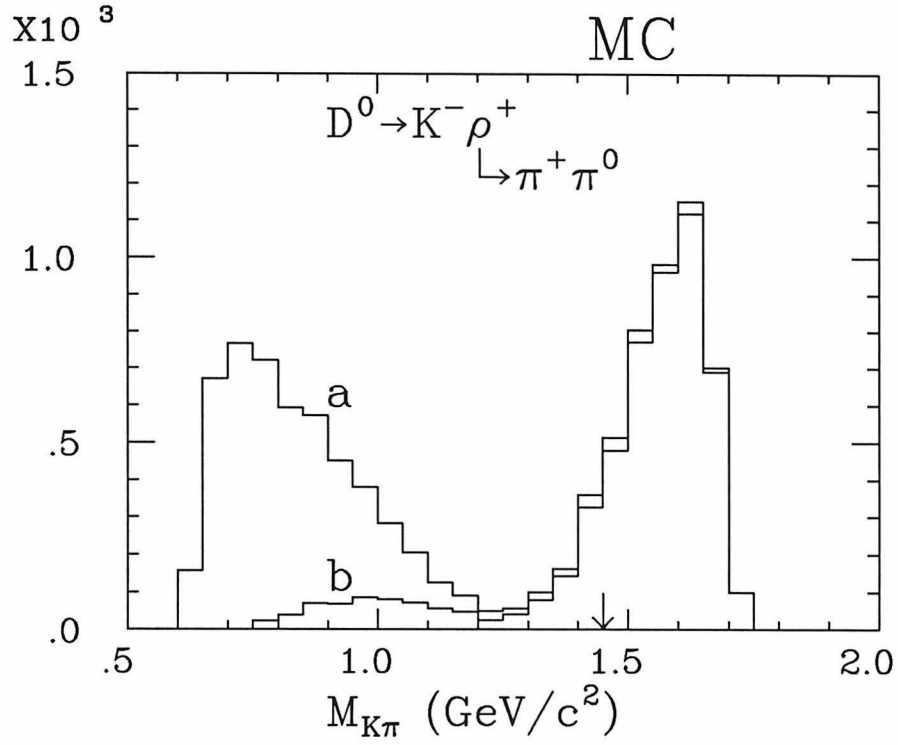

Figure 4.7. $M_{K^-\pi^+}$ distributions for $D^0 \to K^-\rho^+$, $\rho^+ \to \pi^+\pi^0$ where the D^0 is from a D^{*+} decay. No momentum smearing is applied. (a) without any cuts and (b) with ΔM and $\sin\theta_{D\pi}$ cuts. The higher of the two peaks of the histogram *a* corresponds to the cases where the π^+ from the ρ^+ is emitted forward carrying most of the ρ^+ energy; for them, the loss of the π^0 does not significantly worsen the $\mathbf{P}_{D^*}$ resolution. The arrow indicates the pair mass cut used in the analysis.

and what is plotted is the difference. The shape expected from the Monte Carlo (solid curve) is overplotted. They are statistically consistent. From Fig. 4.5 and 4.6, one obtains the estimation of the contribution of each decay modes to the *difference* between the right-sign and wrong-sign samples which is summarized in Table 4.7.

4.4.3 D^* Momentum Correction

Except for the $K^-\pi^+$ decay mode, not all of the decay products of D^0 are detected. When there is a missing track(s), the sum of the measured momenta of the leading, nonleading, and π_{D^*} tracks are on the average smaller than the true D^* momentum. The fraction of the candidates for which there is a missing track(s) is, as can be seen in Fig. 4.5 and 4.6, a function of $M_{K\pi}$. Thus, we correct the measured D^* momentum, which is a sum of the three measured momenta, by multiplying a correction factor which is a function of $M_{K\pi}$. The correction curve is obtained from the Monte Carlo separately for the K and π-mode. The ratio $P_{D^*}(\text{true})/P_{D^*}(\text{measured})$ is fitted to a second order polynomial(Figure 4.9). The curves for the two modes are similar.

This correction has a side benefit of giving a better D^* momentum resolution for the $K^-\pi^+$ decay mode where all the decay products of a $D^{*\pm}$ are detected. The effect of momentum smearing of each track is such that when $M_{K\pi}$ is higher (lower) than the nominal D^0 mass, then the measured P_{D*} is likely to be overestimated (underestimated). Thus, by making a $M_{K\pi}$ dependent momentum correction, a better P_{D^*} resolution can be obtained. In fact, the average P_{D^*} resolution for this mode improves from 10% to 3% with the correction. The curve crosses 1.0 level at around the nominal D^0 mass for the both modes as expected. In the $M_{K\pi}$ region where the $K^-\pi^+$ and other decay modes overlap, one correction factor is applied to the two different kinds of effects that can distort the D^* momenta, one by the missing particles and the other by the momentum smearings. However, the correction factors for these two effects are found to be the same within the statistical error in the region of significant overlap.

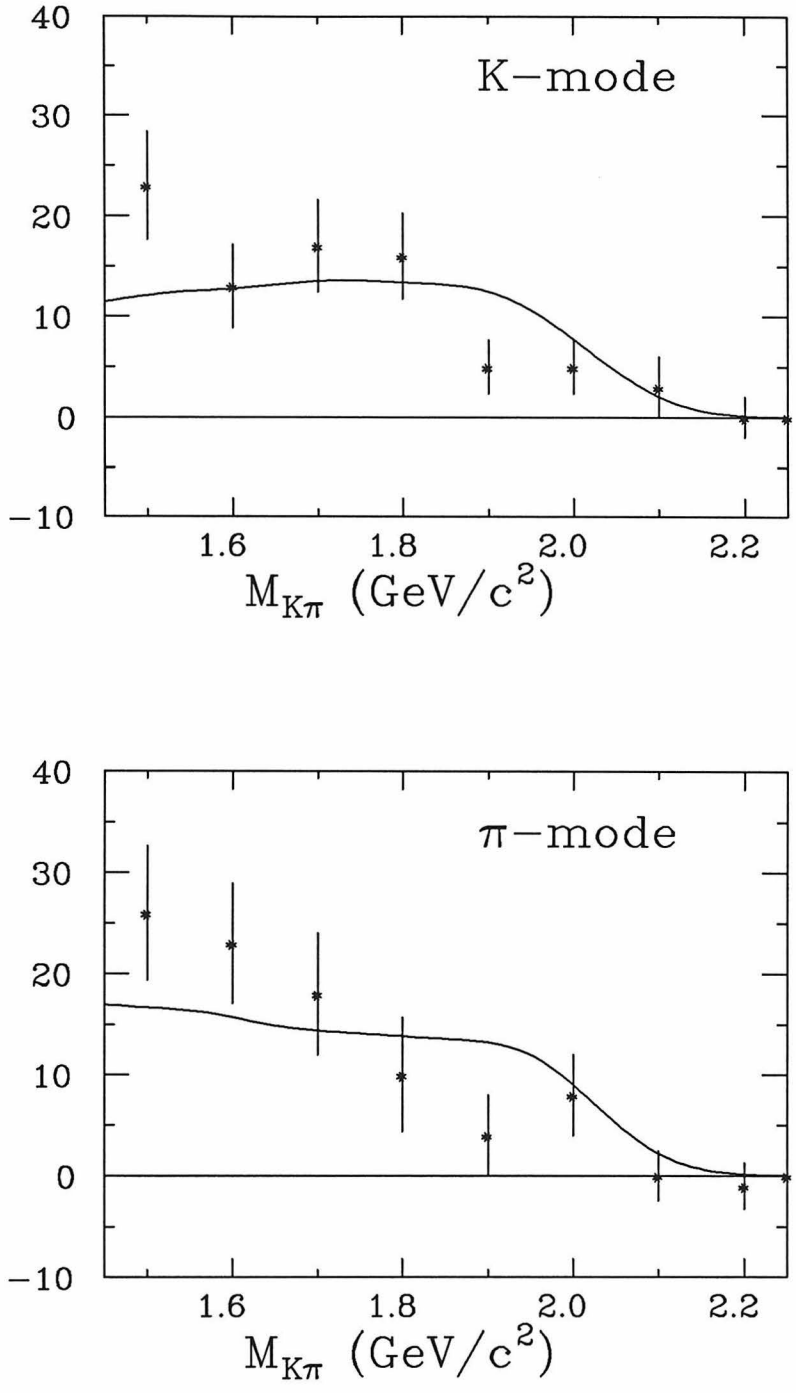

Figure 4.8. The $M_{K\pi}$ distribution in the final $D^{*\pm}$ samples for the K-mode and the π-mode. Each point is the difference between the number of right-sign combinations and that of wrong-sign combinations. The solid curves shows the expected shape from the Monte Carlo.

Table 4.7. Monte Carlo estimation of the contribution of various D^0 decay modes to the difference of the right-sign and wrong-sign samples.

decay mode	$K^-\pi^+$	$K^-\pi^+\pi^0$	K^-X^*	other modes
K-mode(%)	52	27	21	≈ 0
π-mode(%)	59	28	13	≈ 0

* Excludes $K^-\pi^+$, $K^-\pi^+\pi^0$, and decay modes with a K^+.

Figure 4.10 shows the resulting over-all D^* momentum resolution. It can be seen that there are two components, a narrow peak at the center that has a width of 3% and a wide distribution with a width of 12%. The narrow component is due to the $K^-\pi^+$ decay mode and the wider component is due to the other decay modes of D^0 for which there is an missing momentum.

4.4.4 Detection Efficiency Corrections

The detection efficiency for the decay $D^{*+} \rightarrow D^0\pi^+_{D^*}$ in each D^* momentum bin is defined to be,

$$\epsilon \equiv \frac{\#(\text{Right sign})_i - \#(\text{Wrong sign})_i}{\#(D^{*+} \rightarrow D^0\pi^+_{D^*})_i},$$

where the subscript i refers to the i-th momentum bin and there is no restriction on the decay channels of D^0. The number of the decays $D^{*+} \rightarrow D^0\pi^+_{D^*}$ is counted over the 4π solid angle for hadronic events that pass the hadron cuts.

The detection efficiency defined above contains the branching fractions of D^0 to final particles. This is because each D^0 decay mode cannot be separated clearly even though the dominant mode is $K^-\pi^+$ as shown in Table (4.7). Therefore, the detection efficiency is a linear function of the branching ratios used in the Monte Carlo.

If the Monte Carlo is a good enough representation of reality (besides the D^0 branching fractions), then the efficiency obtained from it can be directly applied to the measured difference between the right-sign and wrong-sign samples to estimate

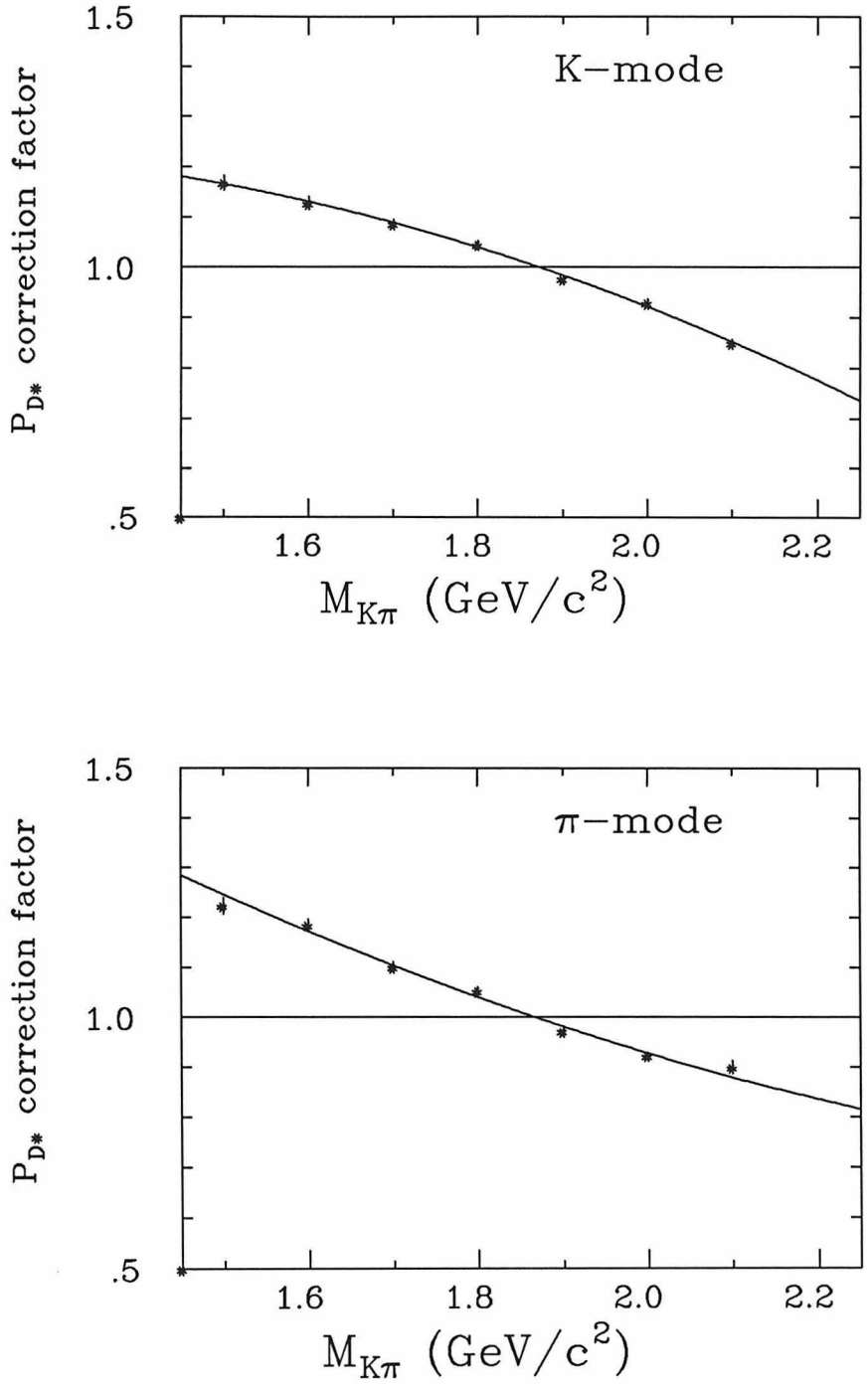

Figure 4.9. The D^* momentum correction factor, $P_{D^*}(\text{true})/P_{D^*}(\text{measured})$, as a function of the measured $M_{K\pi}$ for the K and π mode separately. The points are obtained by the Monte Carlo, and the curves are the result of fits to second order polynomial.

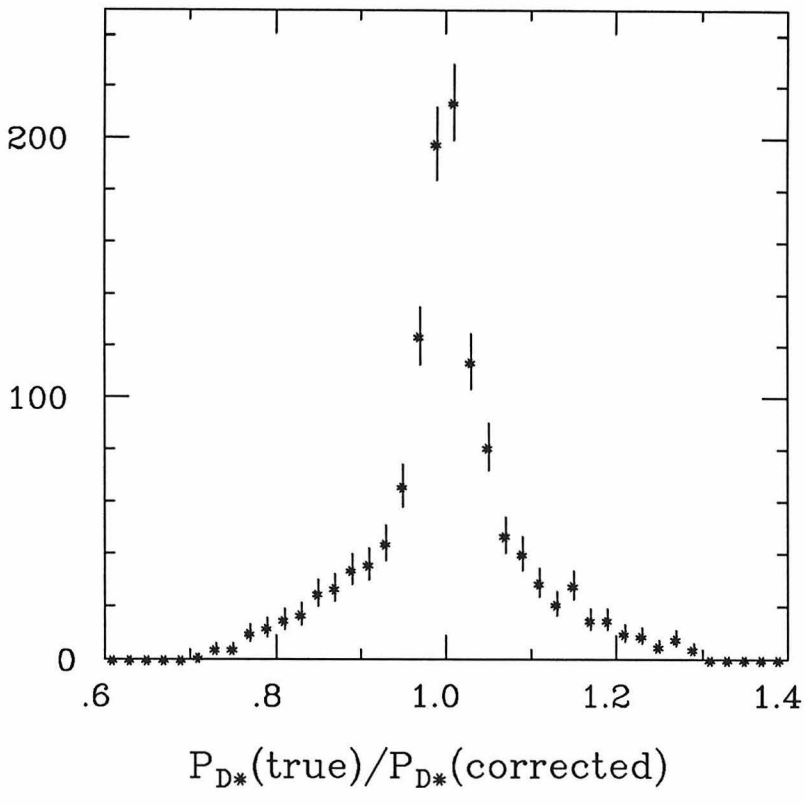

Figure 4.10. The D^* momentum resolution. The ratio of the corrected P_{D^*} to the true P_{D^*}. The narrow component ($\sigma = 3\%$) is from the $K^-\pi^+$ decay mode and the wide component ($\sigma = 12\%$) is from other decay modes of D^0.

the number of D^*'s that decayed to $D^0\pi^+_{D^*}$. However, there are slight residual differences between the data and the Monte Carlo that are difficult to be completely removed. And a small difference in the single track efficiency can become significant when many tracks are combined to form a candidate. Therefore, critical components of the D^* detection efficiency need to be checked both in the data and the Monte Carlo, and corrections have to be made when necessary.

The detection efficiency can be divided into two parts; one is the efficiency for the individual tracks to be found and to pass the cuts, and the other is due to the cuts involving multiple tracks such as the opening angle and invariant mass cuts. The latter is checked by changing the momentum resolution and angular resolution of tracks in the Monte Carlo over the range of uncertainty. The resulting change in the detection efficiency is found to be negligible. On the other hand, the differences in the individual track efficiencies have significant effects. The efficiency correction for the individual tracks can be divided into two parts; the efficiency that a track is found and the effect of decays in flight and nuclear interactions.

4.4.5 Track Finding Efficiency

The track finding efficiency can be roughly estimated by how close two tracks can come and both be found. By scanning the lost tracks in single event displays of Monte Carlo events, it is found that the inefficiencies are almost all due to overlapping tracks. If a track is isolated, then the finding efficiency is similar to that for the tracks in the low multiplicity events such as $e^+e^- \rightarrow e^+e^-e^+e^-$ where the efficiency is found to be greater than 99%.

The closeness of tracks, or the badness of overlapping, may be measured by the azimuthal angle of tracks at a radius of 25 cm which is about the first layer of the CDC. For each track, the angle $\Delta\phi_{\rm min}$ is defined to be the ϕ angle at $r = 25$ cm to the closest track, where all tracks are required to be within the geometrical acceptance. Figure 4.11 shows the distribution of $\Delta\phi_{\rm min}$ for the Monte Carlo and the data. The momentum of the track to be plotted is required to be greater than 1.0

GeV/c, while no momentum cut was made to the second track that forms $\Delta\phi_{\rm min}$ with the first track. The histogram (solid line) in (a) is the $\Delta\phi_{\rm min}$ distribution when the track finding efficiency is assumed to be 100 %, and the case when only the found tracks are used is shown by points with error bars.

The dip at small $\Delta\phi_{\rm min}$ of the latter is due to the inefficiency caused by overlapping tracks. In fact, 75% of the tracks that are not found is in the region $\Delta\phi_{\rm min} < 0.05$ radian in the histogram plot.[173] The corresponding plots for the data, (b), show that the area of the dip is bigger than for the Monte Carlo by a factor 1.8. The histogram plot in (b) is the same as the histogram plot in (a) except that it is scaled to fit the data in the region $0.06 < \Delta\phi_{\rm min} < 0.16$ radian. The track finding efficiency is roughly the square root of the ratio of the two distributions because each entry to the plot is associated with a pair of tracks that forms $\Delta\phi_{\rm min}$. Even though the reality is slightly more complicated, this ansatz is found to reproduce the true track finding efficiency in the Monte Carlo, which is also shown in the figure. Assuming that the track finding inefficiency scales with the size of the dip, the inefficiency in the data is 1.8 ± 0.4 times the inefficiency in the Monte Carlo. The error reflects, among others, the lack of knowledge on the fraction of lost tracks that are in the region of the dip in the data, which was assumed to be the same 75% as for the Monte Carlo. The over-all track finding efficiency in the Monte Carlo is 95.1 %, which leads to an estimated efficiency of 91.2 ± 2.0% in the data.

Thus, the D^* finding efficiency evaluated by the Monte Carlo will be multiplied by $[(91.2 \pm 2.0)/95.1]^3 = 0.88 \pm 0.07$ to take into account the difference in the track finding efficiency between the data and the Monte Carlo. One possible explanation for this discrepancy is that the performance of the multiple hit recording in the drift chambers is not as good as the design.

4.4.6 Decays in Flight and Nuclear Interactions

The decays in flight and nuclear interactions of charged pions and kaons are not simulated in the Monte Carlo. A nuclear interaction at the beam pipe region or the

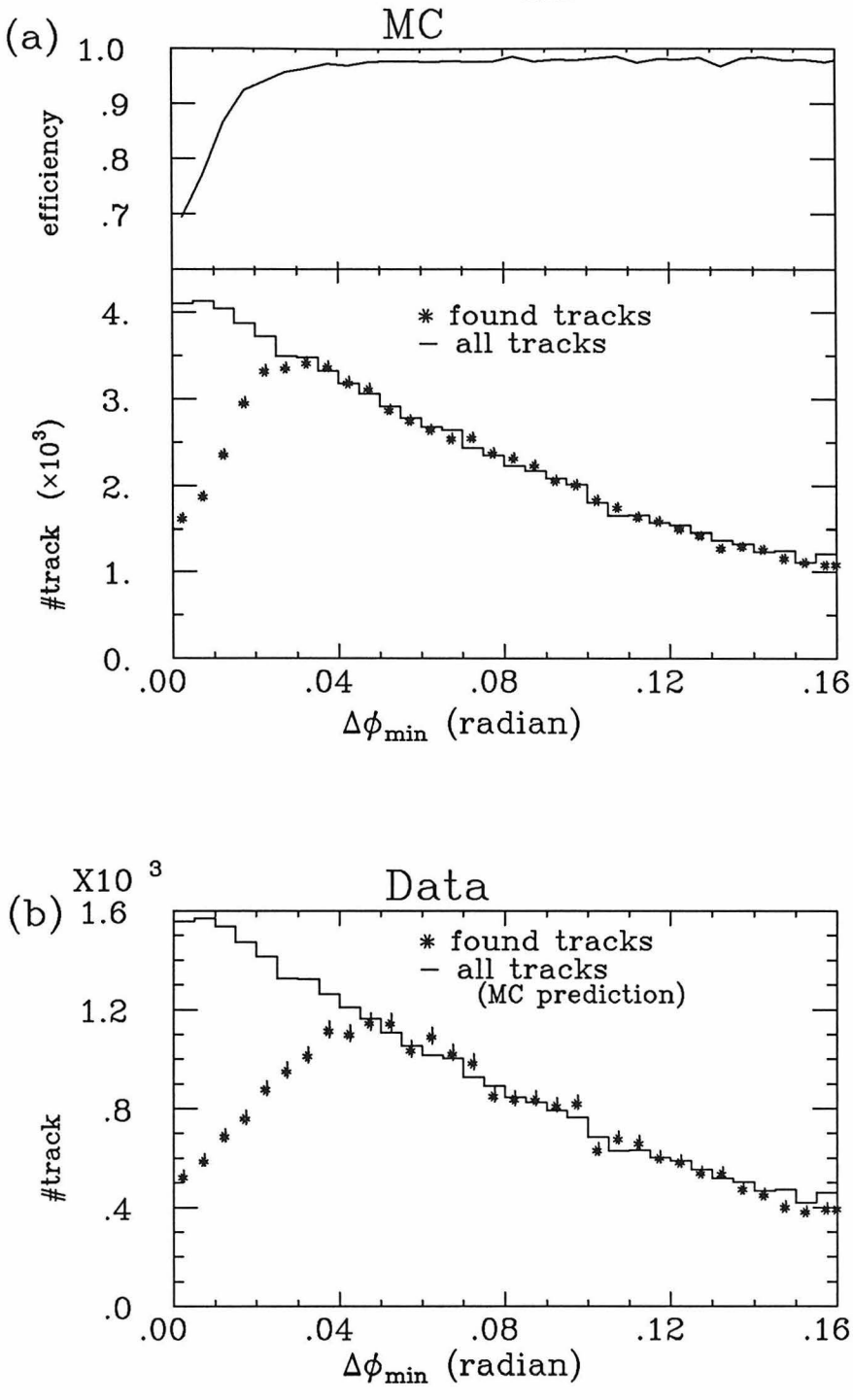

Figure 4.11. The track finding efficiency can be estimated by looking at how closely two tracks can be found. The ϕ angle from a given track to the closest track, $\Delta\phi_{\text{min}}$ (measured at $r = 25$ cm), is plotted for (a) the Monte Carlo and (b) the data. The histogram in (a) is the distribution when a 100 % track finding efficiency is assumed. In (b), the same histogram is scaled to fit the data in the region $0.06 < \Delta\phi_{\text{min}} < 0.16$ radian. The true track finding efficiency in the Monte Carlo is also shown in (a). The dip near $\Delta\phi_{\text{min}} = 0$ is larger for the data.

walls between the IDC and the CDC will almost always result in the loss of the track. The material is mostly aluminium which has a collision length of[174] 71 gr·cm^{-2}. The amount of material averaged over all runs (two types of beam pipe have been used) is 0.75 gr·cm^{-2} which leads to 1.1 % loss per track. Thus, the correction factor due to nuclear interactions is $(1 - 0.011)^3$=0.97. In addition, the nuclear interactions between the inner chambers and the outer chambers affect the leading track since the leading particle is required to have hits also in outer drift chambers. The corresponding amount of material is 3.9 gr·cm^{-2} of mostly aluminium which results in additional 5 % loss of leading tracks. Thus, the inefficiency due to nuclear interactions is $0.97 \times (1-0.05) = 0.92 \pm 0.02$, where the error reflects the uncertainty in the cross sections and the type and amount of materials.

The loss due to the decays in flight of pions or kaons is a function of their momentum, so the correction to the D^* detection efficiency also depends on the D^* momentum. Figure 4.12 shows the fraction of D^*'s lost by decays in flight of pions and kaons for the K-mode and π-mode separately. The Monte Carlo events are used to estimate the loss assuming that a candidate is lost when any of the three tracks decay inside a fiducial volume, which is defined to be inside $r = 35$ cm for the π_{D^*} track and the nonleading track, and inside $r = 140$ cm for the leading track. The former is about 15 cm inside of the outermost CDC layer which corresponds to the 9th layer from inside, and the latter is right inside the outer chambers. Most of the decays appear as kinks that distort the momentum or simply cause the track to be lost or fail the cuts, and there is uncertainty in how many of D^*'s with a decaying track actually fail to be included in the final sample. The systematic error is taken to be 1/2 of the correction to reflect this uncertainty. The data points are fit to second order polynomials to be used in the calculation of the cross sections.

In summary, the corrections applied to the detection efficiencies directly obtained from the Monte Carlo are,

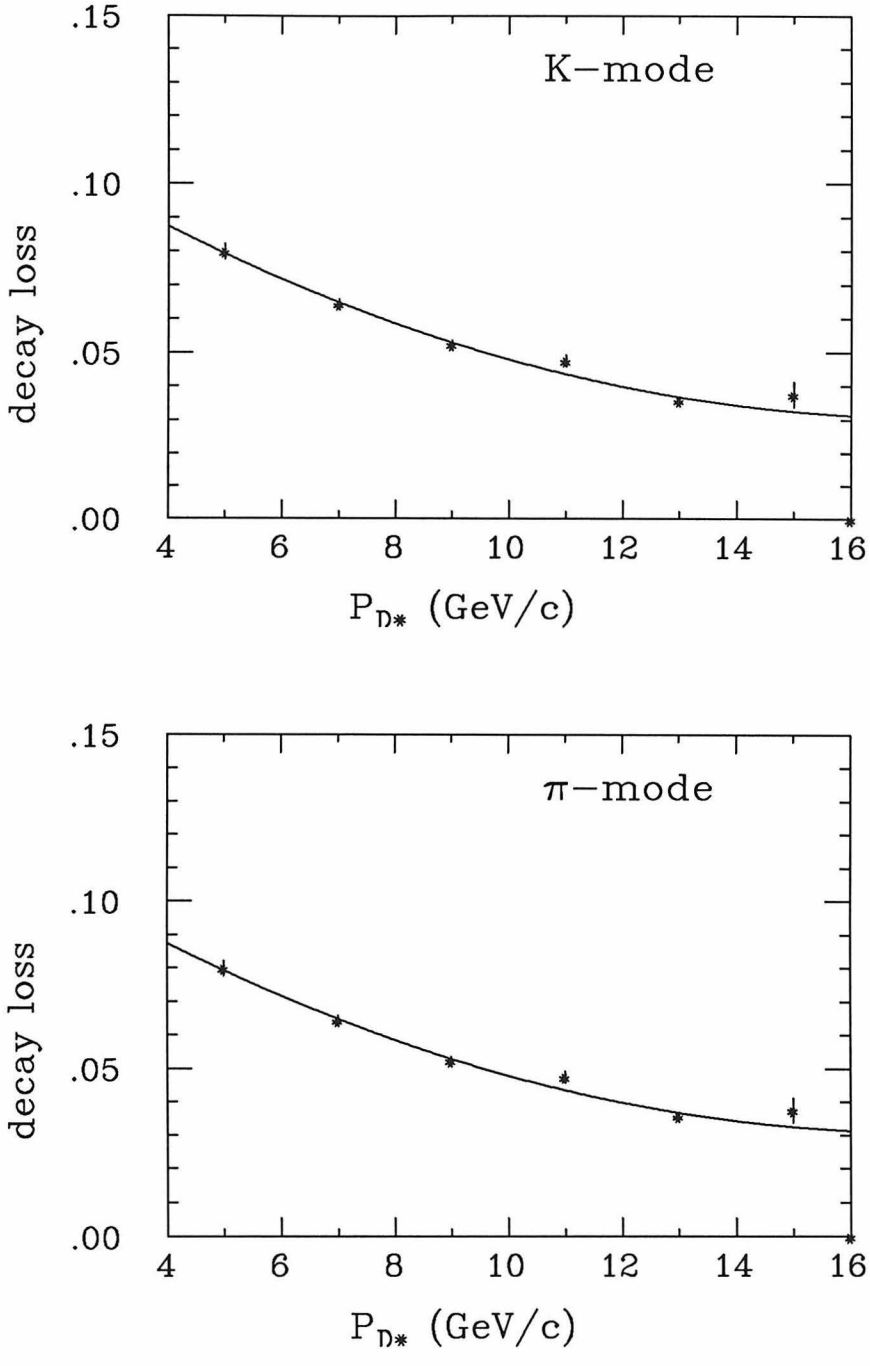

Figure 4.12. The estimated fraction of D^*'s that are lost by decays in flight for the K-mode and π-mode D^*'s. The curves are results of fit to a second order polynomial.

1) The difference in tracking efficiency (0.88 ± 0.07),

2) Nuclear interactions (0.92 ± 0.02), and

3) Decays in flight, as shown in Fig. 4.12.

We take the product of the three to obtain the final correction factor for the detection efficiency and denote it as $\epsilon_{\rm corr}$.

4.4.7 $d\sigma/dx$: Separately for the K-mode and The π-mode

Figure 4.13(a) shows the x distribution for the K-mode candidates and the corrected detection efficiency is plotted in (b). The parameter x is defined to be

$$x \equiv P_{D^*}/P_{\rm max}, \qquad \text{where} \quad P_{\rm max} \equiv (E^2_{\rm beam} - M^2_{D^*})^{1/2} \tag{4.1}$$

where M_{D^*} is the nominal D^* mass of 2.010 GeV/c^2. The momentum P_{D^*} has been corrected by the correction factor shown in Fig. 4.9, and is measured in the laboratory frame. The range of x is (0,1) for any beam energy except for some pathological cases. An alternative definition of x could be $E_{D^*}/E_{\rm beam}$ which has a threshold at $x = M_{D^*}/E_{\rm beam}$. We choose to use the definition (4.1) because it makes the comparison with measurements at different energies easier. The corresponding plots for the π-mode is shown in Figure 4.14.

We restrict ourselves to the region $x > 0.35$ in order to avoid the region of small detection efficiency. To get the cross section in each x bin, the following formula is used:

$$\begin{aligned} s\frac{d\sigma}{dx} &= 4E^2_{\rm beam}\frac{n_{\rm r-w}\sigma_0 R_{\rm had}}{\epsilon {\rm Br}(D^{*+} \to D^0\pi^+_{D^*})N_{\rm had}\Delta x} \\ &= 0.114 \times 10^{-4}\frac{n_{\rm r-w}}{\epsilon\Delta x} \quad (\mu{\rm b}\cdot{\rm GeV}^2), \end{aligned} \tag{4.2}$$

where

s is the invariant mass squared of the e^+e^- system.

$E_{\rm beam}$ is the beam energy (14.5 GeV),

$n_{\rm r-w}$ is the count in the bin [#(right sign)$-$#(wrong sign)],

ϵ is the corrected detection efficiency for the decay $D^{*+} \to D^0\pi^+_{D^*}$,

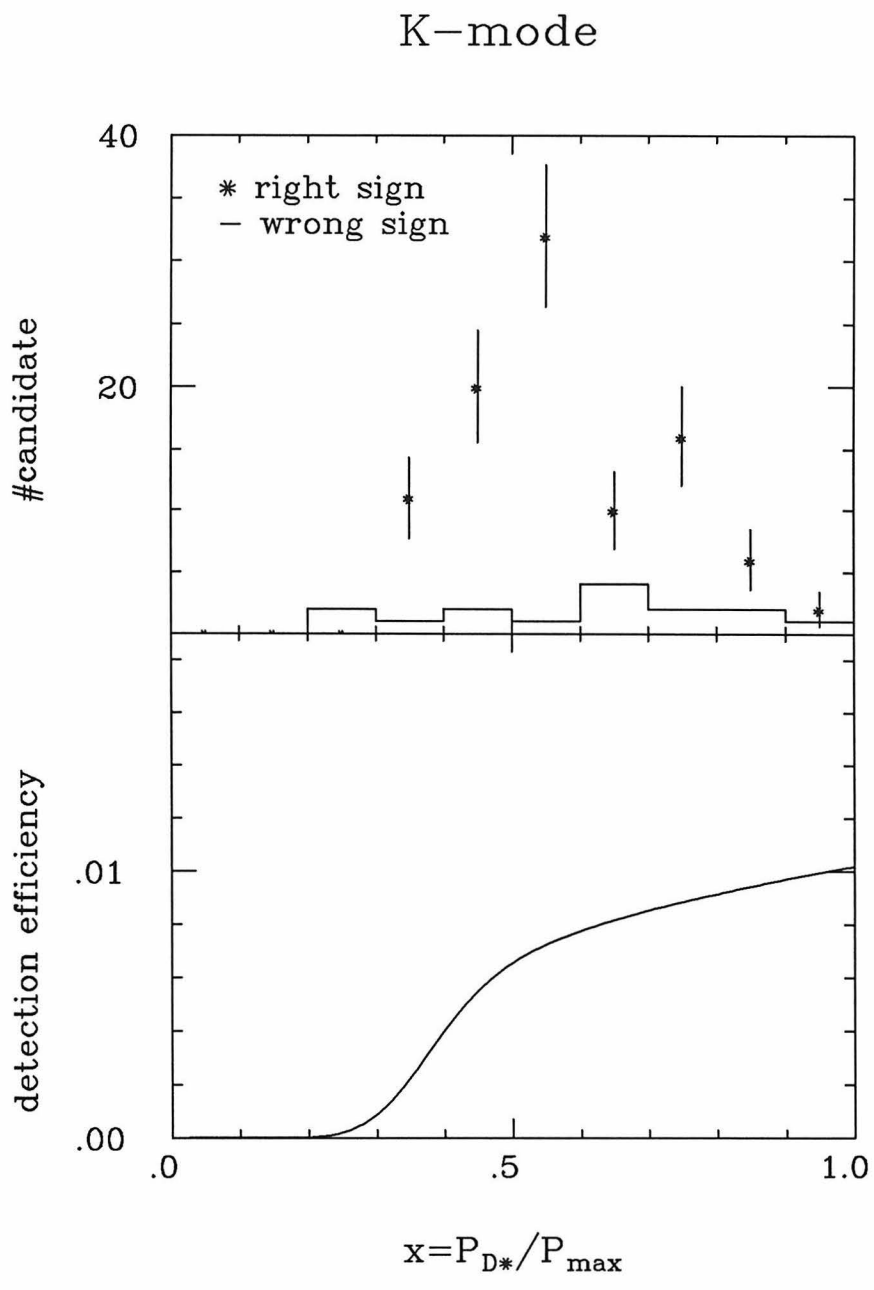

Figure 4.13. The raw $x \equiv P_{D^*}/P_{\max}$ of the K-mode D^* candidates, where $P_{\max} \equiv (E^2_{\rm beam} - M^2_{D^*})^{1/2}$. The corrected K-mode detection efficiency as a function of x is shown in the bottom plot. The detection efficiency contains the D^0 branching fractions [but not $\mathrm{Br}(D^+ \to D^0 \pi^+_{D^*})$].

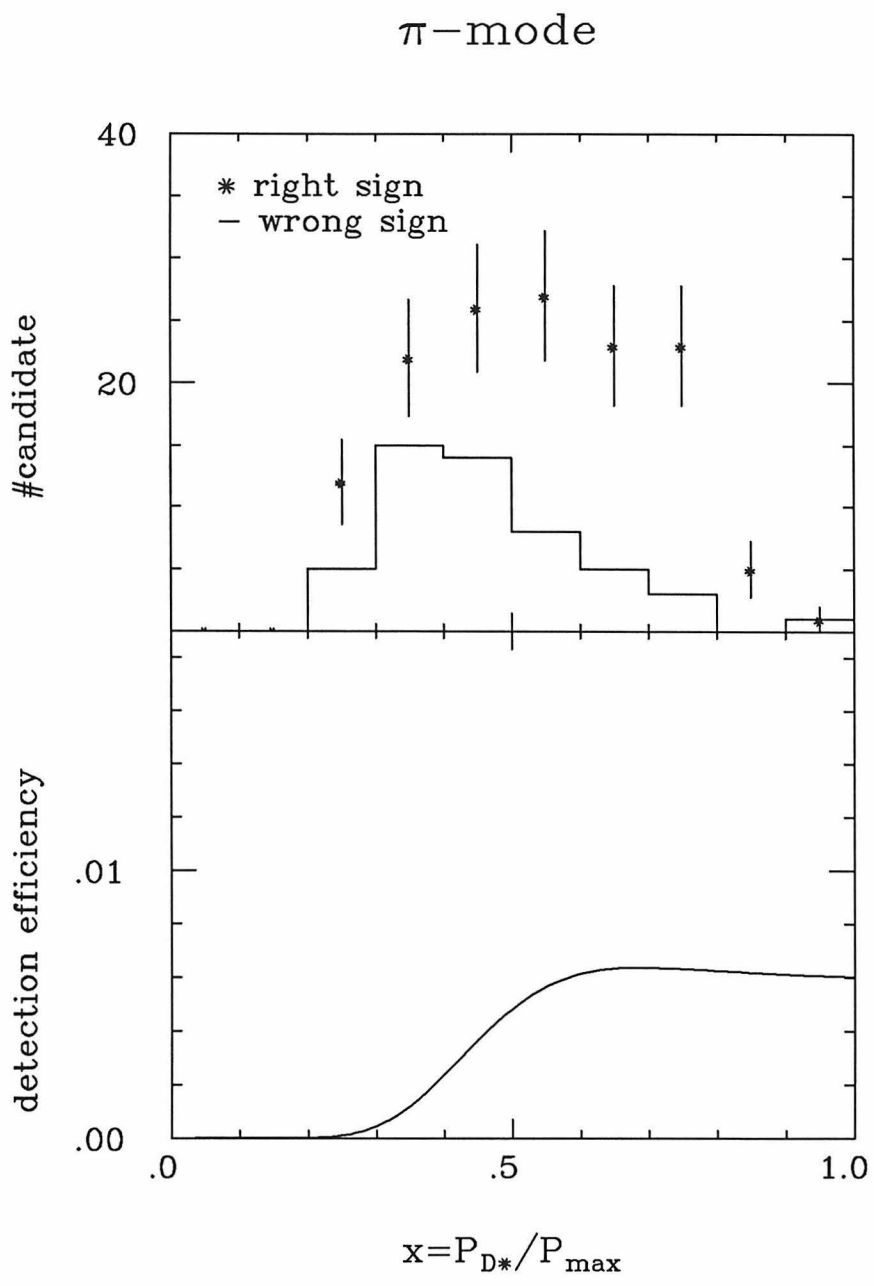

Figure 4.14. The raw $x \equiv P_{D^*}/P_{\max}$ of the π-mode D^* candidates, where $P_{\max} \equiv (E^2_{\rm beam} - M^2_{D^*})^{1/2}$. The corrected π-mode detection efficiency as a function of x is shown at the bottom. The detection efficiency contains the D^0 branching fractions.

σ_0 is the 1st order QED cross section for $e^+e^- \to \mu^+\mu^-$ (0.103 nb),

$R_{\rm had}$ is the hadronic cross section via single photon in unit of σ_0 including the radiative correction (3.9±0.2),

$N_{\rm had}$ is the number of events in the multihadron dataset (46549), and

Δx is the bin width.

The value used for the Br($D^{*+} \to D^0\pi^+_{D^*}$) is 0.64±0.11 by the Particle Data Group[70]. The most recent value is by the MARK II collaboration[175] and is 0.44±0.10, which was, unlike above, measured without assuming the isospin symmetry in D^{*+} decays. We choose to use the former because the isospin symmetry is expected to be a good symmetry in this case.

Table 4.8 summarizes the observed number of events, efficiencies, and the $D^{*\pm}$ production cross section in each x bin for both the K-mode and π-mode samples. The final efficiency ϵ is the product of the raw efficiency $\epsilon_{\rm raw}$, which is directly obtained from the Monte Carlo, and the correction factor $\epsilon_{\rm corr}$ described in the previous subsection. The resulting differential cross sections are shown in Figure 4.15. The errors are statistical only and do not include the uncertainties in the decay branching ratios. However, the branching ratios do not affect the shape of the x distribution significantly. The $M_{K\pi}$-dependent correction to the measured D^* momentum makes the final shape insensitive to the uncertainty in the relative sizes of the various decay branching fractions.

4.4.8 $d\sigma/dx$: Two Modes Combined

The results from the two samples are consistent with each other, and can be combined bin by bin statistically. The result is shown in Table 4.9.

Also listed in Table 4.9 are the estimated contributions from b quark decays and the cross sections after they are subtracted. Figure 4.16 shows the momentum distribution of $D^{*\pm}$'s coming from b quarks and c quarks, separately and combined. The combined distribution is consistent with our measurement. The relevant assumptions used in the Monte Carlo are,

Table 4.8. Observed number of events ($n_{\mathrm{r-w}}$), Monte Carlo raw efficiency (ϵ_{raw}), efficiency correction factor (ϵ_{corr}), final efficiency (ϵ), and the $D^{*\pm}$ production cross section ($s \cdot d\sigma/dx$) for several x bins. The detection efficiencies include the D^0 branching fractions used in the Monte Carlo (see Table 4.6).

(a)			K-mode			
x_{low}	Δx	$n_{\mathrm{r-w}}$	ϵ_{raw}	ϵ_{corr}	ϵ	$s \cdot d\sigma/dx$ (μb $\cdot$ GeV^2)
0.35	0.15	23 ± 5.2	0.0082	0.753	0.0062	0.28 ± 0.07
0.50	0.15	33 ± 6.2	0.0098	0.764	0.0075	0.33 ± 0.07
0.65	0.15	18 ± 5.1	0.0116	0.773	0.0089	0.15 ± 0.05
0.80	0.20	6 ± 3.2	0.0129	0.780	0.0101	0.03 ± 0.02

(b)			π-mode			
x_{low}	Δx	$n_{\mathrm{r-w}}$	ϵ_{raw}	ϵ_{corr}	ϵ	$s \cdot d\sigma/dx$ (μb $\cdot$ GeV^2)
0.35	0.15	15 ± 7.7	0.0053	0.744	0.0039	0.29 ± 0.16
0.50	0.15	32 ± 7.2	0.0084	0.760	0.0063	0.38 ± 0.10
0.65	0.15	25 ± 6.1	0.0079	0.771	0.0061	0.31 ± 0.09
0.80	0.20	5 ± 2.7	0.0079	0.780	0.0062	0.05 ± 0.03

1. $b \rightarrow c$ 100% of the time.[176]
2. The b quark fragmentation function is sharply peaked toward x=1.[177]
3. $\Gamma(c \rightarrow D^{*+})/\Gamma(c \rightarrow \mathrm{all})$ is the same for the charm quarks generated at e^+e^- vertex as those from b quark decays.

The first two are well established experimentally. The fraction of charms accounted for by D^*'s is not accurately measured either in bottom hadron decays or in charm quark fragmentations at high energy.[178] Theoretically, the third assumption seems reasonable. The estimated fraction of $D^{*\pm}$'s from b decays for $x > 0.35$ is estimated to be 8%. The corresponding plots with and without the bottom contribution are shown in Figure 4.17(a).

The solid curves in Fig. 4.15 and 4.17 are the results of the fits to the parametrization suggested by Peterson *et al.*[Equation (2.26)] for the heavy quark

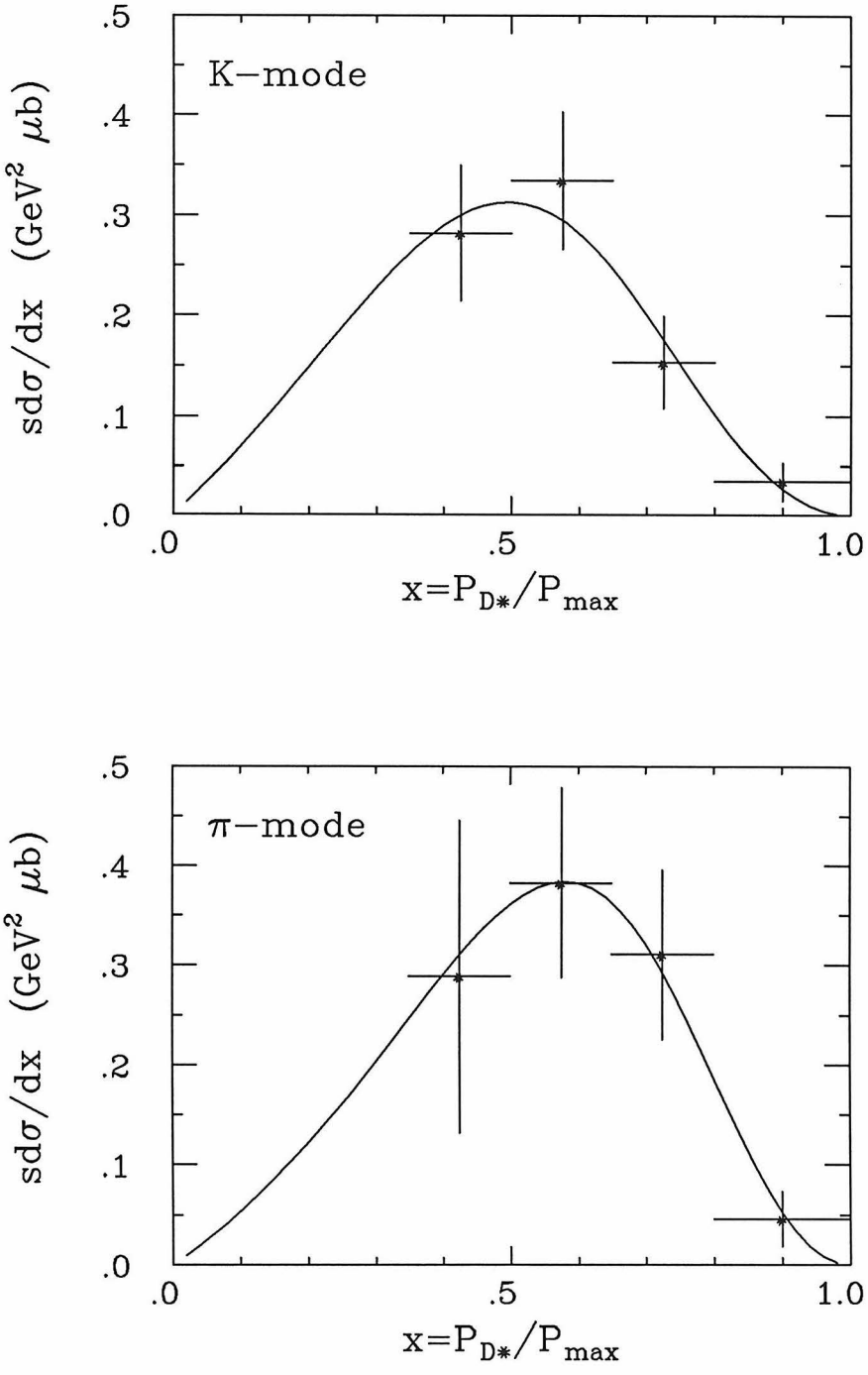

Figure 4.15. The differential cross sections obtained from the K-mode and π-mode samples are shown separately. The solid curves are the result of fit to the parametrization described in the text.

Table 4.9. The differential cross section obtained by combining the results for the K-mode and π-mode of Table 4.8. The fraction of $D^{*\pm}$'s from b quarks and the cross section after it is subtracted are also shown for each x bin.

$x_{\rm low}$	$s \cdot d\sigma/dx$ (μb $\cdot$ GeV^2) all $D^{*\pm}$'s	fraction of $D^{*\pm}$'s from b	$s \cdot d\sigma/dx$ (μb $\cdot$ GeV^2) without $D^{*\pm}$'s from b
0.35	0.28 ± 0.06	0.16	0.24 ± 0.05
0.50	0.35 ± 0.06	0.05	0.33 ± 0.05
0.65	0.19 ± 0.04	0.02	0.18 ± 0.04
0.80	0.04 ± 0.02	0.01	0.04 ± 0.02

fragmentation function at high energy. For the fit parameter, we used x^0 which is the value of x where the function $f(x)$ has its maximum, instead of ε in (2.26). It is related to ε by the simple relation $\varepsilon = x^0 + 1/x^0 - 2$. This variable has the trivial geometrical interpretation and also makes the fit better behaved than ε in the sense that it gives more symmetrical errors. The results of the fit for the combined data are $x^0 = 0.53 \pm 0.04$ (or $\varepsilon = 0.42^{+0.12}_{-0.10}$) for the data with the bottom quark contribution, and $x^0 = 0.55 \pm 0.04$ (or $\varepsilon = 0.37^{+0.11}_{-0.09}$) for the data without the bottom quark contribution.

The total $D^{*\pm}$ production cross section for $x > 0.35$ can be obtained by adding up the cross sections in all x bins. The results are $\sigma_{D^{*\pm}}(x > 0.35) = 0.16 \pm 0.02 \pm 0.02$ nb and $0.14 \pm 0.02 \pm 0.02$ nb for the data with and without the bottom contribution, respectively. The first error is statistical and the second is systematic. The systematic error accounts for the uncertainty in detection efficiencies for particular decay chains of $D^{*\pm}$, but does not include uncertainties in the branching fractions used for $D^{*\pm}$ and D^0. Two of the most important branching fractions are $\mathrm{Br}(D^{*+} \to D^0\pi^+)$ and $\mathrm{Br}(D^0 \to K^-\pi^+)$, for which we used 64% and 3.0%, respectively. As mentioned earlier, the most recent measurement with a new method gives $4.9 \pm 0.9 \pm 0.5\%$ for the latter, and if this number turns out to be correct, then all the cross sections above need be scaled down by a factor of about 0.6. Thus,

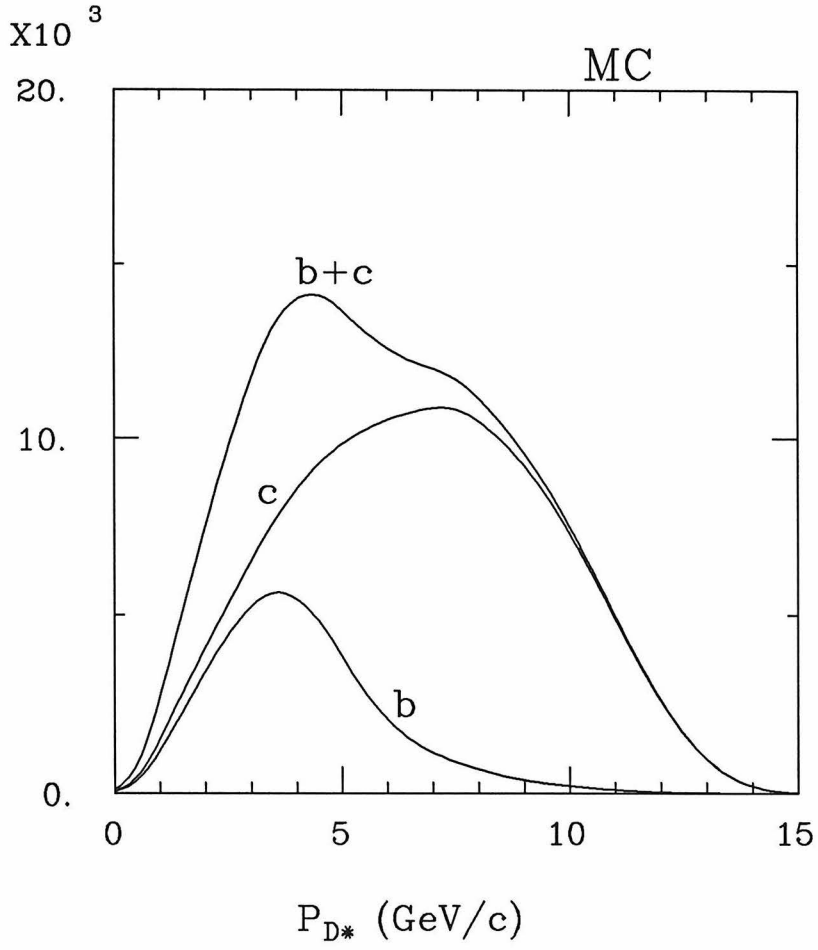

Figure 4.16. The contribution from b and c quarks to $D^{*\pm}$ production in the Monte Carlo used.

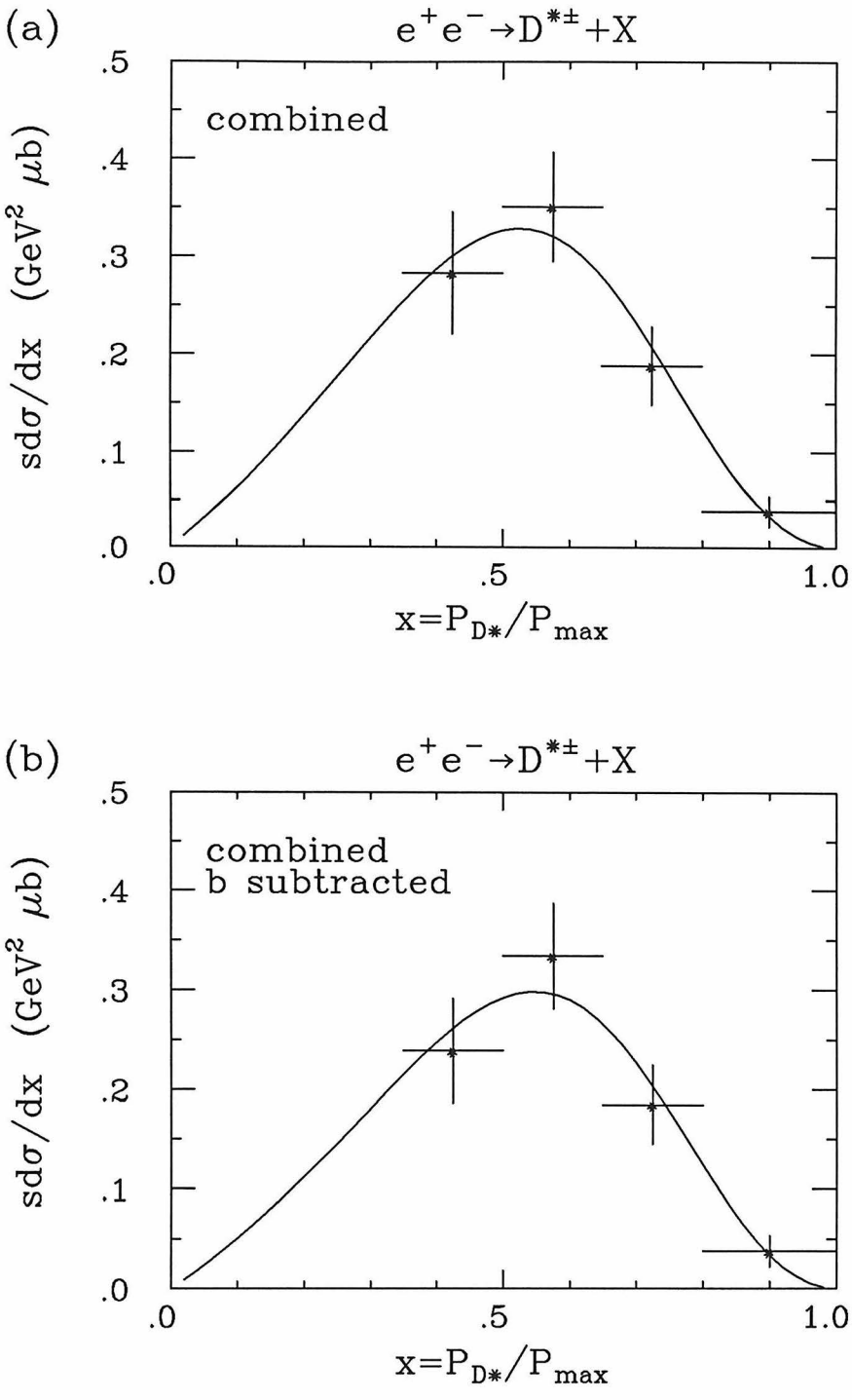

Figure 4.17. The differential cross sections obtained by combining the results from the K-mode and π-mode samples, (a) without and (b) with the bottom contribution subtracted. The solid curves are the result of fit to the function described in the text.

at the moment, the largest uncertainty in the total cross section arises from the branching ratios.

Assuming the shape given by (2.26), one can estimate the fraction of D^* in the region $x > 0.35$ to calculate the total production cross section for the whole range. For the bottom subtracted combined data the fraction is 0.78 ± 0.10 where the error is mostly due to the uncertainty of the shape of the fragmentation function below $x = 0.35$. This gives a total production cross section of $0.18 \pm 0.02 \pm 0.03$ nb. Table 4.10 summarizes the results of fit and the total cross sections for the various datasets.

Table 4.10. Results of fit to the curve (2.26) and total $D^{*\pm}$ production cross sections for the various datasets. The branching fractions used are $\mathrm{Br}(D^{*+} \to D^0\pi^+) = 64\%$ and $\mathrm{Br}(D^0 \to K^-\pi^+) = 3\%$. The systematic errors do not include the errors in the branching fractions.

	ε	x^0	$\sigma_{D^{*\pm}}(x > 0.35)$ (nb)	$\sigma_{D^{*\pm}}(x > 0)$ (nb)
K-mode	$0.52^{+0.21}_{-0.16}$	0.49 ± 0.06	$0.15 \pm 0.02 \pm 0.02$	$0.20 \pm 0.03 \pm 0.03$
π-mode	$0.30^{+0.13}_{-0.10}$	0.58 ± 0.06	$0.19 \pm 0.04 \pm 0.02$	$0.23 \pm 0.05 \pm 0.03$
combined	$0.43^{+0.12}_{-0.10}$	0.53 ± 0.04	$0.16 \pm 0.02 \pm 0.02$	$0.21 \pm 0.02 \pm 0.03$
combined b-subtracted	$0.37^{+0.11}_{-0.09}$	0.55 ± 0.04	$0.14 \pm 0.02 \pm 0.02$	$0.18 \pm 0.02 \pm 0.03$

4.5 Summary and Discussion

4.5.1 Total Cross Section

The total cross section with the bottom contribution subtracted is measured to be $0.18 \pm 0.02(\mathrm{stat}) \pm 0.03(\mathrm{sys})$ nb ($0 < x < 1$). The systematic error includes the uncertainties in the detection efficiency, the shape of the fragmentation function below $x < 0.35$, the luminosity, but not the branching ratios. Since the neutral partner of $D^{*\pm}$ is expected (from isospin symmetry) to be produced in the same

amount, the total D^* production inferred from our measurement is 0.360 $\pm$ 0.04 $\pm$ 0.06 nb. The total cross section includes the radiative correction for the initial state radiation through the value of $R_{\rm had}$ used in the formula (4.2).

The QCD corrected cross section for the c or $\bar{c}$ production [Formula (2.9) with $\alpha_s = 0.16$] is 0.145×2 = 0.29 nb. This indicates that the D^* production dominates the charm source. This is in agreement with the more direct measurements of the D^*/D production ratio by the HRS[167] and the CLEO[162] experiments. Simple spin statistics predicts the ratio D^*/D to be 3/1.

If we use the recent measurement, $\mathrm{Br}(D^0 \rightarrow K^-\pi^+) = 4.9 \pm 0.9 \pm 0.5$, and assume that the relative ratios between the relevant D^0 branching fractions as used in the Monte Carlo are correct, then our $D^{*\pm}$ cross sections become 0.10±0.02±0.02 nb ($x > 0.35$) before the bottom contribution is subtracted and 0.11 $\pm$ 0.02 $\pm$ 0.02 nb ($x > 0$) after the bottom contribution is subtracted. With these values, our measurement is still consistent with the pseudoscalar D mesons being produced as frequently as their vector partners, and there is a room left for other charmed particles such as F mesons and charmed baryons. Although these charmed particles have been observed in e^+e^- annihilations,[179,180] their production cross sections have not been determined.

4.5.2 Charm Fragmentation Function

Figure 4.18 shows the comparison of our measurement with other experiments. The x distribution without the bottom subtraction is compared with experiments at similar energies as ours, and the one with the subtraction is compared with the results from lower energies where the bottom contribution is not present or can be ignored. All points are normalized to $\mathrm{Br}(D^{*+} \rightarrow D^0\pi^+) = 64\%$, $\mathrm{Br}(D^0 \rightarrow K^-\pi^+)$ = 3.0%, and the same definition of x. The MARK I points are averages of D^0 and $D^\pm$ cross sections where the latter is normalized to $\mathrm{Br}(D^+ \rightarrow K^-\pi^+\pi^+)$ of 4.6%.

The measurements at lower energies are more consistent between themselves than those at higher energies. This is because the statistics are higher and the

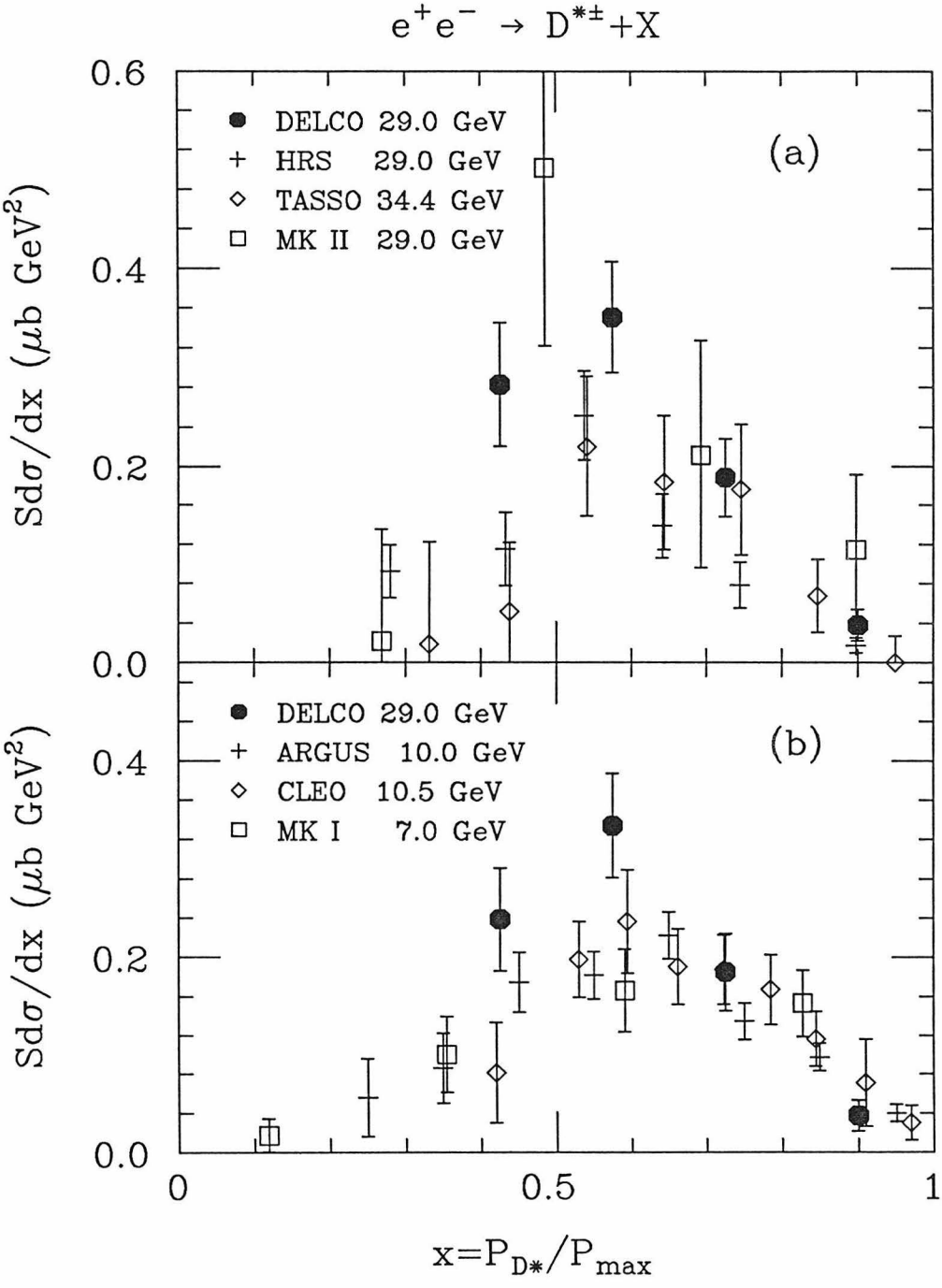

Figure 4.18. Our measurements of the x distribution of D^* (a) without and (b) with the bottom contribution subtracted are compared with other experiments. All points are normalized to $\mathrm{Br}(D^{*+} \to D^0\pi^+) = 64\%$ and $\mathrm{Br}(D^0 \to K^-\pi^+) = 3.0\%$. The MARK I points are averages of D^0 and $D^\pm$ cross sections where the latter is normalized to $\mathrm{Br}(D^+ \to K^-\pi^+\pi^+)$ of 4.6%. (Ref. 162 through 167).

multiplicity per event is lower (thus, less background) at lower energies.

The charm fragmentation functions at various energies are consistent with each other and harder than the light quark fragmentation functions which are peaked at small x. Thus, this supports the plausibility argument discussed in Chapter 2: the heavier the quark is, the harder the fragmentation function becomes. The effect of gluon radiation is expected to be larger at higher energy which results in softer fragmentations.[181] The distribution near $x = 1$ in Fig. 4.18(a) seems to be slightly suppressed relative to Fig. 4.18(b). This may be an indication of the hard gluon effect. For a definite answer, a better measurement is needed at our energy or at even higher energy.

Using the measured fragmentation function, we can now estimate the string breakup probability b assuming the string model with a uniform string breaking probability. In order to compare with the experimental measurement, the initial state radiation is added to the Monte Carlo of Fig. 2.8(not the LUND Monte Carlo). The effect of the initial state radiation is to generate a small tail at small x and to reduce $< x >$ by about 4.5 %. The hard gluon emission is not included.

Figure 4.19(a) shows the result of the fit. A large number of events are generated for different values of b and the data are fit to the resulting fragmentation functions. For $m_c = 1.7$ GeV and $\kappa = 0.2$ GeV^2, the string breaking probability is $b = 0.019 \pm 0.005$ GeV^2. There is an ambiguity in what value to use for the charm quark mass and the string tension κ. As discussed in Chapter 2, the fragmentation function in the string model is determined by the parameter

$$\alpha = \frac{1}{2}\frac{m_c^2 b}{\kappa^2}.$$

This is precisely true in the limit $E_{\text{beam}} \to \infty$, and is a good approximation even at the SPEAR energy of E_{CM} =7 GeV [as long as we use the definition (4.1)]. Thus, the uncertainties in m_c and κ are easily translated into an error in b. Using

$m_c = 1.7 \pm 0.3$ GeV and $\kappa = 0.2 \pm 0.03$, the string breakup probability is then

$$b = 0.019 \pm 0.005 \pm 0.009 \quad \text{GeV}^2.$$

The hard-gluon effect is ignored in the fit above. The effect is expected to be smaller at lower energies: the string is uniform and straight. Thus, the result of the ARGUS group is fit similarly in Fig. 4.19(b). The expected shape fits the measurement well, and gives $b = 0.033 \pm 0.004$ GeV^2.

The yoyo model of meson combined with the string breaking probability gives the decay rate of a meson as a function of its mass. A simple calculation gives

$$\Gamma = \frac{mb}{2\kappa} \sim \frac{m(GeV)}{20} \quad (GeV),$$

where $\kappa = 0.2$ GeV2 and $b = 0.02$ GeV2 are used. This estimation ignores quantum selection rules and admittedly is a crude one. However, a quick look through the particle data table can show that this is a reasonable estimate.

4.6 Forward-Backward Asymmetry

The detection efficiency as a function of $\cos\theta$ is flat up to $|\cos\theta| = 0.6$ and then drops sharply. Table 4.11 shows the numbers of D^* candidates generated in the forward direction and in the backward direction. The candidates outside $|\cos\theta| = 0.6$ are rejected. If a D^{*+} (D^{*-}) is generated in the same z direction as the incoming electrons (positrons) it is defined to be in the forward direction.

The measured asymmetry is thus $(57 - 103)/(57 + 103) = -0.29 \pm 0.11$. The error is statistical only. The expected asymmetry from the interference of the single photon exchange diagram and the Z^0 exchange diagram is given by the formula (2.15) and the value is -5.5 %. The QED diagrams and D^*'s from bottom quarks also contribute to the asymmetry, but the effect is much smaller than our measurement error. The sign of the asymmetry is as expected, but the measured

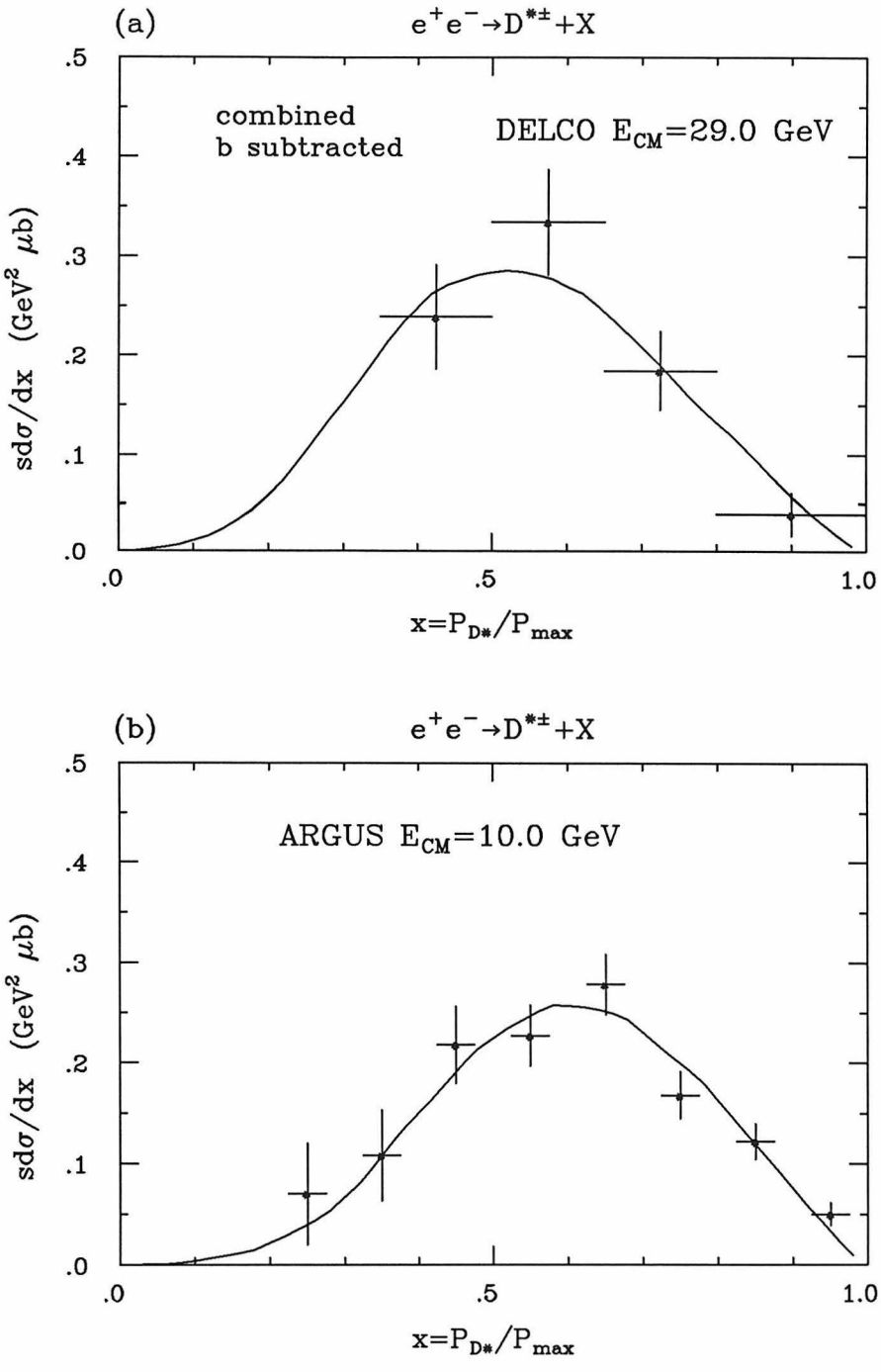

Figure 4.19. (a) The prediction of the string model is fit to the measurement. The parameters used are κ =0.2 GeV^2, m_c =1.7 GeV, and the result of the fit is $b = 0.019 \pm 0.005$ GeV^2. (b) A measurement at a lower energy (by the ARGUS group) is fit in the same way. The shape is well represented by the string model.

Table 4.11. The forward-backward asymmetry of the D^* production. The numbers of D^* candidates generated in the forward direction and in the backward direction are shown for the two modes separately and for the combined sample. If the charm number of D^* is negative, the direction is inverted. All candidates are required to satisfy $|\cos\theta| < 0.6$.

		R	W	R−W
K-mode	Forward	38	9	29
	Backward	56	6	50
π-mode	Forward	53	25	28
	Backward	77	24	53
K-mode + π-mode	Forward	91	34	57
	Backward	133	30	103

value is about two standard deviations from the expected value. At this stage, it is regarded as a statistical fluctuation.

Several other experiments have also measured the forward-backward asymmetry of $c\bar{c}$ production using D^*'s. The values are $A = -0.28 \pm 0.13$ by TASSO[165] (-0.14 expected), $A = -0.14 \pm 0.09$ by JADE[164] (-0.14 expected), and $A = -0.15 \pm 0.09$ by HRS[182] (-0.095 expected). The error bars are still large; clearly a higher statistics are needed.

Chapter 5.

Measurement Of The D^0 Lifetime

The lifetime of D^0 has been measured in various environments[183] including the e^+e^- annihilation,[184] where the crossing point of the two tracks from each D^0 decay is measured with respect to the center of e^+e^- beams. In this chapter I will describe a measurement of the D^0 lifetime obtained by a maximum likelihood method using the impact parameters of individual tracks of D^0 decays.

5.1 STRATEGY

The D^0 candidates are selected in the decays of charged D^*'s, and the criteria for the D^* candidates have been described in the previous chapter. For each of the two charged tracks from the D^0 decay, the impact parameter b is defined in the plane perpendicular to the beam axis (xy plane) and with respect to the beam center measured by the beam position monitor (Figure 5.1). The sign of b is positive if the inner product of the D^0 momentum in xy plane, $\vec{P}_{\perp D^0}$, and the vector from the beam center to the point of closest approach on the track, $\vec{b}$, is positive, and the sign is negative if the inner product is negative. The two cases are shown in Fig. 5.1.

If a D^0 is created at the beam center given by the beam position monitor, and if the track is measured without errors, then the impact parameter b is always positive and given by $d_\perp \sin\theta$, where $d_\perp$ is the decay distance of D^0 projected onto the xy plane, and θ is the angle between $\vec{P}_{\perp D^0}$ and the track direction in the xy plane.

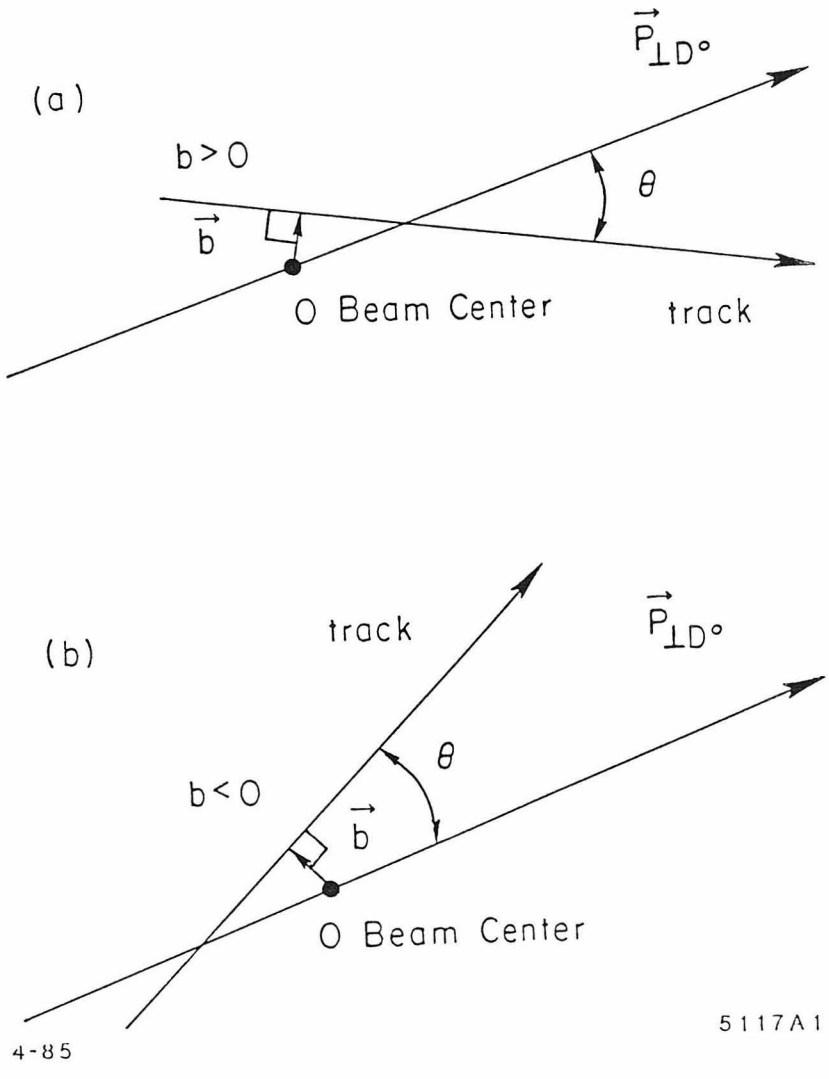

Figure 5.1. The definition of the impact parameter and its sign. All parameters are defined in the plane perpendicular to the beam axis. The point O is the beam center given by the beam position monitor. The impact parameter b is defined as $|\vec{b}|$ with the sign of $\vec{b} \cdot \vec{P}_{\perp D^0}$. The cases for positive and negative b are shown in (a) and (b) respectively.

The true impact parameter distribution is smeared because of the measurement errors and because the true primary vertex is only approximated by the beam center given by the beam position monitor. As shown in detail in later sections, these errors can be well approximated by a gaussian plus a flat background, where the width of the gaussian depends on the configuration of each track. The probability that a track is not from a D^0 decay also varies from track to track.

In order to extract the D^0 lifetime from the impact parameters, we have chosen to employ a maximum likelihood method which allows us to make the most out of the information available. In the following sections, we will discuss the components of the analysis.

5.2 Components of Analysis

5.2.1 Beam Position Monitor

The beam position monitors are located ± 3.74m from the interaction point. Each consists of four electrodes (buttons) placed inside the vacuum pipe which pick up pulses generated by the passing beam bunches. A total of eight pulse heights from the buttons are recorded for the bunch corresponding to each event and from these the beam centroid position at the interaction region is calculated event by event.

In Figure 5.2, the interaction points of Bhabha events are compared with the beam center measured by the beam position monitor. For a Bhabha track emitted almost vertically (within ± 0.25 radian in ϕ), the x coordinate of the vertex is well approximated by the x coordinate of the origin of the track. The y coordinate is obtained similarly using the tracks emitted almost horizontally (within ± 0.20 radian). Fig. 5.2(a) and (c) show the x coordinate values in the laboratory frame and relative to the beam position monitor value, respectively. Fig. 5.2(b) and (d) show the same for the y coordinate. Even though the fluctuation of the beam position is as large as 3 mm, it can be seen that the beam position monitor is

tracking the true beam center reasonably well.

5.2.2 Beam Sizes

There are three data blocks with different configurations which correspond to the three operational years, 1982, '83, and '84. The tracking qualities are roughly the same for the three.

The beam cross section is approximated by a 2-dimensional gaussian with widths σ_x and σ_y. Then the error in the impact parameter due to the beam size at an azimuthal angle ϕ is given by

$$\sigma_{\text{beam}}(\phi)^2 = \sigma_x^2 \cos^2\phi + \sigma_y^2 \sin^2\phi. \tag{5.1}$$

The beam size is obtained by measuring the width of the impact parameter distribution of Bhabha tracks and then subtracting the measurement error in quadrature. The measurement error is estimated by the width of the distribution of the track separation near the beam. A typical measurement error is 240 μm for Bhabha tracks. Figure 5.3 shows the measured σ^2_{beam} as a function of ϕ for the '83 data. The smooth curve is a fit to the expected shape (5.1) with σ_x and σ_y as parameters. The results are summarized in Table 5.1 for the three datasets. The values calculated from the machine parameters of the storage ring [Formula (3.6)] are also listed. The calculation ignores non-linear and incoherent effects such as beam-beam interactions, which probably is the source of the discrepancy between the measured and expected values; however, the agreement is reasonable.

It is worth noting that the measured beam sizes are the true beam sizes convoluted with the resolution of the beam position monitor, which are what we need for the fit of D^0 lifetime, since the D^0 tracks are also measured with respect to the beam position given by the beam position monitor. In passing, we also note that the resolution of the beam position monitor is at least better than the quoted beam sizes: it is better than 100 μm in the y direction, and probably similar in the x direction.

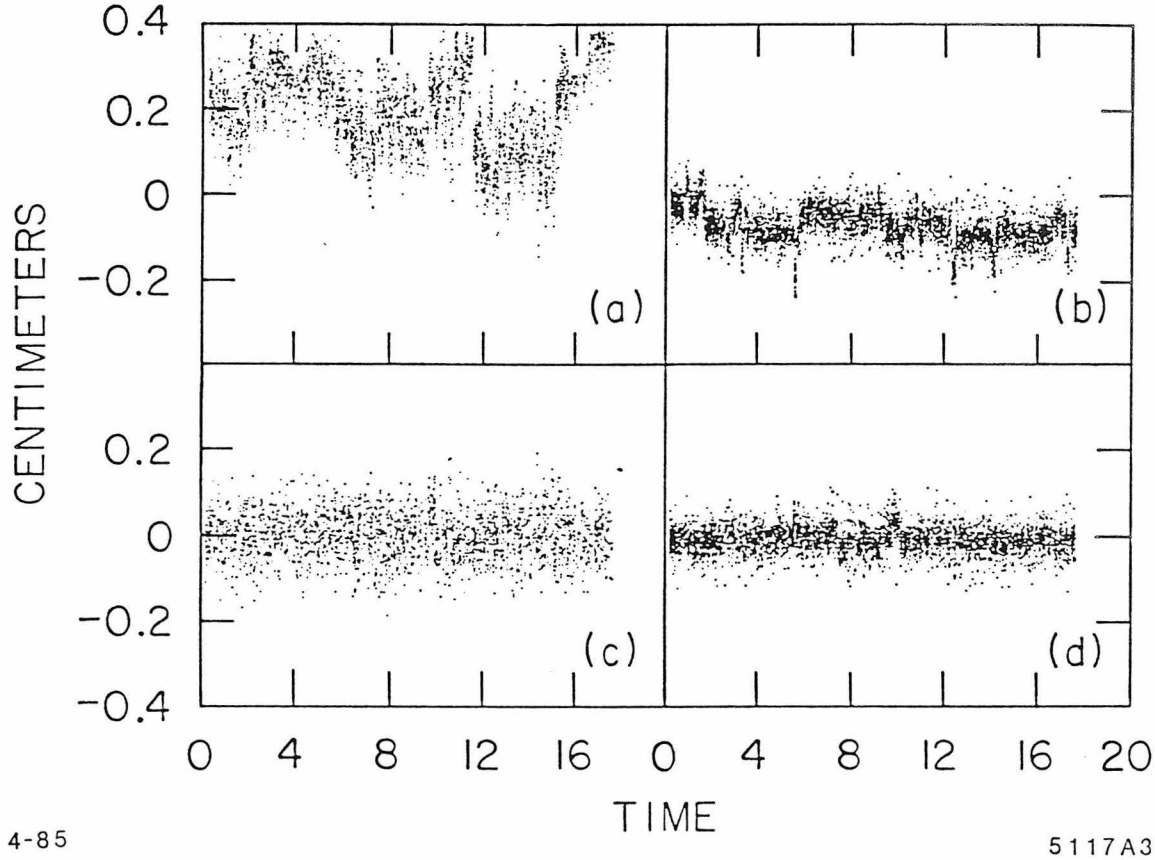

Figure 5.2. The x coordinate of the interaction points of Bhabha events, in the detector frame (a), and relative to the beam position given by the beam position monitor (c). The horizontal axis is the time in an arbitrary unit. The same set of figures for the y coordinate is given in (b) and (d). The time range shown corresponds to the '83 data, which accounts for about one half of the whole data.

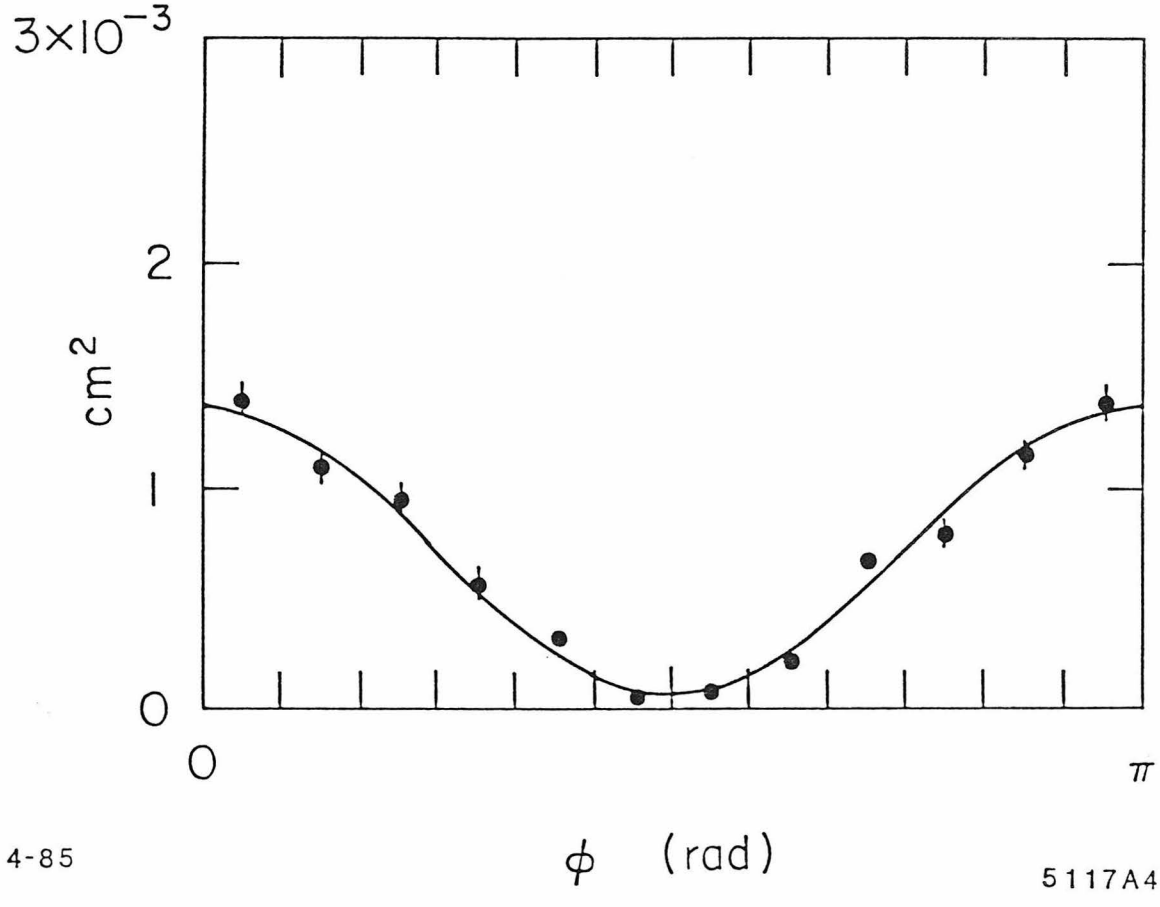

Figure 5.3. The beam variance vs ϕ ('83 data). The measurement errors have been already subtracted. The solid curve is the result of the fit to the shape $\sigma_x^2 \cos^2\phi + \sigma_y^2 \sin^2\phi$.

Table 5.1. Beam sizes obtained from Bhabha tracks and those expected from the machine parameters of the storage ring [Formula (3.6)]. Values are shown separately for the three datasets.

(μm)		82	83	84
measured	σ_x	462 ± 6	369 ± 6	342 ± 4
	σ_y	113 ± 10	75 ± 17	83 ± 12
expected	σ_x	380	420	420
	σ_y	$\lesssim 100$	$\lesssim 100$	$\lesssim 100$

5.2.3 *Measurement Error in Hadronic Events*

There are three contributions to the impact parameter error σ

$$\sigma^2 = \sigma^2_{\text{beam}} + \sigma^2_{\text{m.s.}} + \sigma^2_{\text{trk}}, \tag{5.2}$$

where

σ_{beam} is given by (5.1),

$\sigma_{\text{m.s.}}$ is due to the multiple scattering at the beam pipe and the inner wall of the IDC, and

σ_{trk} is due to the tracking errors inside the drift chambers.

We use the following formula[70] for $\sigma_{\text{m.s.}}$

$$\sigma_{\text{m.s.}} = \frac{r_{\text{eff}}}{\cos\lambda}\frac{0.0141}{P\beta}\sqrt{\frac{X}{\cos\lambda}}\left(1+\frac{1}{9}\log_{10}\frac{X}{\cos\lambda}\right), \tag{5.3}$$

where

r_{eff} is the effective average radius of the materials before the tracking volume, which is 9.1 cm and 9.0 cm for the '82/3 datasets and the '84 dataset respectively. The difference is due to the new thin beam pipe installed for the '84 dataset.

λ is the angle of the track away from the plane perpendicular to the beam axis,

P, β are the momentum (in GeV/c) and the velocity of the particle, and

X is the total amount of material in the direction perpendicular to the beam axis

(in radiation length), which is 2.25% and 1.28% for the '82/3 datasets and the '84 dataset respectively.

This formula is good to a few percent in the cases of interest. There are, however, non-gaussian components due to plural and single scatterings. They will be treated as part of the flat background.

The error $\sigma_{\rm trk}$ includes the measurement error of each drift chamber hit, the effect of taking wrong hits (i.e., the partial confusion in tracking), and the effect of multiple scattering inside the tracking volume due to the gas, wires, and other materials along a track. The track fitting program returns an estimated error for the impact parameter, $\sigma_{\rm fit}$, assuming that all the points associated with the track are correct and the measurement error of each point is properly estimated. Even though it is a useful indication of the quality of the measured impact parameter, a correction has to be made to obtain a realistic $\sigma_{\rm trk}$ in actual hadronic events.

In order to obtain the functional form of the correction, general hadronic tracks are divided into $\sigma_{\rm fit}$ bins. In each bin the impact parameter distribution[185] is fitted with a gaussian plus a flat background. The flat background is expected from strange particle decays, nuclear interactions, etc. In principle, the decay products of heavy hadrons can broaden the distribution. However, a Monte Carlo study has shown that the effect is negligible in estimating $\sigma_{\rm trk}$.[186]

Also, the root-mean-squares of $\sigma_{\rm m.s.}$ and $\sigma_{\rm beam}$ are calculated for the tracks in each $\sigma_{\rm fit}$ bin and are quadratically subtracted from the measured width to get $\sigma_{\rm trk}$. Figure 5.4 shows the resulting $\sigma_{\rm trk}$ as a function of $\sigma_{\rm fit}$. The broken lines show the root-mean-squares of $\sigma_{\rm m.s.}$ and $\sigma_{\rm beam}$, which have been subtracted in each bin. The curve is a fit to the correction function.

In Figure 5.5, the impact parameter distribution is shown for each σ bin, where σ is obtained by (5.2). The curve in each plot is the result of fit with a gaussian plus a flat background, where the width of gaussian is fixed to the expected value. The functional shape gives a good fit in all σ bins. Also, even though $\sigma_{\rm trk}$ is inferred in each $\sigma_{\rm fit}$ bin and not in each σ bin, the final expected resolution well matches the

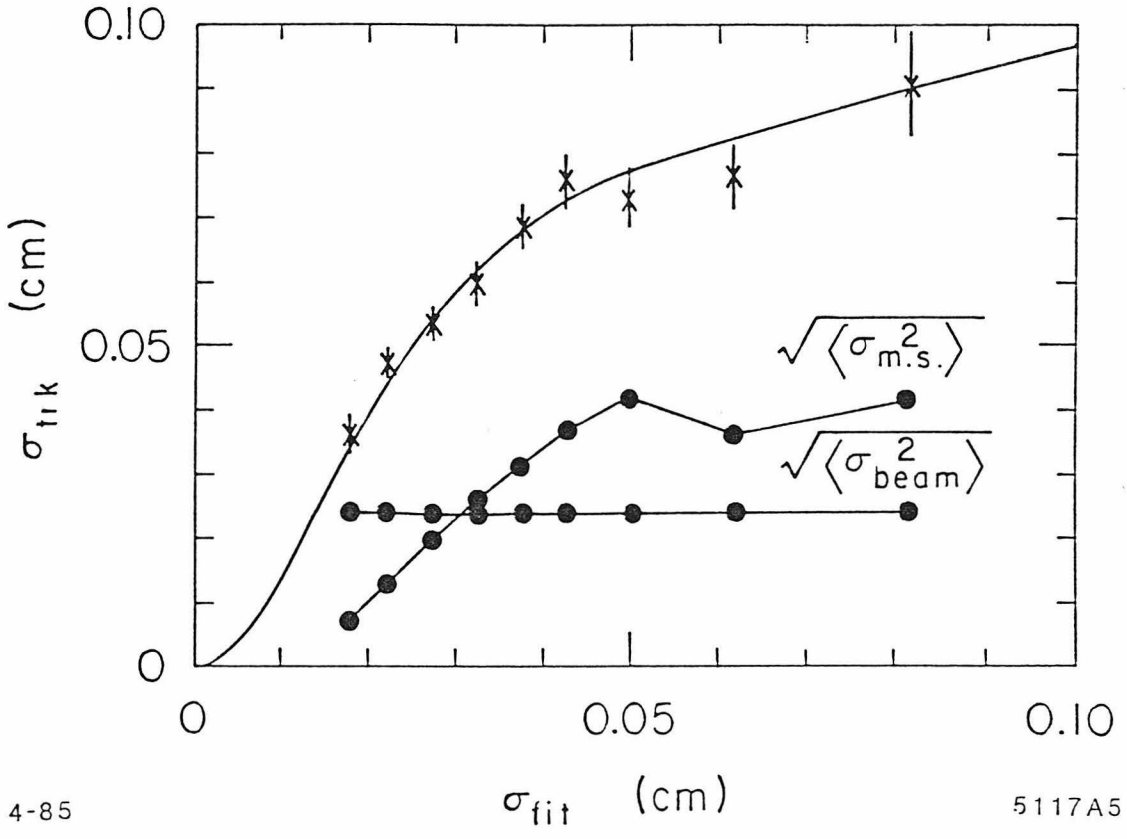

Figure 5.4. The error due to the tracking $\sigma_{\rm trk}$ is plotted against the error given by the track fitting program, $\sigma_{\rm fit}$. The solid curve is a function fitted to the data points. The broken lines show the root-mean-squares of $\sigma_{\rm m.s.}$ and $\sigma_{\rm beam}$ in each bin.

real resolution in each σ bin.

5.2.4 D^0 Track Selection

There are 14 candidates overlapping the K-mode and the π-mode which we will classify as K-mode. The tracks of the wrong-sign candidates are not used in the lifetime fit except in the estimation of the non-D^0 background. There are $97 + 139 - 14 = 222$ right sign candidates or 444 tracks in total (Table 4.4).

Then, the following cuts are made to the candidate tracks:

1. P greater than 250 MeV/c. This is to reject tracks with a large error in impact parameter; it rejects 5 out of the 444 tracks.
2. $\eta \sin\theta > 0.4$, where $\eta \equiv P_{\perp D^0}/M_{D^0}$ and θ is defined in Fig. 5.1. This is the ratio of the impact parameter to the decay distance of D^0 when errors are ignored. The larger this value is, the more weight the track has in the lifetime determination. And if it is zero, the track does not contribute to the lifetime measurement. Thus, even though this cut eliminates 174 out of 439 tracks, it does not degrade the statistical error of the fit while making the average impact parameter less sensitive to the background. Figure 5.6 shows the $\eta \sin\theta$ distributions for all the D^0 candidate tracks in the data. It can be seen that most of the tracks rejected are the leading tracks.
3. $|b|$ <2.5 mm. This defines the window of impact parameter; it removes 4 more tracks, leaving 261. Note that the D^* selection already requires that $|b| < 3.0$ mm. The only reason why we do not use 3 mm as the cut is that we want to move the window up and down by 0.5 mm to check the effect of the window on the final result.

Figure 5.7 shows the impact parameter distribution after the cuts. The distribution is clearly shifted in the positive direction, and the mean of the distribution is 174.5±44.5 μm. The curve overplotted is the result of the fit described later.

Two different control samples are checked:

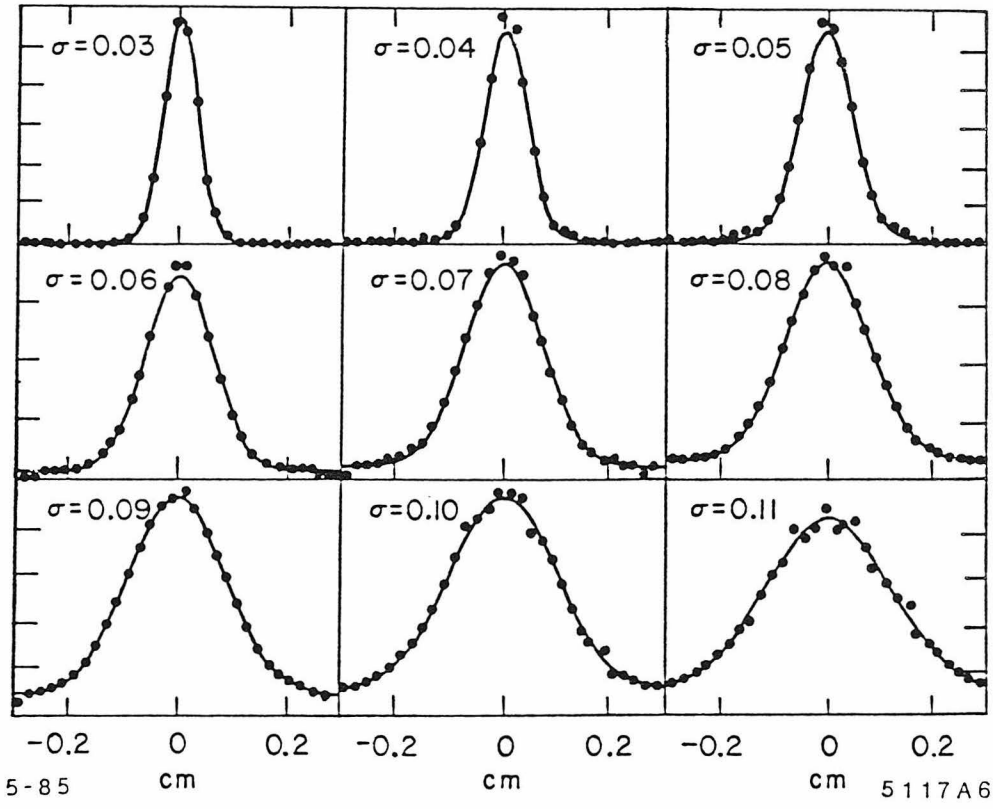

Figure 5.5. The impact parameter distributions in hadronic events for each bin of the overall expected error, σ. In each plot, the center value of σ is indicated in unit of cm, and the curve is the result of fit with the expected gaussian plus a flat background.

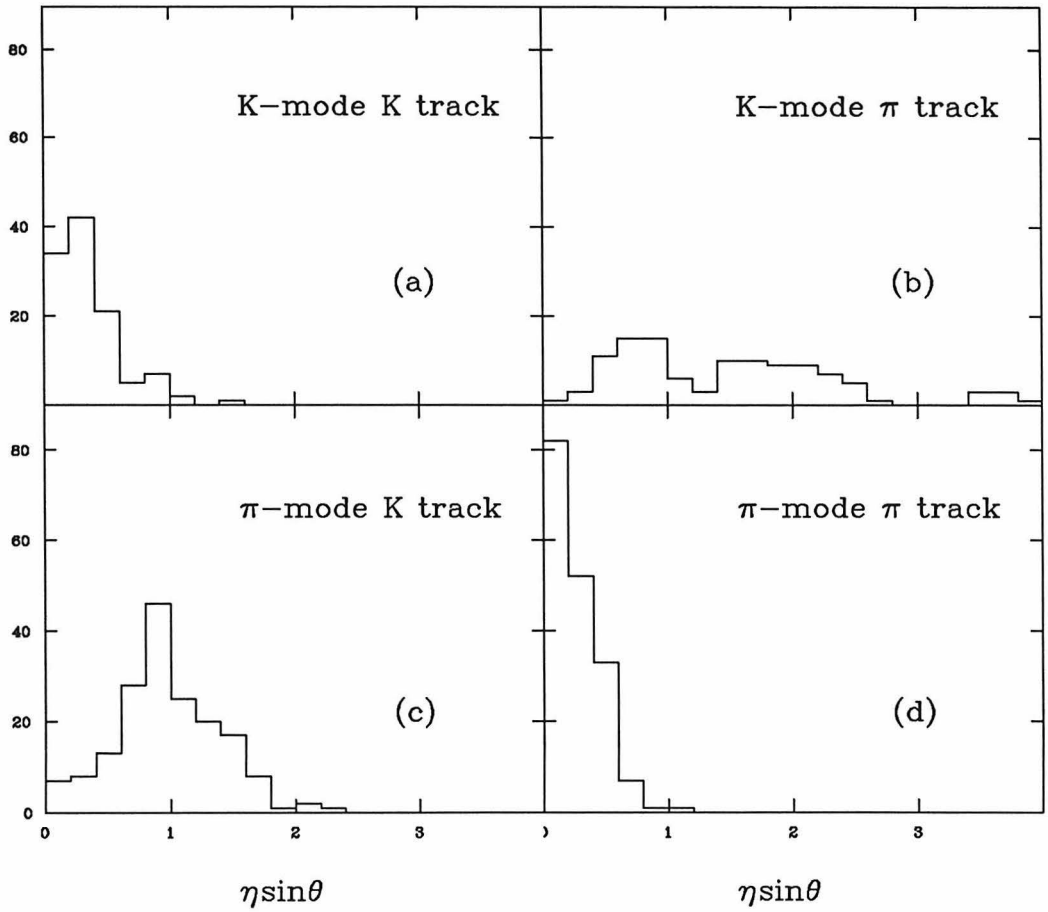

Figure 5.6. The distribution of $\eta \sin\theta$, which is a measure of the sensitivity of each track to the D^0 lifetime, is shown for each track category in the D^0 sample. The leading tracks (K-mode K tracks, and π-mode π tracks) are less sensitive than the non-leading tracks.

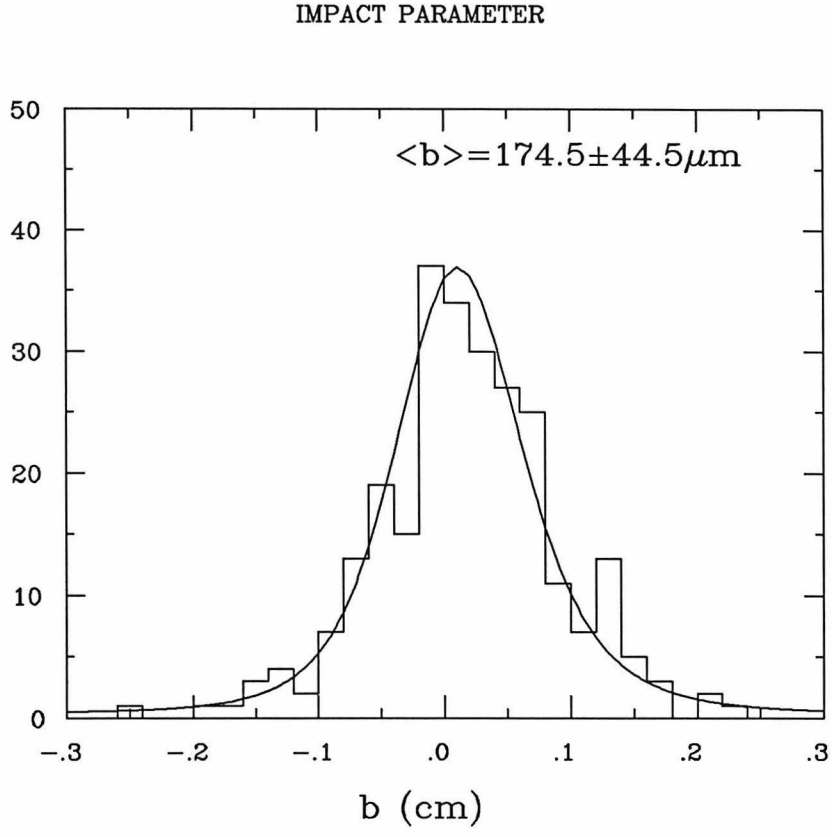

Figure 5.7. The impact parameter distribution for the final D^0 candidate tracks in the D^* sample. The solid curve is the result of the likelihood fit.

(a) General hadronic tracks with $P > 250$ MeV/c and $|b| < 2.5$ mm, where the thrust axis is used as the D^0 direction. The positive direction on the axis is defined such that the angle between the track and the axis is less than 90 degrees in xy plane.

(b) The sample of tracks kinematically similar to the D^0 tracks. It is formed by taking all the D^0 candidates selected just as before but without the information of the Čerenkov counter and without combining them with π_{D^*} candidates.

The impact parameter distributions for the two control samples are shown in Figure 5.8, and the results are summarized in Table 5.2. The corresponding shapes for the Monte Carlo[187] are overplotted in Fig. 5.8 as dashed curves, and their mean values are also included in Table 5.2. Positive mean values are expected because of strange and heavy particle decays, and the discrepancies between the data and the Monte Carlo can be comfortably accommodated within the uncertainties in the production rates and the lifetimes of these particles (in particular bottom hadrons).

The mean value of the impact parameter is not shifted by nuclear interactions, gamma conversions, Coulomb scattering at the beam pipe region, or small misalignments of the drift chambers. Although they do contribute to the error, the changes in the measured impact parameter due to these sources are expected to be symmetric and do not alter the mean value.

5.2.5 Estimation of Background

5.2.5.1 Non-D^0 Tracks

To study non-D^0 background, we compare the right-sign and wrong-sign samples. The background in the D^* sample has the same amount of right-sign and wrong-sign combinations. Therefore, the number of right signs minus the number of wrong signs indicates the number of true D^*'s for which both the leading track and the π_{D^*} track are found correctly. However, the non-leading tracks populate the same momentum region as the average hadronic tracks and are more easily contaminated than the leading tracks are. Also, the Cabibbo-suppressed decays of

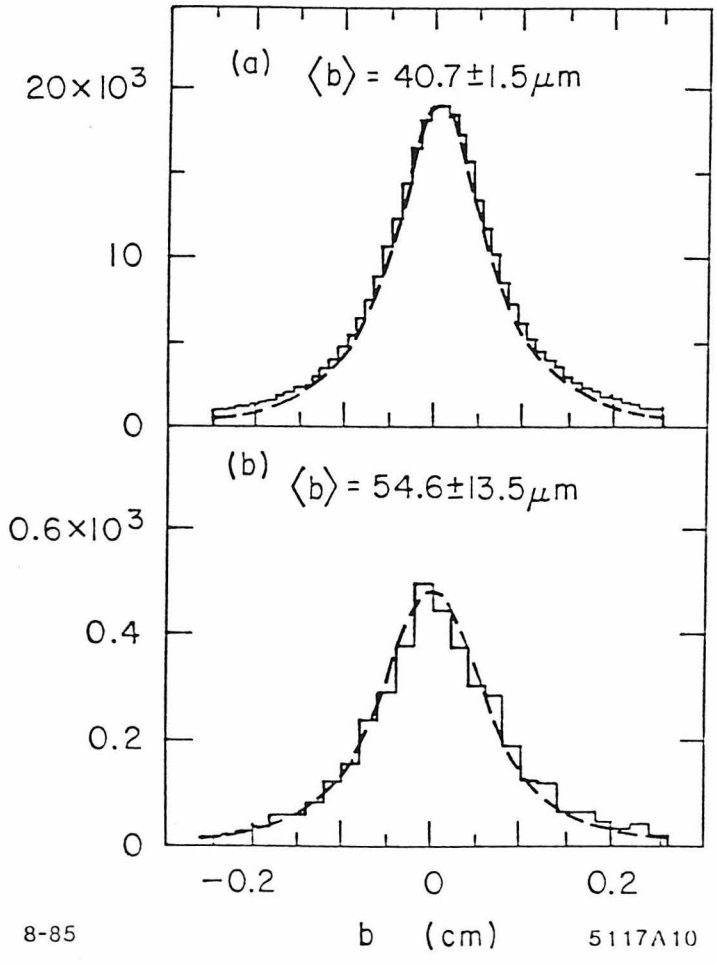

Figure 5.8. The impact parameter distributions for: (a) the general tracks in hadronic events and (b) the tracks kinematically similar to the D^0 tracks. The corresponding distributions for the Monte Carlo are overplotted (dashed curves).

Table 5.2. The means of the impact parameter for the D^0 sample and the two control samples: (a) for the general hadronic tracks and (b) for the tracks kinematically similar to the D^0 candidate tracks.

$< b >$ (μm)	data	MC
D^0 candidates	174.5±44.5	—
(a) general tracks	40.7±1.5	34.9±1.6
(b) selected tracks	54.6±12.0	43.4±11.7

D^0 that generate a wrong-sign kaon contribute to the wrong-sign K-mode sample. In addition, when a D^0 decay contains multiple charged pions, a wrong-sign pion can become the leading pion candidate thus contributing to the wrong-sign π-mode sample even if the tracks are genuinely from a D^*. Therefore, the number of right signs minus wrong signs has to be multiplied by a correction factor to get the number of candidates for which the track of interest is correctly found. We assume the $D^0 - \overline{D}^0$ mixing to be negligible in this chapter.

The correction factor $r_{\rm corr}$ is obtained by the Monte Carlo according to

$$r_{\rm corr} = \frac{(\#\text{ of correct tracks in the right-sign sample})}{(\#\text{ of right signs}) - (\#\text{ of wrong signs})}.$$

Table 5.3 summarizes the result. The purity is defined to be the probability that the track is truly from a D^0 decay. The first errors in the purities are statistical and the second errors systematic. The systematic errors are due to the uncertainty in the correction factors. For the leading tracks, the uncertainty comes mostly from our imperfect knowledge on the decay branching fractions of D^0. The non-leading tracks have larger systematic errors corresponding to the added contamination.

5.2.5.2 D^*'s from b-quarks

Since a decay of b-quark almost always creates a c-quark,[176] we expect some of the D^*'s in our dataset to come from the decays of b-flavored particles. The average $c\tau$ of the b-hadrons is relatively long and of the order of several hundred

Table 5.3. The fraction of the tracks from D^0 decays (purity) in each track category. The definition of the correction factor $r_{\rm corr}$ is given in the text.

		$r_{\rm corr}$	Purity
K-mode	K	1.09	$0.94 \pm 0.03 \pm 0.02$
	π	0.93	$0.80 \pm 0.03 \pm 0.04$
π-mode	K	1.16	$0.67 \pm 0.07 \pm 0.07$
	π	1.48	$0.85 \pm 0.09 \pm 0.05$

microns,[65,66] which substantially changes the impact parameters of the D^0 tracks originating from b-flavored hadrons.

The fraction of D^*'s coming from b-quarks has been estimated in the previous chapter as a function of the D^* momentum. The amount of contamination is similar for K tracks and π tracks, and the mean of the impact parameter for these tracks, κ_b, is found to be flat in $\eta \sin\theta$. With the average b lifetime of 350 μm,[66] and the D^0 lifetime of 136 μm, κ_b is estimated to be 210 μm. It does not depend strongly on the D^0 lifetime.

5.3 Likelihood Fit of D^0 Lifetime

5.3.1 D^0 Lifetime Likelihood Function

For N measurements of impact parameter, b^i $(i = 1, N)$, in which each event is characterized by a set of parameters $\mathbf{a}^i$, the likelihood function for $l \equiv c\tau$ is given by

$$L(l) = \prod_{i=1}^{N} f(b^i, l, \mathbf{a}^i), \quad f(b^i, l, \mathbf{a}^i) = \frac{f^0(b^i, l, \mathbf{a}^i)}{\int_{b_1}^{b_2} f^0(b, l, \mathbf{a}^i) db}, \tag{5.4}$$

where f and f^0 are the single event likelihood function with and without the effect of the impact parameter window, respectively, and (b_1, b_2) defines the window. The

actual function to be minimized, $\mathcal{L}$, is defined by

$$\mathcal{L}(l) \equiv -2 \log L(l) = -2 \sum_{i=1}^{N} \log f(b^i, l, \mathbf{a}^i). \tag{5.5}$$

The function f^0 is a convolution of an exponential with decay constant $\kappa = l\eta \sin\theta$ and a gaussian with width σ, and can be written using the complementary error function,[188]

$$f^0(b, l, \mathbf{a}) \equiv f^0(b, \kappa, \sigma) = \frac{1}{2\kappa} \exp\left(\frac{\sigma^2}{2\kappa^2} - \frac{b}{\kappa}\right) \operatorname{erfc}\left[\frac{1}{\sqrt{2}}\left(\frac{\sigma}{\kappa} - \frac{b}{\sigma}\right)\right], \tag{5.6}$$

where f^0 is a function of l only through κ, and both κ and σ are functions of $\mathbf{a}$. The shape of f^0 as a function of b is shown in Figure 5.9 for $\sigma = 500$ μm and several different κ's. The integration of f^0 needed in (5.4) is given by

$$\int_{b_1}^{b_2} f^0(b, \kappa, \sigma) db = \frac{1}{2}\left[e^{2\alpha x - \alpha^2} \operatorname{erfc}(x) + \operatorname{erf}(x - \alpha)\right]_{x_1}^{x_2}, \tag{5.7}$$

where

$$\alpha = \frac{\sigma}{\sqrt{2}\kappa}, \quad \text{and} \quad x_k = \frac{1}{\sqrt{2}}\left(\frac{\sigma}{\kappa} - \frac{b_k}{\sigma}\right) \quad (k = 1, 2). \tag{5.8}$$

The non-D^0 background is handled by adding a term which represents the distribution of the general background shape. We take it to be $\beta f^0(b, \kappa_B, \sigma)$, where β is the background fraction (1−purity) (see Table 5.3), σ is the expected impact parameter resolution for the track, and κ_B is a global constant that arises because the background does include genuinely positive impact parameters. We use a value $\kappa_B = 54.6$ μm from Fig. 5.8(b). Even though the true distribution is not exactly a convolution of an exponential and a gaussian, this approximation is good enough, and the result is insensitive to the exact shape. The b-quark contamination is handled in the same way by adding $\delta f^0(b, \kappa_b, \sigma)$ to the likelihood function, where δ is the fraction of the tracks originating from b-quarks and κ_b is the mean impact parameter for those tracks.

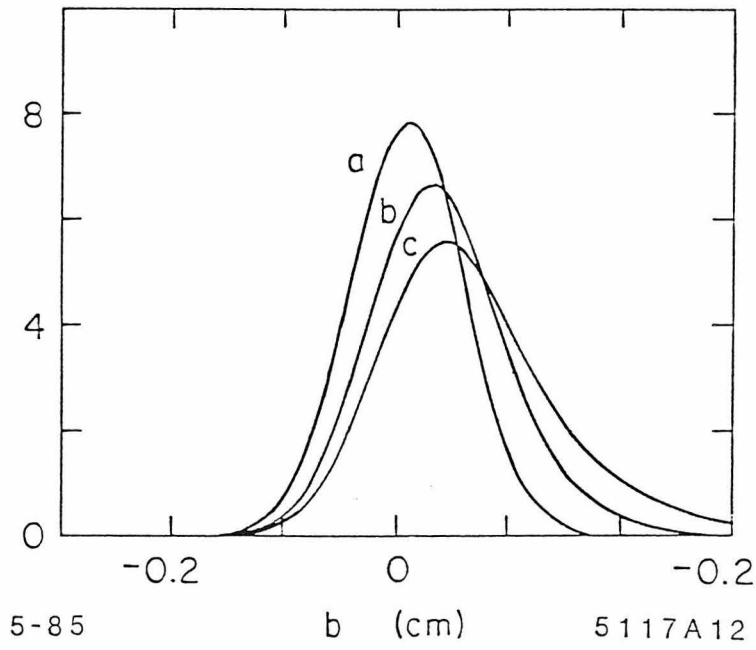

Figure 5.9. The shape of $f^0(b, \kappa, \sigma)$ [formula (5.6)] is shown for $\sigma = 500$ μm (fixed) and κ =100 (a), 400 (b), and 700 μm (c).

The flat background of the impact parameter distribution cannot be reliably estimated *a priori* for the D^0 tracks from the general hadronic tracks because the sources of flat background are different for the two samples. Instead, we take the level of flat background, γ, to be the second parameter of the fit.

Putting everything together, our final properly normalized single event likelihood function is

$$f(b,l,\mathrm{a}) = A\left[(1-\beta-\delta)f^0(b,\kappa,\sigma) + \beta f^0(b,\kappa_B,\sigma) + \delta f^0(b,\kappa_b,\sigma) + \gamma\right] \qquad (5.9)$$

with

$$A = \left[(1-\beta-\delta)\int_{b_1}^{b_2} f^0(b,\kappa,\sigma)db \right. \\ \left. +\beta\int_{b_1}^{b_2} f^0(b,\kappa_B,\sigma)db + \delta\int_{b_1}^{b_2} f^0(b,\kappa_b,\sigma)db + (b_2-b_1)\gamma\right]^{-1},$$

where,

f^0 is a function given by (5.6), and its integration is given by (5.7),

$\kappa = l\eta\sin\theta$, with $\eta = P_{\perp D^0}/M_{D^0}$,

σ is the overall error in the impact parameter, and given by (5.2),

β is the background fraction and given by Table 5.3,

κ_B is a constant (54.6 μm) that represent the positive mean impact parameter of the background,

δ is the fraction of tracks that come from b-quarks (Table 4.9),

κ_b is the mean impact parameter of the D^0 tracks originating from hadrons containing b-quarks (210 μm),

γ is a constant that represents the flat background, which is the second parameter of the fit.

The one-sigma contour of the fit is shown in Figure 5.10, and the results for the individual parameters are $c\tau = 160 \pm 50$ μm and $\gamma = 0.080^{+0.061}_{-0.044}$ cm^{-1}. The value

of γ corresponds to a flat background of about 4% of the total area. The effect of the flat background is not large.

5.3.2 Goodness of Fit and Bias Check

One way to check the goodness of fit is to bin the impact parameters into a histogram and compare it to the expected shape from the result of the fit. The expected shape is given by

$$\left[\sum_{i=1}^{N} f(b, l^0, \mathbf{a}^i)\right] \Delta b,$$

where f is given by the formula (5.9), Δb is the bin width of the histogram, and the lifetime l^0 is the result of the fit. The curve is overplotted in the Fig. 5.7. The χ^2 of the fit is 10.3 for 10 degrees of freedom.[189]

Another way to check the fit, which is independent of the binning, makes use of the similarity between $\mathcal{L}$ and χ^2. The function $\mathcal{L}$ is equivalent to χ^2 up to a constant offset when the function f's are all gaussian with each measurement representing a single data point of the χ^2 estimation. In the case of χ^2, the expected distribution of the minimum is a function of the number of degree of freedom and is well known. For $\mathcal{L}_{\min}$, the expected distribution is not known *a priori*, but can be estimated by a simulation as follows. Using the result of the fit l^0, one impact parameter is generated for each track of the data according to the formula (5.9) using the same σ, κ's etc. as used in the likelihood fit. Then, taking these impact parameters as input data, the likelihood analysis is repeated and $\mathcal{L}_{\min}$ is calculated. The process is repeated from the beginning many times to generate the distribution of $\mathcal{L}_{\min}$. If the fit is good, the measured $\mathcal{L}_{\min}$ should be inside the central distribution. The result is shown in Figure 5.11. The arrow indicates the observed value of $\mathcal{L}_{\min}$. The goodness of the fit is reasonable with a 70% chance of getting a better $\mathcal{L}_{\min}$ than the one observed.

As a byproduct, the bias of the fit is checked by the distribution of $c\tau$ that

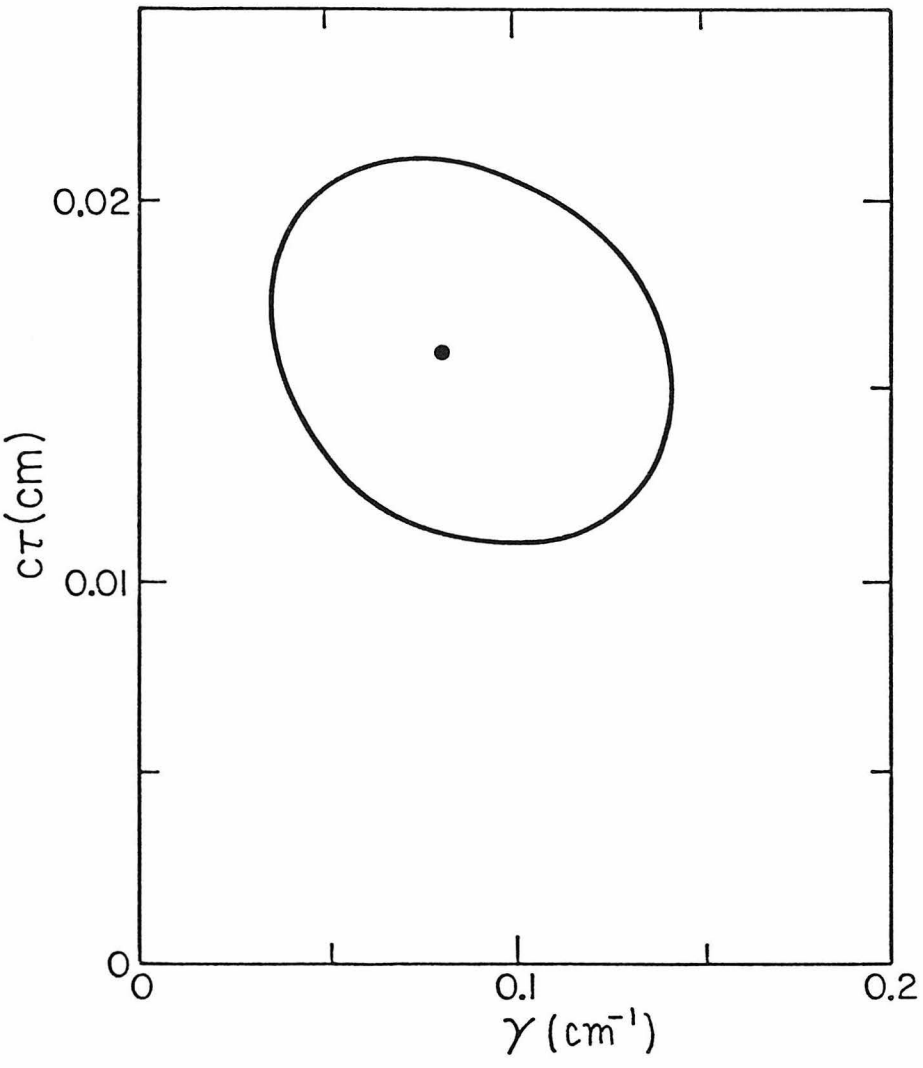

Figure 5.10. One sigma contour of the likelihood fit. The two parameters are the level of the flat background, γ, and the D^0 lifetime $c\tau$. The result for $c\tau$ is $160 \pm 50\mu$m.

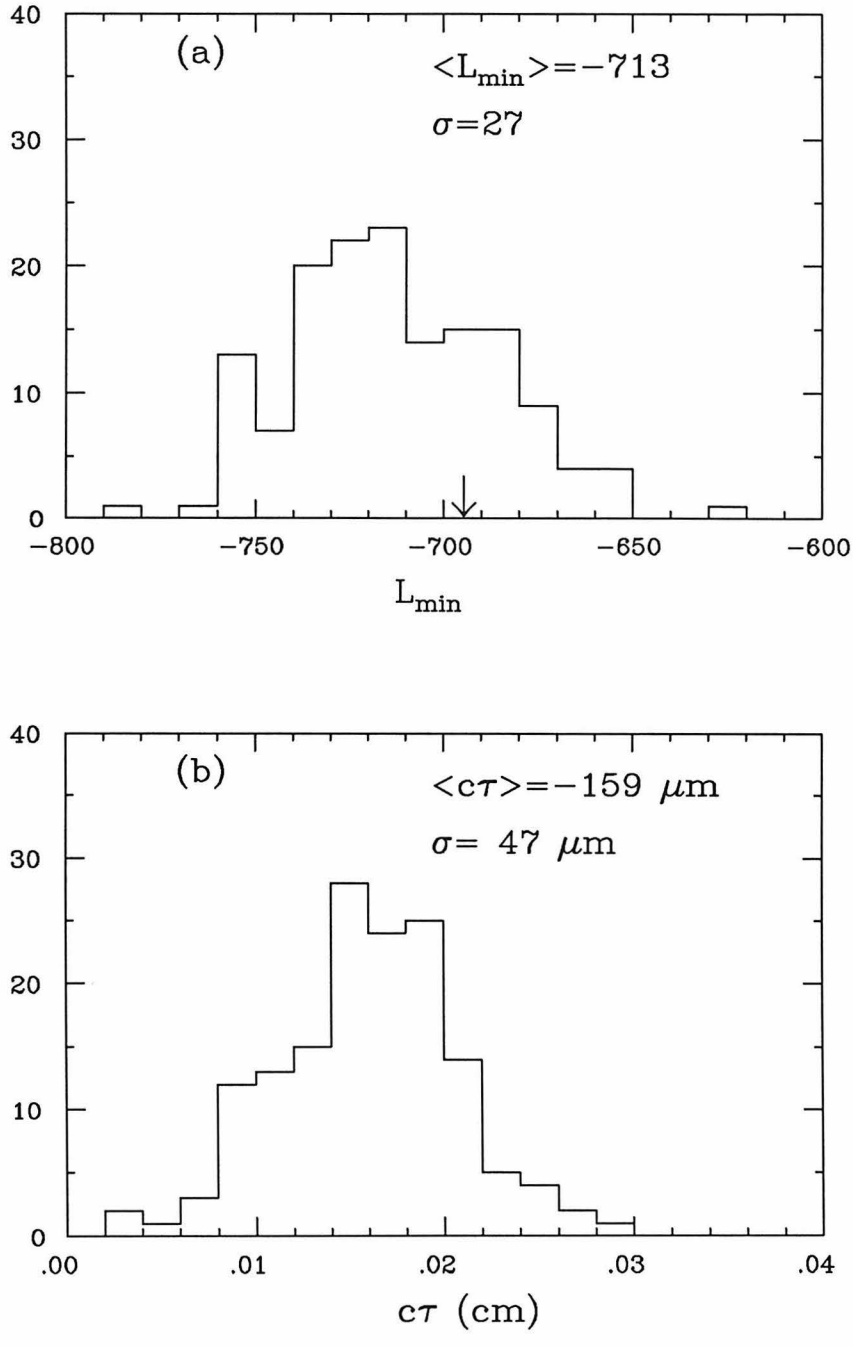

Figure 5.11. (a) The simulated $\mathcal{L}_{\min}$ using the measured $c\tau$ of 160 μm and the actual configuration of each of the 261 tracks. The arrow indicates the $\mathcal{L}_{\min}$ for the actual data. The distribution of $c\tau$ obtained at the same time is shown in (b).

corresponds to each of the simulated $\mathcal{L}_{\min}$. It is shown in Fig. 5.11(b). The mean of the reconstructed $c\tau$'s agrees well with the input, namely the method is bias-free within the statistical error. Also, the width of the distribution (47 μm) is in good agreement with the range of one sigma estimated by $\mathcal{L} - \mathcal{L}_{\min} < 1$, which is ± 50 μm.

5.3.3 Systematic Errors

1) Non D^0 Background (β, κ_B)

The systematic errors of the estimation of non-D^0 background in Table 5.3 are likely to have positive correlations, and have been added linearly. The statistical errors in Table 5.3, on the other hand, are added quadratically. The combined error in $c\tau$ is found to be symmetric and ± 4 μm. The other parameter related to the non-D^0 background is the mean of the impact parameters, κ_B, for those tracks. We used a value of 54.6 μm as determined from tracks kinematically similar to the D^0 candidates [Fig. 5.8(b)]. We estimate the error of κ_B to be ± 15 μm which corresponds to ± 3 μm in $c\tau$. The overall error from the non-D^0 background is then ± 5 μm.

2) Bottom Contribution (δ, κ_b)

The *relative* contribution from b-quarks depends on the ratio of the two ratios $Br(b \to c \to D^{*\pm})/Br(b \to c \to X)$ and $Br(c \to D^{*\pm})/Br(c \to X)$. The first ratio refers to the charm quarks created in b decays, and the second to the charm quarks created by e^+e^- annihilations. In the Monte Carlo, the two ratios were assumed to be the same. When the ratio of the ratios is varied between 4 and 1/4, the resulting $c\tau$ changes at most ± 3 μm. The value of the average b-hadron lifetime, κ_b, also affects the result; we change the average b-lifetime between 0.7 and 2.3×10^{-12} sec[65,66] to get corresponding $c\tau$ errors of $^{+6}_{-7}$ μm. Since the above two systematics are not correlated, they are added in quadrature to give $^{+7}_{-8}$ μm.

3) Mass Assignments

The mass assignment affects the lifetime through the multiple scattering error

$\sigma_{\text{m.s.}}$. The leading tracks are selected by the Čerenkov counter and the effect of the misidentification is negligible. Also, the non-leading tracks in the K-mode can be safely assumed to be pions. However, the non-leading 'K' tracks in the π-mode are not all kaons. Even if we assume them to be all pions the resulting $c\tau$ increases by only 3 μm.

4) Track Momentum Cut

Removing the cut changes the result by less than 1 μm. Setting the cut at 750 MeV/c instead of 250 MeV/c removes 49 tracks, giving a lifetime of 157^{+56}_{-55} μm. Thus, there is no indication of bias from the track momentum cut.

5) Impact Parameter Window

Our fit is relatively insensitive to the window because of the inclusion of the flat tail in the likelihood function. Changing the cut value in the range $\pm$0.5mm around the standard value of 2.5 mm, the variation in $c\tau$ is found to be $^{+7}_{-4}$ μm.

6) Expected Impact Parameter Error (σ)

There are several factors that contribute to the expected error in the impact parameter as shown in (5.2). However, they are highly correlated in the sense that the result has to fit the impact parameter distribution in the final data. The χ^2 of the expected impact parameter distribution to the binned data increase at least one unit when the σ's are scaled by 0.9 and 1.1, which in turn translates to the error in $c\tau$ of $^{+14}_{-7}$ μm. The smaller the σ, the larger the lifetime.

7) $\eta \sin\theta$ Cut

This cut removes the tracks that have little significance in the fit. Removing the cut brings in 174 tracks and the lifetime becomes 150 ± 59 μm. No significant improvement in the error is observed. We take the systematic error due to this cut to be $^{+0}_{-10}$ μm.

8) Errors In η And $\sin\theta$

The direction and the momentum of the D^0 are well determined. The resolutions of η and $\sin\theta$ are found to have negligible effects on the result.

The above items are expected to be independent of each other; thus, they are

added quadratically. The items that have to be treated linearly have been already done so inside each category. The final overall systematic error in $c\tau$ is $^{+18}_{-16}$ μm.

5.4 Summary and Discussion

We have measured the lifetime of D^0 meson using the impact parameters of D^0 tracks with respect to the beam center given by the beam position monitor. The maximum likelihood method used has been found to be bias-free and insensitive to nuclear interactions and gamma conversions at the beam pipe, small misalignments of drift chambers, uncertainties in backgrounds, and the specific choice of cuts used. The resulting $c\tau$ is $160 \pm 50^{+18}_{-16}$ μm which corresponds to the lifetime of $(5.3 \pm 1.7^{+0.6}_{-0.5}) \times 10^{-13}$sec. This is consistent with the world average[183] $(3.9 \pm 0.4) \times 10^{-13}$sec.

If the semileptonic decays do not depend on the flavor of the spectator quark, the semileptonic decay rate of D^0 should be the same as that of D^+. However, the semileptonic decay rate of D^+ may be larger than that of D^0 by $\sim$ 10% if the annihilation channel, $c\bar{d} \rightarrow e^+\nu +$ gluons, which is Cabibbo suppressed, is not helicity suppressed.[88] This may be checked by comparing the ratio of the lifetimes with the ratio of the semileptonic branching fractions. If the semileptonic decay rate is the same for the two mesons, the two ratios should be equal. Using the world average of the $D^{\pm}$ lifetime[183] $(8.2^{+1.1}_{-0.9}) \times 10^{-13}$sec, we obtain $\tau_{D^+}/\tau_{D^0} = 1.6 \pm 0.6$, which is compared with the recent measurement[172] $\mathrm{Br}(D^+ \rightarrow eX)/\mathrm{Br}(D^0 \rightarrow eX) = 2.3^{+0.5+0.1}_{-0.4-0.1}$. Thus, the data are consistent with the same semileptonic decay rates for D^0 and D^+. However, the non-helicity-suppression of the annihilation channel of D^+ in semileptonic mode is not ruled out.

The standard theory can predict the D^0 semileptonic decay rate as a function of the effective charm quark mass [Formula (2.37)]. The large exponent, 5, of the charm quark mass indicates that small variations in m_c result in large changes in Γ^{QCD}_{SL}. Thus, a measurement of the semileptonic decay rate can determine the

effective quark mass precisely. As discussed in Chapter 2, the effective quark mass is a measure of the phase space available to the decay, and expected to be larger than the current quark mass, which is estimated to be[12] around 1.2 GeV/c^2, and smaller than the D^0 mass. Our D^0 lifetime, together with the D^0 semileptonic branching fraction[172] of 7.5$\pm$1.1$\pm$0.4%, gives a D^0 semileptonic decay rate Γ_{SL}^{QCD} of $(1.4\pm0.5)\times10^{11}\text{sec}^{-1}$. Using $m_s/m_c = 0.28\pm0.05$ and $\Lambda = 150\pm100$ MeV [with the formula (2.10)], the effective charm quark mass in a D^0 meson is $m_c = 1.54 \pm 0.12$ GeV/c^2, which is consistent with the typical constituent mass of charm quark, $M_{J/\psi}/2$, but substantially larger than the current mass. The charm quark mass obtained also coincides with the theoretical prejudice on what mass to use in the formula (2.37), which is typically from 1.5 to 1.6 GeV/c^2.

The ratio $\tau_{D^+}/\tau_{D^0} = 1.6 \pm 0.6$ is consistent with unity, but it suggests a shorter lifetime for D^0. Other experiments have also measured the D^0 lifetime with similar sizes of error bars, and a brute-force world average without including our measurement is $(3.9 \pm 0.4) \times 10^{-13}$ sec[183]. If we include our data, the average becomes $(4.0\pm0.4)\times10^{-13}$ sec and the ratio τ_{D^+}/τ_{D^0} is then 2.1$\pm$0.3, which is the same as $\text{Br}(D^+ \to eX)/\text{Br}(D^0 \to eX) = 2.3^{+0.5+0.1}_{-0.4-0.1}$ within the errors. However, the averaging of different experiments is always dangerous, and in order to check further the consistency of the semileptonic branching ratios and the lifetimes of D^0 and D^+ and specifically the annihilation contribution to the D^+ semileptonic decays, we need an experiment with a better resolution and a higher statistics with a capability to observe both D^0's and D^+'s.

Chapter 6.

Upper Limit on $D^0 - \overline{D}^0$ Mixing

In the previous analyses, it has been assumed that there is no $D^0 - \overline{D}^0$ mixing. The $D^0 - \overline{D}^0$ mixing would change the relative sign of π_{D^*} and the leading track resulting in wrong-sign combinations. In this chapter, we will use our data to set an upper limit on $D^0 - \overline{D}^0$ mixing.

6.1 The Signal and Backgrounds

We will use only the K-mode sample because of its relative cleanliness. There are 97 right signs and 15 wrong signs (Table 4.4). In order to estimate the amount of $D^0 - \overline{D}^0$ mixing in the data, the number of wrong-sign combinations expected in the absence of mixing has to be determined. The probability that a kaon misidentification results in a wrong-sign candidate is found to be less than 1 %, and its contribution to the wrong-sign sample is dominated by other backgrounds. This is because the misidentifications are due to gross momentum mismeasurements, which tend to push the events outside the signal region. The inefficiency of the Čerenkov counter itself for a pion well above pion threshold is less than 10^{-3} with 90 % confidence level. There are two major sources of the background: the random combinatorial background and the Cabibbo-suppressed decays of D^0.

The combinatorial background is estimated from a large sample of events generated by the standard Monte Carlo, which is put through the same D^* selection criteria as the data, where genuine D^* combinations are eliminated. By normalizing the background shape for $\Delta M > 0.2$ GeV/c^2 in Figure 6.1(a), the combinatorial

background in each of the right and wrong samples is estimated to be 16.8 events. This leads to $(16.8 \times 2)/(97 + 15)$ =30.0 % of the whole sample (the right-sign and wrong-sign samples) being the combinatorial background. The estimated background shape is shown in Fig.6.1(a) as a dashed line.

Among the Cabibbo-suppressed decay modes of D^0, only the K^-K^+ mode makes a significant contribution. The detection efficiencies for other Cabibbo-suppressed modes are found to be small due to a mass misassignment and/or higher multiplicity decay modes. The ratio of the K^-K^+ channel to the $K^-\pi^+$ channel is measured to be $11.3 \pm 3.0\%$ by the MARK II[171] and $12.5 \pm 1.8 \pm 1.0\%$ by MARK III.[172] The average is $12.1 \pm 1.7\%$. The Monte Carlo simulation is used to estimate the fraction of genuine D^* candidates that result in the wrong-sign sample (feedthrough probability), and the result is 2.6 %. In the above, the genuine D^* candidates are defined to be the ones with both the leading track and the π_{D^*} track correctly found, and the result has been adjusted to be consistent with $Br(K^-K^+)/Br(K^-\pi^+) = 12.1$ % (in the Monte Carlo, the ratio is 8.7 % as seen in the table 4.6).

6.2 Likelihood Function and Result

In order to construct the likelihood function for $D^0 - \overline{D}^0$ mixing, we need the probability that a given candidate in the sample is wrong-sign for a given mixing parameter r. Let b be the background fraction and d the feedthrough probability. One half of the background is wrong-sign; thus, it gives a term $b/2$. The fraction $1-b$ of the sample consists of true D^*'s, of which the fraction r undergoes $D^0 - \overline{D}^0$ mixing, of which the fraction $1-d$ ends up as wrong-sign. For the true D^*'s that do not undergo $D^0 - \overline{D}^0$ mixing, the fraction d becomes wrong-sign because of the feedthrough effect. Thus, the probability that a given candidate is wrong-sign is

$$\frac{b}{2} + (1-b)[r(1-d) + (1-r)d] = (1-b)(1-2d)r + (1-b)d + \frac{b}{2}.$$

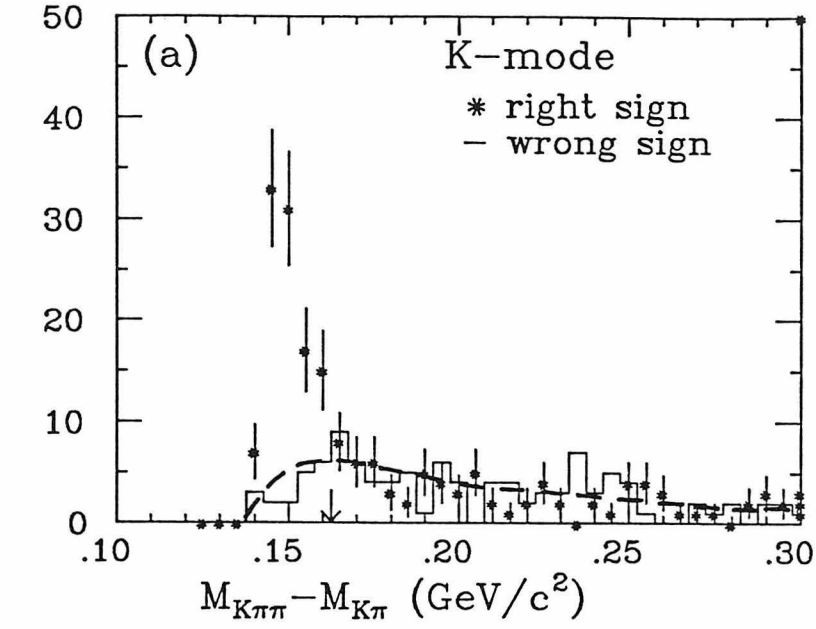

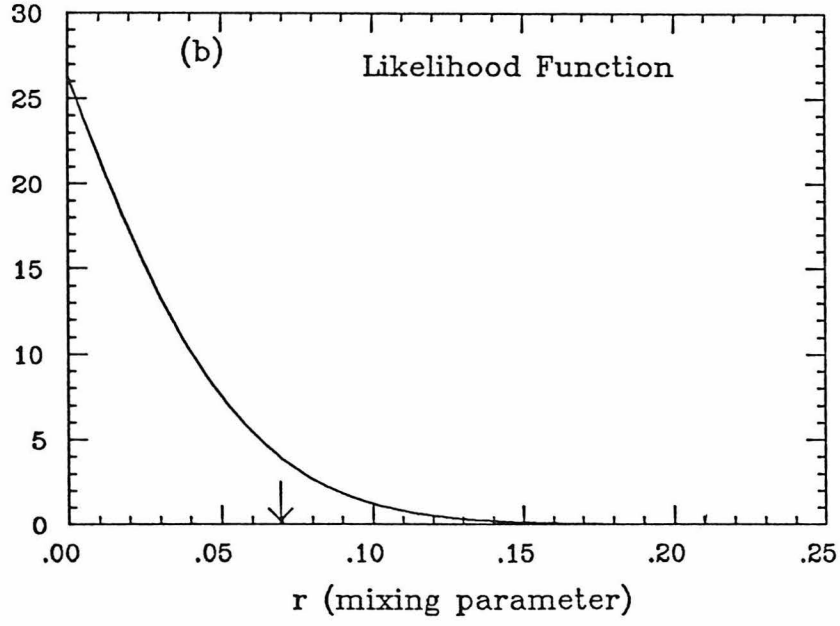

Figure 6.1. (a) The expected background shape obtained by the Monte Carlo is overplotted on the mass difference distributions for the K-mode samples. (b) The likelihood function for the $D^0 - \overline{D}^0$ mixing parameter r. The 90 % confidence level limit is 6.9 %, and indicated by the arrow. The inclusion of the systematic error raises the upper limit to 8.3 %.

Using a binomial distribution, the likelihood function for the mixing parameter r defined by (2.63) is

$$P(r) = f_w(r)^{n_w}[1 - f_w(r)]^{n_r},$$

where

$$f_w(r) = (1-b)(1-2d)r + (1-b)d + \frac{b}{2},$$

is the probability that a candidate is wrong-sign given the mixing parameter r, with

n_r is the number of right signs observed (97),

n_w is the number of wrong signs observed (15),

b is the fraction of background in the whole sample (30.0 %), and

d is the feedthrough probability (2.6%).

The likelihood function is shown in Fig. 6.1(b). The 90% confidence level upper limit r_0 is given by,

$$\frac{\int_0^{r_0} P(r)dr}{\int_0^{\frac{1}{2}} P(r)dr} = 0.9,$$

which gives $r_0 = 6.9\%$.

If the background level is overestimated, the upper limit on $D^0 - \overline{D}^0$ mixing will be underestimated. In our case the background estimate is 16.8 events. Together with the feedthrough due to the Cabibbo-suppressed decays, the expected number of wrong-sign events when there is no mixing is 18.8. The systematic error in the estimated wrong-sign background due to the uncertainties in the background shape and the contribution from Cabibbo-suppressed D^0 decay modes is estimated to be within ± 4 events. We move the background estimation by 4 in the direction that increases the upper limit (namely reduce the expected background). This raises the upper limit on r from 6.9% to 8.3%.

In the presence of CP violation, the mixing parameter is not the same for D^0 and $\overline{D}^0$. In such a case our experimental limit refers to a certain average of the two mixing rates.

6.3 Summary and Discussion

We have set an upper limit on the $D^0 - \overline{D}^0$ mixing using the π/K separation capability of the Čerenkov counter. Including the systematics, the limit is r <8.3 %, where r is defined by (2.63). The likelihood function includes the effect of the combinatorial background and the Cabibbo-suppressed decays of D^0.

The current best upper limit on $D^0 - \overline{D}^0$ mixing is 4.4%[190] and comes from a measurement of wrong-sign double muon production in pion and proton interactions with iron. However, the inclusive nature of the experiment requires a set of assumptions on the mechanism[191] of D^0 production. In contrast, D^{*+} decays provide a model independent method of studying $D^0 - \overline{D}^0$ mixing. The previous upper limits using D^* are 16 % by MARKII,[192] 23% by TASSO,[193] and 11 % by ARGUS.[166] For the experiments with other methods, see Ref. 194.

As discussed in Chapter 2, the mixing rate can be expressed in terms of the masses and decay widths of the two mass eigenstates of the $D^0 - \overline{D}^0$ system (assuming CP invariance). Using the formula (2.63), our limit of 8.3% on r gives the limits on the x and y parameters: $x \equiv \delta m/\Gamma_+ < 0.45$ and $y \equiv \Gamma_-/\Gamma_+ < 0.41$. The D^0 lifetime measured in the previous chapter is considered as the inverse of the average lifetime Γ_+^{-1}. Thus, with $\Gamma_+ = (5.3 \times 10^{-13}\text{sec})^{-1} = 1.2 \times 10^{-12}$ GeV, the limits on δm and Γ_- are,

$$\delta m < 5.4 \times 10^{-13} \text{ GeV}, \quad \Gamma_- < 5.0 \times 10^{-13} \text{ GeV}.$$

Since the mixing can be caused either by the mass difference or by the decay rate difference of the two mass eigenstates, the limit on the mixing results in the limits on these quantities.

Also, the upper limit on the mass difference leads to a stringent limit on charm-changing neutral currents. From the formula (2.67), the limit on the effective coupling constant G_{eff} is 1.3×10^{-11} GeV^{-2}, where we used $B = 1$, $f_D = 0.15$

GeV, and $m_D = 1.865$ GeV. Equivalently, the result can be written as

$$\frac{G_{\text{eff}}}{2\sqrt{2}G_F} < 4 \times 10^{-7}.$$

Strictly speaking, this is for vector boson couplings which are purely right-handed or purely left-handed. Generally, however, the result is of the same order for scalar couplings (e.g., Higgs) or for mixtures of right-handed and left-handed couplings.

Suppose there is a $c \to u$ neutral current that couples to Z^0:

$$\frac{\bar{g}}{2}(g_L\,\bar{c}_L\gamma_\mu u_L + g_R\,\bar{c}_R\gamma_\mu u_R)Z^\mu$$

where $\bar{g} \equiv e/(\sin\theta_W \cos\theta_W)$, and the coupling coefficients g_L and g_R define the strengths of the left-handed and right-handed currents respectively. To be clear about the normalization, the corresponding Lagrangian term for a neutrino in the standard model is

$$\frac{\bar{g}}{2}(\bar{\nu}_L\gamma_\mu\nu_L)Z^\mu.$$

The resulting mass difference is given by[195]

$$\delta m^{(Z)} = \frac{G_F}{\sqrt{2}} f_D^2 m_D \left\{ (g_L - g_R)^2 + \frac{1}{3}\left[g_L^2 + g_R^2 + 4 g_L g_R \left(\frac{m_D}{m_c + m_u} \right)^2 \right] \right\}. \quad (6.1)$$

In deriving the above formula, the B parameter is set to 1, and factorization is assumed with the color factors properly taken into account. Taking $m_D = m_c + m_u$ and $f_D = 0.15$ GeV, our upper limit on the mass difference translates to the following limit on the coupling coefficients:

$$g_L^2 + g_R^2 - \frac{g_L g_R}{2} < 1.2 \times 10^{-6}$$

or $g_L, g_R < 1.1 \times 10^{-3}$.

These limits are much smaller than the ones obtained by the production and decay of charmed quarks by a charm-changing neutral current. The upper limits

on g_L and g_R by processes such as $\nu_\mu N \to \nu_\mu c$ and $c \to e^+e^-X$ are typically 0.1 to 0.3,[195] and thus about two orders of magnitude larger than the upper limit set by $D^0 - \overline{D}^0$ mixing.

QCD corrections similar to the ones used for the non-leptonic decays in Chapter 2 may be applied to the formula (6.1). For certain combinations of α_s and the ratio g_L/g_R, however, the mass difference is highly suppressed leading to larger upper limits on a charm-changing neutral current.[195] This is reminiscent of the suppression of the decay $D^0 \to \bar{K}^0\pi^0$ where the QCD-corrected Hamiltonian combines the initial quark pairs in a almost purely color-octet state. As discussed earlier, however, this is true only if factorization is valid, and there are many reasons to believe that it may not be valid. Thus, the limit quoted above is probably insensitive to QCD corrections when non-perturbative effects such as valence gluons are also taken into account.

The doubly Cabibbo-suppressed decay $D^0 \to K^+\pi^-$ can directly contribute to the wrong-sign signal. This corresponds to $f = K^-\pi^+$ in the formula (2.64). The absolute value of the amplitude ratio $\kappa \equiv A(D^0 \to K^+\pi^-)/A(D^0 \to K^-\pi^+)$ is expected from the naive quark model to be of order $\sin^2\theta_c \sim 0.05$, where θ_c is the Cabibbo angle. As can be seen from (2.64), the effect of κ is small for the values of x and y we are concerned about here (namely ~ 0.4).

Within the framework of the standard model, the $D^0 - \overline{D}^0$ mixing is likely to be dominated by long distance effects, and the theoretical upper limit is ~ 0.002 (see Chapter 2). Our upper limit is still well above this value. In the future experiment that probes below 1 % level, the doubly Cabibbo-suppressed decay can become a limiting factor. One possible solution is to measure the decay

$$\psi'' \to D^0\overline{D}^0 \to (K^-\pi^+)(K^-\pi^+) \quad \text{or} \quad (K^+\pi^-)(K^+\pi^-).$$

The $D^0\overline{D}^0$ pair is generated in the state $D^0\overline{D}^0 - \overline{D}^0D^0$ because the orbital angular momentum of the pair is one (or $C = -$). The resulting interference effect cancels the effect of the doubly Cabibbo-suppressed decay leaving only the mixing effect.

The wrong-sign right-sign ratio

$$\frac{N[(K^-\pi^+)(K^-\pi^+)] + N[(K^+\pi^-)(K^+\pi^-)]}{N[(K^-\pi^+)(K^+\pi^-)]}$$

directly gives the mixing parameter p defined by (2.62) with $\xi = 0$ (i.e., CP is assumed).

Chapter 7.

Conclusion

While there is no doubt about the excitement and possibility of unexpected discoveries at newly opened high energy frontiers, many important experiments can be done only at certain energies. The charmonium states continue to be essentially the only place for the detailed study of the charmed mesons, and the neutral kaon system is so far the only place we can study CP violation, to name only two.

The energy at PEP is optimum for the D^0 lifetime study. At the ψ'', the D^0 lifetime experiment cannot be done because the velocity of the D^0's is almost zero leading to small impact parameters. At the Z^0 energy, on the other hand, the increasing multiplicity of event makes the combinatorial background more difficult to handle.

There is another important reason why the D^* analyses presented here are possible at our energy. As emphasized many times, the crucial component of the analyses is the π/K separation provided by the Čerenkov counter with the range of separation between 2.6 GeV/c to 9.2 GeV/c. At center-of-mass energies of 3 to 5 GeV, it is impossible to use the gas threshold Čerenkov counter for the separation of K and π. And at higher energy than ours, a lighter gas would be needed to cover the higher momentum region, which would reduce the light yield. In either case, one cannot effectively utilize the Čerenkov counter without complicated techniques such as pressurization or ring imaging. The π/K separation thus provided by the Čerenkov counter made it possible for us to reduce and control the background of D^* sample and to set an upper limit on $D^0 - \overline{D}^0$ mixing.

The D^* physics in general can be divided into three categories:

1. It can serve to tag charm events. For example, one can study the cross section and the forward-backward asymmetry of $c\bar{c}$ production. One can also study event shapes, charged multiplicity, etc., and compare them with those of general events.
2. One can study the hadronization of quarks by the momentum distribution of the D^*. Namely, the fragmentation function of the charmed quark can provide useful information on hadronization in general.
3. It provides a clean D^0 factory. The low Q value of the decay $D^{*+} \rightarrow D^0\pi^+$ makes it possible to find D^0's in environments where it is difficult otherwise. Using the D^0's thus obtained, one can study its lifetime and $D^0 - \overline{D}^0$ mixing. Similarly, if the decay $D^{*+} \rightarrow D^+\pi^0$ is detected, it can be used as a D^+ factory.

We have investigated at least one subject in each of the three categories, and the measurement was found consistent with the standard model in each subject. The D^*'s were found to be produced abundantly as expected. The D^0 lifetime measurement led to an estimate of the D^0 semileptonic decay rate, which was found consistent with the theoretical prediction. The D^0 lifetime and the upper limit on $D^0 - \overline{D}^0$ mixing together gave a limit on the charm-changing neutral current, which is highly suppressed in the standard model.

In some cases, the information obtained was more than just a verification of the standard model. The difference of the lifetimes of D^0 and D^+ indicated a certain mechanism to suppress the nonleptonic decay rate of D^+ or to enhance that of D^0, while the charm fragmentation function provided a strong case for the string picture of hadronization.

The standard model, however, is far from complete. The hadronization process is still poorly understood, the nonleptonic decays are just beginning to be sorted out, and there are fundamental questions left to be answered such as the number of generations, the still unobserved Higgs boson(s), and the possible extention to a larger symmetry group.

These problems can be attacked at various energy ranges. Often low-energy experiments such as the rare kaon decays and CP violation probe the interaction of much heavier quarks. On the other hand, the information obtained for $D^0 - \overline{D}^0$ mixing or $B^0 - \overline{B}^0$ mixing stimulates further studies on $K^0 - \bar{K}^0$ mixing, and the hadronization model developed for heavy quarks sheds light on the physics of strong resonances. Through interactions between different kinds of physics, different points of view, or different techniques, we can attain a better understanding of nature, which, I believe, is one.

Appendix A.

The V − A 3-body Phase-Space Factor

For the $V-A$ decay $f_0 \to f_1 f_2 \bar{f}_3$, the phase space correction factor [see (2.44)] is given by[88]

$$I(x_1,x_2,x_3) = 12\int_{(x_1+x_2)^2}^{(1-x_3)^2} \frac{d\xi}{\xi}(\xi-x_1^2-x_2^2)(1+x_3^2-\xi)W(\xi,x_1^2,x_2^2)W(1,x_3^2,\xi), \quad (A.1)$$

where

$$W(a,b,c) = \Big[(a-b-c)^2 - 4bc\Big]^{1/2}$$

and $x_i = m_i/m_0$. In the massless limit, where $m_i \to 0 (i = 1,2,3)$, f_1 and f_2 have the same energy spectrum peaking at the high energy end, while the spectrum of $\bar{f}_3$ peaks in the middle. This is reflected in (A.1) as the symmetry between x_1 and x_2. If only one of the three final fermions is massive, (A.1) simplifies to

$$\begin{aligned} g(x) \equiv I(x,0,0) =& I(0,x,0) = I(0,0,x) \\ =& 1 - 8x^2 - 24x^4 \ln x + 8x^6 - x^8. \end{aligned}$$

Figure A.1 shows $I(x_1,x_2,x_3)$ for $x_2 = 0$ (a) and for $x_2 = x_3$ (b). The case (a) applies to $c \to su\bar{s}$, $b \to cs\bar{c}$, etc., when current masses are used. The case (b) applies to $c \to us\bar{d}$ when constituent masses are used. Since the current masses of u and d are small (a few MeV), the nonleptonic decay is suppressed with respect to the semileptonic decay by the mass effect only when the constituent masses, which are about 200 to 300 MeV for u and d, are used.

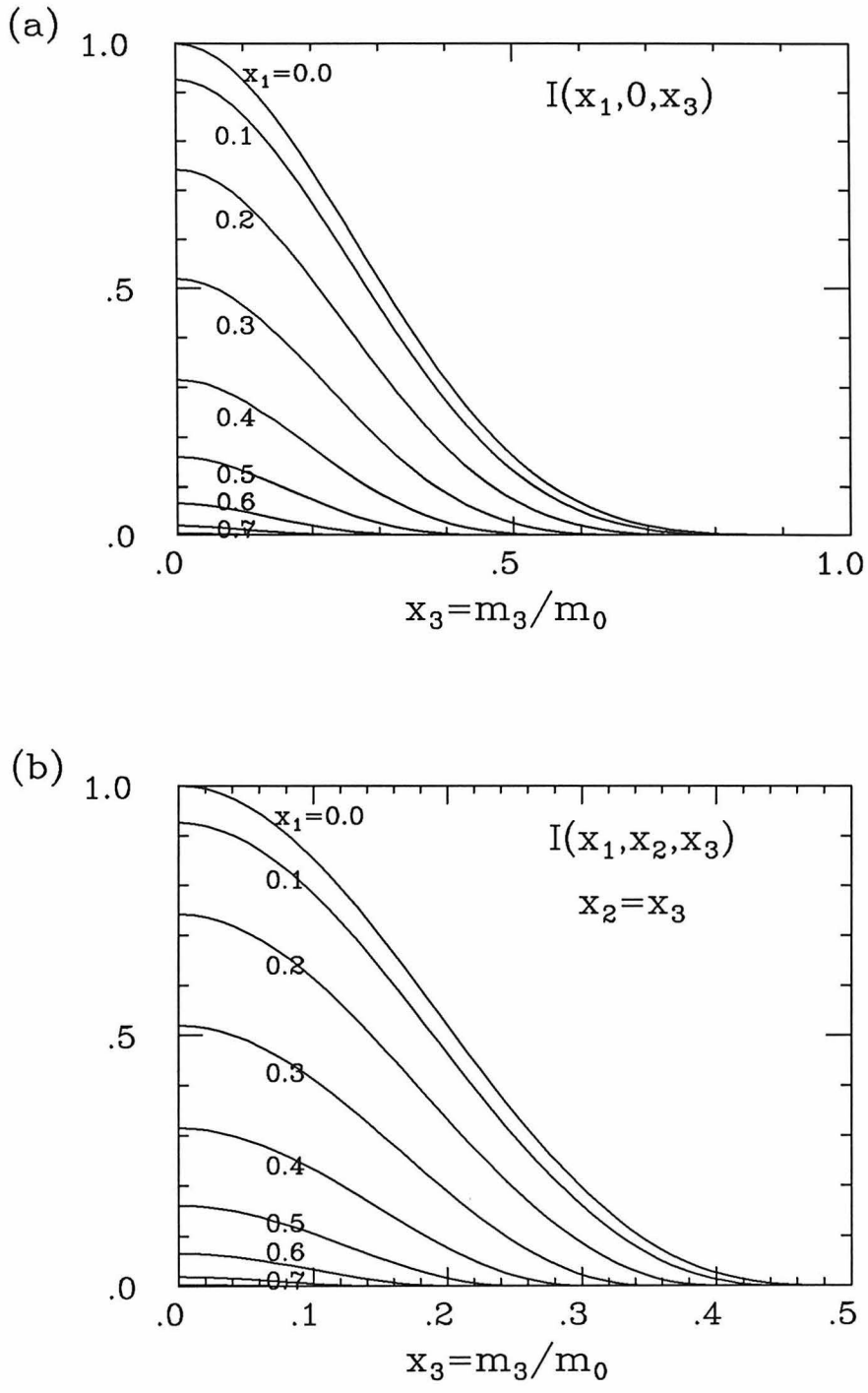

Figure A.1. The $V - A$ phase space correction factor $I(x_1, x_2, x_3)$ is shown for $x_2 = 0$ (a) and for $x_2 = x_3$ (b).

Appendix B.

$D^0 - \overline{D}^0$ Mixing Formulae

Here, we will derive the formulas for the mixing rates, (2.62) and (2.64). From (2.57) and (2.54), the time evolutions of $|D_1\rangle$ and $|D_2\rangle$ are given by

$$|D_i(t)\rangle = e_i|D_i\rangle, \quad e_i \equiv \exp(-im_i t - \frac{\gamma_i}{2}t) \quad (i = 1, 2). \tag{B.1}$$

Solving (2.56) for $|D^0\rangle$ and $|\overline{D}^0\rangle$, we obtain

$$\begin{aligned} |D^0\rangle &= \frac{1}{2A(1+\epsilon)}(|D_1\rangle + |D_2\rangle) \\ |\overline{D}^0\rangle &= \frac{1}{2A(1-\epsilon)}(|D_1\rangle - |D_2\rangle). \end{aligned} \tag{B.2}$$

The $|D_1\rangle$ and $|D_2\rangle$ components in (B.2) evolve according to (B.1). Thus, a state that is purely $|D_0\rangle$ ($|\overline{D}^0\rangle$) at $t = 0$ will evolve to $|D^0(t)\rangle$ ($|\overline{D}^0(t)\rangle$) at time t, where

$$\begin{aligned} |D^0(t)\rangle &= \frac{1}{2}\left[(e_1 + e_2)|D^0\rangle + \frac{1-\epsilon}{1+\epsilon}(e_1 - e_2)|\overline{D}^0\rangle\right], \\ |\overline{D}^0(t)\rangle &= \frac{1}{2}\left[(e_1 + e_2)|\overline{D}^0\rangle + \frac{1+\epsilon}{1-\epsilon}(e_1 - e_2)|D^0\rangle\right]. \end{aligned} \tag{B.3}$$

First, we assume $\overline{D}^0 \not\to f$ and $D^0 \not\to \bar{f}$; thus, for a state that is $|D^0\rangle$ at $t = 0$, the decay probability to the final state f ($\bar{f}$) in the time interval $(t, t+dt)$ is proportional to $|\langle D^0|D^0(t)\rangle|^2$ ($|\langle\overline{D}^0|D^0(t)\rangle|^2$). We define the 'intensities' to be

$$\begin{aligned} I_D(t) &\equiv |\langle D^0|D^0(t)\rangle|^2, \qquad I_{\overline{D}}(t) \equiv |\langle\overline{D}^0|D^0(t)\rangle|^2, \\ \bar{I}_D(t) &\equiv |\langle D^0|\overline{D}^0(t)\rangle|^2, \qquad \bar{I}_{\overline{D}}(t) \equiv |\langle\overline{D}^0|\overline{D}^0(t)\rangle|^2, \end{aligned}$$

and, from (B.3), they are given by

$$
\begin{aligned}
I_D(t) = \bar{I}_{\overline{D}}(t) &= \frac{1}{4}(e^{-\gamma_1 t} + e^{-\gamma_2 t} + 2e^{-\Gamma_+ t}\cos\,\delta m t), \\
I_{\overline{D}}(t) &= \frac{1}{4}\frac{1-\xi}{1+\xi}(e^{-\gamma_1 t} + e^{-\gamma_2 t} - 2e^{-\Gamma_+ t}\cos\,\delta m t), \\
\bar{I}_D(t) &= \frac{1}{4}\frac{1+\xi}{1-\xi}(e^{-\gamma_1 t} + e^{-\gamma_2 t} - 2e^{-\Gamma_+ t}\cos\,\delta m t),
\end{aligned}
\tag{B.4}
$$

where $\Gamma_\pm \equiv \frac{1}{2}(\gamma_1 \pm \gamma_2)$, $\delta m = m_2 - m_1$, and ξ is defined by (2.60). We assume that $\Gamma(D^0 \to f) = \Gamma(\overline{D}^0 \to \bar{f})$, or more precisely, $|\langle f|H_W|D^0\rangle| = |\langle \bar{f}|H_W|\overline{D}^0\rangle|$, where H_W is the Hamiltonian responsible for the decays. Then, the mixing rate p is simply given by the ratio of the corresponding intensities integrated over time:

$$
\begin{aligned}
p \equiv \frac{Br(D^0 \to \bar{f})}{Br(D^0 \to f)} &= \frac{\int_0^\infty I_{\overline{D}}(t)dt}{\int_0^\infty I_D(t)dt} = \frac{1-\xi}{1+\xi}\cdot\frac{\frac{1}{\gamma_1}+\frac{1}{\gamma_2}-\frac{2\Gamma_+}{\Gamma_+^2+\delta m^2}}{\frac{1}{\gamma_1}+\frac{1}{\gamma_2}+\frac{2\Gamma_+}{\Gamma_+^2+\delta m^2}} \\
&= \frac{1-\xi}{1+\xi}\cdot\frac{1-\alpha}{1+\alpha},
\end{aligned}
\tag{B.5}
$$

where

$$
\alpha = \frac{\Gamma_+^2 - \Gamma_-^2}{\Gamma_+^2 + \delta m^2}.
$$

Similarly,

$$
\bar{p} \equiv \frac{Br(\overline{D}^0 \to f)}{Br(\overline{D}^0 \to \bar{f})} = \frac{\int_0^\infty \bar{I}_D(t)dt}{\int_0^\infty \bar{I}_{\overline{D}}(t)dt} = \frac{1+\xi}{1-\xi}\cdot\frac{1-\alpha}{1+\alpha}. \tag{B.6}
$$

Thus, (2.62) has been derived.

Next, we will consider the case when $\overline{D}^0$ can also decay to f and D^0 to $\bar{f}$. For simplicity, we take f to be a state consisting of two spin-0 particles, assume CP invariance, and choose the phase convention for f and $\bar{f}$ such that $CP|f\rangle = |\bar{f}\rangle$. Then,

$$
\begin{aligned}
\langle f|H_W|D^0\rangle &= \langle f|(CP)^\dagger(CP)H_W(CP)^\dagger(CP)|D^0\rangle = \langle \bar{f}|H_W|\overline{D}^0\rangle, \\
\langle f|H_W|\overline{D}^0\rangle &= \langle f|(CP)^\dagger(CP)H_W(CP)^\dagger(CP)|\overline{D}^0\rangle = \langle \bar{f}|H_W|D^0\rangle,
\end{aligned}
$$

which leads to the corresponding relations between amplitudes:

$$\begin{aligned} a &\equiv A(D^0 \to f) = A(\overline{D}^0 \to \bar{f}), \\ b &\equiv A(\overline{D}^0 \to f) = A(D^0 \to \bar{f}). \end{aligned} \tag{B.7}$$

We define $A_f(t)$ $(A_{\bar{f}}(t))$ to be the amplitude that a state that is purely D^0 at $t = 0$ decays to f $(\bar{f})$ at time t. Similarly, $\bar{A}_f(f)$ and $\bar{A}_{\bar{f}}$ are defined for a state that is purely $\overline{D}^0$ initially. From (B.7), they are given by

$$\begin{aligned} A_f(t) &= a\langle D^0|D^0(t)\rangle + b\langle \overline{D}^0|D^0(t)\rangle, \\ A_{\bar{f}}(t) &= a\langle \overline{D}^0|D^0(t)\rangle + b\langle D^0|D^0(t)\rangle, \\ \bar{A}_f(t) &= a\langle D^0|\overline{D}^0(t)\rangle + b\langle \overline{D}^0|\overline{D}^0(t)\rangle, \\ \bar{A}_{\bar{f}}(t) &= a\langle \overline{D}^0|\overline{D}^0(t)\rangle + b\langle D^0|\overline{D}^0(t)\rangle. \end{aligned}$$

Using (B.3) with $\epsilon = 0$ (CP is conserved), we have

$$A_f(t) = \bar{A}_{\bar{f}}(t), \qquad A_{\bar{f}}(t) = \bar{A}_f(t). \tag{B.8}$$

The mixing rates are still defined by (2.61). Thus,

$$\begin{aligned} p =& \frac{\int_0^\infty |A_{\bar{f}}(t)|^2 dt}{\int_0^\infty |A_f(t)|^2 dt} \\ =& \frac{\int_0^\infty |(e_1 - e_2)a + (e_1 + e_2)b|^2 dt}{\int_0^\infty |(e_1 + e_2)a + (e_1 - e_2)b|^2 dt} \\ =& \frac{1 - \alpha'}{1 + \alpha'}, \end{aligned} \tag{B.9}$$

where

$$\alpha' = \frac{1 - |\kappa|^2 - 2|\kappa| x \sin\phi}{1 + |\kappa|^2 + 2|\kappa| y \cos\phi} \cdot \frac{1 - y^2}{1 + x^2}, \tag{B.10}$$

$$x = \frac{\delta m}{\Gamma_+}, \quad y = \frac{\Gamma_-}{\Gamma_+},$$

and

$$\kappa \equiv |\kappa| e^{i\phi} = b/a.$$

Because of (B.8), $\bar{p} = p$.

In the SU(3) limit, the quark model and factorization gives $\kappa = \tan^2 \theta_c$ (real), where θ_c is the Cabibbo angle. Together with the assumption that x, y and κ are small and of the same order, (B.9) reduces to

$$p = \kappa^2 + \kappa y + \frac{1}{2}(x^2 + y^2),$$

which was first derived by Kingsley *et al.*[196]

At first glance, it may seem that the phase ϕ in (B.10) can be rotated away by redefining the relative phase of $|D^0\rangle$ and $|\overline{D}^0\rangle$. In fact, if one adopts the phase convention $|\overline{D}^0\rangle \equiv e^{-i\phi} CP|D^0\rangle$ instead of $|\overline{D}^0\rangle \equiv CP|D^0\rangle$, the parameter $\kappa \equiv A(\overline{D}^0 \to f)/A(D^0 \to f)$ becomes real and positive. The definition of $|D_1\rangle$ and $|D_2\rangle$, however, is such that they are CP eigenstates when CP is a good symmetry. Namely, the definition of $|D_i\rangle$ is now (assuming CP)

$$\begin{aligned} |D_i\rangle \equiv & \frac{1}{\sqrt{2}}(|D^0\rangle \pm CP|D^0\rangle) \\ = & \frac{1}{\sqrt{2}}(|D^0\rangle \pm e^{i\phi}|\overline{D}^0\rangle). \end{aligned}$$

Also, the equations (B.7) change to

$$\begin{aligned} a \equiv A(D^0 \to f) &= e^{i\phi} A(\overline{D}^0 \to \bar{f}), \\ b \equiv A(\overline{D}^0 \to f) &= e^{-i\phi} A(D^0 \to \bar{f}). \end{aligned}$$

With these required changes, one recovers (B.9) and (B.10) even though κ is now real and positive. Thus, ϕ is a physical parameter.

REFERENCES

1. S. Sakata, Prog. Theor. Phys. **16**, 686 (1956); M. Gell-Mann, Phys. Rev. **125**, 1267 (1962); Y. Ne'eman, Nucl. Phys. **26**, 222 (1961).
2. P. Tarjanne and V. Teplitz, Phys. Rev. Lett. **11**, 447 (1963); M. Gell-Mann, Phys. Lett. **8**, 214 (1964); D. Amati *et al.*, Phys. Lett. **11**, 190 (1964); B. Bjorken and S. Glashow, Phys. Lett. **11**, 255 (1964); Z. Maki and Y. Ohnuki, Prog. Theor. Phys. **32**, 144 (1964); Y. Hara, Phys. Rev. **134**, B701 (1964).
3. S. Weinberg, Phys. Rev. Lett. **19**, 1264 (1967); A. Salam, in Proceedings of the 8th Nobel Symposium (Almqvist & Wilksells, Stockholm, 1968).
4. S. Glashow, Iliopoulos, and Maiani, Phys. Rev. D**2**, 1285 (1970).
5. J. Aubert *et al.*, Phys. Rev. Lett. **33**, 1404 (1974); J. Augustin *et al.*, Phys. Rev. Lett. **33**, 1406 (1974).
6. The status on the eve and right after the discovery is vividly described in; M. Gaillard, B. Lee, and L. Rosner, Rev. Mod. Phys. **47**, 277 (1975).
7. M. Perl *et al.*, Phys. Rev. Lett. **35**, 1489 (1975).
8. S. Herb *et al.*, Phys. Rev. Lett. **39**, 252 (1977).
9. UA1 collaboration (G. Arnison *et al.*), Phys. Lett. **122B**, 103 (1983) and Phys. Lett. **126B**, 398 (1983).
10. UA1 collaboration (G. Arnison *et al.*), Phys. Lett. **147B**, 493 (1984).
11. For example, T. D. Lee, 'Particle Physics and Introduction to Field Theory,' (Harwood Academic Publishers, 1981); L. Okun, 'Leptons and Quarks,' (North Holland, 1982); D. Perkins, 'Introduction to High Energy Physics,' 2nd ed. (Addison-Wesley, 1982); E. Commins and P. Bucksbaum, 'Weak Interactions of Leptons and Quarks,' (Cambridge University Press, 1983); H. Georgi, 'Weak Interactions and Modern Particle Theory,' (Benjamin/Cummings, 1984), to name a few. The proliferation of textbooks on the subject testifies to the maturity of the standard model.
12. The current quark masses are evaluated at Q^2 =(quark mass)^2. J. Gasser

and H. Leutwyler, Phys. Rep. **87**, 77 (1982).

13. G. Sterman and S. Weinberg, Phys. Rev. Lett. **39**, 1436 (1977).
14. The cross section is the combined yield from both the electron and the positron in the initial state.
15. G. Bonneau and F. Martin, Nucl. Phys. **B27**, 381 (1971).
16. F. Berends and R. Kleiss, Nucl. Phys. **B178**, 141 (1981).
17. S. Brodsky, C. Carlson, and R. Suaya, Phys. Rev. D**14**, 2264.
18. F. Berends, K. Gaemers, and R. Gastmans, Nucl. Phys. **B63**, 381.
19. For example, see; F. Berends, R. Kleiss and S. Jadach, Nucl. Phys. **B202**, 63 (1982). When the CM energy is close to regions with many resonances, such as just above the charm threshold, numerical estimation of hadron part of the vacuum polarization is necessary. However, our beam energy is sufficiently far from resonances that quark loop approximation is adequate when proper masses are used (Table 1.1).
20. T. Appelquist and H. Georgi, Phys. Rev. D**8**, 4000 (1973).
21. For a review of experimental values of Λ, see, for example, G. Lepage, in the Proceedings of the 1983 International Symposium on Lepton and Photon Interactions at High Energies (Ithaca, 1983).
22. J. Ellis, M. Gaillard, and G. Ross, Nucl. Phys. **B111**, 253 (1976).
23. We follow the notation used in M. Böhm and W. Hollik, Nucl. Phys. **B204**, 45 (1982).
24. A. Bodek, in the Proceedings of the 15th Spring Symposium on High Energy Physics, vol. 1, (Leipzig, 1984) p. 234; J. Knobloch, *ibid.*, p. 235; M. Davier, *ibid.*, p. 238.
25. D. Gross and F. Wilczek, Phys. Rev. Lett. **30**, 1343 (1973); H. Politzer, Phys. Rev. Lett. **30**, 1346.
26. K. Wilson, Phys. Rev. D**10**, 2445 (1974).
27. Y. Nambu, Phys. Lett. **80B**, 372 (1978).
28. J. Bjorken, informal remarks at the New York Academy of Science Conference

on High Energy Physics, 1973 (unpublished); A. Casher, J. Kogut, and L. Susskind, Phys. Rev. D**10**, 732 (1974); A. Casher, H. Neuberger, and S. Nussinov, Phys. Rev. D**20**, 179 (1979).

29. This can be seen as follows. Because of the longitudinal invariance of flux tube, at far from edges, the rapidity distribution should stay the same when boosted longitudinally. On the other hand, the definition of rapidity is such that its distribution is simply displaced when boosted. Thus, the distribution has to be flat.
30. R. Field and R. Feynman, Phys. Rev. D**15**, 2590 (1977); and Nucl. Phys. **B136** 1 (1978).
31. A. Ali, E. Pietarinen, and J. Willrodt, DESY Internal Report, DESY T-80/01.
32. P. Hoyer, Acta. Phys. Polon. **B11**, 133 (1980).
33. B. Andersson, *et al.*, Phys. Rep. **97**, 31 (1983); T. Sjöstrand, Comp. Phys. Commun. **27**, 243, (1982) and Comp. Phys. Commun. **28**, 229, (1983).
34. X. Artru and G. Mennessier, Nucl. Phys. **B70**, 93 (1974); X. Artru, Phys. Rep. **97**, 147 (1983).
35. T. Gottschalk, Nucl. Phys. **B239**, 325 (1984); *ibid.* 349 (1984).
36. K. Johnson and C. Thorn, Phys. Rev. D**13**, 1934 (1976).
37. M. Lüscher, G. Münster, and P. Weisz, Nucl. Phys. **B180**, 1 (1981).
38. Y. Nambu, Lectures at the Copenhagen Summer Symposium (1970); P. Goddard, J. Goldstone, C. Rebbi, and C. Thorn, Nucl. Phys. **B56**, 109 (1973); Also, see Ref. 34.
39. For recent review of the experimental data as well as the effect of the quark mass, see; F. Lizzi and C. Rosenzweig, Phys. Rev. D**31**, 1685 (1985). A simple derivation can be found in the text book by D. Perkins (Ref. 11 p. 175).
40. The converse is not necessarily true. The 135° kinks in Fig. 2.5(b) does not carry local energy-momentum, while the 90° kink is a gluon with local

energy-momentum.

41. C. F. Weizsäcker, Z. Phys. **88**, 612 (1934); E. J. Williams, Phys. Rev. **45**, 729 (1934).
42. G. Altarelli and G. Parisi, Nucl. Phys. **B126**, 298 (1977).
43. K. Konishi, A. Ukawa, and G. Veneziano, Nucl. Phys. **B157**, 45 (1979).
44. R. Odorico, Nucl. Phys. **B172** 157 (1980); P. Mazzanti and R. Odorico, Phys. Lett. **95B**, 133 (1980).
45. F. Paige and S. Protopopescu, published in the Proceedings of Snowmass Summer Study (Snowmass, 1982) p. 471.
46. D. Amati and G. Veneziano, Phys. Lett. **83B**, 87 (1979).
47. R. Field and S. Wolfram, Nucl. Phys. **B213**, 65 (1983).
48. T. Gottschalk, Nucl. Phys. **B214**, 201 (1983).
49. B. Webber, Nucl. Phys. **B238**, 492 (1984); G. Marchesini and B. Webber, Nucl. Phys. **B238**, 1 (1984).
50. A. Mueller, Phys. Lett. **104B**, 161 (1981).
51. The constant $\beta \equiv 1/(kT)$ is adjusted so that the mean value of m_0 becomes the typical hadronic scale.
52. M. Suzuki, Phys. Lett. **71B**, 139 (1977).
53. T. Gottschalk, Nucl. Phys. **B227**, 413 (1983).
54. J. Bjorken, Phys. Rev. D**17**, 171 (1978).
55. C. Peterson *et al.*, Phys. Rev. D**27**, 105 (1983). S. J. Brodsky and C. Peterson and N. Sakai, Phys. Rev. D**23**, 2745 (1981).
56. M. Bowler, Z. Phys. **C11**, 169 (1981).
57. Strictly speaking, the fragmentation function does not depend on E_q when $E_q^2 b/\kappa^2 \gg 1$ and $E_q \gg m_Q$.
58. B. Andersson, G. Gustafson, and B. Söderberg, Z. Phys. **C20**, 317 (1983).
59. M. Kobayashi and T. Maskawa, Prog. Theor. Phys. **49**, 652 (1973). The original parametrization can be obtained from the one in the text by the transformations $s_1 \to -s_1$, $s_2 \to -s_2$ and $\theta_3 \to \theta_3 + \pi$ (up to a typo in the

original paper).

60. R. Shrock and L-L Wang, Phys. Rev. Lett. **41**, 1692 (1978); E. Paschos and U. Türke, Phys. Lett. **116B**, 360 (1982), and references therein.
61. M. Bourquin *et al.*, Z. Phys. **C21**, 27 (1983). Also, see Ref. 60.
62. H. Abramowitz *et al.*, Z. Phys. **C15**, 19 (1982).
63. J. Lee-Franzini, in the Proceedings of the Europhysics Topical Conference: Flavor Mixing in Weak Interactions, (Erice, 1984) p. 217. The data used are from W. Bacino *et al.*, Phys. Rev. Lett. **43**, 1073 (1979).
64. A. Chen *et al.*, Phys. Rev. Lett. **52**, 1084 (1984); C. Klopfenstein *et al.*, Phys. Lett. **130B**, 444 (1983).
65. N. Lockyer *et al.*, Phys. Rev. Lett. **51**, 1316 (1983); E. Fernandez *et al.*, Phys. Rev. Lett. **51**, 1022 (1983); M.Althoff *et al.*, Phys. Lett. **149B**, 524 (1984).
66. D. Klem *et al.*, Phys. Rev. Lett. **53**, 1873 (1984).
67. K. Kleinknecht, Comm. Nucl. Part. Phys. **14**, 219 (1984). The data from the D meson semileptonic decay were not used, but the result is not sensitive to the inclusion of the data. A more conservative numbers are given by F. Gilman in Rev. Mod. Phys. **56**, 296 (1984). Also, see; K. Kleinknecht and B. Renk, Phys. Lett. **130B**, 459 (1983); F. Gilman and J. Hagelin, Phys. Lett. **133B**, 443 (1983); E. Paschos, B. Stech, and U. Türke, Phys. Lett. **128B**, 240 (1983); L-L Chau and W-Y Keung, Phys. Rev. D**29**, 592 (1984).
68. See, for example, B. Stech, in the Proceedings of the Europhysics Topical Conference: Flavor Mixing in Weak Interactions, (Erice, 1984) p. 735; H. Harari, a talk given at the 12th Annual SLAC Summer Institute on Particle Physics (1984), WIS-85/7/-Ph.
69. L. Wolfenstein, Phys. Rev. Lett. **51**, 1945 (1983).
70. Particle Data Group, Rev. Mod. Phys. **56**, (1984).
71. Obtained from $|\epsilon_K| \approx (2|\eta_{+-}| + |\eta_{00}|)/3$. The values for $|\eta_{+-}|$ and $|\eta_{00}|$ are from Ref. 70.

72. The relevant numbers used are $\lambda = 0.22$, $m_c = 1.5$ GeV, and $\Lambda(\mathrm{QCD}) = 0.1$ GeV. The condition $m_t << m_W$ is not used. L. Wolfenstein, to be published in the Proceedings of the Fifth Moriond Workshop on Heavy Quarks, Flavor Mixing, and CP Violation, (La Plagne, 1985), CMU-HEP-85-2.

73. R. Shrock and S. Treiman, Phys. Rev. D**19**, 2148 (1979); J. Donoghue *et al.*, Phys. Lett. **119B**, 412 (1982); P. Ginsperg and M. Wise, Phys. Lett. **127B**, 111 (1983); J. Bijnens, H. Sonoda, and M. Wise, Phys. Rev. Lett. **53**, 2367 (1984).

74. The long-distance effect might change the theoretical prediction substantially. L. Wolfenstein, Nucl. Phys. **B160**, 501 (1979).

75. A. Ali and T. Young, Phys. Lett. **65B**, 275 (1976); V. Barger and R. Phillips, Phys. Rev. D**14**, 80 (1976); I. Hinchliffe and C. Llewellyn-Smith, Nucl. Phys. **B114**, 45 (1976); W. Wilson, Phys. Rev. D**16**, 742 (1977); K. Yamada, Phys. Rev. D**22**, 1676 (1980), and references therein.

76. See the second reference in Ref. 63.

77. Ref. 6; X. Pham and R. Nabavi, Phys. Rev. D**18**, 220 (1977); J. Cortes, Phys. Rev. D**24**, 2529 (1981). Also, see Ref. 78.

78. M. Suzuki, Nucl. Phys. **B145**, 420 (1978); N. Cabibbo and L. Maiani, Phys. Lett. **79B**, 109 (1978); A. Ali and E. Pietarinen, Nucl. Phys. **B154**, 519 (1979); N. Cabibbo, G. Corbo, and L. Maiani, Nucl. Phys. **B155**, 93 (1979).

79. E. Bloom and F. Gilman, Phys. Rev. Lett. **25**, 1140 (1970).

80. G. Altarelli *et al.*, Nucl. Phys. **B208**, 365 (1982).

81. R. Baltrusaitis *et al.*, Phys. Rev. Lett. **54**, 1976 (1985).

82. M. Gaillard and B. Lee, Phys. Rev. Lett. **33**, 108 (1974); G. Altarelli and L. Maiani, Phys. Lett. **52B**, 351 (1974).

83. G. Altarelli, N. Cabibbo, and L. Maiani, Phys. Rev. Lett. **35**, 635 (1975).

84. R. Rückl, U. of Munich Habilitationsschrift, PRINT-83-1063.

85. G. Altarelli *et al.*, Phys. Lett. **99B**, 141 (1981) and Nucl. Phys. **B187**, 461 (1981).

86. The paramter h is given by

$$h = \left(\frac{31}{4} - \pi^2\right) + \frac{19}{4}\frac{c_-^2 - c_+^2}{2c_+^2 + c_-^2} + 3\frac{\alpha_s(Q^2) - \alpha_s(M_W^2)}{\alpha_s(Q^2)}\frac{c_+^2\rho_+ + c_-^2\rho_-}{2c_+^2 + c_-^2}$$

with $\rho_+ = -0.47, -0.51, -0.57$ and $\rho_- = 1.36, 1.48, 1.65$ for $n_f = 4, 5, 6$ respectively.

87. The regularization scheme in QCD used throughout this chapter is the modified minimal subtraction scheme ($\overline{MS}$-scheme).

88. U. Baur and H. Fritzsch, Phys. Lett. **109B**, 402 (1982).

89. In the figures 2.11(a) and 2.11(b), the Λ for the LLA calculation is renormalized at each point to give the same α_s as given by the improved formula (2.45) with the nominal Λ value.

90. V. Mathur and T. Rizzo, Phys. Rev. D**16**, 3343 (1977).

91. J. Ellis, M. Gaillard, D. Nanopoulos, Nucl. Phys. **B100**, 313 (1975).

92. The estimates from $M_{D^*} - M_D$, the potential model, and the MIT bag model are consistent and give $f_D = 100$ to 150 MeV. E. Golowich, Phys. Lett. **91B**, 271 (1980); H. Krasemann, Phys. Lett. **96B**, 397 (1980); M. Suzuki, UCB-PTH-85/32.

93. H. Fritzsch and P. Minkowski, Phys. Lett. **90B**, 455 (1980).

94. M. Bander, D. Silverman, and A. Soni, Phys. Rev. Lett. **44**, 7 (1980).

95. B. Bernreuther, O. Nachtmann, and B. Stech, Z. Phys. **C4**, 257 (1980). They also speculated about a deviation from $V - A$ interaction due to soft gluon effects.

96. Y. Igarashi, S. Kitakado, M. Kuroda, Phys. Lett. **93B**, 125 (1980).

97. K. Shizuya, Phys. Lett. **100B**, 79 (1981).

98. H. Sawayanagi *et al.*, Phys. Rev. D**27**, 2107 (1983).

99. B. Ward, Phys. Rev. D**28**, 1215 (1983).

100. I. Bigi, Phys. Lett. **90B**, 177 (1980).

101. N. Despande, N. Gronau, D. Sutherland, Phys. Lett, **90B**, 431 (1980).

102. V. Barger, J. Leveille, and P. Stevenson, Phys. Rev. D**22**, 693 (1980).

103. It is assumed that the probability that the spectator $\bar{u}$ quark is annihilated by another u quark is small (OZI rule).

104. I. Bigi and M. Fukugita, Phys. Lett. **91B**, 121 (1981).

105. H. Albrecht *et al.*, DESY preprint 85-048 (1985).

106. J. Hauser, PhD thesis, California Institute of Technology, CALT-68-1275 (1985).

107. D. Fakirov and B. Stech, Nucl. Phys. **B133**, 315 (1978); N. Cabibbo and L. Maiani, Phys. Lett. **73B**, 418 (1978).

108. H. Fritzsch, Phys. Lett. **86B**, 343 (1979).

109. J. Donoghue and B. Holstein, Phys. Rev. D**21**, 1334 (1980).

110. N. Deshpande, M. Gronau, and D. Sutherland, Phys. Lett. **90B**, 431 (1980); N. Gronau and D. Sutherland, Nucl. Phys. **B183**, 367 (1981).

111. M. Bonvin and C. Schmid, Nucl. Phys. **B194**, 319 (1982).

112. B. Guberina *et al.*, Phys. Lett. **89B**, 111 (1979).

113. Y. Koide, Phys. Rev. D**20**, 1739 (1979).

114. I. Bigi, Z. Phys. **C6**, 83 (1980).

115. T. Kobayashi and Y. Yamazaki, Prog. Theor. Phys. **65**, 775 (1981).

116. R. D. Peccei and R. Rückl, in the Proceedings of the Ahrenshoop Symposium (Ahrenshoop, 1981).

117. G. Altarelli and L. Maiani, Phys. Lett. **118B**, 414 (1982).

118. N. Bilic, B. Guberina, and J. Trampetic, Nucl. Phys. **B248**, 261 (1984).

119. R. Baltrusaitis *et al.*, Phys. Rev. Lett **55**, 150 (1985).

120. M. Suzuki, Phys. Rev. Lett. **43**, 818 (1979).

121. M. Glück, Phys. Lett. **88B**, 145 (1979).

122. L. Abbott, P. Sikivie, and M. Wise, Phys. Rev. D**21**, 768 (1980).

123. A. Sanda, Phys. Rev. D**22**, 2814 (1980).

124. J. Finjord, Nucl. Phys. **B181**, 74 (1981).

125. V. Barger and S. Pakvasa, Phys. Rev. Lett. **43**, 812 (1979); M. Gavela *et al.*, Phys. Lett. **87B**, 249 (1979).

126. D. Sutherland, Phys. Lett. **90B**, 173 (1980). Also, Ref. 109 and 110.

127. T. D. Lee, R. Oehme, and C. N. Yang, Phys. Rev. **106**, 340 (1957).

128. For example, see the text by T. D. Lee in Ref. 11.

129. A. Pais and S. Treiman, Phys. Rev. D**12**, 2744 (1975); L. Okun and V. Zakharov, and B. Pontecorvo, Lett. Nuovo Cimento **13**, 218 (1975).

130. When CP is not conserved, r can exceed $1/2$, or equivalently p can exceed 1.

131. One of the two could be a spin-1 particle, since it still involves only one helicity amplitude A_{00}. When more than one helicity amplitude is involved, they have to be treated as different channels.

132. If the current is right-handed, the result is the same. In general, the contribution comes from only the part of the Hamiltonian that combines the initial-state fermion pair in a parity-minus state as well as the the final-state fermion pair. The calculation of the coefficient involves a Fierz transformation.

133. S. Glashow and S. Weinberg, Phys. Rev. D**15**, 1958 (1977).

134. M. Gaillard and B. Lee, Phys. Rev. D**10**, 897 (1974).

135. A. Datta and D. Kumbhakar, Z. Phys. **C27**, 515 (1985).

136. R. Rockmore and T. Yao, Phys. Rev. Lett. **18**, 501 (1967); K. Kang and D. Land, Phys. Rev. Lett. **18**, 503 (1967), and references therein.

137. J. Donoghue, E. Golowich and R. Holstein, Phys. Lett. **135B**, 481 (1984); I. Bigi and A. Sanda, Phys. Lett. **148B**, 205 (1984); M. Pennington, Phys. Lett. **153B**, 439 (1985).

138. L. Wolfenstein, Carnegie-Mellon U. Preprint CMU-HEP85-10; J. Donoghue *et al.*, U. of Massachusetts Preprint UMHEP-233.

139. We ignore the contribution from the penguin diagram in this section. If the KK, $\pi\pi$ rate difference is due to the penguin diagram, then the corresponding diagram for $D^0 - \overline{D}^0$ mixing is the 'siamese-penguin' diagram, which then has to be added to the box diagrams. J. Donoghue, E. Golowich, and G.

Valencia, UMHEP-234.

140. PEP design report, LBL-4288, SLAC-189, UC-28.

141. R. Helm *et al.*, SLAC-PUB-3070.

142. J. Jackson, 'Classical Electrodynamics,' (John Wiley & Sons, 1975), p. 661.

143. M. Sands, 'The Physics of Electron Storage Rings — An Introduction,' SLAC-121 (1970).

144. J. Paterson, a private communication.

145. A. Breskin *et al.*, Nucl. Instrum. Methods. **124**, 189 (1975).

146. D. Ouimette and D. Porat, IEEE Trans. Nucl. Sci. **29**, 290 (1982).

147. R. Early, PEP-NOTE-326 (1979) unpublished.

148. I. Tamm and I. Frank, Doklad. Akad. Nauk. SSSR **14**, 107 (1937).

149. I. Tamm, J. Phys. **1**, 439, (1937).

150. A. Bodek *et al.*, Z. Phys. **C18**, 289 (1983).

151. Y. Tomkiewicz and E. Garwin, SLAC-PUB-1277 (1973).

152. J. Heintze *et al.*, Nucl. Instrum. Methods, **138**, 641 (1976).

153. S. Wemple, J. Chem. Phys. **67**, 2151 (1977).

154. H. Hinterberger and R. Winston, Rev. Sci. Instr. **37**, 1094 (1966).

155. G. Eigen and E. Lorenz, Nucl. Instr. Methods. **166**, 165 (1979).

156. P. Carlson, Nucl. Instrum. Methods. **158**, 403 (1979).

157. The cuts used are $P < 2$ GeV/c, and $n_e > 3$.

158. D. Ouimette, D. Porat, A. Tilghman, and C. Young, IEEE Trans. Nucl. Sci. **30** No.1, 328 (1983).

159. A forward-backward energy-asymmetry cut is also used to help reject two-photon interactions. This cut was found to have negligible effect on the final hadron sample that had passed other cuts.

160. H. Yamamoto, J. Comput. Phys. **52**, 597 (1983).

161. G. J. Feldman *et al.*, Phys. Rev. Lett. **38**, 1313 (1977); P. Avery *et al.*, Phys. Rev. Lett. **44**, 1309 (1980); R. Bailey *et al.*, Phys. Lett. **132B**, 237 (1983); M. Althoff *et al.*, Phys. Lett. **138B**, 317 (1984).

162. C. Bebek *et al.*, Phys. Rev. Lett. **49**, 610 (1982);

163. J. Yelton *et al.*, Phys. Rev. Lett. **49**, 430 (1982).

164. W. Bartel *et al.*, Phys. Rev. Lett. **146B**, 121 (1984).

165. M. Althoff *et al.*, Phys. Lett. **126B**, 493 (1983).

166. H. Albrecht *et al.*, Phys. Lett. **150B**, 235 (1985).

167. M. Derrick *et al.*, Phys. Lett. **149B**, 519 (1984)

168. The amount of the proton contamination depends on how many protons are generated above 3.2 GeV/c, and the Monte Carlo is consistent with the recent measurement of baryon production at PEP. H. Aihara *et al.*, Phys. Rev. Lett. **52**, 577 (1984).

169. The Monte Carlo reproduces the measured short and long distance charge correlations. Thus this effect is already taken into account in Table 4.5. The Bose Einstein effect, however, is not simulated in the Monte Carlo, which enhances the same sign pions when they are close in phase space. This can potentially enhance $K^-\pi^+\pi^+$ (right-sign) combinations over $K^-\pi^+\pi^-$ (wrong-sign) combinations. However, it is found that the momenta of the two pions in a typical D^* candidate are different enough that the effect is negligible.

170. R. Peruzzi *et al.*, Phys. Rev. Lett. **39**, 1301 (1977); D. Sharre *et al.*, Phys. Rev. Lett. **40**, 74 (1978); M. Piccolo *et al.*, Phys. Lett. **70B**, 260 (1977); V. Vuillemin *et al.*, Phys. Rev. Lett. **41**, 1149 (1978).

171. G. S. Abrams *et al.*, Phys. Rev. Lett. **43**, 481 (1979); R. Schindler *et al.*, Phys. Rev. D**24**, 78 (1981).

172. R. H. Schindler, California Institute of Technology Report No. CALT-68-1161, and Proceedings of the 22nd International Conference of High Energy Physics, Leiptzig, DDR, July 1984, to be published. Also, R. Baltrusaitis *et al.*, Phys. Rev. Lett. **54**, 1976 (1985).

173. In the Monte Carlo, a charged track is said to be 'found' when there is at least one found track for which more than half of the hits on it are actually

generated by that particle.

174. By Ref. 70. The number is for neutrons at $80 - 240$GeV. The pions and kaons in the energy range of our interest (a few tenths to a few GeV) have similar cross sections.

175. M. Coles *et al.*, Phys. Rev. D**26**, 2190 (1982).

176. An upper limit on $\Gamma(b \to ul\nu)/\Gamma(b \to cl\nu)$ of 4% has been set by A. Chen *et al.*, Phys. Rev. Lett. **52**, 1084 (1984).

177. For example, see D. Koop *et al.*, Phys. Rev. Lett. **52**, 970 (1984).

178. S. Csorna *et al.*, Phys. Rev. Lett. **54**, 1894 (1985); Also see Ref. 162 and 167.

179. A. Chen *et al.*, Phys. Rev. Lett. **51**, 634 (1983); H. Aihara *et al.*, Phys. Rev. Lett. **53**, 2465 (1984); M. Althoff *et al.*, Phys. Lett. **136B**, 130 (1984); H. Albrecht *et al.*, Phys. Lett. **153B**, 343 (1985).

180. G. Abrams *et al.*, Phys. Rev. Lett. **44**, 10 (1980).

181. H. Georgi and H. Politzer, Nucl. Phys. **B136**, 445 (1978).

182. M. Derrick *et al.*, Phys. Lett. **146B**, 261 (1984).

183. See, for example: N. Reay, in the Proceedings of the International Symposium on Lepton and Photon Interactions at High Energies, (Ithaca, 1983).

184. J. Yelton *et al.*, Phys. Rev. Lett. **52**, 2019 (1984).

185. The sign of impact parameter for the general hadronic events is defined to be the sign of the z component of $\vec{t} \times \vec{b}$, where $\vec{t}$ is the track direction. Thus, the distribution of b is expected to be symmetric around zero.

186. The effect may be estimated as follows: If the thrust axis is used as the D^0 direction, the general hadronic tracks have $< b > \sim +40\mu$m (see Section 3.5). When this is added in quadrature to the typical resolution of $\sim 500\mu$m, it increases by only $\sim$0.3%.

187. The $c\tau$'s used in the Monte Carlo are; 420 μm for hadrons containing a b-quark, 130 μm for D^0, 280 μm for D^+, 60 μm for F^+, and 70 μm for Λ_c.

188. The large round-off error that occurs when κ is small can be avoided by

using the approximation $xe^{x^2}\mathrm{erfc}(x) = 0.564190 - 0.274030/x^2$ for x^2 greater than $\approx$50. For example see: M. Abramowitz and I. Stegun, 'Handbook of Mathematical Functions,' (National Bureau of Standards, 1972) p. 316.

189. Bins with small number of counts have been combined.

190. A. Bodek *et al.*, Phys. Lett. **113B**, 82 (1982).

191. It was assumed that charm particle pairs are created incoherently. However, if $D^0 - \overline{D}^0$ pairs are produced in a $C = -$ state (which is the case for Ψ'' decays) then the fraction of same sign di-muons could be half that expected for incoherent cases. Thus, if such production modes dominate the D^0 component in the observed di-muons, then the quoted upper limit could be underestimated by up to factor of 2. See R. Kingsley, Phys. Lett. **63B**, 329 (1976).

192. G. Feldman *et al.*, Phys. Rev. Lett. **38**, 1313 (1977). Also, see G. Goldhaber *et al.*, Phys. Lett. **69B**, 503 (1977).

193. W. Altohoff *et al.*, Phys. Lett. **138B**, 317 (1984).

194. The other experiments that set upper limits on $D^0 - \overline{D}^0$ mixing are, P. Avery *et al.*, Phys. Rev. Lett. **44**, 1309 (1980) (11 %); J. Aubert *et al.*, Phys. Lett. **106B**, 419 (1981) (20 %); R. Bailey *et al.*, Phys. Lett. **132B**, 237 (1983) (7%).

195. F. Buccella and L. Oliver, Nucl. Phys. **B162**, 237 (1980).

196. R. Kingsley, S. Treiman, F. Wilczek, and A. Zee, Phys. Rev. D**11**, 1919 (1975).